Investigation of the Solid Electrolyte Interface on $LiMn_2O_4$ through Neutron Reflectometry

by

Brian Bruce Kitchen

A dissertation submitted in partial fulfillment
of the requirements for the degree of
Doctor of Philosophy
(Nuclear Engineering and Radiological Sciences)
in The University of Michigan
2015

Doctoral Committee:

Professor David K. Wehe, Chair
Associate Professor Bart Bartlett
Joseph A. Dura, National Institute of Standards and Technology
Professor Gary S. Was

For all the people who made this possible. My wife who pushed me to do my best, my kids who made me realize there is more to life, my family for all their support. Thank you to all the friends I made, to those who helped me in word and in deed, and to those who challenged me to do better.

ACKNOWLEDGEMENTS

I owe Dr. Joe Dura at NIST a great deal for his contribution to my work; from mentoring to teaching, this effort would not have been possible without him. I would like to thank Professor Wehe for taking me on as a student following the departure of my first advisor. I owe Dr. Mike Hartman a great deal of thanks. Mike first brought me on as a graduate student and taught my a great deal, even more than I realized when he left for greener pastures. All the staff at the Lurie Nanofabrication Facility (LNF) and the Electron Microbeam Analysis Laboratory (EMAL) at the University of Michigan. Finally the staff at the National Institute of Standards and Technology (NIST) who aided me along this journey.

TABLE OF CONTENTS

LIST OF FIGURES

Figure

LIST OF TABLES

Table

LIST OF APPENDICES

Appendix

ABSTRACT

Investigation of the Solid Electrolyte Interface on $LiMn_2O_4$ through Neutron Reflectometry

by

Brian Kitchen

Chair: Professor David Wehe

The Solid Electrolyte Interface (SEI) is of significant importance to successful operation of new high-energy-density lithium-ion batteries. The SEI governs chemical interaction between the electrode (cathode or anode) and the electrolyte in addition to modulating the diffusion of lithium between the mediums. SEI stability throughout the lifetime of the lithium-ion battery is essential for long-term stable operation. While both the anode and cathode exhibit an SEI growth, the anode growth is much thicker and more easily probed. In contrast the SEI on the cathode is very thin on the order of nanometers and has proven to be much more difficult to probe *in-situ*.

This dissertation focuses on the application of Neutron Reflectometry (NR) to the study of the SEI on a $Li_xMn_yO_z$ thin-film cathode. A cathode which meets the stringent morphological requirements for NR is developed with a roughness <2 nm rms. The thin-film cathode is produced by a sol-gel spinning technique on a silicon substrate with platinum and silicon dioxide thin films which serve as charge collection and buffer layer. A method of electro-depositing lithium on a copper thin-film is developed to produce a dendrite-limited lithium thin-film anode to serve as the

counter/reference electrode in an experimental cell. An electrochemical NR sample cell is built to produce a fully-functional full-cell battery for *in-operando* NR experimentation.

Two *in-operando* NR experiments are performed where one sample is allowed to sit at an open-circuit, and the other has the potential held slightly above the reported open-circuit value for $LiMn_2O_4$ to prevent self-discharge. NR results indicate a SEI of thickness between 10-16 nm is formed immediately upon introduction of electrolyte. The scattering length density of the SEI which forms during the open circuit experiment is observed to be lower than that of the SEI on the potential hold experiment. The thickness of the cathode layer is observed to increase throughout the experiment to an extent which is not explainable by known volume expansion of $LiMn_2O_4$ through a Jahn-Teller effect. The SEI formed by cycling the battery prior to allowing self-discharge to form $LiMnO_2$ is observed to prevent significant degradation of the cathode layer.

CHAPTER I

Introduction

The use of power has come to be the essence of the modern economy. Electrical power is used to provide energy for transportation, manufacturing, entertainment, and communications. However, the use of power has resulted in global warming, limited fossil-fuels, and massive air pollution in cities. As a result of these issues with power, the scientific community as well as the consumer have been pressing toward more efficient uses of power as well as renewable power. Batteries, in conjunction with electric motors, are a method in which energy may be used more efficiently to provide power for many applications. Batteries are much more efficient than the internal combustion engine for transportation in that efficiency losses due to heat are limited. Lithium-ion batteries have a higher gravimetric and volumetric storage storage capacity than Nickel-Metal Hydride, the previous generation of secondary (rechargeable) battery, and are more suited to technologies where weight and size of the power supply is important.

Batteries have been used extensively since the first batteries were commercially produced. Initially batteries were used to power devices such as flashlights, radios, and other devices which had a small load where the battery would last for an extended period of time. As battery technology has evolved to store more power for longer periods of time, the devices in which they are used have evolved to utilize this

power for our benefit. Current applications range from medical technologies, portable electronics, electric vehicles, and others. In order to be viable for the diverse range of applications, future battery technologies must be robust with large storage capacities along with being highly-stable to charge cycling for long term, heavy usage.

Lithium-ion batteries have been the front-runner in energy storage since they have been commercially available for almost every application where high-energy density, deep depth of discharge, and rechargeablility are required. Lithium being the lightest metal (M= 6.9 g mol^{-1} and $\rho = 0.5$ g cm^{-3}) as well as the most electropositive (-3.04 V vs standard hydrogen electrode) allows for a higher gravimetric and volumetric energy density than any other metal(1; 2). Current lithium-ion batteries have been limited to lower-energy density intercalation materials, generally with carbon anodes, in order to maintain consistent operability. With rapid development of portable electronics and electric transportation, it is necessary to develop high-energy density materials with consistent operability in order to keep up with consumer demands. Battery energy density has slowly progressed, increasing only by a factor of 5 in the last 200 years(3) as opposed to the well known Moore's las, in which electronic processing power doubles every 18 months. The major focus in lithium battery research is to increase capacity while maintaining cyclability in order to more readily meet the needs of the power consumer in which current lithium-ion battery technology falls short. While capacity is highly desired from lithium-ion batteries, capacity is a problem more readily solved than the cyclability problem.

Poor cyclability and performance in a lithium-ion battery is due to the rapid loss of lithium from the production of a Solid Electrolyte Interphase (SEI)(4) and the impedance rise associated with SEI evolution(5; 6). The formation and growth of the SEI is due to a thermodynamic instability between the electrode and the electrolyte(7). This instability is a result of the highly oxidizing or reducing nature of the electrodes in the battery. The highly oxidative or reductive nature of the

electrodes is required in order to produce a high-voltage battery such as lithium-ion, but the large chemical potential associated with this nature results in parasitic reactions between the electrode and the electrolyte. On immersion in an electrolyte, a lithium-ion cathode will immediately react with the electrolyte to form a passivation layer on the surface of the electrode(8). In contrast, an anode (not including lithium metal) will form an SEI upon its first charge. Since battery capacity is directly related to the amount of lithium free to move from the cathode to the anode, when lithium is removed from the system through an irreversible reaction, the capacity decreases. Performance of the lithium-ion battery is dependent on the kinetic diffusion of lithium through the SEI and a poor stability SEI will result in significant ageing of the electrodes. SEI thickness and stability are dependent on the electrode material, the electrolyte solvent, the electrolyte salt, additives, and the temperature at which the battery is operated(9). Additives, surface structure, and electrolyte composition are the main areas where improvements in SEI stability may be achieved(10).

Performance of the lithium-ion battery is directly tied to the thickness and composition of the SEI layer. The SEI introduces an interfacial diffusion barrier where the resistance to lithium diffusion is influenced by the diffusion distance as well as the phases through which lithium must diffuse. This interfacial resistance is observed as impedance which will affect the level of current which may be drawn from the battery. The impedance rise may be due to the thickness of the SEI layer(5), as well as evolution of the SEI composition and morphology(11). Once the SEI layer is initially formed upon electrolyte/electrode contact, chemical reactions will continue to occur on a much longer time frame which result in evolution of the layer. This is commonly referred to as ageing. The rate of ageing is highly dependent on the storage temperature as the evolution is believed to be dependent on kinetic processes in the SEI as well as thermodynamic driving forces. The effects of ageing are more important on the cathode electrode, and are highly dependent on the State of Charge

(SOC)(7). On the anode electrode, ageing is more limited and while some parasitic corrosion can be observed, the impact on battery life is more limited than cathode ageing. Battery cell power has been shown to fade upon storage while charged, and the fade is directly related to the SOC and storage temperature(6).

The stability of the SEI through charge cycling as well as storage is the most important factor in retaining capacity(12) in lithium-ion batteries. The SEI separates the electrode from the electrolyte, while serving as a charge transfer medium for the lithium-ions. The first charge of the battery forms the SEI on an anode(13), when the battery is discharged the SEI can become damaged. Damage may be in the form of SEI dissolution, change in electrode dimension (i.e. swelling or contraction) which can cause crack formation in the SEI. If the SEI is cracked, then lithium-ions are again lost to repairing the SEI on the following charge/discharge cycle. Additionally, the layer may dissolve, or self-discharge over time which will also reduce the amount of lithium available for the system(4). The continuous formation of secondary reaction products results in a thickness increase as well as a morphological change to the SEI which has been suggested to be the primary cause of impedance rise. It has been suggested(14; 15; 16; 17) that some components of the SEI may be soluble in the electrolyte solution and partial dissolution of the SEI may occur. Over time, these components of the SEI may dissolve and leave behind an exposed electrode which will react with the electrolyte and further reduce available lithium. The dissolved species may also drift from one electrode to the other and further react with the opposite electrode resulting in some polimerization of SEI components as well as proton production(7). These processes can significantly reduce capacity in very few cycles. Tarascon(1) in a recent review of challenges in future Li-battery research describes the necessity for developing a better understanding of the SEI interface. The review points out that in order to develop material couplings with advanced energy storage properties, a sound understanding of the SEI and protocols to better

analyze the SEI must be realized.

The purpose of this thesis is to shed light on the electrolyte/electrode interface on Lithium Manganese Oxide ($LiMn_2O_4$). $LiMn_2O_4$ is a cathode material which is highly desirable from a commercial standpoint. Compared to the currently ubiquitous $LiCoO_2$ cathode design, $LiMn_2O_4$ has some significant commercial advantages. Manganese is more abundant than cobalt and is currently about 15x cheaper per mole than cobalt (based upon current market price of \$1/lb for manganese vs \$13.90/lb for cobalt as of 06/12/14). $LiMn_2O_4$ is more environmentally friendly, it inherently produces a higher voltage vs Li/Li^+, and rapid oxygen release of the de-lithiated cathode (resulting in fire) occurs at a temperature high enough to be considered a safety non-issue making it a good choice for automotive purposes(18). There are some major issues to address prior to commercialization of $LiMn_2O_4$, namely the significant corrosion of the cathode surface in an acidic electrolyte, especially while charged(19) and at elevated temperatures(20). Those significant issues can and are currently being addressed through surface coatings and introduction of new chemical phases on the surface of $LiMn_2O_4$ to inhibit the degradation and loss of active material. The key to commercialization of $LiMn_2O_4$ is a better understanding of the electrolyte/electrode interface and how the degradation processes occur.

The work in this thesis documents the development of a lithium anode, a thin-film $LiMn_2O_4$ cathode, an electrochemical cell suitable for neutron reflectometry, and the use of neutron reflectometry to study the electrolyte/$LiMn_2O_4$ interface as well as changes in the $LiMn_2O_4$ thin-film as a function of charge cycling and potential hold. The anode is developed by using a novel dynamic electrodeposition method where a silicon wafer with a copper thin-film is immersed in an electrolyte bath and spun with a masked lithium counter electrode serving as the lithium source. This novel method allowed fairly uniform deposition of lithium across the surface of the silicon wafer without obvious lithium dendrite buildup. The cathode was developed

with minimal surface roughness on the order of 2 nm to be suitable for neutron reflectometry in addition to having characteristic $LiMn_2O_4$ electrochemical response. The electrochemical cell was designed to fully electrically insulate the battery cell while allowing in-flow and out-flow of electrolyte in addition to a novel method of electrode contact on the anode surface. Neutron reflectometry was performed on two samples with different conditions; the first where the sample was allowed to sit at an open circuit potential which drifts with time, and the second where the cell potential was held throughout the neutron reflectometry measurements.

CHAPTER II

Background

A battery is an electrochemical energy storage device intended to provide a portable power supply and is composed of four essential components: anode, cathode, electrolyte, and separator. The anode is the electrode where an oxidation-reaction occurs during discharge and an electron is donated to an external circuit. The cathode is the electrode where a reduction-reaction occurs during discharge and the electron is accepted from the external circuit. When a secondary battery is charged these reactions reverse and therefore oxidation occurs on the cathode and reduction occurs on the anode. The electrolyte is a electronic insulator, but also must provide the essential function as an ionic-conduction medium. The separator functions to prevent contact between the anode and cathode while not inhibiting the electrolyte function. In some cases the separator and electrolyte are the same material such as in lithium-polymer battery types. Figure **??** shows schematically how the electrochemical battery cell functions during the discharging and charging steps.

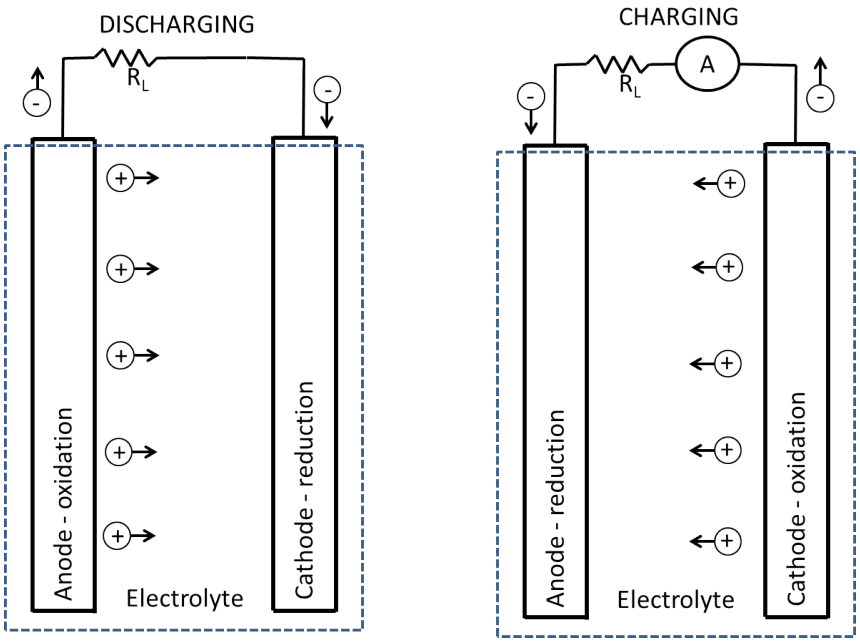

Figure 2.1: General schematic description of an electrochemical energy storage device highlighting the movement of ions and electrons while charging or discharging the electrochemical cell. While discharging ions move toward the cathode in the electrolyte and electrons travel through an external circuit with a load resistance before meeting the ion in the cathode. While charging a current supply pumps electrons to the anode which forces ions to leave the cathode and diffuse through the electrolyte to neutralize at the anode.

There are two types of batteries: primary and secondary. Primary batteries are intended to be single-use and involve irreversible reaction mechanisms. Secondary battery types involve reversible reaction mechanisms and can be recharged.

The voltage and capacity of the battery are implicitly dependent upon the materials used to construct the battery. The voltage is dependent upon the chemical potentials of the anode and cathode and is related to the difference in the free energy of the half cells. Generally in electrochemistry the experimenter is interested in the processes occurring at one of the two electrodes. As the processes which occur on either electrode are primarily dependent upon the potential difference between the electrodes, each electrode can be treated independently of the other within consideration of the potential difference. A half-cell is defined as the anode or cathode in the

electrolyte without a second electrode. Two half-cells make up a oxidizing-reducing couple, meaning reduction of one electrode leads to oxidation of the other electrode. An example of a half-cell can easily be shown from a charge-unbalanced chemical equation of a typical commercial battery chemical design:

$$LiCoO_2 + C \rightleftharpoons Li_{0.5}CoO_2 + LiC_6 \tag{2.1}$$

In this case there are two half-cells:

$$LiCoO_2/Li/Li^+$$

$$Li^+/Li/C$$

where $LiCoO_2$ vs Li/Li^+, and Li/Li^+ vs C are the two individual half cells, where Li/Li^+ is a terminology used to describe the half-cell material versus the metal/metal ion. Each half-cell material cannot be described in terms of its free energy of an ion without a corresponding alternate electrode. $LiCoO_2$ has no potential in an electrolyte without another electrode for which a thermodynamic couple can be made. The Li/Li^+ terminology is used to allow an electrochemical description of the half-cell by itself through the assumption that it is opposite the metal whose ion is transported through the electrolyte. When two half-cells are placed into a couple such as inserting both materials into the electrolyte the half-cell description (vs Li/Li^+) is no longer needed as there are two materials which make a thermodynamic couple.

In the full-cell described in equation 2.1, each side of the electrochemical equation 2.1 has a free energy balance described as reactants (R) and products (P):

$$G_R = \mu_{Li_{cathode}} N_{Li_{cathodeR}} + \mu_{Co} N_{Co} + \mu_O N_O + \mu_C N_C$$

$$G_P = \mu_{Li_{anode}} N_{Li_{anode}} + \mu_{Li_{cathode}} N_{Li_{cathodeP}} + \mu_{Co} N_{Co} + \mu_O N_O + \mu_C N_C$$

where μ is the chemical potential of an atom in the cell, and N is the number density of that atom. In a lithium-ion battery the assumption is that the anode, cathode, and electrolyte structure all remain stable in the energy balance equation. Lithium-ions in the electrolyte are free to move wherever their energy is the lowest by virtue of the highly ion-conductive nature of the electrolyte. This means that the free-energy difference is only dependent upon the chemical potential difference of lithium between the anode and cathode:

$$\Delta G = \mu_{Li_{anode}} N_{Li_{anode}} + \mu_{Li_{cathode}} N_{Li_{cathodeP}} - \mu_{Li_{cathode}} N_{Li_{cathodeR}}$$

$$\text{where, } N_{Li_{cathodeR}} = N_{Li_{anode}} + N_{Li_{cathodeP}} \text{ or,}$$

$$N_{Li_{cathodeP}} = N_{Li_{cathodeR}} - N_{Li_{anode}} \text{ therefore,}$$

$$\Delta G = (\mu_{Li_{anode}} - \mu_{Li_{cathode}}) N_{Li_{anode}} \tag{2.2}$$

The free-energy difference is also related to voltage through the Nernst equation (21):

$$\Delta G = -nFE \tag{2.3}$$

where E is the potential difference (i.e. Voltage), n is the number of atoms transferred, and F is Faraday's constant. Combining equations 2.2 and 2.3 gives:

$$E = \frac{-(\mu_{Li_{anode}} - \mu_{Li_{cathode}})}{F}$$

which shows that the potential difference in an ideal lithium-ion battery is due to the potential difference of lithium between the anode and cathode.

2.1 History of lithium-ion batteries

Lithium secondary battery research began sometime shortly after the second world war. It is hard to determine when lithium was first identified as an ideal electrochemical storage material; however, defense department reports indicate research was ongoing at the outset of the cold war as documented in quarterly progress reports(22; 23). Original lithium secondary battery designs enlisted the use of lithium metal as the anode(24). There was significant effort placed into lithium metal as an anode(25) because of the significant energy density potentially available, figure 2.2.

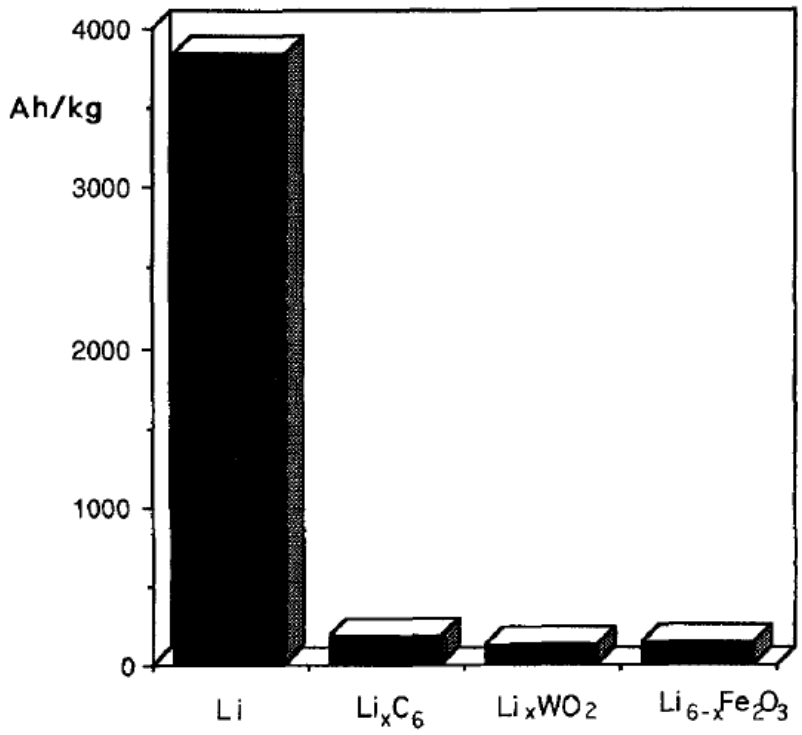

Figure 2.2: Specific capacity for Li_xC_6 (x=0.5), Li_xWO_2 (x=1), and $Li_{6-x}Fe_2O_3$ (x=1) anodes in comparison with that of Li metal.(26)

Lithium metal for all of its theoretical praise, was never successfully implemented

as an anode for secondary battery applications. The primary reason for moving away from lithium metal anodes was safety in nature(1). Lithium metal when re-depositing on the anode during the charging step does so dendritically, where small thin nano-wires grow toward the cathode(27; 28). After a number of charging steps these dendrites can penetrate separators and when they come in contact with the cathode the short circuit can lead to a significant amount of heat and hydrogen gas release. The heat may ignite the gas leading to an explosion which is of obvious safety concern. The dendrite problem was never successfully addressed and as such anodic research drifted toward potential substitutes, namely graphite.

Dendritic growth is a result of the passivating layer on lithium metal changing the charge transfer kinetics at the lithium metal/electrolyte interface(28). Passivation occurs due to the significant electropositive nature of lithium metal and results in a plethora of chemical species when the metal comes in contact with any polar aprotic solution(29). The passivating layer alters the uniformity of the current density by introducing a non-uniform resistance at the interface and as such preferentially deposits lithium in high current density regions(30). Passivation to an extent reduces the active surface area of the lithium metal anode as some of the passivation chemical species do not allow lithium diffusion at the same rate in which it is being deposited(29). In addition to this mechanism, it has been shown that these areas of uneven deposition of lithium and dendrite nucleation sites are also related to the subsurface structure of the lithium anode(31). The non-uniform diffusion through the passivation layer from the electrolyte to the lithium metal leads to a non-uniform lithium deposition and leads to a local surface area increase. That change can not be accommodated by the passivated film and cracking will occur, which accelerates the deposition of lithium in that area. Not only does dendritic growth prove to be a safety issue, it also results in significant loss of active lithium due to re-formation of the passivation layer which irreversibly consumes lithium. As the passivation layer

grows due to these processes total available lithium for electrochemical cycling can be reduced to unusable levels. The significant passivation of lithium metal, coupled with dendritic growth, precludes lithium metal anode commercialization by limited lifetimes as the passivation layer reduces capacity and dendrites can lead to catastrophic failure of the battery.

The first lithium-ion battery was commercialized by Sony in 1991(32). This commercialization was the initial culmination of a technology which had spent the previous two decades working out design problems. Lithium-ion batteries as they are currently commercially produced are based upon several significant advances in battery design around this time; the rocking-chair design where ions are shuttled between the anodes without precipitating lithium metal, the discovery of lithiated transition metal oxides $LiMO_2$ (M = Mn, Co, Ni), and the implementation of carbon as an anode material.

2.1.1 Graphitic anode

In the 1980's a search was on for a suitable secondary lithium-ion battery anode. It was known at this point that lithium metal was too unstable due to dendrite formation to be of commercial use for safety reasons. Much effort was applied to lithium-aluminum alloys (33) as an anode as it retained a significant portion of the energy density of lithium metal. However, Li-Al alloys underwent significant swelling/contraction each cycle and eventually was recognized that it could not work commercially as the alloy capacity would diminish quickly due to damage from the volume change which can be as large as 97%(34). In the search for alternatives it was discovered that decomposition products from some polymers could be used as an anode. Kanno(35) was the first to publish a study on the use of carbon fibers as an anode material in addition to polymeric breakdown products. It seems there was some indication that carbon was the reason why these polymeric decomposition

products could be used as an anode (35). It was suggested through x-ray diffraction that lithium intercalated into the carbon matrix and could be useful as a negative electrode. This result led to significant research regarding carbon as an anode and led to the feasibility of a rocking-chair type secondary battery.

Carbon as an anode was a significant advancement for several reasons. It has a very small potential vs Li/Li^+ (26) and therefore the large initial potential difference between a lithiated spinel vs Li/Li^+ is generally preserved as shown in figure 2.3. Additionally carbon has a relatively large energy density (370 mA/g)(36), it is fairly stable to volume changes(26), is already electrically conductive so an additional conductive material in the anode is unnecessary, and most important commercially is that it is exceedingly cheap.

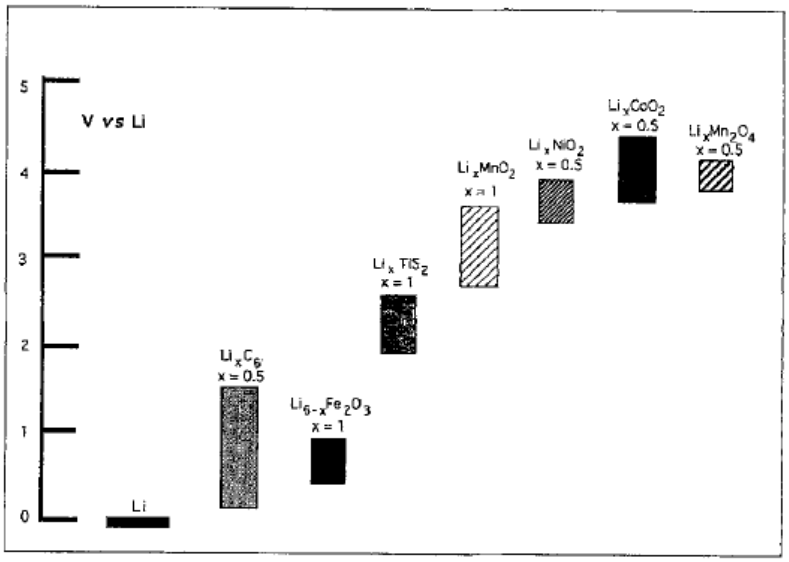

Figure 2.3: Potential ranges (vs. Li) of various Li-insertion compounds, calculated for the exchange of xLi equivalents per mole.(26)

Carbon does have some drawbacks; such as the voltage rise as a function of lithium loading. As the amount of lithium in the carbon lattice increases, the potential vs. lithium increases(37). From an applications perspective, this is very undesirable because the it makes power management difficult especially in cases where a constant

voltage is desired instead of just a constant load. Graphite has an additional drawback in that one of the best organic solvents for lithium-ion applications, Propylene Carbonate (PC), is incompatible due to co-intercalation of the PC with lithium in-between the graphene sheets resulting in exfoliation and breakdown of the carbonaceous anode in the first charge cycle (38). The solution to this problem was to transition to Ethylene Carbonate (EC) which has some disadvantages, namely its high melting point (34^oC) which prevents very low temperature operation even when mixed with other solvents to prevent solidification.

2.1.2 Rocking-Chair design

The rocking-chair design for lithium batteries was developed to inhibit dendritic lithium deposits on lithium metal(39; 40; 26). Rocking-chair designs for lithium-ion batteries inhibits dendritic growth by removing a lithium metal phase from the battery. The anode and cathode in a rocking-chair design are such that both electrodes store lithium within the crystal structure and the core structure is unchanged when lithium is inserted or removed (intercalated/de-intercalated). A visual description of this process can be found in figure 2.4 where it is shown that the metal ions sit in planes between the host material and therefore when lithium ions are moved from one electrode to the other the overall structure of the electrode does not change.

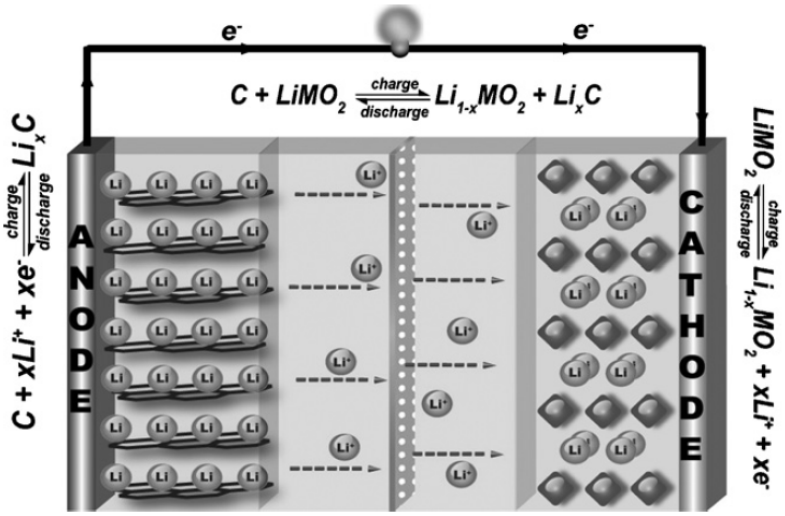

Figure 2.4: A representation of the rocking chair design. The carbonaceous anode graphene sheets allow lithium to diffuse into the graphite structure. Similarly the transition metal oxide cathode allows lithium to diffuse between the planes of octahedrally coordinated transition metal with oxygen. (41)

Initial rocking chair designs utilized negative electrodes such as $LiWO_2$ or $Li_6Fe_2O_3$ and a positive electrode such as TiS_2 or WO_3 (42; 43). These cell designs worked well, but are unmarketable systems as they have low achievable current rates due to slow diffusion of lithium in the electrode in addition to low energy density and difficulty in manufacturing. These cells were developed with lithium inserted into the anode through a separate cell where lithium would be opposite a WO_2 electrode as an example. The electrode with lithium inserted would be removed from this cell and coupled with a cathode where it could then be used for energy storage. This method of manufacturing proved to be unmarketable, but these designs did prove the efficacy of the rocking chair model and led to a search for better materials which would fill this role. It was not until the discovery of lithiated transition metal oxides that mainstream energy storage research moved toward the rocking chair design.

2.1.3 Lithiated Transition Metal Oxides

The discovery of lithiated transition metal oxides led to significant advances in lithium-ion battery designs as they have a large potential vs. Li/Li^+ and are lightweight, achieving a goal of high energy density. The lithiated transition metal oxides can also be very stable in a lithium-ion battery and have shown to maintain capacity for very long lifetimes when in a tailored battery system. The lithiated transition metal oxides have very small volume changes when de-intercalating/intercalating as they retain their crystal structure up to various degrees of lithium de-intercalation. This point is very important because without a significant change in the structure this system can be essentially reversible without taking into account electrolyte breakdown on the electrodes. Additionally, the small volume change is important as large volume changes can break up the passivation layer on the cathode/anode and remove lithium from the system through re-formation of the passivation layer.

The current most commercially available lithium-ion battery contains a $LiCoO_2$ cathode, which was initially discovered as a practical cathode in the early 1980s (44) around the time rocking-chair designs were initially being introduced. The success of the $LiCoO_2$ design was quickly followed by research in other similar compounds such as $LiNiO_2$, $LiVO_2$, $LiCrO_2$, $LiMnO_2$, and $LiMn_2O_4$(45; 46). Of these transition metal oxides the most promising were $LiCoO_2$, $LiNiO_2$, $LiMnO_2$, and $LiMn_2O_4$ however each has its own limitations. $LiCoO_2$ suffers from an irreversible phase change if more than half of the lithium is removed(47). $LiNiO_2$ has many advantages for being a cathode material including higher energy density than $LiCoO_2$, better stability in organic electrolytes because it has a lower potential in the fully charged state vs $LiCoO_2$. However, it is very difficult to produce without impurity phases which can rapidly reduce the capacity during operation(48) and is therefore commercially impractical. $LiMnO_2$ has a higher reversible capacity than $LiCoO_2$, and is much cheaper to produce. $LiMnO_2$ has two polytypes, a monoclinic and a orthorhombic, and both

undergo a progressive phase change to the spinel $Li_2Mn_2O_4$ after a few cycles. The progress for this phase change results in a highly disordered structure and significant loss of capacity is realized (49). $LiMn_2O_4$ has a slightly lower reversible capacity than $LiCoO_2$, but it has three main advantages including low-energy requirements for synthesis, cheap materials costs, and oxygen generation from a short-circuit leading to fire does not occur easily. These advantages make it a very attractive cathode material, especially for electric vehicles; however, $LiMn_2O_4$ undergoes significant corrosion in the delithiated state particularly at higher temperatures. Corrosion is defined generally as the toll which the degradation pathways take on the usefulness of the cathode material. Corrosion can be due to disproportionation or cracking from the formation of tetragonal phases due to the Jahn-Teller effect.

2.2 Lithium Manganese Oxide

2.2.1 Structure

$LiMn_2O_4$ is a spinel structure (space group Fd3m) with oxygen ions in the 32e site, Mn ion in the 16d site, and Li in the 8a site. In the structure oxygen ions are octahedrally coordinated with Mn, and lithium sits in a tetrahedral site bounded by oxygen from the MnO_6 octahedra. A representation of this structure is found in figure 2.5.

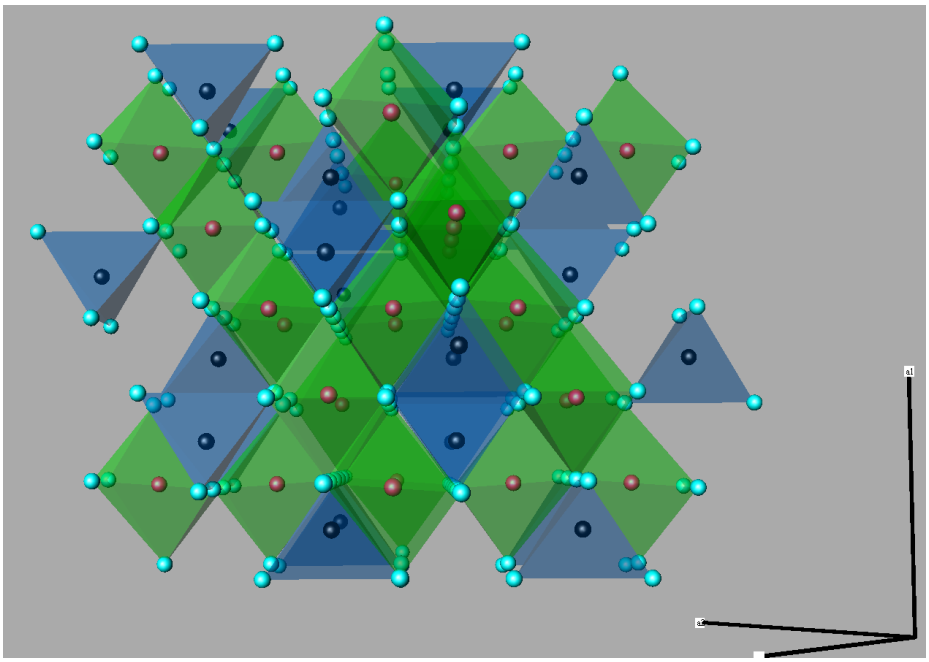

Figure 2.5: $LiMn_2O_4$ structure representation Fd3m, lattice parameter 8.248$\mathring{A}$. Lithium, Oxygen, and Manganese are represented as black, light-blue, and red, respectively.

Lithium sits within channels which allow diffusion without significant change in the spinel structure. Lithium may be removed from the structure electrochemically until a loading of x$\sim$0.28(50; 51). As lithium is removed from the structure a general contraction of the lattice parameter occurs (52). This contraction occurs in a single phase until approximately 34% of the initial lithium loading remains, at which point a λ-MnO_2 phase emerges as observed by x-ray diffraction (XRD) shown in figure 2.6. The gradual change in lattice parameter allows for relaxation to occur and prevents cracking of the crystal. $LiMn_2O_4$ sits between $LiMnO_2$ and λ-MnO_2 on the isothermal phase diagram shown in figure 2.6. While $LiMn_2O_4$ is capable of bringing more lithium into the lattice matrix and converting to $LiMnO_2$, this process is typically avoided due to the Jahn-Teller effect causing serious damage to the structure. The Jahn-Teller effect is a bond length distortion of a symmetric structure which contains a degenerate electronic state in order to remove the degeneracy and lower the overall energy of the local system (53). A more detailed explanation may be found in a later

section describing the degradation of $LiMn_2O_4$.

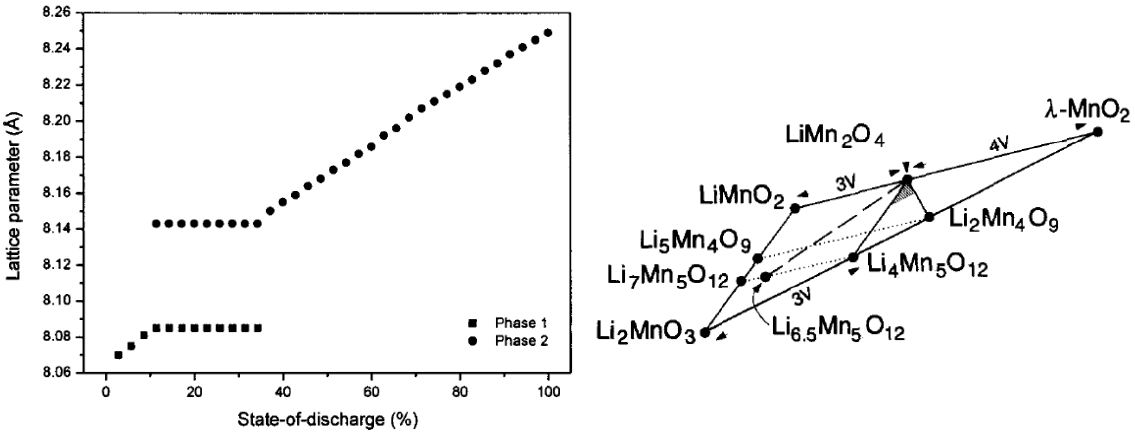

Figure 2.6: Left:Lattice parameter of $Li_xMn_2O_4$ as a function of state of discharge where 100% discharge corresponds to a x=1.0 and 0% discharge corresponds to an unknown lithium loading(52). Right: Isothermal region of Li-Mn-O phase diagram(54).

2.2.2 Electrochemical Performance

$LiMn_2O_4$ has a unique electrochemical response amongst the lithiated transition metal oxides. A typical galvanostatic discharge curve from electrochemically delithiated λ-MnO_2 can be found in figure 2.7. The two-stage process by which lithium de-intercalates from the $LiMn_2O_4$ structure is due to an ordering of lithium on half of the tetrahedral 8a sites(55). The two peaks in the Cyclic Voltammogram (CV) from figure 2.7 are generally separated by 150 mV and the transition in voltage is attributed to a composition of $Li_{0.5}[Mn_2]O_4$(50), where the second peak at a larger voltage is attributed to the removal of Li_x less than x$\sim$0.5.

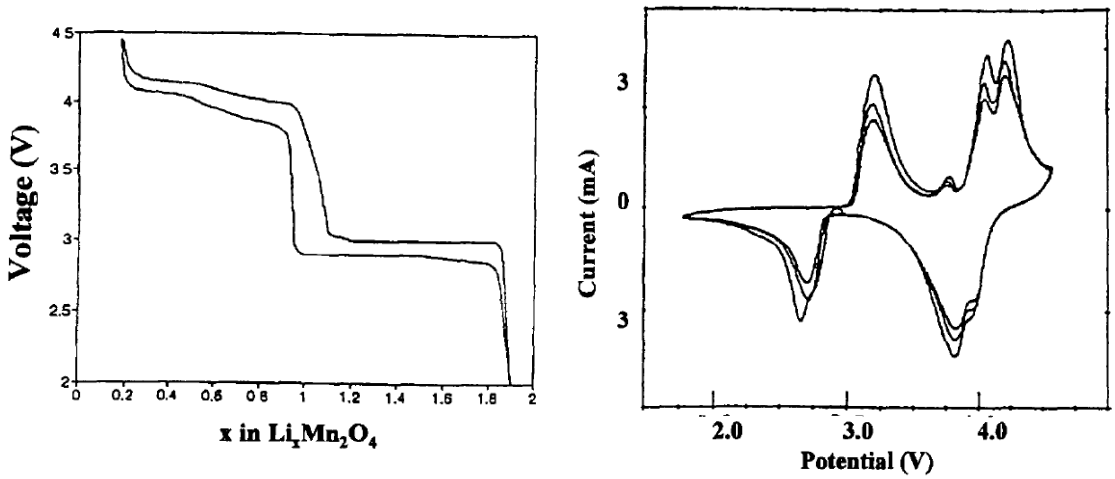

Figure 2.7: Left:The electrochemical profile of a Li/Li$_x$[Mn$_2$]O$_4$ cell over the range 0<x <2(55). Right: The cyclic voltammogram of a typical Li[Mn$_2$]O$_4$ electrode vs. a metallic lithium reference electrode(55) for three cycles. A cycle begins around 3 V, the voltage is reduced to below 2 V where lithium is removed from the cathode. The voltage is then brought up to 4.4 V which corresponds to the insertion of lithium into the cathode. The voltage is ramped between these two extremes until following the third cycle where the CV is stopped around the original starting voltage.

LiMn$_2$O$_4$ has a theoretical capacity of 148.2 mAh/g (56) when utilizing the 4-V region. If the 3-V region could be utilized reversibly the capacity would double, and the energy density would increase by 2/3 (56). This, however, is not practically useful for two reasons: cathode degradation in the 3-V region, and the voltage drop of >1.2 V would make designing a device to utilize the battery very difficult.

In some stoichiometric cases, additional features may be observed in electrochemical testing. Three typically observed additional plateaus in galvanostatic testing, and peaks in CV testing are found at 3.3, 3.95, and 4.5 V (57). Figure 2.8 shows a incremental capacity voltammogram and galvanostatic testing on a tailored sample to display the features.

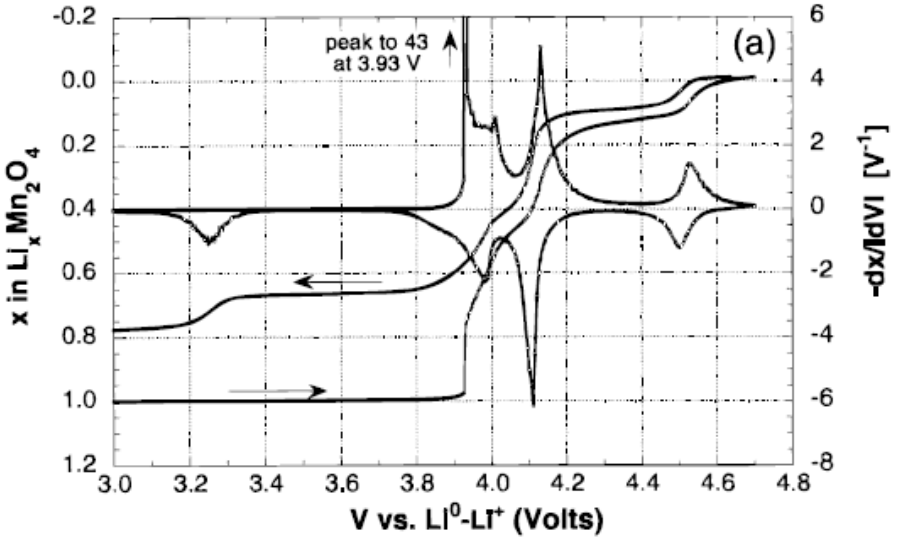

Figure 2.8: Lithium content and incremental capacity of $LiMn_2O_4$ ex-β in a first cycle between 3.0 and 4.8 V, as obtained from EPS protocol with 5 mV potential steps and a minimum redox current equivalent to a C/50 regime. (57)

Palaćin determined through High-Resolution Transmission Electron Microscopy (HRTEM) that the additional features are a result of a double hexagonal layer phase within the spinel structure. This phase transformation is suggested to be a result of Mn ions migrating from 16d lattice sites to 16c sites. It was further suggested that the larger unit-cell parameter samples showed greater phase transformation and can be related to defects in the material.

2.2.3 Degradation

There are currently three separate effects which have been attributed to capacity loss in $LiMn_2O_4$ cathodes: the Jahn-Teller effect, dissolution of Mn^{2+} created due to disproportionation from acidic electrolyte, and the instability of organic electrolytes at high voltages. Each of these effects contributes to capacity fade in its own way. Jahn-Teller distortion leads to instability in the cohesion of the localized unit cell, disproportionation dissolves the manganese framework, and the specific effect of

unstable organic electrolytes is currently being determined.

2.2.3.1 Jahn-Teller effect

The Jahn-Teller effect in $LiMn_2O_4$ occurs due to the oxidation state of Mn in the spinel structure. The Jahn-Teller effect is a distortion of a bond length in order to remove degeneracy in the electronic state (53). This effect typically occurs in transition metals with an odd-numbered oxidation state. When an octahedrally or tetragonal coordinated atom has an odd-numbered oxidation state there are two degenerate electronic states which is inherently unstable. In order to reduce the energy of the coordinated atom a set of bond lengths which are 180° opposite either lengthen or contract. This change in bond length reduces the degeneracy, but also consequently reduces the local symmetry.

Mn can have oxidation states between II-VII, where the Mn^{2+} state is the most stable. Manganese in $LiMn_2O_4$ exists in a $Mn^{3.5+}$ oxidation state where generally equal parts of the Mn^{3+} and Mn^{4+} oxidation states exist simultaneously in the structure. If a cycling rate is used which is greater than the bulk diffusion rate of Li^+ in $LiMn_2O_4$ a buildup of lithium on the surface occurs This buildup of lithium on the surface results in an concentration increase of Mn^{3+} oxidation states at the surface. This increase of Mn^{3+} at the surface results in an immediate Jahn-Teller transition changing the structure from a cubic lattice where (c/a)=1.0 to a tetragonal (c/a)=1.16(54), with an accompanying 6.5% volume increase (58). This volume expansion is too large for the structure to manage and significant deterioration of the structure occurs.

This issue is particularly relevant in high-current applications due to lithium diffusion into the bulk particle. As lithium loading up to x=2.0 can be accommodated by $Li_xMn_2O_4$ if a current is drawn on the battery which results in a higher current than the diffusion rate of lithium, excess Li^+ will occur in the layers closest to the electrolyte(55; 59). This will result in localized Jahn-Teller distortion and is one of

the attributable causes for capacity fade in $LiMn_2O_4$ cathodes.

Two methods were developed to inhibit Jahn-Teller effects from occurring. The first is limiting the potential window which $LiMn_2O_4$ operates. By preventing the potential from dropping below 3V Jahn-Teller effects are significantly reduced. The second method was to dope the Mn lattice with small amounts of Li^+ which raise the overall oxidation state of Mn above $Mn^{3.5+}$(54; 60). It has been observed that maintaining the oxidation state above $Mn^{3.5}$ prevents Jahn-Teller effects from occurring.

2.2.3.2 Disproportionation

Disproportionation in $LiMn_2O_4$ was initially hypothesized before $LiMn_2O_4$ was discovered as a rocking-chair cathode material. Hunter (61) first reported on the existence of λ-MnO_2 from an investigation of $LiMn_2O_4$ in acidic solutions. Hunter found that lithium removal approached an asymptotic concentration with low pH, where the remaining lithium was homogeneously distributed. In testing the acidic solution for lithium content it was discovered that some Mn concentration was present. This concentration was attributed to formation of Mn^{2+} since Mn^{3+} and Mn^{4+} are stable in the acid solution used. Hunter proposed a disproportionation reaction as in equation 2.4 where the lithium oxide and manganese oxide dissolve into the acidic solution.

$$2LiMn_2O_4 \rightarrow Li_2O + 3MnO_2 + MnO \tag{2.4}$$

where,

$$2Mn^{3+} \rightarrow Mn^{2+} + Mn^{4+}$$

A typical $LiMn_2O_4$ test cell would include an electrolyte composed of 1M $LiPF_6$ salt dissolved in a mixture of Ethylene Carbonate (EC), and either Dimethyl Carbon-

ate (DMC) or Diethyl Carbonate (DEC) or a mixture of the two. Disproportionation in this cell has been considered to be the result of unintentional residual water in the solvent reacting with the $LiPF_6$ salt to produce HF as in equation 2.5(62). The HF created in this reaction actually increases the total amount of H_2O in the system through equation 2.6(62). The coupling of equations 2.5 and 2.6 results in an exponential increase in dissolved Mn and breakdown of the cathode.

$$LiPF_6 + H_2O \rightarrow POF_3 + LiF + 2HF \tag{2.5}$$

$$2LiMn_2O_4(s) + 4H^+(aq) \rightarrow 3MnO_2 + Mn^{2+}(aq) + 2Li^+(aq) + 2H_2O(aq) \tag{2.6}$$

As a result of the requirement for the electrolyte to be acidic the electrolyte salt plays a large role in disproportionation acid dissolution of the spinel. Research on the salt contribution to acid formation showed that in a $C/LiMn_2O_4$ cell with a Propylene Carbonate/1,2-dimethoxyethane (PC/DME) solvent and a variety of salts(63) where the cell was held at a potential of 4.2 V (vs. Li/Li^+). Jang determined that for five different common lithium-ion salts the solvent oxidation leading to acid formation followed the trend as shown in figure 2.9.

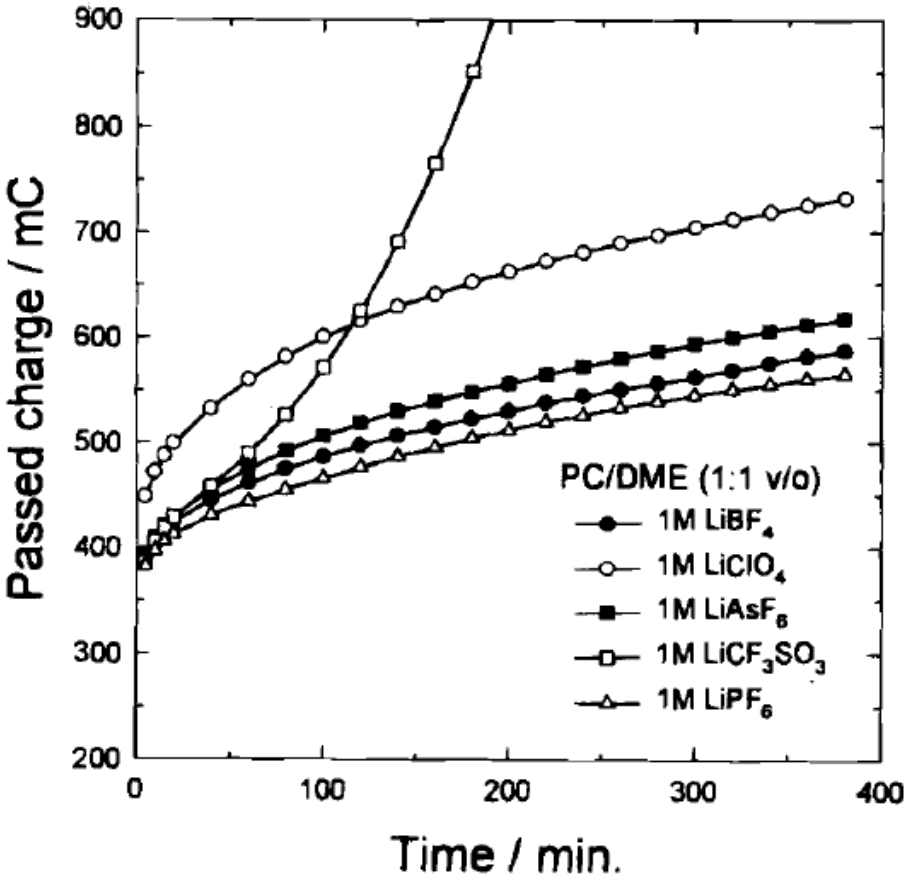

Figure 2.9: Accumulated charges passed during solvent oxidation in different salt solutions (PC/DME). The electrode potential was stepped from 3.2 V to 4.2 V (vs. Li/Li^+). (63)

Figure 2.9 did not take into account the initial formation of acid from the immediate salt/solvent mixture; however, Jang showed that $LiPF_6$ has an initial formation of acid attributed to the salt reacting with water dissolved in the solvent. Jang also explored the concentration of Mn^2+ dissolved in the electrolyte with the same salt/solvent mixture shown in figure 2.10 and noted a slightly different trend which is attributed to the inital acid formation of $LiPF_6$.

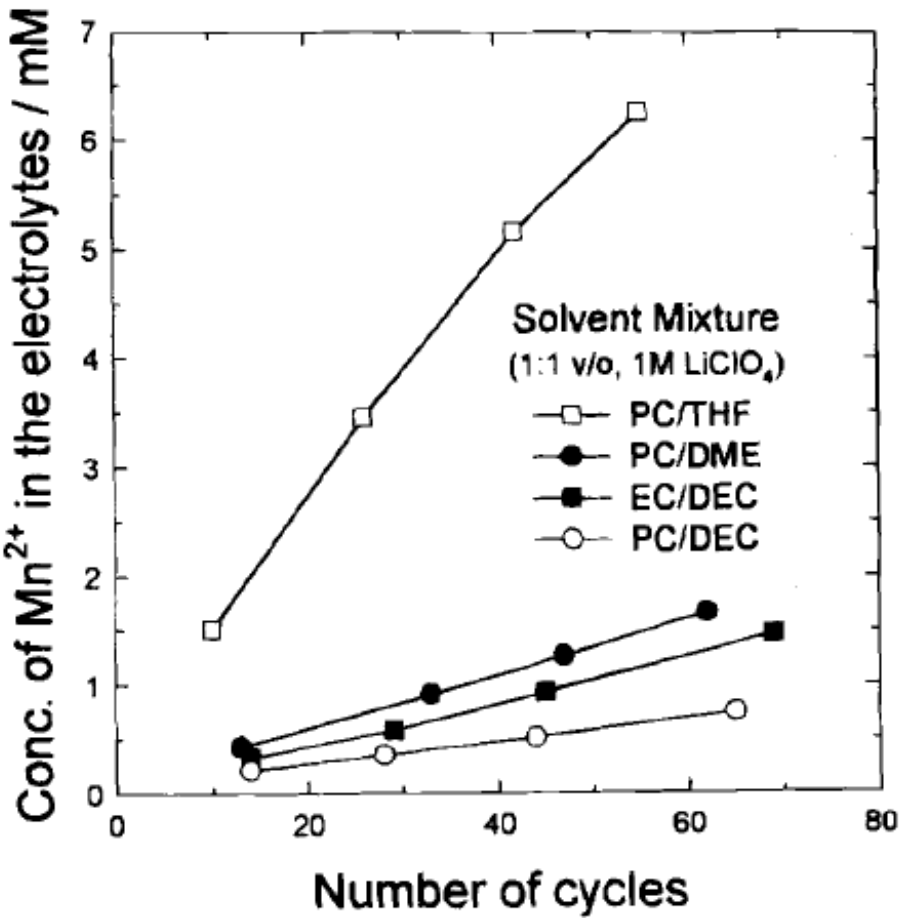

Figure 2.10: Dissolved Mn^{2+} contents in different salt solutions (PC/DME) which were monitored while a composite electrode (spinel:Ketjenblack EC:Tefflon binder = 72:20:8 wt. ratio) was polarized at 4.2 V (vs Li/Li^+). (63)

In general research on $LiMn_2O_4$ has focused on the $LiPF_6$ salt as a result of findings such as these. While $LiPF_6$ does have drawbacks, most notably HF formation, the research community has primarily focused on this salt due to the lowest disproportionation and manganese dissolution. Significant work has been put into reducing water content in solvents to the lowest concentration achieveable in order to reduce the overall HF contriubtion to the system. However, in cases where water content is not as easily controlled this salt may not be the optimal choice for testing.

2.2.3.3 Electrolyte decomposition

Decomposition of the organic solvents and salts in the electrolyte on the surface of $LiMn_2O_4$ is extremely important in regard to the passivation of the electrode surface. Electrolyte oxidation can have a huge impact on the operation of the $LiMn_2O_4$ cathode for many reasons. Electrolyte oxidation on $LiMn_2O_4$ can lead to self-discharge (64; 65; 66; 67; 68), manganese dissolution (69; 67; 70; 71), and formation of the SEI (72; 67; 73; 74).

Self-discharge of $LiMn_2O_4$ is a problem for several reasons: i) stored power loss over time ii) potential for Jahn-Teller distortion iii) creation of break-down products. This phenomena is thought to be a result of electrolyte oxidation and is a product of lithium re-intercalation(64; 65; 66; 68). Guyomard(64) suggested an equation which described the pathway for self-discharge, which was expanded upon by Erikkson (67) to equation 2.7.

$$LiMn_2O_4 + 3xLi^+ + xE \rightarrow Li_{1+3x}Mn_{2-x}O_4 + xMn^{2+} + xE^+ \tag{2.7}$$

where E represents electrolyte solvent, and E^+ represents oxidation of the electrolyte solvent. Preferential oxidation of electrolyte solvents are not addressed here.

This equations show all three effects of self-discharge. First, lithium is re-intercalated into the cathode reducing cathode capacity. Second, if Li/Mn ratio goes much above 1/2 Jahn-Teller effects will occur leading to the production of a $Li_2Mn_2O_4$ phase. The $Li_2Mn_2O_4$ phase is unstable and will decompose into Li_2MnO_3 and MnO (75). Lastly, oxidized electrolyte products are produced which may be complicit in further chemical reactions on the electrode surface.

Manganese dissolution has also been tied to electrolyte oxidation bi-products on the surface of carbon, where carbon is used to improve the conductivity of the cathode

material (69). Jang found that the extent of manganese dissolution varied with carbon content, where a lower carbon content resulted in lower amounts of Mn-dissolution. This result is important because all lithium-ion battery cathodes involve a mixture of the cathode material, carbon, and a binder. The extent of dissolution was also tied to the charged state, where the cathode charged above 4.3 V showed significantly greater manganese dissolution.

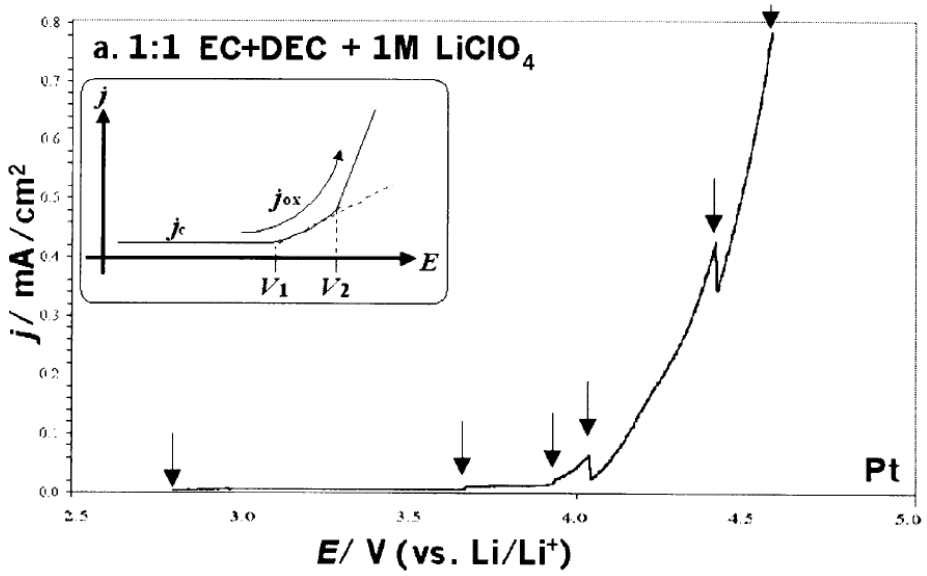

Figure 2.11: An example of the potentiodynamic behavior of 1M $LiClO_4$ in EC+DEC during in-situ, FTIR spectroelectrochemical experiments: current density vs. potential (j vs E.) during anodic, linear potential scan voltammetry (LSV) at 5 mV s^{-1}. The x-axis shows the potential versus lithium metal and is read in volts. The peaks in the j vs. E curves [arrows] were formed at potentials in which FTIR measurements were carried out. (The potential scanning was stopped and the electrode kept at a constant potential during the measurements, and therefore the current dropped). The insert shows how the onset potentials for the oxidation were found: by extrapolation of the tangents to the j vs. E curves. j_c is the capacitive current density before oxidation started; j_{ox} (which usually has two slopes, as shown) is the oxidation current density; V_1 and V_2 denote the apparent onset potentials for the beginning of the oxidation process and its acceleration, respectively; V_1 is obtained at the interchange of the tangent to j vs. E with j_c and V_2 is obtained at the interchange between the two tangents to j vs. E as shown(76).

In addition to decomposition on the cathode material, the charge collector metal on the cathode may be involved in electrolyte oxidation. Moshkovich (76) found that

various mixtures of solvents and salts resulted in oxidation of the current collector vs. Li/Li^+. A short table of results from this work can be found in table 2.1. A visual representation of the oxidation current is found in figure 2.11 where the current density as a function of voltage for a platinum electrode with 1 M $LiClO_4$ Ethylene Carbonate:Diethyl Carbonate (EC:DEC).

Table 2.1: Onset potentials for the oxidation processes of the various solutions on Pt, Au, and Al electrodes. The first number in each line (left number) is the onset potential for oxidation (V_1 in Fig. 2.11), while the second potential (right number) relates to the increase in the slope of j vs. E at higher potentials (i.e. an acceleration of the oxidation process was observed)(76)

Solution	Salt	Au	Pt	Al
9:1 EC:DEC	$LiAsF_6$	3.8	3.4	3.4
1:1 EC:DEC	$LiAsF_6$	3.9; 4.4	3.6; 3.8	
1:3 EC:DEC	$LiAsF_6$	3.6; 3.8		
1:1 EC:DMC	$LiAsF_6$	3.55; 3.73		3.4; 3.7; 4.3[a]
DMC	$LiAsF_6$		3.7; 4	
1:1 EC:DEC	$LiClO_4$		3.7; 4	
1:1 EC:DEC	$LiPF_6$	3.65; 3.73		
1:1 EC:DMC	$LiPF_6$	3.55; 3.76	3.45	3.3
1:1 EC:DEC	Imide	3.88; 4.3		
1:1 EC:DEC	Methide	3.86; 4		

[a] In these experiments, two accelerations of the oxidation process could be observed (i.e. a considerable increase in the slope of j vs. E at the potentials indicated).

Aluminum is the standard current collector as it is low-cost and lightweight. However, as can be observed from table 2.1 aluminum is not necessarily inert with respect to the electrolyte at high voltages. These results indicate that care should be taken when considering the current collector material in regard to stability of both the collector and the electrolyte. Degradation of the current-collector may result in a disconnect between electrochemically active material and the external circuit.

2.2.4 Electrolyte Interface

The electrolyte interface is the most important aspect of ion-migration in a battery. The electolyte/electrode interface is where chemical reactions occur which may influence the performance of the battery. Between de-solvation of Li^+ in a lithium-ion battery and migration into the bulk material there exists a window where the Li^+ ion and may undergo a spontaneous side reaction. These side reactions can eventually lead to a protective surface film which also acts as an ionic conductor, but they may also lead to a highly resistive film or one which is easily dissolved into the electrolyte. This electrolyte/electrode interfacial layer was previously defined as the SEI. A resistive film leads to higher cell impedance which restricts the practical current density in the cell, and can also result in polarization which reduces capacity. Polarization is the difference between the true cathode potential and the measured potential. With polarization effects the measured voltage is higher than the true equilibrium voltage of the cathode and as such when charging the battery if a voltage cutoff is used to stop charging, a large polarization will lead to a a deficit of charge. Additionally, as Li^+ is inherently consumed through the production of the SEI, an unstable SEI which may be dissolved can result in constant side-reactions which continuously reduce the total available Li^+ content.

$LiMn_2O_4$ has a native Li_2CO_3 on the surface (77; 78; 5). Literature suggests that the carbonate film on the pristine electrode is a result of either a precursor, or what is considered more likely is a reaction between Li and CO_2 in the atmosphere during processing steps(77). Research has shown that upon introduction into the electrolyte, even without external electrochemical driving forces, the inherent Li_2CO_3 passivation layer dissolves(67). Upon storage for extended periods of time Eriksson (67) showed that the chemical species in the SEI are very similar to those found following electrochemical cycling. It was suggested that the kinetics of formation were more favorable during cycling as a result of transport effects in the electrolyte.

That result is in-line with those of Guyomard and Tarascon (79; 64) which suggest that oxidative decomposition of the electrolyte is correlated to the surface area and therefore is a surface-catalyzed process which should result in a uniform passivation of the cathode. Aurbach (78) found similar impedance behavior in three different salt solutions which indicate a surface layer inhibiting lithium-diffusion existed and was certain to impact lithium diffusion kinetics in lithium-ion batteries.

Most work on passivation on $LiMn_2O_4$ utilize $LiPF_6$ or $LiAsF_6$ salts because of their more ubiquitous use in industrial production. It has been observed however that the solvent plays a significant role in the surface chemistry of $LiMn_2O_4$ and the breakdown of solvents result in polycarbonates on the surface of the cathode(67). Eriksson also observed that the composition of the surface layer was different between samples which were stored and samples which were cycled, suggesting that decomposition products from carbonate oxidation are precursors for slower polymerization reactions.

Hirayama(80; 81) utilized epitaxial thin films in conjunction with X-Ray Reflectometry (XRR) and X-Ray Diffraction (XRD) to study the SEI on individual planes. Hirayama determined that the planar orientation was of significance between both storage and during cycling. XRR results showed the <111> plane when soaked in electrolyte dissolved the impurity surface layer and replaced it with an SEI layer. Conversely, the <110> plane showed dissolution of the impurity surface layer, but no subsequent development of an SEI layer. It was suggested (81) that the surface of the epitaxial $LiMn_2O_4$ thin-film underwent a surface rearrangement upon the first charge. This rearrangement was tied to manganese dissolution only in the <110> sample, and following 10 cycles they show through TEM the <110> sample had a thicker overall SEI formation.

The significant result from research related to the SEI is that the composition and stability are directly tied to $LiMn_2O_4$ performance. Understanding and controlling

the SEI on cathode material is one of the most important aspects of lithium-ion battery operation. A better understanding of morphological changes while operating is necessary in order to advance the potential of $LiMn_2O_4$ as a cheap, long-lifetime, commercial battery cathode material.

2.3 Neutron and X-ray Reflectometry

Reflectometry is a technique used to study the structure and density of thin-films in the normal direction to the surface. Neutron and x-ray reflectometry are objectively the same technique, but rely on interacting with matter in different ways. Neutrons interact with atomic nuclei, whereas x-rays interact in the electron shell. Reflectometry utilizes the elastic (specular) reflection of radiation as a function of angle on thin-films to determine the structure and density. A basic figure of the reflectometry instrument is shown in figure 2.12 where the incident angle of the beam matches the transmitted angle of the beam. The slits used to define the beam profile are very thin at low angles so as to only capture the specular reflected peak. The two slits before the sample are used to define the divergence of the incident beam. The two slits following the sample are used to reject background scattering. For x-ray reflectometry the beam slits are typically held constant where as for neutron reflectometry the beam slits change with angle so as to maintain the footprint of the beam on the sample. Maintaining the footprint provides a better characterization of the sample as the region which is reflecting the beam does not change. This also helps in data collection as neutron sources are typically of lower intensity than x-ray sources and larger slit sizes result in a higher intensity neutron beam.

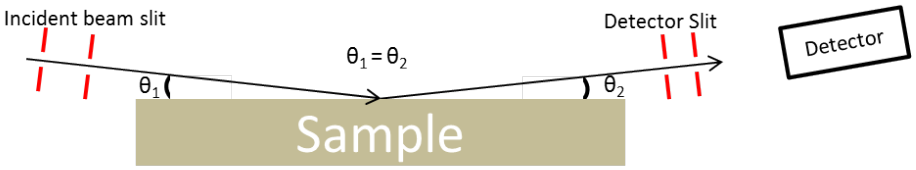

Figure 2.12: A basic representation of a reflectometer where a beam of radiation travels through a slit to create a thin beam which impinges on the sample surface. The beam is reflected and the specular (same angle as incident) portion of the reflected beam passes through a slit in front of the detector to mask non-specular reflection.

While x-ray reflectometry (XRR) is very useful as an thin-film probe, the main purpose of this thesis is to study a $LiMn_2O_4$ thin-film *in-operando*. X-rays have very little penetrating power into materials, and are not sensitive to very light elements which are considered to be the main constituents of a SEI. Neutrons are very sensitive to light elements, are highly penetrating in most materials, are non-damaging at low-energies, and have isotopic sensitivity. These properties make neutrons a more idealized probe for studying interfacial and near-interface properties of an operational cathode.

2.3.1 NR Theory

In order to develop equations describing neutron reflectometry(82; 83), the neutrons must be described as waves. In the monochromatic, constant source case the neutron wavelength is related to its energy through equation 2.8

$$\lambda = \frac{h}{\sqrt{2mE}}, \tag{2.8}$$

where m is the neutron mass, h is Planck's constant, and E is the energy of the neutron. In neutron reflectometry with a constant wavelength source, the neutron is considered to be time-independent, therefore the wave function in free-space is described by equation 2.9

$$\psi\left(\vec{r},t\right)=I\left(E\right)e^{i\left(\vec{k}\vec{r}\right)}, \tag{2.9}$$

where $\vec{r}$ is the spatial position, I(E) is the wave amplitude, and $\vec{k}$ is the incident wave vector. The incident wave vector $\vec{k}$ is given by $(2\pi)/\lambda\hat{i}$ or $\sqrt{2mE/\hbar^2}$, where $\hat{i}$ is a directional unit vector. Momentum transfer $\vec{Q}$ is the difference between the incident and reflected wave vectors, the magnitude of which is given by,

$$q=\frac{4\pi\sin\Theta_i}{\lambda} \tag{2.10}$$

The three dimensional steady-state Schrödinger equation is given by equation 2.11

$$\bigtriangledown_{\vec{r}}^2\psi\left(\vec{r}\right)+\left[\vec{k}_{iz}^2-\frac{2m}{\hbar^2}V\left(\vec{r}\right)\right]\psi\left(\vec{r}\right)=0, \tag{2.11}$$

where the potential V is the Fermi pseudopotential given in equation 2.12

$$V\left(\vec{r}\right)=\frac{2\pi\hbar^2}{m}\rho\left(\vec{r}\right), \tag{2.12}$$

where the scattering length density (SLD) $\rho\left(\vec{r}\right)$ is given in equation 2.13.

$$\rho\left(\vec{r}\right)=\sum_{i}^{n}N\left(\vec{r}\right)_i b\left(\vec{r}\right)_{c,i} \tag{2.13}$$

where $\mathrm{N}(\vec{r})_i$ is the number density of atom i, and $\mathrm{b}(\vec{r})_{c,i}$ is the bound coherent cross section of atom i. It should be clearly stated that neutron bound coherent cross sections are isotope dependent and therefore the isotopic makeup of each atomic species must be accounted for in the determination of the SLD. This ability to isotopically label samples for neutron scattering studies is one of the significant advantages which neutron scattering has over x-ray scattering. In this work the only consideration is specular reflection in which the measurement is only concerned with the thin-film in the z-direction. This means we assume $\rho\left(\vec{r}\right)$ is homogeneous in the x and y directions

and we are averaging over the coherence length of the neutron. This assumption is only correct if inhomogeneities in the sample are much smaller than the neutron coherence length. Additionally, specular reflection implies that the wave vector only changes in the z-direction and therefore the 3-D time-independent Schrödigner equation with the Fermi pseudopotential reduces to equation 2.14,

$$\left(\frac{d^2}{dz^2} + k_{iz}^2 - 4\pi\rho\left(z\right)\right)\psi\left(z\right) = 0 \tag{2.14}$$

where,

$$k_{fz}^2 = k_{iz}^2 - 4\pi\rho\left(z\right) \tag{2.15}$$

which is the 1-D time-independent Schrödinger equation. The probability of finding a neutron described by the wave equation in space given a particular momentum can be determined by the square of the modulus of the 1-D Schrödinger equation $|\psi|^2$.

There is an assumption to be made in regard to the SLD,

$$\rho\left(z\right) = \begin{cases} Nb, & z \to \infty\,(backing) \\ 0, & z \to -\infty\,(fronting) \end{cases}$$

This assumption in a real-world application may actually be relaxed depending upon the "fronting" and "backing" medium. In some cases, such as a sample in air, this treatment of the solution is very valid where the air is the "fronting" medium and the "backing" medium is the sample substrate. In a case such as the sealed electrochemical cell utilized in this work, the assumption would be different. The "fronting" medium would be the silicon substrate, and the "backing" medium would be the electrolyte.

For this description of NR theory we will assume the system is a single slab of material in a vacuum. The solution to the 1-D time-independent Schrödinger equation

is the equation for a wave in free space interacting with a potential ρ (Figure 2.13) results in two equations describing the wave in free space and in the potential,

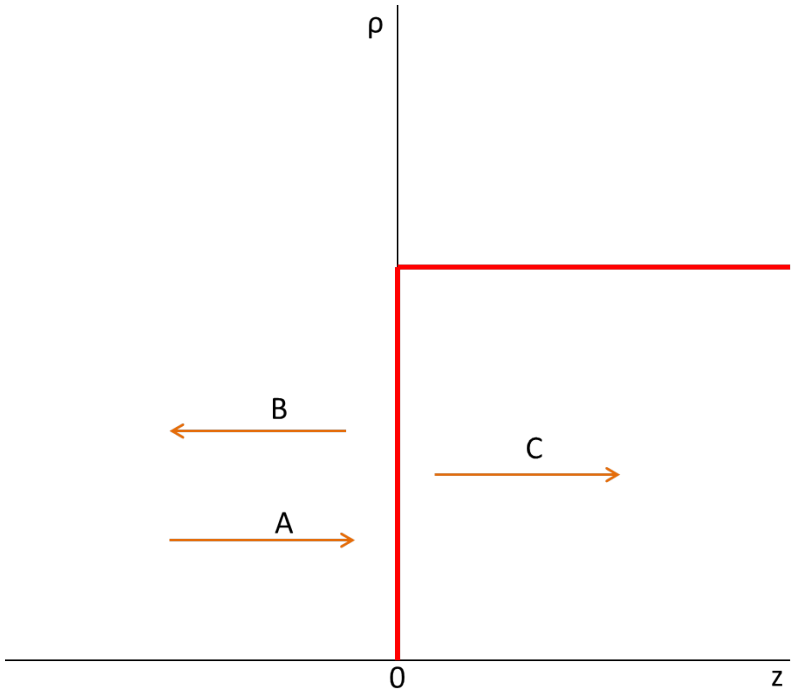

Figure 2.13: Representation of a wave traveling in free space encountering a potential with a reflected and transmitted component.

$$\psi_0 (z < 0) = Ae^{(ik_{iz}z)} + Be^{(-ik_{iz}z)} \tag{2.16}$$

$$\psi_1 (z > 0) = Ce^{(ik_{fz}z)} \tag{2.17}$$

where A is the incident wave amplitude (equal to 1), B is the reflected wave amplitude, and C is the transmitted amplitude. For multi-layer samples the number of equations equals the number of layers and a matrix is developed which requires the solution to the Schrödinger equation and its derivative to be continuous at each interface. For the step potential case described above this matrix appears as:

$$\begin{pmatrix} \psi_0(0) \\ \frac{\delta\psi_0(0)}{\delta z} \end{pmatrix} = \begin{pmatrix} \psi_1(0) \\ \frac{\delta\psi_1(0)}{\delta z} \end{pmatrix} \Rightarrow \begin{pmatrix} 1+B \\ ik_{iz}(1-B) \end{pmatrix} = \begin{pmatrix} C \\ ik_{fz}C \end{pmatrix} \tag{2.18}$$

where the reflected amplitude B is,

$$B = \left(\frac{k_{iz} - k_{fz}}{k_{iz} + k_{fz}} \right) \tag{2.19}$$

The actual detected neutron intensity is related to the square of the modulus of the reflected wave amplitude (Reflectivity=B B^*). This is a very important point to be made because it means that without special experimentation it is not possible to retrieve the phase of the reflected vector. As a result of one can not invert those collected reflectometry data but instead must be fit to determine the SLD profile. In general the fitting solutions are not unique, it is possible that two symmetry related profiles have the exact same reflectivity as a function of Q. In order to maximize the confidence in a chosen model, a detailed characterization and understanding of the sample must be accomplished. This characterization provides a means with which to select between different models which fit those data equally well.

As the neutron wave behaves similarly to light and utilizes the same mathematical construct to define the wave, the neutron wave exhibits similar optical properties such as refraction. In equation 2.15 we find the relation to index of refraction n where,

$$n = \frac{k_{fz}}{k_{izZ}} = \sqrt{1 - 4\pi\rho(z)/k_{iz}^2} \tag{2.20}$$

from Snell's law (equation 2.21) an incident angle can be determined where below that angle the incident neutron wave is totally externally reflected.

$$cos(\Theta_i) = n * cos(\Theta_f) \tag{2.21}$$

From equation 2.21, if Θ_f is zero then no part of the incident wavefunction is

transmitted into the medium and the entire wave is reflected. Solving for Θ_i gives,

$$\Theta_i = \sqrt{\frac{Nb}{\pi}}\lambda \tag{2.22}$$

Finally the resulting critical wave vector is,

$$q_c = \frac{4\pi \sin\left(\sqrt{\frac{Nb}{\pi}}\lambda\right)}{\lambda} \simeq \sqrt{16\pi Nb} \tag{2.23}$$

The critical wave vector can be an important quantity as it provides a means with which to gauge the fitted angle offset of the detector in addition to the density of the layer which creates the critical edge, if a critical edge exists. If the incident angle is set to values beyond the critical angle and transmission into the thin-film structure occurs, transmission and reflection begin to occur at each thin-film interface within the structure. Figure 2.14 shows a representation of wavevector scattering off interfaces in a hypothetical thin-film structure. The detected neutron intensity is a superposition of all the reflected waves which arise from each interface.

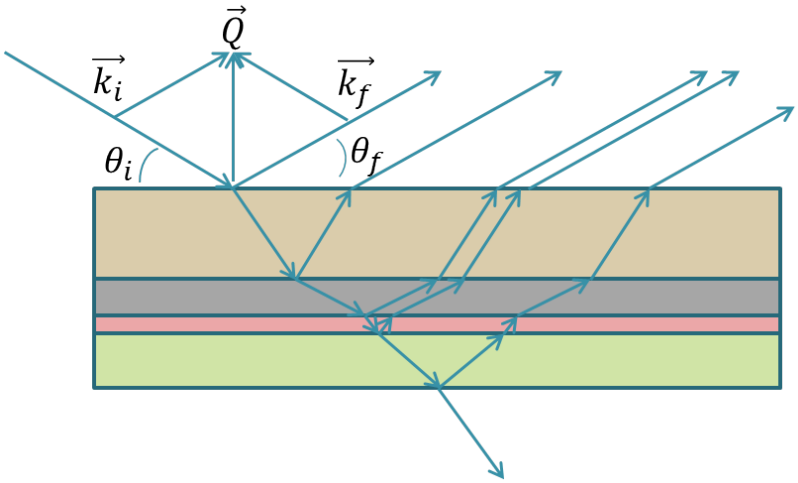

Figure 2.14: Cross-sectional representation of multi-layer neutron reflection at interfaces in a hypothetical structure.

There are three components of a reflectometry dataset which should be explained visually; the Kiessig fringe, the critical edge, and the total-reflection plateau. Figure

2.15 shows hypothetical 50 $\mathring{A}$, 100 $\mathring{A}$, and 200 $\mathring{A}$ Pt thin-films on silicon. The Kiessig fringe is a feature of reflectometry which is used to determine the thickness of a thin-film layer. The periodicity of a Kessig fringe is defined as (2 π)/L, where L is the thickness of the layer. The critical edge vector Q_c is determined through equation 2.23. It can be observed in figure 2.15 the the critical edge vector is constant between the two hypotheical samples. This is due to the critical edge being dependent upon the SLD of the layer, and not dependent upon any other factor. The total reflection plateau can be observed at all Q-values below the critical edge. These features become more complicated as multiple layers, absorption effects, and sample warp come into effect.

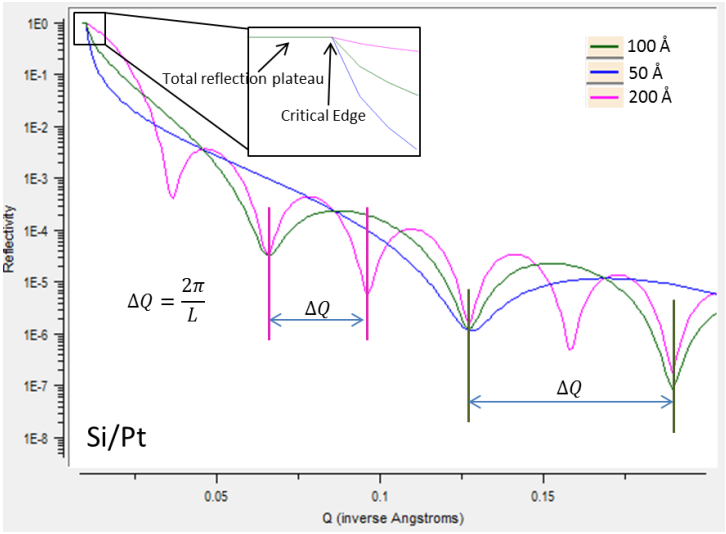

Figure 2.15: Synthetic data highlighting the features of a reflectometry curve assuming platinum thin-film on silicon at two different thicknesses.

2.3.2 XRR Theory

While XRR is utilized widely in this thesis, a thorough description of the method will not be included. The technique is essentially the same as NR, where the main difference occurs in the scattering center. Neutrons are scattered by the nucleus, x-rays are scattered by the electron cloud. This difference in scattering center results in a different SLD, but the overarching concept and solution to the wave equations

remain the same. One useful element to explain about XRR data is the lack of a critical edge due to absorption of x-rays in the sample. While a critical-edge does exist, the intensity is not flat below the critical edge due to absorption. Absorption occurs with neutrons as well, but the effect of absorption is orders of magnitude smaller and does not show a pronounced effect in the critical edge as in XRR.

2.4 X-ray Photoelectron Spectroscopy

XPS is a technique which utilizes the photoelectric effect to quantitatively determine composition on the surface of a sample. This technique can be used to not only identify the stoichiometry of the sample in parts per thousand, but also to gain some chemical bond information based upon the chemical binding energy shift. XPS typically works by bombarding a material surface with a monochromatic x-ray beam of low energy (Al K_α $\sim$1.5keV) to drive the photoelectric effect. Photoelectrons ejected by the atoms in the surface are counted through an hemispherical electron energy analyzer which preferentially blocks all electrons except those in a very tight energy window on the order of 0.5 eV resolution. The preferential energy selection allows for scanning through a wide energy window only counting electrons of a specific energy enabling a quantitative measurement. Each XPS instrument is calibrated to determine the relative sensitivity factors (RSF) for each element which is related to the probability of the photoelectric effect occurring in each elemental species. The calibrated RSF is necessary to due slight differences in each XPS instrument and therefore the RSF for each instrument is slightly different. The energy of each detected photoelectron is determined through the equation(84),

$$E_p = h\nu + E_x - \Delta p \tag{2.24}$$

where E_p is the energy of the detected electron, hν is the energy of the incident

photon, E_x is the core electron gound state, and Δ p is the chemical binding state energy.

To determine chemical composition each peak of interest in the XPS spectra is corrected for background and fit with a Voight function approximation to determine peak centroid, FWHM, and integrated peak area. The peak areas for multiple peaks are corrected for their individual relative sensitivity factor for each element and the ratio of these corrected peak areas provides a quantitative determination of stoichiometry. One significant limitation for XPS in this work is the inability to probe H atoms in addition to a very weak sensitivity to Li. Additionally the spot size of the x-ray beam is small compared to the sample surface and therefore the composition may not necessarily be constant over the entire sample surface. In this work XPS is primarily used to examine the stoichiometry of the $LiMn_2O_4$ surface film.

2.5 Cyclic voltammetry

Cylic voltammetry(CV) is a characterization technique typically used for determination of onset potential for reactions (21). The technique works by ramping voltage at a constant rate from a starting value (typically the open circuit potential) to a voltage on the other side of the redox reaction then back to the starting value (figure 2.16). Throughout the voltage ramp, the current is monitored to examine the onset potential for a particular reaction. When a voltage is reached which allows the onset of a reaction step, such as de-intercalation or intercalation of lithium, the current will rise quickly. Once the reaction is complete the current drops again until the next onset voltage is reached if one exists. Typically a very slow voltage ramp rate is used to prevent any polarization effects from buildup of ions due to rates which exceed the bulk diffusion rate of the electrodes. Fast rates can be used to determine properties such as the state-of-health of the cathode in which CV curves are compared against the previous curve to examine changes in maximum peak intensity and

potential shift. Change in peak intensity can indicate phase change and active area loss. Potential shift indicates increasing IR drop (85) in the system which can be attributed to greater charge resistance in the cell namely from electrolyte breakdown on either the anode or cathode.

In this work CV curves are used to serve three purposes: a means of characterizing the active electrode materials (i.e. is it $LiMn_2O_4$), a means of cycling the cathode from discharged to charged and back to discharged, and as a means of determining the state-of-health of the system. As was previously discussed the CV curve for $LiMn_2O_4$ is very distinct (figure 2.7) and enables a fast determination of whether the material is roughly $LiMn_2O_4$.

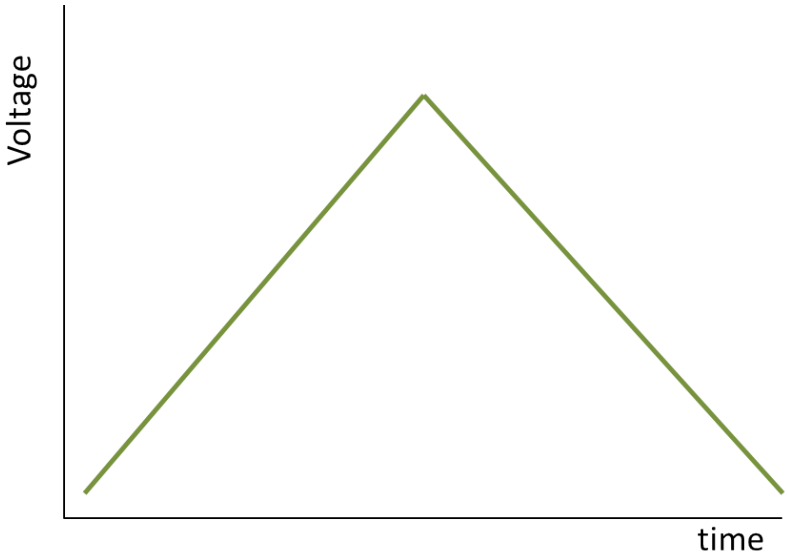

Figure 2.16: Voltage vs time profile for a Cyclic Voltammetry experiment. Current from the cell would be monitored throught the potential ramp where peaks in current relate to the onset potential for that particular redox process

A qualitative measure for monitoring behavior of an electrochemical cell can come from examining the integrated anodic and cathodic currents. Figure 2.16 shows a typical CV voltage ramp profile. When the slope of the voltage ramp is positive the current is assumed to be anodic in this system as lithium is being stripped from the cathode and moved to the anode. Conversely, when the slope is negative the

current is attributed to the cathode as lithium will be stripped from the anode and intercalated into the cathode. Due to polarization and electrolyte breakdown effects there is a background current which must be deconvolved from the overall total current collected. In this work it is assumed that current from intercalation/de-intercalation of lithium are independent of the charging current and the total current is of the form:

$$I_{tot} = I_{elec} + I_{BV} \tag{2.25}$$

where I_{tot} is the total observed current, I_{elec} is the electrode current contribution, and I_{BV} is the electrode current due to capacitive charging and electrolyte breakdown. The electrode current contribution is the current of interest to examine changes in the electrode as a function of cycling. The charging/breakdown current must be removed from the total current and is assumed to follow the Butler-Volmer (BV) dependence, which describes the current due to electrical charge transfer at the electrode surface (21). This is assumed to be valid as electrolytic breakdown should not occur in the bulk material of the electrode. The BV equation is defined as,

$$I_{BV} = A * j_0 \left(e^{\frac{\alpha_a nF}{RT}(E-E_{eq})} - e^{-\frac{\alpha_c nF}{RT}(E-E_{eq})} \right) \tag{2.26}$$

where A is the electrode active surface area, j_0 is the exchange current density, α_a and α_c are the anode and cathode charge transfer coefficients, F is the Faraday constant, R is the universal gas constant, T is the system temperature, n is the number of electrons involved in the charge transfer process, E is the applied voltage, and E_{eq} is the system open circuit or equilibrium potential.

2.6 Atomic Force Microscopy

Atomic Force Microscopy (AFM) is a surface analysis technique which has many capabilities; however, in this work the only process used is the basic tapping method(86). AFM works by using a cantilever with a very sharp probe where the tip has a radius of curvature on the order of nanometers and a laser reflecting off the end of the cantilever. The laser reflection off the probe is directed onto a planar photodiode which montiors the displacement of the probe from a reference point. In this work a tapping mode is used where the AFM probe is vibrated up and down at a frequency very close to the resonance frequency of the probe. The oscillation is on the order of 10's of nm, and as the probe is brought in close contact with the surface of the sample the Van der Waals force between the probe and surface reduce the amplitude of the oscillation indicating the surface is been reached. An AFM image is constructed by rastering in one direction (x-direction) and taking many datapoints along the direction constructing a series of height points. The probe is then shifted very slightly (y-direction) in a direction normal to the initial raster direction and then the probe is rastered again (x-direction). Once a large number of x-direction rasters have been acquired at varying y-direction points a 3-D plot can be produced which will show the sample surface morphology.

AFM in this work is used to examine the surface roughness of samples at many points. This is used as an additional piece of information in fitting XRR and NR results in addition to aiding the parameter space search to determine optimal fabrication conditions for the cathode sample.

CHAPTER III

Methods

The primary goal of this work is to examine layer density and thickness changes in a thin-film $LiMn_2O_4$ cathode under several conditions; while holding at an open-circuit potential, while holding at various potentials, and after cycling. The means of *in-situ* examination is through neutron reflectometry (NR), utilizing a potentiostat to perform electrochemical operations on the test-cell. In this work a $LiMn_2O_4$ thin-film was developed which met the stringent requirements for NR in terms of sample morphology, a lithium anode was developed which enables an operational electrochemical cell, and an NR *in-operando* sample holder was developed to allow for three-electrode potentiostatic control.

3.1 Cathode development

In order to apply NR, several morphological requirements must be met. The thin-film must be smooth, on the order of <2nm rms roughness, must be on the order of 100's of $\mathring{A}$ thickness, and must have uniform thickness over $\sim$ 2 inches in diameter. An additional requirement for electrochemistry is that a charge collection layer exists with which to make contact. Ideally, these thin-films would approach theoretical density, or even be epitaxial. That requirement was not met in this work as access to a deposition tool which can meet those requirements was not found. Future work on

this method should include a dedicated source for a deposition tool which may allow uniform deposition of the cathode thin film over several inch diameter surfaces.

The substrate used to spin the sol-gel on is chosen from silicon wafers of different thicknesses and sizes. In this work two types are used: 4" diameter/ 5 mm thick boules for NR experiments and 4" diameter/ 0.5 mm thick wafers. Prior to any film deposition the wafers are RCA cleaned using mixtures of chemicals. The wafer is intitially washed in DI water and placed in a bath of boiling Hydrogen Peroxide and Ammonium Hydroxide for 10 minutes to remove all organic contaminants. The sample is then removed from the bath and placed in a DI-washing bath, followed by insertion into a boiling bath of Hydrogen Peroxide and Hydrochloric acid for another 10 minutes to strip any metal contamination from the wafer. The wafer is then washed again in a DI-bath and placed into a bath of HF which is diluted from concentrated HF with DI water to a 10:1 (H_2O:HF) mixture. The wafer is removed after 30 seconds and is again placed in a DI-bath. If the wafer is thin (i.e. 0.5mm thick) then the wafer is placed in a wafer holder and inserted into a Spin-Rinse-Dry apparatus which does what its name implies. The wafer is washed in DI, spun at high rates of speed to remove water left on the wafers, and finally blown dry with dry N_2. If the wafer is thick (i.e. 5mm thick) the wafer can not be inserted into the Spin-Rinse-Dryer and is instead blown dry with dry N_2. The wafers are then inserted into a dry-oxidation tool and are brought to 1000 °C under vacuum. Once at temperature an oxygen gas valve is opened and thermal oxidation of the silicon surface occurs. The wafers have a thermal oxide grown with 500 to 1000 $\mathring{A}$ thickness. A $\sim$100 $\mathring{A}$ thick layer of platinum is sputtered onto the oxide to act as the charge-collection layer. The cathode layer is spun onto the platinum surface with various spinning parameters to minimize the surface roughness.

In this work the cathode is prepared through a previously reported sol-gel method (87; 88). All sol-gel preparation took place in a glove box with a ultra-high purity

helium atmosphere. Manganese(III)-acetylacetonate ($Mn(CH_3COCHCOCH_3)_3$) and lithium-acetylacetonate ($LiCH_3COCHCO\text{-}CH_3$) were mixed in a 2:1 molar ratio. Several ratios (1.95:1, 2.08:1, 1.99:1, 2:1) around 2:1 molar were explored to find the ideal mixing ratio. These powders were dissolved in a 1:3 (v/v) mixture of acetic-acid:1-butanol and magnetically stirred for 10 hours. The solution was filtered first through a fine-frit büchner funnel (pore size 4-5.5 μm diameter) with a vacuum attachment into a 25 ml flask. It was observed that the solution filtered so slowly that a slight vacuum must be applied in order to draw the solution through the frit. A *vacuubrand* MZ-2C chemical pump with two catch flasks was attached to a feedthrough which has a ball-valve on the inside and outside of the glove box. The vacuum line was attached to the Büchner funnel and the ball-valve was slowly opened. Once it is observed that the fluid begins to drip into the catch flask from the funnel the valve is shut. If the vacuum drawn is significant solvents will evolve and a precipitate is observed on the frit.

Following the fine-frit filter, a 0.22 μm teflon filter is used to filter the sol-gel further. The sol-gel in the catch flask from the büchner funnel is drawn into a syringe, and the teflon filter is attached to the Luer-lock tip of the syringe. The sol-gel is filtered into sample vials which are capped with rubber stoppers. It is important to emphasize the stoppers and sample vials must be clean, with no dust or other matter on them. The stoppers and vials are first washed with a residue-free detergent (Alconox), rinsed with DI-water, rinsed with acetone, blown dry with dry/filtered air, and placed into the glove box antechamber vacuum for 4 hours prior to use. It was noted that any residue or dust on either the stopper or sample vial would lead to undesired features in the spun sol-gel film. Stoppers were secured with aluminum wire for transport to a class 1,000 clean room.

Silicon wafers with SiO_2/Pt thin films are placed on a vacuum chuck for a spinner with laminar exhaust flow. The spinner is tested prior to drawing the sol-gel to

ensure the spinning parameters are correct. Spinning speeds between 3,000 and 3,750 rpm were investigated in addition to timing for the spread option at 500 rpm. The spinner first spreads the sol-gel at 500 rpm for a 2 seconds to cover the surface, then the spinner rapidly accelerates to the desired spinning speed for 30 seconds.

Approximately one (1) ml sol-gel is drawn into a syringe utilizing a needle through the stopper on the sample vial to extract the sol-gel. Two important observations were made: first, exposure of the sol-gel to the atmosphere for any length of time resulted in observable defects in the thin-film. Second, only one spun film per sample vial was possible without the inclusion of defects into the thin-film. After drawing the sol-gel into the syringe, the syringe is inverted so the tip points away from the ground, the needle is inserted into a wipe, and the plunger is depressed until it can be observed that all the bubbles are removed from the syringe. The needle is then removed, and the syringe is quickly placed over the wafer approximately one centimeter from the wafer surface. The plunger is then depressed in a single fluid motion, the syringe is quickly withdrawn, and the spinner is immediately started. Multiple depressions of the plunger resulted in un-even films in addition to defects. If the spinner were not immediately started the leading edge of the sol-gel would begin to evaporate solvent and would result in a poor surface coating.

Following spinning the sample is moved to a hot-plate at 320 °C to dry for 10 minutes. Following drying the samples are moved to a box-furnace which is already heated, varying temperatures (650 °C , 700 °C , 750 °C , 800 °C) were investigated. The samples are placed into a quartz boat and a lid was placed over the boat. The boat and lid are inserted into the furnace and two quartz tubes are inserted which allow in-flow and out-flow of ultra-high purity N_2/O_2 mixture for annealing the thin-films. The samples remain in the furnace for varying times (650 °C/10 min, 650 °C/15 min, 650 °C/20 min) and the boat is then removed to a steel plate to cool. An example of the finished cathode can be found in figure 3.1.

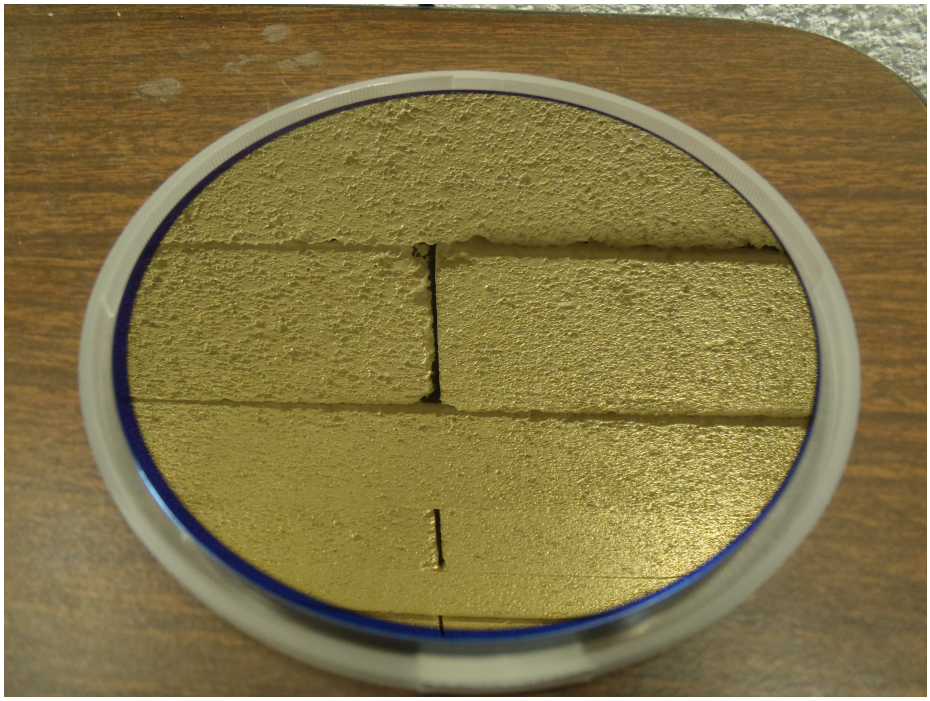

Figure 3.1: An example of a $LiMn_2O_4$ thin-film cathode for NR experiments. The cracks in the image are only reflection from the brick wall behind the sample due to the angle required to focus on the 4" diameter wafer.

Samples are typically characterized through AFM for surface roughness, XRR for surface roughness, warp, and film density, and the electrochemical performance is tested through electrochemical CV and galvanostatic methods. As stated in the background, the electrochemical performance of $LiMn_2O_4$ is very unique to the Li-Mn-O system and is used to ensure the sample generally consists of electroactive material. XRR in conjunction with NR are utilized to determine approximate density of the film in addition to thickness. XPS is used in limited cases to examine the Mn/O ratio for the process parameters determined ideal for NR experiments.

3.2 Anode development

The anode used for the NR full-cell experiments was produced through electro-deposition of lithium onto a copper thin film. Typically, electro-deposition of lithium produces a very dendritic structure(89). Yang et al. discovered that under dynamic

electrolyte conditions (magnetic stirring) and a high deposition rate (2 mA/cm^2) dendritic growth could be suppressed. In this work an apparatus was constructed which enables uniform coverage of a copper thin-film on a silicon substrate by spinning the substrate in an electrolyte bath. The electrolyte bath throughout this work is a 1M $LiClO_4$ salt dissolved in 1:1 (v:v) EC:DMC. Following deposition the substrate is washed in a 1:1 (v:v) EC:DMC mixture to remove any salt residue. EC from the rinse dries as a solid on the substrate after the DMC evaporates off due to the high volatility of DMC. The substrate is then rinsed with pure DMC to remove EC from the surface. Substrates are then placed on a hot-plate at 80 °C for 10 hours to evaporate adsorbed DMC.

The substrate in this work was initially silicon wafers with a 100 nm copper thin film. As will be detailed these suffered from significant copper corrosion and delamination. Additionally it quickly became obvious that lithium was being drawn into the silicon even after the potential was removed from the thin-film. The second design of the substrate included a 100 nm thermal oxide between the silicon wafer and the copper thin-film. This resulted in significantly less copper corrosion, but retained the lithium diffusion into the silicon wafer. The final design included a titanium buffer layer between the silicon oxide and copper thin-films. This design had the same copper corrosion as after adding the oxide layer, but prevented lithium diffusion into the silicon wafer.

Initial attempts at lithium electro-deposition were fraught with problems. A simple cell as drawn in figure 3.2 was the starting point for this work. It is composed of a piece of teflon machined to hold a circular piece of lithium metal and a stir bar sitting on the metal to allow for magnetic stirring. A silicon wafer with a copper thin-film has a piece of copper tape attached to the surface and the working electrode lead is attached to the tape. A current is applied which is $\sim$2 mA/cm^2 for 10 minutes. It was determined that this method too was unsuitable for two reasons. The first being

the non-uniform coverage as a result of small height differences on the lithium surface from forming the circular lithium counter electrode. The second being difficulty in stirring the electrolyte at a sufficient rate to prevent dendritic formation. When stirring too fast significant electrolyte could be lost from the stage, or a vortex would form preventing sustained contact at the center of the wafer.

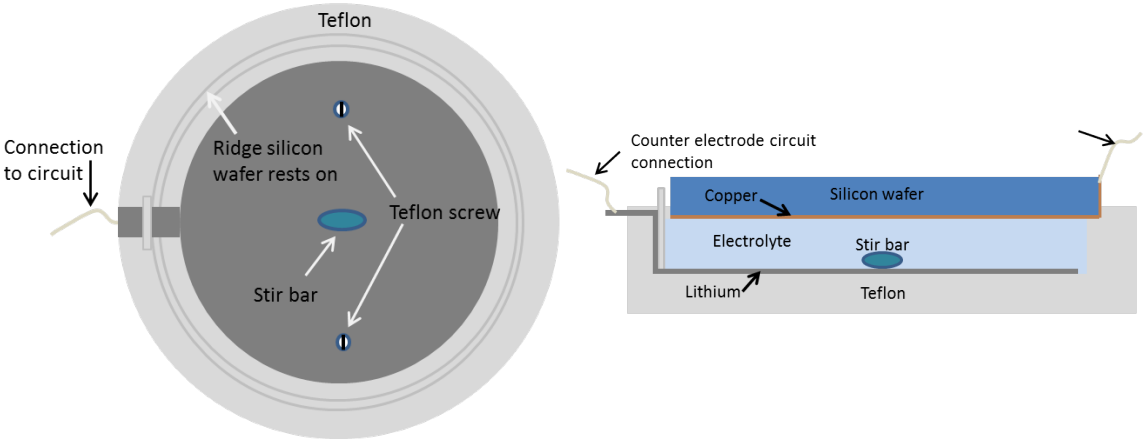

Figure 3.2: Left: Top down visualization of the first lithium electro-deposition cell. Right: Cross-section of first lithium electro-deposition cell.

Additional problems at this stage of development included lithium diffusion into silicon as well as difficulty in protecting the electrical connection to the copper thin-film. As stated earlier, the initial electro-deposition stage utilized the silicon/copper thin-film design for the deposition surface. A very surprising finding was the 'disappearing lithium' problem. After a rough lithium layer was successfully deposited, after several days of storage in an argon glove box, the lithium had apparently disappeared. Instead the surface which had been covered (albeit poorly) with gray lithium metal now was corroded (bare) copper. There was no obvious residue indicating chemical change as would be expected if the electro-deposited lithium were creating carbonate, nitrate, or hydroxide which are the typical lithium corrosion pathways. Upon fracturing the wafer, discoloration along the cross section showed the lithium had migrated into the silicon wafer.

An improvement to the original electro-deposition design came by replacing the circular lithium metal with a radial section of approximately 20°. As can be observed in figure 3.3 the change was relatively small; however, it resulted in better uniformity and coverage within the radial section than the circular metal counter electrode. Full coverage of the wafer was achieved through depositing for 10 minutes at ∼2 mA/cm^2 (based upon the surface area of the counter electrode), then rotating the wafer by ∼20° and repeating the deposition. The most significant result from this change was observing the edge effects from the counter electrode. Where the lithium edges faced the copper thin-film, greater deposition occurred. This should be expected, but was not surmountable in this design. The same issue with stirring the electrolyte occurred with this small change as with the original design and it was determined that a complete re-thinking of the deposition stage was necessary.

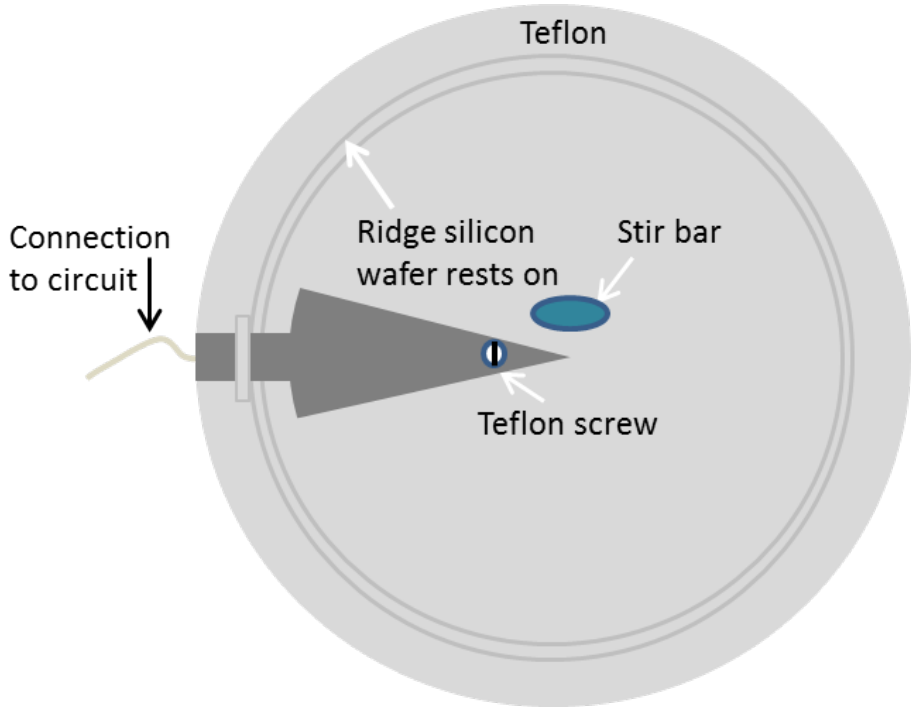

Figure 3.3: Second design of lithium electro-deposition stage.

In re-designing the lithium electro-deposition stage several considerations were of priority based upon the previous experience in attempts at lithium deposition.

First and foremost, it was apparent that stirring the electrolyte would not achieve the desired dendrite-free surface. Second, it was obvious that the slow rotation by hand would not result in a uniform coverage. There was either too much overlap due to the edge effect and ridges built up, or too much space would be in-between the deposited sections. The solution was discovered by removing the necessity to stir the electrolyte; instead, the wafer should be the object rotating. Figure 3.2 shows the final design for the lithium deposition apparatus.

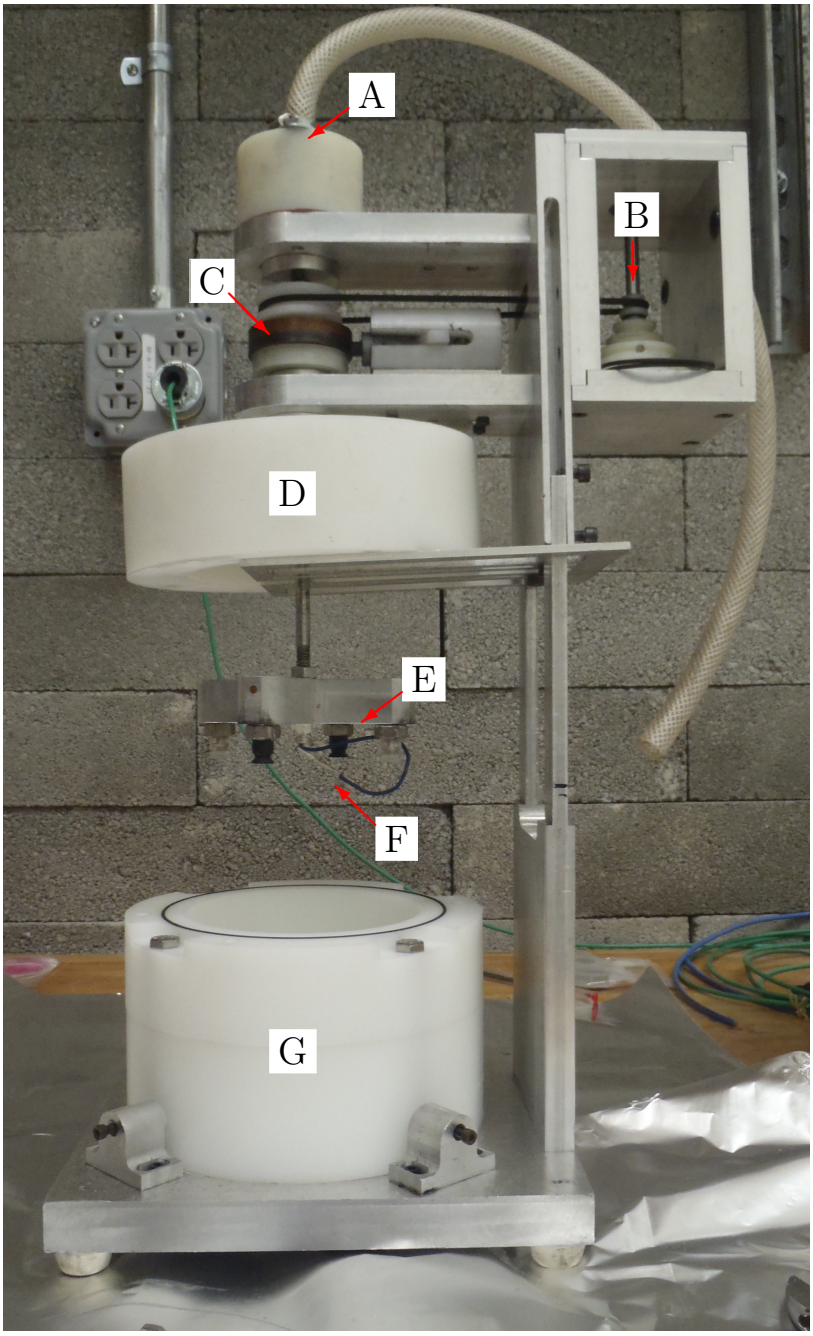

Figure 3.4: Final design of lithium electro-deposition apparatus. A) Vacuum cup, B) Stepping pulley, C) Rotating electrical connector, D) Deposition chamber lid, E) Vacuum chuck, F) Wafer electrical connector, G) Deposition chamber

The apparatus works by utilizing a vacuum line feed-through into the glove box, pulling a vacuum on the vacuum cup. The vacuum cup is a hollow cylinder which sits over the end of the spindle. The spindle is a 1/4" OD stainless-steel tube, and is press-

fit into two sealed bearings which are also press-fit into aluminum supports. A third bearing is utilized in the deposition chamber lid to prevent wobbling of the vacuum chuck in the deposition chamber. The vacuum is transferred down the spindle to the vacuum chuck, which is a cross with 1/8" holes drilled to meet grooves machined into the spindle. The cross-piece has a suction cup at each end of the cross which hold the wafer when vacuum is drawn. Figure 3.5 presents a closer view of these features.

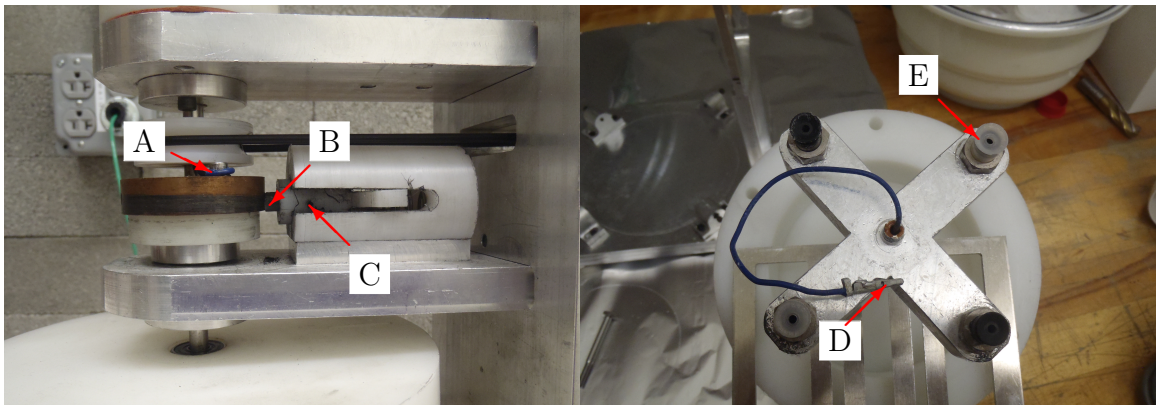

Figure 3.5: Left: Rotating electrical connection A) Copper block with wire attached which runs through spindle, B) Spring loaded graphite rod connects the rotating copper block to the wire which inserts into the hole at C). Right: Vacuum chuck D) Electrical connector attaches to the wafer, E) vacuum suction cup.

The vacuum cups are made from two materials as it is known most synthetic rubbers swell in the presence of organic solvents. Both types were used to gain an understanding of which would perform better in the environment. It was expected one material would perform better in the organic solvents over time; however, it never became an issue in the testing where either cup-type exhibited signs of swelling or degradation.

An electrical connection to the wafer is made through the rotating electrical connector (see figure 3.5). Attached to the copper block is a wire which is drawn through the spindle and sealed at both its inlet and outlet by an epoxy. The pin-type connectors between the apparatus and the wafer are protected by a HDPE housing.

The deposition chamber is composed of two pieces (figure 3.6). The bottom piece of the deposition chamber houses the lithium metal sheet used as a lithium source for electro-deposition. A 30° radial section is cut 0.095" deep which a 0.1" thick lithium metal sheet resides in. A groove cut through the wall of the deposition chamber extending the radial section is used to pass lithium foil out of the chamber to make electrical contact. The lithium sheet protrudes ∼1 cm from the edge of the chamber, is trimmed, has a copper wire set on it and is folded back on itself into the chamber wall. It was found that the only electrolyte leakage path through the bottom/top chamber interface occurred at this point. The folded lithium is compressed by the top of the deposition chamber and provides a seal in conjunction with the Viton gasket. The compression of lithium metal also serves as an effective means of holding the copper wire securely ensuring a good connection.

The top of the lithium deposition chamber has a 20° radial section removed which sits on top of the section which houses the lithium sheet. This effectively masks the sharp edges of the lithium sheet and removes the issues resulting from edge effects on the electric field. Additionally, a 1/4" diameter HDPE rod with a slit to hold the tip of the lithium sheet is inserted in the center hole to mask the tip of the lithium sheet. The ID of the deposition chamber is intentionally only 0.1" greater than the OD of the wafer to prevent the vacuum chuck from wobbling too far in the event the wafer is loaded off-center. An alignment piece was machined which sits inside the top of the deposition chamber and allows the wafer to be centered on the vacuum chuck which also ensures a balanced weight distribution.

Figure 3.6: Left: Bottom of the lithium deposition chamber A)30° radial section where lithium metal sheet resides, B) Lithium metal extending from the radial section sits in this channel. The extension protrudes from the edge of the chamber by ∼1 cm, is folded back upon itself and a copper wire is sandwiched between. This fold is compressed by the top of the chamber to create a seal in conjunction with the Viton gasket. Right: Top of the lithium deposition chamber C) 20° radial section which masks the edges of the lithium sheet. D) Alignment hole for machining purposes. The hole during operation has a 1/4" diameter HDPE rod with a slit which holds the tip of the lithium sheet masking the tip (not shown).

The wafer for electro-deposition is comprised of a silicon substrate, a 100 nm SiO_2 thermal oxide, a 7 nm Ti buffer layer, and finally 100 nm Cu. Figure 3.7 highlights the features on the backside of the wafer. There are four holes water jet into the wafer at 1.65" from the center, two are 180° opposite, the other two are offset from the first two by 15°. The purpose of the four holes are as follows: the two 180° opposite holes are used for in-flow and out-flow of electrolyte. One of the 15° offset holes is used for a reference electrode inlet, and the other is used to secure a copper post for better connection to the copper thin-film. The offset holes are designed to be closer to the neutron beam in order to minimize the potential for background scattering off of the copper post and a stainless steel tube used to house the reference electrode. The copper post is inserted into the assigned hole, and is epoxied into place.

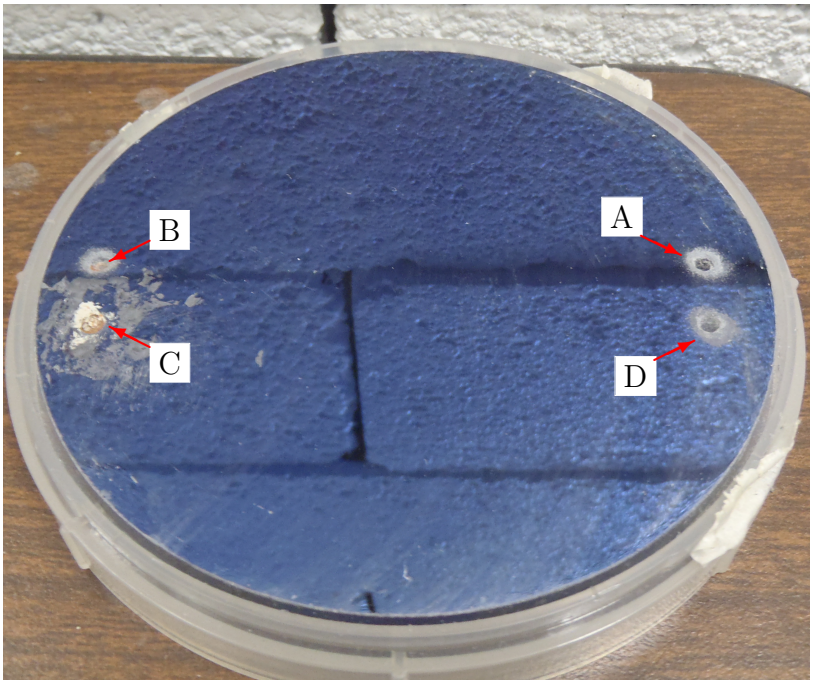

Figure 3.7: Four holes show are for: A) In-flow, B) Out-flow, C) Copper post for electrical connection to the copper thin-film, D) Reference electrode inlet.

The post on the backside is filed down, coated in conductive silver paint, and a piece of copper tape secured to a wire is epoxied over the post, see figure 3.8. The front-side of the wafer with the copper thin film has the post covered in a thin-coating of silver paint, then is epoxied over to ensure the connection is protected. The pin-type wire connection between the lithium electro-deposition apparatus and the wafer is protected by a HDPE housing. The housing is composed of two pieces where a lid with a rubber gasket is used to prevent incursion of electrolyte. If the connection is not protected then lithium from the electrolyte salt will plate onto the connection and prevent deposition on the wafer surface.

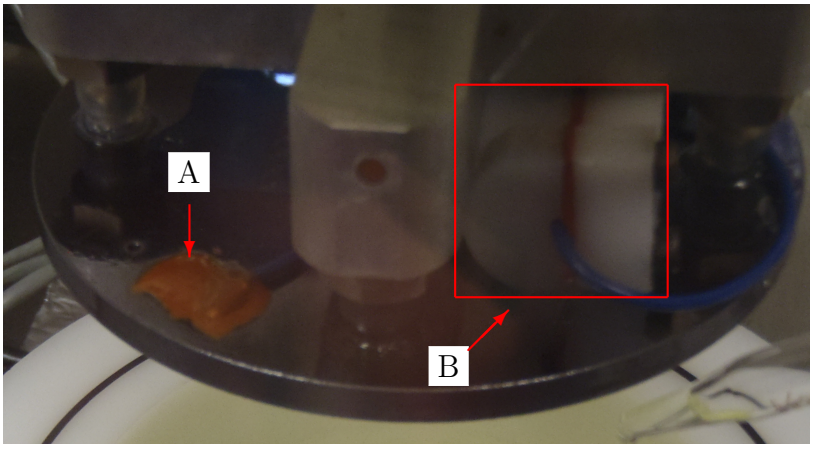

Figure 3.8: Anode wafer in vacuum chuck highlighting the wire connections: A) Copper post with silver paint, covered by copper tape connected to a wire, covered by epoxy B) HDPE housing protecting the pin-type connection between the lithium electro-deposition apparatus and the wafer.

While this design was quite successful in electro-depositing lithium one significant change in operation from the previous designs is the inability to use galvanostatic methods to deposit lithium. While attempts were made to level the wafer on the vacuum chuck, it is not perfectly flat. While attempting to hold the rotating wafer at a constant current the potentiostat/galvanostat (Princeton Applied Research Model 263A) was unable to compensate for the fast change required given the speed at which the wafer is rotating ($\sim$ 100 rpm). The potentiostat/galvanostat would overload when attempting to deposit at constant current. It was determined that the potential could be controlled adequately allowing the current to fluctuate. One issue with this method is the change in current over time. The current does not stay at a single value, so while the voltage is chosen by the observed current at the start of deposition, the current may increase over time beyond the desired $\sim$2 mA/cm^2.

This section shows the development of a lithium electro-deposition device along with several iterative approaches. An apparatus was built which rotates the silicon wafer in an electroylte while maintaining an electrical couple between a lithium-metal source and the silicon wafer. A successful approach was employed which enables

uniform lithium coverage on a silicon wafer with a copper thin-film.

3.3 Neutron reflectometry reference electrode

A reference electrode is very useful when exploring electrochemical systems. A 3-electrode cell is composed of a working electrode (typically the cathode), counter electrode (typically the anode), and a reference electrode. The purpose of the reference electrode is to measure the potential of the cathode electrode. A potentiostat utilizes the reference electrode to control the cell by measuring the potential of the cathode and delivering or pulling current from the anode in order to change to potential of the cathode to a desired level.

Standard reference electrodes include the standard hydrogen electrode, normal hydrogen electrode, copper-copper(II) sulfate electrode, and others. In the case of lithium-ion electrode testing these typical reference electrodes are impractical due to the aqueous nature of the electrolyte in the standard reference. In practice, lithium-ion electrode testing utilizes a psuedo-reference electrode, typically lithium metal. A difficulty encountered in utilizing lithium metal for a reference electrode is the unstable nature in air. A lithium wire could be used as a reference in the neutron reflectometry cell; however, the hazards associated with lithium metal in the air are problematic in addition to the corrosion aspect in air. A solution was discovered by utilizing a copper wire, Teflon needle, lithium metal, stainless steel tube, and a Swagelok fitting. Teflon has an effective melting point of 326.8 °C; however, liquid alkali metals are known to react with Teflon in an electrochemical manner producing LiF and C as byproducts (90). This creates a problem as the reference electrode must be electrically insulated in order to function correctly, but a method was developed which, when applied well, results in an acceptable outcome. While a glass tube could be used instead of Teflon for insulating purposes, it becomes impractical when considering insertion into the electrochemical cell given bending of the reference is

required.

The actual pseudo-reference developed in this work involves only the Teflon needle, copper wire, and lithium metal. Lithium metal in a glove box is heated in an alumina crucible to slightly over the melting point. Lithium metal melts at a temperature of 180.5 °C, but practically the temperature of the crucible was raised to 200 °C to ensure thorough heating of the metal given some radiative loss of the exposed metal. The thermocouple is placed in-between the heating element and the crucible to and held by a temperature controller. The copper wire is drawn into a Teflon needle to 3-5 mm from the tip of the needle, leaving 5-7 cm wire exposed on the Luer-lock end of the needle. The needle is attached to a syringe, preferably a glass syringe, with the excess wire residing in the body of the syringe. The needle is inserted deep into the molten lithium, beyond the end of the copper wire, and the plunger on the syringe is very gently pulled. The purpose of this procedure is to draw molten lithium into the Teflon needle. Care must be taken at this point, if the plunger is drawn too quickly or too far a violent reaction can take place between the Teflon and lithium metal. The reaction scale is quite small, and only results in fracturing the needle body, thereby ruining the electrode. The glass syringe offers an important feature; it has a greater mass than a plastic syringe. It was determined that a pressure which draws lithium, but prevents the violent reaction can be achieved by holding onto the glass plunger and allowing the weight of the syringe body to create a negative pressure within the syringe. When performed correctly the drawing process takes on the order of 15 seconds, and the needle is quickly removed from the molten lithium metal. A representative figure of this setup is shown in figure 3.9.

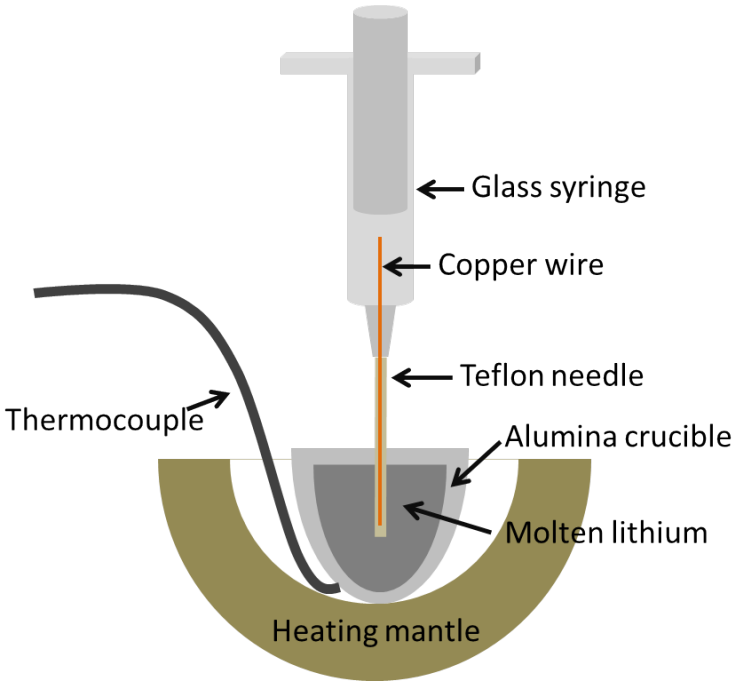

Figure 3.9: Fabrication setup of the lithium pseudo-reference electrode. A Teflon needle with a copper wire is inserted into molten lithium at ~200 °C. The plunger tip is held and the weight of the glass syringe is used to draw lithium into the needle and into contact with the copper wire.

Following removal of the Teflon needle from the molten lithium, a razor is used to remove the outermost ~0.5 mm of the needle to expose fresh lithium metal. This also separates the now hardened lithium on the exterior of the Teflon needle from that which is inside the needle and can be easily removed. If the process is unsuccessful in coupling the copper and lithium it is advised to discard the needle and prepare another. Re-insertion and melting the lithium in the needle body requires too much time in the molten lithium and so far has been unsuccessful in producing a successful reference electrode.

The reference electrode is tested by placing the lithium tip into an electrolyte bath versus a piece of lithium metal and observing the open circuit voltage as a function of time. If the potential does not register as zero, or fluctuates as a function of time beyond the resolution of the potentiostat, the reference is deemed unacceptable.

3.4 Neutron reflectometry electrochemical test cell

An electrochemical test cell was developed which meets the necessary parameters for neutron reflectometry. The necessary design functions are: electrochemically functional, and low neutron scatter materials for background reduction. A view of the NR cell mounted in the MAGIK NR instrument at the National Institue of Standards and Technology (NIST) Center for Neutron Research (NCNR) is found in figure 3.10.

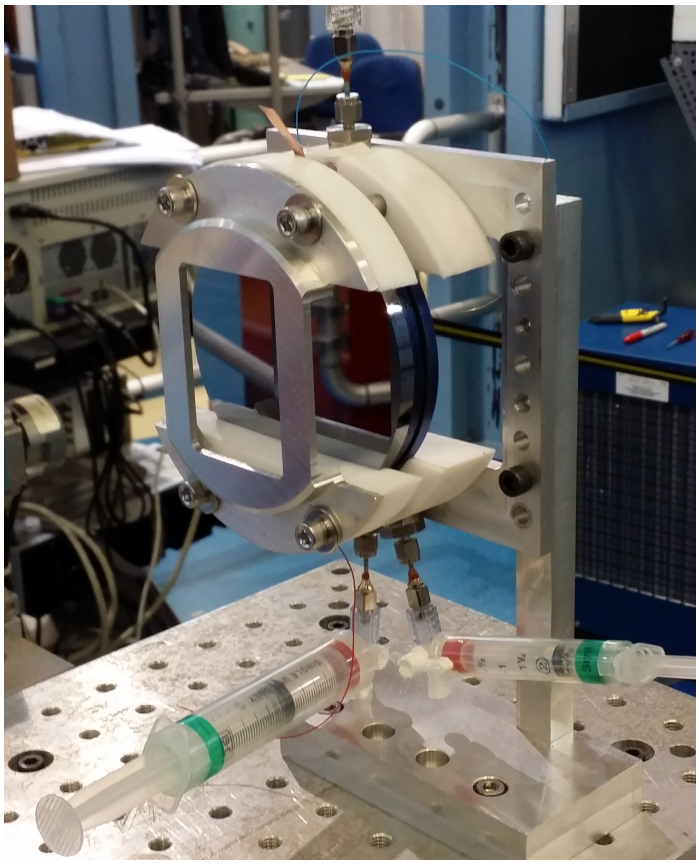

Figure 3.10: NR electrochemical cell installed on the MAGIK beamline at the NIST NCNR.

In figure 3.10 a reference electrode is not utilized. While the reference electrode does improve electrochemical measurements, it was decided that without being able to draw air out of the reference input while injecting electrolyte the potential of introducing bubbles into the neutron footprint was too high. A re-design should be implemented on the reference electrode port to allow for a syringe to draw air out

of the vacant space and fill with electrolyte to remove this potential. In figure 3.10 the reference electrode was replaced with another electrolyte-filled syringe and the in-port as well as the reference-port are used to fill the cell.

The electrochemical cell is assembled in a Ultra High Purity Helium glove box with H_2O levels <0.3 ppm, and O_2 levels <3 ppm. The gas in the electrochemical cell is removed via a 3rd syringe not shown in figure 3.10. This third syringe is drawn while the other two syringes shown are pushed to ensure gas is removed from the cell.

3.4.1 Electrochemically functional cell

Electrochemically functional generally requires consideration of three parameters: electrically insulating, electrical contact, and separation of electrodes. The cell is made electrically insulating by utilizing Teflon as the main body which provides the clamping force for the two electrodes. Electrical contact is made through two contacts on the anode, one contact on the cathode, and one to the reference electrode if it is used. The two contacts on the anode are made through the copper post used to electrodeposit lithium (figure 3.11), and by a copper tape epoxied onto the surface.

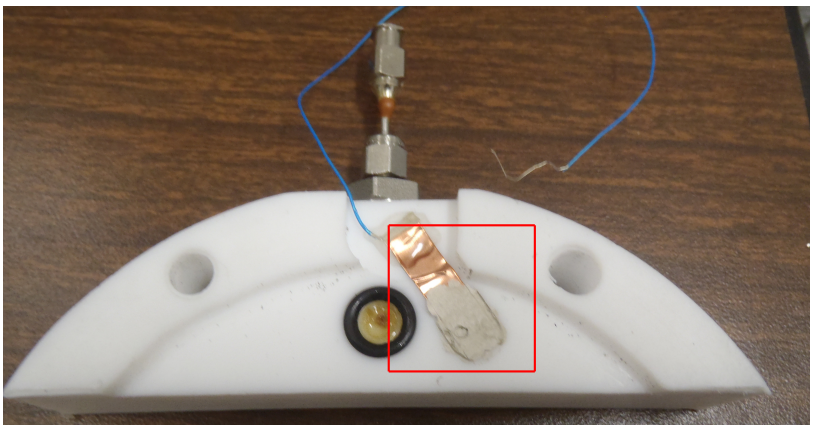

Figure 3.11: One of the two electrical possible electrical connections to the NR electrochemical cell is made through silver paint on a copper tape. The tape sits in a channel below the level which the anode rests, and is epoxied into place with a wire. The wire is connected to the potentiostat through an alligator clip. The round feature in the silver paint shows an indentation from the copper post which enables contact to the anode lithium film.

The copper tape on the anode serves as a redundant connection in the event the copper-post method fails. It has been found the electrochemical response measured through the post is generally better than the epoxied tape method. It is not clear experimentally why one method works better than the other; however, the most likely reason is due to an anodic reduction electrolyte breakdown when depositing lithium on the anode copper thin-film. The copper-post is electrically connected to the lithium deposition surface by a silver paint and is protected by an epoxy covering. The copper-tape method is protected by epoxy, but no allowance for the interfacial layer on the anode surface is taken into account. As the electro-deposition process used to prepare the anode occurs, reduced electrolytic species likely cover the entirety of the anode surface, including area which does not expereince lithium electrodeposition. This surface layer likely does not allow good electrical contact to the copper thin-film and results in poorer electrical contact.

Connection to the cathode is through a strip of copper tape which is epoxied into place. This method is deemed to be more acceptable than the tape on the anode as there is direct contact to the cathode surface, and the thickness of the $LiMn_2O_4$ layer is on the order of $\sim$15 nm which is thin enough to allow transmission of the electric field to the charge collection layer.

The reference electrode, if used, is connected via the copper wire which leads into the Teflon needle. The electrode is inserted into a stainless steel (SS) tube 1/16" diameter which is held in place via a Swagelok face-seal fitting. When the fitting is swaged onto the SS tube the tube is contracted, which contracts around the Teflon needle and creates a seal against electrolyte leakage.

Separation of the electrodes are found through a Kalrez gasket. Kalrez is one of the few polymer gasket materials which is capable of withstanding solvent attack from the organic solvents used in lithium-ion batteries. Most polymeric gasket materials become swollen in contact with electrolyte solvents. While this is acceptable for the

relative short times (days) of a NR experiment for sealing purposes, it is problematic from an alignment perspective of the neutron beam. If the polymeric gasket separating the electrodes swells under operation it can result in a slow, monotonic change in angle of the cathode to the neutron beam. This can result in deviation from the aligned position and would result in poor data collection. Kalrez is able to withstand solvent penetration and attack and is therefore ideal for this purpose. The gasket is designed to maximize surface area while removing any sharp corners which can trap air as well as allow for the copper-tape to be attached to the electrode (figure 3.12). The gasket is 1/64" thick, and approximately 4" in diameter and was made using a CNC-razor on a 6"x6" sheet.

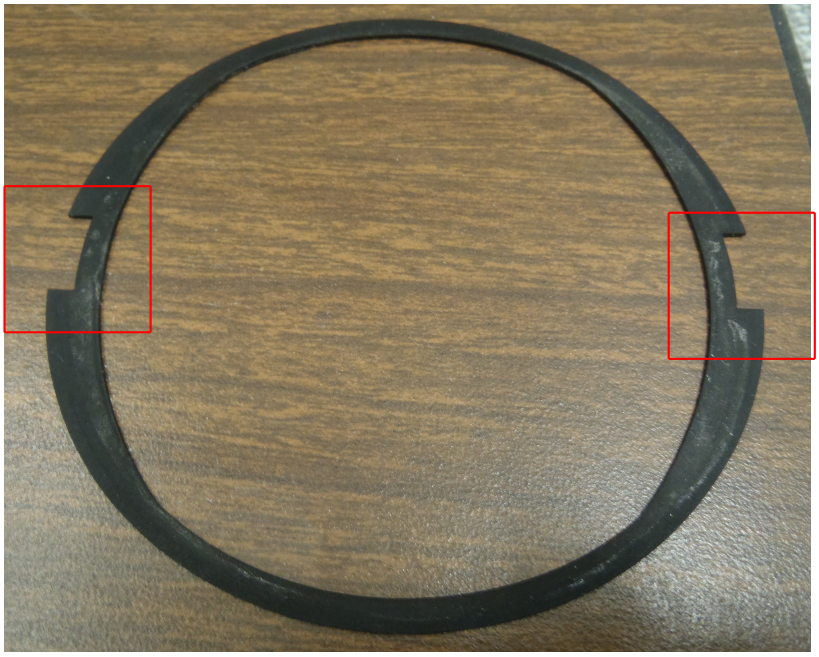

Figure 3.12: Kalrez gasket to separate the electrodes in addition to sealing the electrochemical NR cell. Boxes highlight the location where copper tape is used to make electrical connection to the electrodes.

The gasket design was chosen to maximize surface area while ensuring a good seal was achievable, and solvent could be expected to fill the space. As the gap between cathode and anode is approximately the thickness of the gasket (it is actually less once the gasket is compressed), capillary action is expected to drive the filling of the

space. The gasket was designed without significant corners which might prevent air from being pushed out of the space. The in-let hole is very close to the edge of the gasket thereby allowing the initial electrolyte inclusion to find the gasket wall quickly and move air out as the rest of the space is filled.

3.4.2 Neutron scattering considerations

Neutron scattering contributing to background is a consideration which must be approached by choosing materials which are known to have small scattering cross-sections. Materials which contain hydrogen should be avoided, as well as steels if at all possible. A typical structural material for a neutron scattering experiment is aluminum, which has a low scatter coefficient reducing the potential for background addition. In this NR cell aluminum is used as the upper and lower structural support which compresses Teflon to ensure a seal for the electrochemical cell.

Teflon is used for two purposes in this cell; it is electrically insulating, but also of importance from a background consideration as it is a polymer without hydrogen. The carbon chains in Teflon have fluorine attached to the backbone instead of a typical hydrogen. This greatly reduces the potential for additional scattering within the cell.

Stainless steel is used for the Swagelok fittings, as well as the bolts used to hold the cell together. This choice is unavoidable since aluminum bolt threads can undergo plastic deformation when tightened, and the face-seal fittings were not attainable in another material type.

3.5 Neutron and X-ray reflectometry

3.5.1 Cathode development characterization

XRR is used to investigate the acceptability of sample preparation conditions. XRR results not only provide insight into the roughness and density of the $LiMn_2O_4$ layer, but also provide insight on the extent of warp due to the rapid heating in the annealing step. XRR provides an excellent means of determination of whether the processing parameters are conducive to NR as XRR is qualitatively the same technique. These samples were prepared as described in the cathode development section, with one change being the thin-films in these samples are on 0.5 mm thick substrates. This has the added benefit of examining warp effects on the silicon because minimizing warp in these samples should also minimize warp in the thicker (5 mm) sample case. Table 3.2 shows the list of parameters investigated through XRR. The table describes the sample properties and the angular window used to collect those data. The scan type listed in the table describes whether XRR data are taken as one continuous scan or as a series of split scans. The advantage of split scans are the option to change the counting time per point as well as the intensity of the beam for individual scans which are combined to form the reflectivity dataset. Continuous scans indicate the beam intensity is held constant, and in some cases the time-per-point are held constant. Continuous scans were initially used to examine samples as software limitations prevented changing beam intensity. The use of the Split scan method was enabled through a script written specifically to import datasets with changing counting time and beam intensity.

Table 3.1: Table of samples characterized through XRR for cathode fabrication parameter determination

Condition	anneal temp (°C)	anneal (min)	spin rate (rpm)	scan window ($\AA^{-1}$)	Scan type
Anneal Temp	650	10	3750	0-0.478	Continuous
	700	10	3750	0 - 0.569	Split
	750	10	3750	0 - 0.569	Split
	800	10	3750	0 - 0.255	Split
Anneal Time	650	10	3750	0 - 0.455	Continuous
	650	15	3750	0 - 0.437	Continuous
	650	20	3750	0 - 0.504	Continuous
Spin Rate	650	10	3000	0 - 0.569	Continuous
	650	10	3500	0 - 0.572	Split
	650	10	3750	0 - 0.498	Split

Specular data are collected on a BEDE D1 High Resolution X-Ray Diffractometer, using 100 μm fixed slits to form the beam profile, from 0° theta through several degrees. The scan range varies depending upon the scan method and whether or not data above background are still being collected in a reasonable time-frame. Alignment of the sample in the x-ray diffractometer is performed through an iterative procedure outlined here. All motor movements in this procedure are moved in the same direction when moving to the desired position to prevent effects from backlash. In other words, if a θ-scan is implemented from θ=0 to θ=0.3 in the positive direction, when the desired position is determined the θ-motor is first moved $\sim$0.5 ° in the negative direction beyond the starting θ then the θ-motor is driven to the desired position. By always moving the motors in the same direction as the alignment scan mis-alignment due to finite play in the gearing is minimized.

The starting point in reflectometry alignment involves finding the detector zero position. This position is determined by moving the sample out of the beam and collecting data at various 2θ positions. The maximum intensity is set as the zero position for the detector and is not changed. The sample is moved into the beam in the Z-direction (normal to the surface of the wafer) and the intensity is monitored as a function of Z-position. When the intensity of the beam is $\sim$1/2 of the direct beam the sample is held at that position and the θ-motor is scanned through a wide window of $\sim$1°. Once the maximum value of θ is found the z-motor is again scanned

to determine if a change in z-position is necessary. These two motors are iterated until significant improvement ceases.

Next the sample is scanned in a locked-coupled θ-2θ mode through about 1°-θ (or 2°-2θ). This scan is used to determine a region of the critical edge where alignment in the reflected condition will occur. Typically in this work an alignment angle of 0.15° θ (or 0.3° 2θ) is used. Following determination of alignment position the θ and 2θ motors are driven to the alignment position (considering backlash) and three motors are iterated (Z, θ, and χ). Z and θ-motors have previously been described, whereas χ is the angle between the sample stage normal and the incident x-ray beam plane. The sample is considered aligned when there is no signficant improvement in any of the iterated motors. The θ and 2θ- motors are moved back to the zero position (taking into account backlash), and specular data are collected through the locked-coupled θ-2θ mode.

Background data are collected through offsetting theta 0.1° in the positive and negative directions and collecting data over the same range and counting time as the specular scans. Background data are collected at much wider intervals than specular data as there are no features in the background to examine. Background data collection time is matched to the data collection time. An average of the positive and negative offset background scans are subtracted from the specular data at each specular data point. If a specular data-point exists in between two background points, the background is interpolated and the interpolation is used to determine the background. Background is not a significant contribution at low angles, it only becomes signficant at higher angles where reflectivity drops to near-background levels.

Continuous scan reflectometry data are collected at 20 mA/30 kV and reduced through the software reflred (91) where background is subtracted. Split scan reflectometry data are collected at two intensities 20 mA/30 kV and 40 mA/40 kV. These split-scan data are reduced through a Python script which was written specifically to

allow for changing collection times and beam intensity. The split-scan script works by importing datasets into memory, and scans with varying intensity are identified through the filename structure. An additional two specular datasets must be collected over the same range for the same time at the two intensity levels to determine an intensity ratio with uncertainty. These scaling scans occur in a region where the reflected intensity is low enough to ensure the detector is not exposed to damaging levels of x-rays at the highest power utilized. The scaling factor is determined by averaging the ratio from all points in the two scaling datasets. Uncertainty in the scale factor is determined through standard counting statistics and uncertainty propagation (92).

Datasets are concatenated and overlapping data points are summed by first multiplying the counts per second, as recorded in the file, by the time at that point for each overlapping dataset. The total counts per measurement angle are summed and then divided by the total time for all measurements at that point from all overlapping scans to determine the counts per second. Finally the reflectometry data are normalized to 1 by the maximum value in those data. This normalization is not necessarily correct as warp in the sample can cause focusing or defocusing of the x-ray beam and raise or lower the total counts above what would be expected from a flat sample, also absorption of x-rays would decrease the reflected intensity. The total counts per point could also be lower than expected due to warp. As the reflected beam from a warped sample can be reflected in a angle slightly offset to the detector slit acceptance angle the overall effect is to reduce the intensity of the detected beam. The potential for the intensity to be greater or less than the incident beam intensity leads to normalizing these data by the largest reflectivity measured and utilizing the fitting software to fit a best-value for intensity.

3.5.2 *in-situ* NR cathode experiment

XRR is utilized prior to NR and electrochemical operation in order to provide a comparison as a starting point. In fabricating the cathode several parameters were expected such as thicknesses of the silicon oxide and platinum layers, as well as the densities of the silicon oxide and platinum layers. As was described in the previous chapter, secondary characterization is required in order to ensure an adequate model is determined. In this work XRR is applied in air to cathode samples prior to cell operation. Further, following placement in the electrochemical cell and electrochemical operation in the NR beam, the samples are again examined by XRR for further analysis. A Bruker D8 x-ray reflectometer is used to gather XRR data, reflred (91) is used to reduce those data, and finally Refl1D (93) is used to fit these data to a model.

XRR data were collected in a series of scans allowing for changing the count time per point and point spacing to maintain reasonable statistics while probing a large range of Q. Following NR experimentation of the cathodes in the operational electrochemical cells, the sample cells were stored in air for 4 months. Following the 4 month storage, the cells were first purged with DMC injected through the inlet-port. The cell was then disassembled and the cathode wafer is further rinsed multiple times with DMC. Delamination of the cathode thin-films occurred some time in the storage period which was observed when the sample cell was disassembled. Further, upon rinsing with DMC via-pipette more delamination was observed. Given the resultant delamination, XRR following storage and cleaning the x-ray beam was aligned on the areas of the sample which had the largest regions without delamination.

NR data were collected as a function of cyclic voltammetry cycles, where data were collected as described in tables 3.4 and 3.3 for the open-circuit and potential hold NR experiments. The beam footprint on the sample was chosen to be 1.75" x 1.75" because the sample was large enough to accomodate the footprint size, and the

larger footprint allows for a greater reflected intensity. Data were collected from 0.1° to 10.04° theta for Sample #1 in air and from 0.1° to 6.48° theta for Sample #1 in electrolyte. Data were collected from 0.1° to 8.68° theta for Sample #2 in air and from 0.1° to 6.48° theta for Sample #2 in electrolyte. Background data were collected by offsetting the sample by 0.1° theta in both the positive and negative directions, and collecting data for the same time as the specular scans.

The electrolyte chosen for these experiments is 1M $LiClO_4$ in 1:1 mixture of EC:DMC-d6 where the DMC has had hydrogen exchanged with deuterium resulting in an estimated electrolyte SLD of $3.9*10^{-6}$ $\mathring{A}$. The purpose of this isotopic substitution is two-fold. First deuterium has a very large positive bound coherent scattering length where hydrogen has a negative bound coherent scattering length. Therefore this mixture has a large SLD vs the cathode layer. If hydrogenated electrolyte solvents were used the electrolyte SLD would be estimated around $2.1*10^{-6}$ $\mathring{A}$. Second, it is expected that EC will decompose on the surface of the cathode (70; 71) and leave behind hydrogen which should create fair contrast between the SEI and electrolyte. Contrast between layers, or the magnitude of change in SLD between layers, determines the impact that interface has on the reflectivity profile. If there is little contrast then the certainty about two layers interfacing is low. However, with large contrast the interface has a large influence on the reflectivity profile and subsequently the certainty of those layers are greater.

Table 3.2: XRR conditions on samples used for NR experiments

Sample	Before/After NR	scan window ($\mathring{A}^{-1}$)
Sample #1	Before NR	0-0.7103
Sample #1	After NR	0-1.0638
Sample #2	Before NR	0-0.7103
Sample #2	After NR	0-1.0074

Table 3.3: Details of electrochemical cycles and NR experimental parameters for Sample #2 - 3300 mV hold

NR	electrochemistry	Start (mV)	Inflection (mV)	Inflection (mV)	Stop (mV)
yes	None - In air	-	-	-	-
yes	3300 mV Hold	-	-	-	-
no	CV 1	3300	4500	3250	3300
no	CV 2	3300	4500	3250	3300
no	CV 3	3300	4500	3250	3300
yes	3300 mV Hold	-	-	-	-
no	CV 4 - 10	3300	4500	3250	3300
no	CV 11	3300	4700	3250	3300
no	CV 12	3300	4600	3250	3300
no	CV 13	3300	4700	3250	3300
yes	3300mV Hold	-	-	-	-
no	CV 14 - 18	3300	4700	3250	3300
yes	4000mV Hold	-	-	-	-
no	CV 19 - 23	3300	4700	3250	3300
yes	4300mV Hold	-	-	-	-
no	CV 24 - 26	3300	4700	3250	3300
yes	3300mV Hold	-	-	-	-

Table 3.4: Details of electrochemical cycles and NR experimental parameters for Sample #1 - OCP

NR	electrochemistry	Start (mV)	Inflection (mV)	Inflection (mV)	Stop (mV)
yes	None - In air	-	-	-	-
yes	Open Circuit	-	-	-	-
no	CV 1	3300	4500	3250	3300
yes	Open Circuit	-	-	-	-
no	CV 2	3300	4500	3250	3300

3.5.3 NR data collection

NR data were collected at the MAGIK beam-line at the National Institute of Science and Technology (NIST) Center for Neutron Research (NCNR) (94). Figure 3.13 shows a sample on the MAGIK beamline at the NIST NCNR. The neutron beam is initially defined by a movable slit which is behind the shutter to close to beam. The beam them passes through an aperture which determines the height of the vertical beam, followed by another movable slit. The beam then impinges on the sample and

is reflected through another two movable slits and finally is detected. The two slits prior to the sample help determine the footprint on the sample which is the surface area of the sample which is exposed to the beam. The first two slits are moved in conjunction and are set to equivalent widths, so if slit 1 is 0.2 mm slit 2 would also be 0.2 mm. This equivalence is necessary in order to define the beam. The two slits past the sample are not held at equivalent widths, but a proportional width. The proportionality is designed such that the diverging beam after specular reflection from the surface is collected and not rejected.

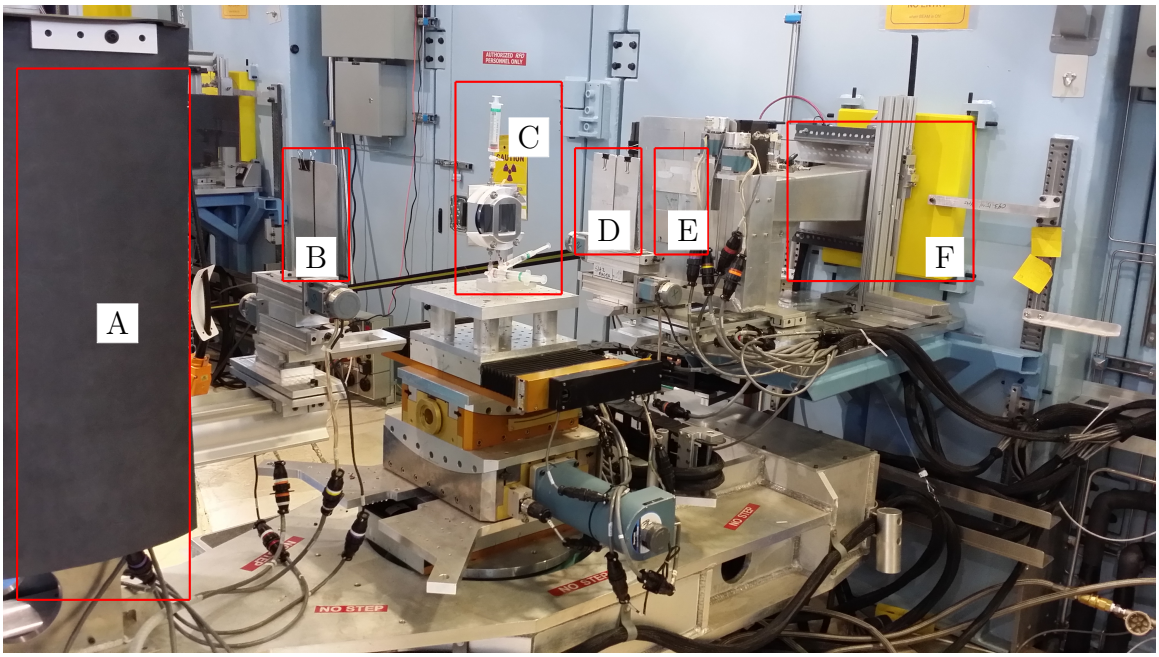

Figure 3.13: A picture of the MAGIK beamline at the NIST NCNR neutron scattering facility. A) Detector housing containing slit 4. B) Slit 3, C) Sample cell on instrument goniometer, D) Slit 2, E) Aperture, F) Shutter behind which is Slit 1

The first slit proceeding the sample is held at 3 times the incident beam width (i.e. incident slits set at 0.02 mm, the slit proceeding the sample is at 0.06 mm). The second slit proceeding the sample and prior to the detector is held at 4 times the incident beam width. All the slits have controllable widths, and are opened as a function of angle which provides two advantages. The first advantage is that enables a greater beam intensity on the sample as a function of angle, and the second is maintaining the

footprint of the beam on the sample surface. As neutron reflection scales as R$\propto Q^{-4}$, increasing the intensity as a function of angle improves statistics at larger values of Q while collecting data in a reasonable period of time. In order to properly reconstruct R(Q) the collected reflection data must be corrected for the intensity shift. A slit-scan is used to correct intensity as a function of slit-width. This involves measuring the direct beam at all slit widths used in these measurements. Attenuators are used to ensure the intensity on the detector remains within a reasonable range throughout the slit scan.

These reflection data are taken in a series of scans with varying slit-widths, counting times, and step-size to balance two considerations: time, and statistics. NR experiments occur at user facilities which offer beam-time through a proposal service. Time must be maximized to collect as many measurements as is possible, while also ensuring enough statistical certainty to provide confidence in results. At the lowest angle scan the reflected intensity is high therefore the time per point can be short. This also lends to using a small step-size to look for any thick layer fringes, as Kessig fringes occur on a period of $\frac{2\pi}{L}$ where L is the layer thickness. The lowest-angle uses a static slit-width as it is not necessary to increase the intensity by opening the slit-width. The first scan is stopped in a region where greater intensity would start to improve results, and the slit is opened to a larger value and varies as a linear function of angle. Subsequent scans increase time-per-point and increase the point-spacing in order to balance the two considerations. A typical set of NR scans for this work would appear as table 3.5

Table 3.5: A typical NR specular scan data collection process detailing the start and stop θ angle, the time-per-point, the point spacing, and whether the slits were held constant

Start (degrees)	Stop (degrees)	time-per-point (s)	point spacing (degrees)	Slit
0.1	0.5	60	0.01	Static
0.5	1.0	15	0.01	Linear
1.0	2.0	30	0.02	Linear
2.0	4.0	30	0.02	Linear
4.0	5.4	30	0.04	Linear

Background data are collected by offsetting the sample 0.1° theta from the specular condition in both the positive and negative directions and collecting data over the same theta range and total time per point as the specular data. In many cases at least two full-angular region scan sets as in table 3.5 were performed and combined in order to create a reflectometry profile. Depending on the number of scans, and if the time varied from those displayed in Table 3.5 the total time for each angular region was summed and background data were collected for that same time period. The point-spacing for background data are much larger than that of specular data because there are no significant point-spacing dependent trends in those background data. Background data curves slightly so the point spacing is chosen to encompass that change, but it is not necessary to have point spacing which are as close as that of those specular data. A table showing a typical background scan is shown in table 3.6. When background data are used to correct specular data, any specular point which lies between two background points has the background determined through an interpolation of those surrounding background points.

Table 3.6: A typical NR background scan data collection process detailing the start and stop θ angle, the time-per-point, the point spacing, and whether the slits were held constant.

Start (degrees)	Stop (degrees)	time-per-point (s)	point spacing	Slit
0.1	0.5	120	0.1	Static
0.5	1.0	30	0.1	Linear
1.0	2.0	60	0.1	Linear
2.0	4.0	60	0.1	Linear
4.0	5.4	60	0.2	Linear

A slit-scan entails collecting direct beam intensity through the silicon wafer (or air depending on the fronting medium) as a function of slit width, where the collection time is determined by the number of counts on a monitor detector. The monitor detector serves as a method of monitoring the neutron intensity change with reactor power. As slight fluctuations in reactor power change the neutron beam intensity, the monitor detector serves as a means for correcting for those fluctuations. The monitor detector sits in front of the first slit and is a ^{3}He pencil detector with an adjustable aperture which collects a proportional flux to that of the flux exiting the first slit (94). Slit-scans are collected for a period of time relating to 10,000 counts on the monitor. As the slit separation gets larger the beam intensity increases quickly. In order to prevent dead-time effects and other necessary detection corrections the total intensity is kept below $\sim$10,000 cps on the detector. In order to compensate for this at wide slit-separations attenuators are used to reduce the beam intensity. The attenuation coefficient is determined by finding the monitor corrected ratio of counts on the detector with and without the additional attenuator as shown in equation 3.1, and the additional uncertainty from the attenuator is determined through equation 3.2.

$$C_{att} = \frac{M_2 D_1}{M_1 D_2} \tag{3.1}$$

$$\sigma_{C_{att}} = \sqrt{\sigma_{M_1}^2 \left(\frac{\partial C_{att}}{\partial M_1}\right)^2 + \sigma_{M_2}^2 \left(\frac{\partial C_{att}}{\partial M_2}\right)^2 + \sigma_{D_1}^2 \left(\frac{\partial C_{att}}{\partial D_1}\right)^2 + \sigma_{D_2}^2 \left(\frac{\partial C_{att}}{\partial D_2}\right)^2}$$

$$\sigma_{C_{att}} = C_{att}\sqrt{\frac{1}{M_1} + \frac{1}{M_2} + \frac{1}{D_1} + \frac{1}{D_2}} \tag{3.2}$$

where C_{att}, M_1, M_2, D_1, D_2 are the attenuator coefficient, monitor counts without and with the attenuator, and the detector counts without and with the attenuator. In order to ensure clarity in this point, the attenuator coefficient as determined by equation 3.1 occurs at a single slit-spacing between no attenuator present and an attenuator. The process for adding further attenuators involves the same process of detecting intensity with and without the additional attenuator, determining the attenuation coefficient from equation 3.1 but in this case the calculated attenuator coefficient is multiplied by the coefficient between the with and without attenuator case as in equation 3.3.

$$C_{twoatt} = \frac{M_4 D_3}{M_3 D_4} * C_{att} \tag{3.3}$$

$$\sigma_{C_{twoatt}} = C_{twoatt}\sqrt{\frac{1}{M_1} + \frac{1}{M_2} + \frac{1}{D_1} + \frac{1}{D_2} + \frac{1}{M_3} + \frac{1}{M_4} + \frac{1}{D_3} + \frac{1}{D_4}} \tag{3.4}$$

where C_{twoatt} is the attenuator coefficient with two attenuators, M_3, M_4 are the monitor counts with one attenuator and two attenuators, and D_3, D_4 are detector counts with one attenuator and two attenuators. C_{att}, M_1, M_2, D_1, D_2 are previously defined and retain their initial description. For clarity it should be noted that the slit

width where the first attenuator coefficient was determined, and the slit width where the two-attenuator coefficient is determined are not the same width. Typically one attenuator will be used up until the intensity is too high for the detector at which time a reasonable slit-width below the limit of the detector is chosen to find the second attenuator coefficient. Through multiplying collected slit-scan intensity by the attenuation coefficients a direct-beam intensity vs slit width is constructed which is used to scale the collected reflection data as a function of slit width. As in the case of background where the slit-width of a specular measurement is not recorded exactly through the slit scan an interpolation is used to find the beam-intensity for that slit-width.

3.5.4 Reducing NR data

While data reduction occurs in the reflred(91) software, the process is detailed here for reader clarity. Specular and background data are divided by the monitor counts at each point. Background are collected at two points, where the sample is offset from the specular condition. The offset is the same angle in both directions and therefore a simple average of the two at each background point can be used to find the background of the specular peak. Specular data are then corrected for the averaged background by subtracting. As was stated previously, background data are not collected at every specular point. Therefore background at specular points which were not collected are determined through a linear interpolation as in equation 3.5, where the uncertainty is given in equation 3.6.

$$p = \frac{Q_2 - Q}{Q_2 - Q_1}$$

$$bkg(Q) = p * B_1 + (1 - p) * B_2 \tag{3.5}$$

$$\sigma_{bkg}(Q) = \sqrt{p^2 * \sigma_{B_1}^2 + (1 - p)^2 * \sigma_{B_2}^2} \tag{3.6}$$

where B_1, B_2 are the background intensities at Q_1, Q_2 where the point at which the background is being interpolated (Q) falls between, bkg(Q) is the interpolated background intensity, and σ_i denotes uncertainty in the quantity i.

Following background subtraction those data are divided by the slit-scan intensity. At each specular point the slit-openings are recorded. Similarly to the background, when performing a slit-scan each slit-opening which is used in the specular scan is not collected and an interpolation is performed in the same manner as in equation 3.5 and the uncertainty is determined through equation 3.6.

In the case where multiple specular, background, or slit-scan values are collected for the same point an inverse variance weighted average is determined. This does not apply to the determination of background in the specular peak from the offset background scans where a direct average is taken. The inverse variance average is determined through equation 3.7, and the uncertainty is given in equation 3.8,

$$w = \sum_i^N \frac{y_i}{\sigma_{y_i}^2}$$

$$y = \sum_i^N \frac{\frac{y_i}{\sigma_{y_i}^2}}{w} \tag{3.7}$$

$$\sigma_y = \sqrt{\frac{y}{w}} \tag{3.8}$$

where y is the inverse variance weighted average, and σ_y is the uncertainty in y. This average is used extensively as all NR data reduced in this thesis are recorded as multiple datasets. These data were collected in this manner so there could be confidence that there are no significant changes in the sample throughout the measurements.

3.5.5 Comparing NR datasets

As stated previously, multiple NR scans were collected between electrochemical maneuvers (i.e. CV scans). The purpose for this is to ensure the sample has reached a steady-state while collecting data as changes do occur on the sample surface. Only scans which were determined to be constant within uncertainty were compiled and reduced as described in section 3.5.4. The comparison between subsequent NR datasets was performed with equation 3.9 and the uncertainty is determined by equation 3.10,

$$D = \frac{R_2(Q) - R_1(\vec{Q})}{R_2(\vec{Q})} \tag{3.9}$$

$$\sigma_D = \frac{R_1(\vec{Q})}{R_1(\vec{Q})}\sqrt{\frac{\sigma^2_{R_2(\vec{Q})}}{R_2(\vec{Q})} + \frac{\sigma^2_{R_1(\vec{Q})}}{R_1(\vec{Q})}} \tag{3.10}$$

where R_2(Q) and R_1(Q) are the two datasets to be compared for changes, D is the fractional change, and σ_D is the uncertainty in D. The result of equation 3.9 is plotted vs Q and the result is examined for any features which would indicate change in the reflectivity. This comparison is also applied between combined datasets at different electrochemical conditions in order to examine whether change occurred following an electrochemical maneuver.

3.5.6 Fitting Reflectometry Data

XRR and NR datasets are fit through the software package Refl1D (93). A model representing the estimation of the sample is provided in a file which is used as a

starting point for determining the best fit to those collected and reduced data. The model file provides thickness, roughness, density, and absorption estimates for every layer in the sample. Model files also provide information such as the estimated range for all fitted parameters, a description of the instrument used, and finally control over parameters such as beam intensity, theta offset, and background. While Refl1D encompasses many fitting algorithms, the most useful in this work is the DiffeRential Evolution Adaptive Metropolis (DREAM) algorithm (95). The DREAM algorithm is a Markov chain Monte Carlo method which uses differential evolution as a genetic algorithm for parameter population evolution. The advantage of using this method for fitting data is the realization of uncertainty in the fitted parameters. The DREAM method not only determines the local minimum, but it is also able to determine an uncertainty in that minimum providing a means of confidence toward the reported parameter values.

The method uses an initial guess for the parameter values and begins searching the parameter space for the best fit. The method has two phases, a burn in phase and a data collection phase. The burn-in phase is intended to find the local minimum, the data collection phase is intended to search the probability space around the local minimums. If the burn-in phase is long enough then once the data-collection phase begins every point in the search space will be visited in proportion to the goodness of fit. These points are put into a histogram and the uncertainty in each parameter is determined by the 68% interval around the mean value. The documentation related to the Refl1D software package indicates that the 95% confidence interval can achieve 2-digit precision when the number of steps is equal to 1000000/(Pa * Pop) where Pa is the number of parameters and Pop is the population of each guess in the data-collection step.

The histograms produced through the DREAM method are helpful further than providing an uncertainty. A histogram not symmetric about the mean may be indica-

tive of a poor model. This may mean that a parameter held constant in the model is incorrect, the model itself might be missing a layer feature, or the reflectometry dataset is poor. The parameter histograms being symmetric about the mean also does not necessarily mean the model exactly represents the sample, but it does mean that the reported parameters are the best-fit achievable for that model. The DREAM algorithm returns an uncertainty which is based upon Bayesian statistics. As it is possible to add many layers to result in a better fit, those layers may not be truely representative of the system being modeled. The Bayesian Information Criterion (BIC) (96) provides a means of determining whether improvements in the goodness of fit due to additional parameters are statistically meaningful. The BIC is shown in equation 3.11,

$$BIC = (n - k) * \chi^2 + kLn(n) \tag{3.11}$$

where n is the number of datapoints in the dataset, k is the number of parameters, and the χ^2 is found from the fit results. The BIC weights the goodness-of-fit by the number of parameters to explore whether improvements in goodness-of-fit is related to the additional parameters or because of better statistical certainty.

3.5.7 Corrections

Sample warp from the anneal step, clamping forces for sealing the cell, and stress in thin-films can result in lower detected reflectivity than is truly reflected. The effect of warp is to modify the angle at which the neutron beam impinges on the sample surface, and the angle at which the sample makes with the detector. The total effect is to reflect part of the neutron beam out of the acceptance angle of the detector, and some portion of the reflected beam can be lost. Or conversely the effect could be to focus the beam into the detector and the collected intensity may be greater than expected. The effects of warp are assumed to be largest away from the sample center.

With that assumption, as the impinging beam angle increases relative to the surface a smaller beam footprint is observed on the sample surface. The footprint of the beam is centered at the sample surface center and therefore the effects of warp should decrease with increasing angle. Further, as the acceptance angle of the detector for the diverging beam after reflection increases, the impact of small additional angle due to warp becomes negligible. At low incidence angles warp can create significant issues when fitting neutron reflectometry data. It is assumed that as the slit window opens more of the neutrons reflected due to warp are collected due to the larger acceptance window. Therefore, only the first scan from the total reflection plateau to θ=0.5°(Q_f) are corrected as this region uses a fixed slit geometry. Beyond Q_f the slit window opens as a linear function of angle and is assumed to collect the specular reflection even when warp is a factor, therefore it is assumed that all datasets beyond Q_f require no correction. The scheme used to correct those data are show in equation 3.13.

$$R_{corrected} = C(Q) * R(Q) \tag{3.12}$$

$$C\left(Q\right) = \begin{cases} C_1\left(Q \leq Q_c\right) \\ C_2\left(Q_c < Q \leq Q_f\right) \end{cases} \tag{3.13}$$

Corrections to those data below the critical edge assume the impact of warp is uniform prior to the critical edge. This assumption is generally correct as the sample surface area which the neutron beam impinges is fairly constant in the small angular window where the critical edge exists. The values which define the critical edge are identified as values which have 95% of the maximum reflectivity intensity. If the number of values identified from 95% maximum reflectivity are below 10, the window is opened to 90% maximum reflectivity. The correction factor for the values below the critical edge and the additional uncertainty from this correction are determined

from equations 3.14 and 3.15,

$$C_1\left(Q \leq Q_c\right) = \frac{1}{\bar{R_C}} = \frac{N}{\sum_i^N R_i} \tag{3.14}$$

$$\sigma_{C_1}\left(Q \leq Q_c\right) = \sqrt{\sum_i^N \frac{\partial C}{\partial R_i}} = \sqrt{\left(\sum_i^N \sigma_{R_i}^2\right) \frac{N^2}{\left(\sum_i^N R_i\right)^4}} \tag{3.15}$$

where C_1 is the correction factor, σ_{C_1} is the additional uncertainty in the correction, N is the number of points used in the correction, R_i is the reflectivity determined at a particular Q value, and i denotes the individual data point.

Data in the first dataset from the region between the critical edge and Q_f are corrected by assuming that the corrected reflectivity at Q_f should be the same as that of the reduced reflectivity of the second scan which begins at Q_f. Therefore the correction factor at Q_f is found through equation 3.16 and the uncertainty in that point is found through equation 3.17.

$$C_2\left(Q_f\right) = \frac{R_2(Q_f)}{R_1(Q_f)} \tag{3.16}$$

$$\sigma_{C_2}\left(Q_f\right) = C_2\left(Q_f\right) \sqrt{\frac{\sigma_{R_2(Q_f)}^2}{R_2(Q_f)^2} + \frac{\sigma_{R_1(Q_f)}^2}{R_1(Q_f)^2}} \tag{3.17}$$

where $R_1\left(Q_f\right)$, $R_2\left(Q_f\right)$ are the measured reflected intensities at the point Q_f for the first and second scans where the slit-widths are 0.05 mm and 0.2 mm respectively, σ_i is the uncertainty in quantity i, and $C_2\left(Q_f\right)$ is the correction factor at point Q_f. The correction between the critical edge and the point Q_f is modeled by a linear dependence. The linear dependence does not necessarily reflect the true effect of warp; however, the effect of warp between the critical edge and Q_f is unknown and a

linear dependence is the simplest model to account for the change in warp as a function of angle. The equations used to determine the correction between the critical edge and Q_f, along with the uncertainty in the correction are found in equations 3.18 and 3.19. The uncertainty equation 3.19 is found through applying the error propagation formula to equation 3.18.

$$C_2\left(Q_c < Q \leq Q_f\right) = \left(\frac{Q_f - Q}{Q_f - Q_c}\right) * C_1 + \left(1 - \frac{Q_f - Q}{Q_f - Q_c}\right) * C_2(Q_f) \tag{3.18}$$

$$\sigma_{C_2}\left(Q_c < Q \leq Q_f\right) = \sqrt{\sigma_{C_1}^2 * \left(\frac{\partial C_2\left(Q_c < Q \leq Q_f\right)}{\partial C_1}\right)^2 + \sigma_{C_2(Q_f)}^2 * \left(\frac{\partial C_2\left(Q_c < Q \leq Q_f\right)}{\partial C_2(Q_f)}\right)^2}$$

$$\sigma_{C_2}\left(Q_c < Q \leq Q_f\right) = \sqrt{\left(\frac{Q_f - Q}{Q_f - Q_c}\right)^2 * \sigma_{C_1}^2 + \left(1 - \frac{Q_f - Q}{Q_f - Q_c}\right)^2 * \sigma_{C_2(Q_f)}^2} \tag{3.19}$$

Equations 3.14, 3.16 and 3.18 are then substituted into equation 3.13 to provide the piecewise defined correction function in equation 3.20.

$$C\left(Q\right) = \begin{cases} \frac{N}{\sum_i^N R_i}, Q \leq Q_c \\ \left(\frac{Q_f - Q}{Q_f - Q_{ce}}\right) * \frac{N}{\sum_i^N R_i} + \left(1 - \frac{Q_f - Q}{Q_f - Q_{ce}}\right) * \frac{R_2(Q_f)}{R_1(Q_f)}, Q_c < Q \leq Q_f \end{cases} \tag{3.20}$$

The uncertainty in equation 3.20 is given by the piecewise function in equation 3.21.

$$\sigma_C\left(Q\right) = \begin{cases} \sqrt{\left(\sum_i^N \sigma_{R_i}^2\right) \frac{N^2}{\left(\sum_i^N R_i\right)^4}}, Q \leq Q_c \\ \sqrt{\left(\frac{Q_f - Q}{Q_f - Q_c}\right)^2 * \left(\sqrt{\left(\sum_i^N \sigma_{R_i}^2\right) \frac{N^2}{\left(\sum_i^N R_i\right)^4}}\right)^2 + \\ \qquad \left(1 - \frac{Q_f - Q}{Q_f - Q_c}\right)^2 * \left(\frac{R_2(Q_f)}{R_1(Q_f)} \sqrt{\frac{\sigma_{R_2(Q_f)}^2}{R_2(Q_f)^2} + \frac{\sigma_{R_1(Q_f)}^2}{R_1(Q_f)^2}}\right)^2}, Q_c < Q \leq Q_f \end{cases} \tag{3.21}$$

The correction from equation 3.20 is applied to the original data-file which requires correction. The correction as a function of Q is multiplied by the number of counts and the resultant value is rounded to the nearest integer as these represent the corrected number of neutrons counted within the timing interval selected for the experiment. That corrected file is then reduced as was described in section 3.5.4. In order to properly account for the additional uncertainty from applying the correction the corrected-reduced file has uncertainty applied in the region $Q \leq Q_f$. The corrected-reduced file contains Q, R, and dR where R is the reflected intensity (normalized) and dR is the uncertainty in R. The R already has had the correction applied, and the dR is slightly perturbed by the correction applied, but is on the same order as the original reduced file. The uncertainty from the correction is applied according to equation 3.22.

$$\sigma_{R_c} = \sqrt{\sigma^2_{dR(Q)} * C(Q)^2 + \sigma^2_{C(Q)} * R(Q)} \tag{3.22}$$

where R(Q) is the corrected-reduced reflectivity at Q, $\sigma_{dR(Q)}$ is the uncertainty in R(Q) at Q, C(Q) is the correction from equation 3.20 at Q, and $\sigma_{C(Q)}$ is the uncertainty in the correction at Q from equation 3.21.

3.6 Electrochemistry

Electrochemistry in this work serves several purposes. It is used as a characterization tool to show the characteristic electrochemical behavior of the sample. It is used to monitor the potential difference between cathode and anode, and is used to move lithium into and out of the sample during NR experiments. There are three primary tools used in this work: Cyclic Voltammetry (CV), potential-hold, and open-circuit monitoring. CV is used to cycle the cell rapidly in addition to looking for character-

istic behavior indicative of the expected sample structure. Potential-hold is used to delay the onset of phase transition in the NR sample due to self-discharge, as well as to electrodeposit lithium. Open-circuit monitoring is used to monitor the potential between the NR sample and the lithium anode.

Samples used for analyzing preparation parameters and preparing for NR experiments are 2 cm x 2 cm squares which are diced from whole 4" silicon wafers with SiO2/Pt thin films. These diced squares have the sol-gel spun onto them and are annealed under various conditions. The electrochemical cell cathode is formed by placing the sample on a glass slide, attaching copper tape to the surface and the slide to make an electrical connection, epoxying over the copper tape to protect the contact from the electrolyte (figure 3.14). An example of a test cell is shown in figure 3.14. An alligator clip is used to make the connection to the slide.

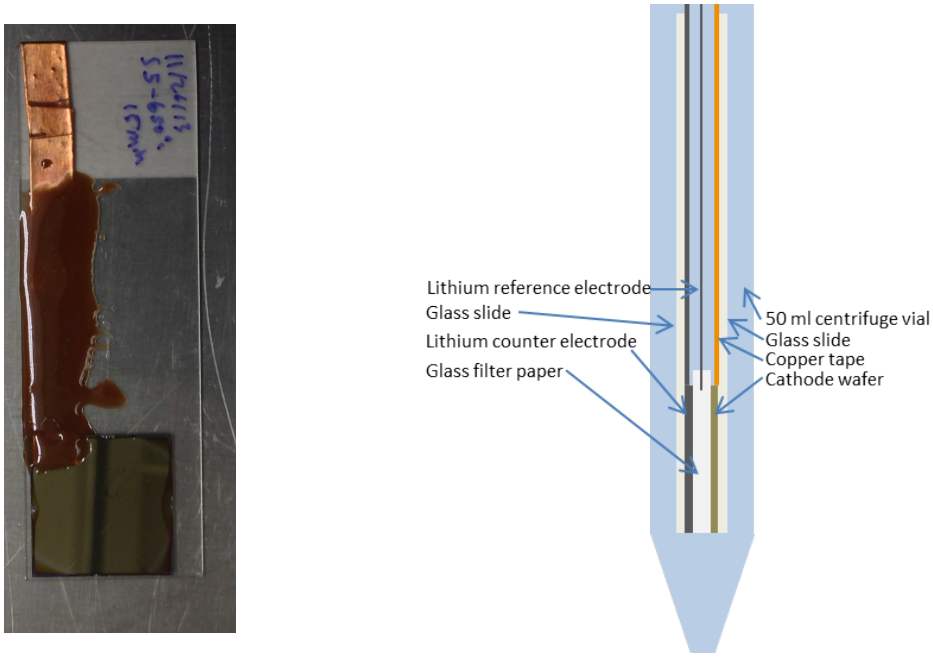

Figure 3.14: Example of a cathode on a glass slide (Left) used for testing small samples for electrochemical activity along with a diagram of a test cell (Right).

The anode in these test cells is composed of lithium metal which is loosely attached to another glass slide by folding the metal over the top of the slide. The lithium metal footprint is cut such that the cathode is completely covered by the counter electrode.

The separator used for these experiments are glass fiber filter paper which is cut into two pieces. A reference electrode is developed by cutting a thin strip of lithium and sandwiching the tip between the two pieces of separator which is further sandwiched between the anode and cathode. The glass slides which form the outer shell of the test cell are then pushed into a 50 ml centrifuge vial, alligator clips attached to wires are connected to each electrode and the wires are passed through holes drilled in the centrifuge tube lid. Approximately 10 ml electrolyte is added to the tube through a pipette.

3.6.1 Cyclic Voltammetry

CV is used to cycle the cell and monitor the health of the cathode. This process is used for two separate purposes. The first is to determine the best processing parameters for developing the cathode to be used in NR work. The second is to cycle the cathode used in NR experiments from discharged to charged and back to discharged while examining the state-of-health of the cathode.

CV data are analyzed for several features such as onset potentials which indicate specific charge transfer reactions, reaction potential peak current, and integrated charge. While specific information about the cathode system such as changes in phase are not discernible through CV, some useful qualitative information can be gleaned. Shifts in onset potentials indicate increased cell resistance, change in peak current indicates a loss in active material, and differences in integrated charge for anodic and cathodic current indicate electrolyte breakdown. Integrated charge can also indicate change in active material.

Integrated charge for CV data is not straightforward as there are multiple events occurring simultaneously while charging. As described in equation 2.25 the observed current is assumed to be composed of two parts, the electrode contribution and the BV contribution. In order to deconvolve the contributions from the electrode diffusion

of lithium versus the electrolyte breakdown the BV contribution must be estimated. The estimate is determined through fitting a function resembling the BV equation to data at both ends of the voltage window where the contribution from lithium diffusion from the bulk is not substantial. Data in those voltage windows are averaged between the anodic and cathodic scans. There is a finite difference in the current depending upon whether lithium is being removed or inserted into the cathode. Therefore for every potential there are two values; one corresponding to driving lithium to the anode and one corresponding to driving lithium to the cathode. Those values are averaged and then the BV equation as described by equation 2.26 is fit to that dataset. The function fit to those data combines constants into fitting parameters and is described in equation 3.23,

$$I_{BV} = P_0 + P_1 * \left(e^{P_2*(V-V_0)} - e^{-P_3*(V-V_0)}\right) \tag{3.23}$$

where, V is the potential, V_0 is the open-circuit potential, P_0 is a current offset, P_1 is the electrode surface area multiplied by the exchange current density, P_2 is the combination of the anode charge transfer coefficient multiplied by the Faraday constant divided by the gas constant times temperature, finally P_3 is equivalent to P_2 but uses the cathode charge transfer coefficient. The fitting routine is implemented in a python code utilizing the least-squares optimization algorithm released by SciPy. The least-squares routine uses the Levenbarg-Marquadt fitting algorithm to non-linear systems. Those fitting constants for each CV measurement are tracked and examined for consistency between cycles.

The fitted I_{BV} function is subtracted from the anodic charging current and that current is added to the cathodic discharging current. This method does not completely account for the multitude of reactions but it does provide a basis for understanding the change which occurs as a function of charge cycling. The expected outcome for this method is a way to track the active changes which occur in the cathode during

electrochemical maneuvers. Trending losses or gains in the current integral describe changes in the cathode as the anode in this work can be considered to be an infinite sea of lithium ions.

3.7 Atomic Force Microscopy

Atomic Force Microscopy (AFM) is utilized to estimate the rms surface roughness for a variety of sample conditions as well as an estimate for sample warp. AFM provides an image of the surface as described in the previous chapter and allows a minor observation of surface crystallization. The surface roughness is a rms-average of the deviation from what the software defines as a baseline surface. The AFM determined warp is derived from the difference between the selected area scanned and the actual area scanned. The AFM software has a black-box program which flattens the image and determines the actual surface area vs the selected area. Warp is determined as the difference between those two areas. The synthesis parameters investigated via AFM were: Spinning-speed, anneal temperature, and anneal time. Table 3.7 provides details for the sample preparation conditions which are explored through AFM.

Table 3.7: Details for AFM measurement parameters.

Anneal temperature		
Anneal temperature (°C)	Spin-speed (rpm)	Anneal time (min)
650	3750	10
700	3750	10
750	3750	10
800	3750	10
Anneal time		
Anneal temperature (°C)	Spin-speed (rpm)	Anneal time (min)
650	3750	10
650	3750	15
650	3750	20
Spin-speed		
Anneal temperature (°C)	Spin-speed (rpm)	Anneal time (min)
650	3000	10
650	3500	10
650	3750	10

3.8 Scanning Electron Microscopy

Scanning Electron Microscopy (SEM) in conjunction with Energy Dispersive X-ray Spectroscopy (EDS) was used to examine the surface of NR samples following a several month rest period. In order to fit into the SEM the thick substrate was machined to ∼2 mm thick from the starting 5 mm, and a 2 cm x 2 cm square was cut out of the 10 cm diameter wafer. The samples were rinsed in DMC following the milling; however, it is apparent that not all silicon dust was removed and therefore EDS spectra in all cases show a contribution of silicon dust.

3.9 X-ray photoelectron spectroscopy

X-ray Photoelectron Spectroscopy (XPS) is used to quantitatively determine the composition of two cathode films prepared with a 3750 rpm spin speed, 650 °C anneal temperature, and 10 minute anneal time. XPS was not used to determine the composition of the samples used in NR experiments as the sample size is far too large to

insert into the instrument. The sample was scanned at 0.5 eV intervals in the range of 10 to 1190 eV. Samples machined for SEM investigations were also placed into the XPS instrument and spectra on the surface were investigated in the same 10 to 1190 eV range.

CHAPTER IV

Results

This chapter details the results for all experiments performed in support of this thesis. The chapter will first detail the experimental results from sample processing parameters including the AFM experiments, XRR experiments, XPS experiments, and electrochemical experiments. Next results from lithium electro-deposition experimentation and sample development are shown, followed by characterizations of NR samples. Results from two NR experiments will be shown, and finally post-NR sample characterization results.

4.1 Sample process parameters

This section shows results from sample processing parameters including AFM, XPS, XRR, and electrochemical experiments. These experiments were performed to determine optimal processing parameters to produce an electro-active thin-film $LiMn_2O_4$ cathode with low surface roughness.

4.1.1 AFM experiments

As discussed in section 3.7 AFM experiments were used to determine the influence of processing parameters on surface roughness and warp. Table 4.1 shows the tabulated results from all processing parameters. In some cases multiple samples are

examined for the same processing parameters. These are included to highlight the variation between sample processing.

Table 4.1: Results from AFM experiments for determining processing parameters.

Anneal temperature (°C)	Spin-speed (rpm)	Anneal time (min)	Average RMS (nm)	Average warp (%)	Area (μm^2)
650	3000	10	0.81	1.64	0.254
650	3500	10	0.55	1.24	0.254
650	3750	10	0.95	1.45	0.254
650	3750	10	1.66	0.91	25.2
650	3750	10	1.37	1.27	4.05
700	3750	10	0.86	1.56	0.254
700	3750	10	3.45	1.42	25.3
750	3750	10	1.65	1.89	0.254
750	3750	10	4.37	4.519	4.2
800	3750	10	6.83	5.52	0.263
650	3750	15	11.26	1.85	1.01
650	3750	20	12.40	2.13	1.01

Values used to construct table 4.1 are plotted in figures 4.1, 4.2, and 4.3.

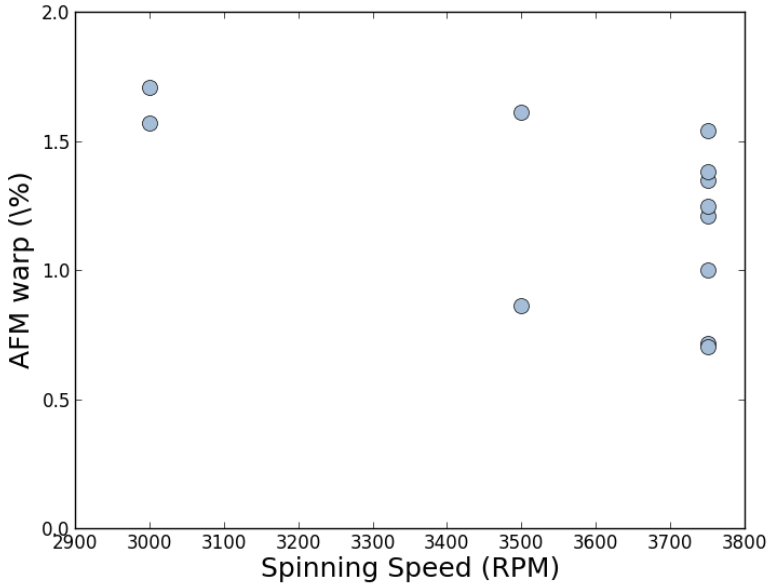

(a) Warp vs spinning speed

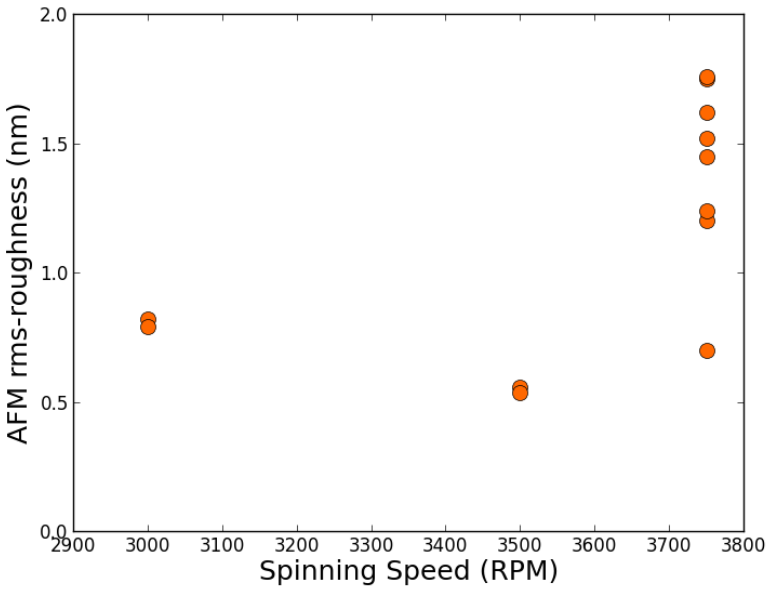

(b) rms-roughness vs spinning speed

Figure 4.1: Top: Experimental data showing dependence of sample warp as a function of spinning speed. Bottom: AFM experimental data showing surface roughness as a function of spinning speed

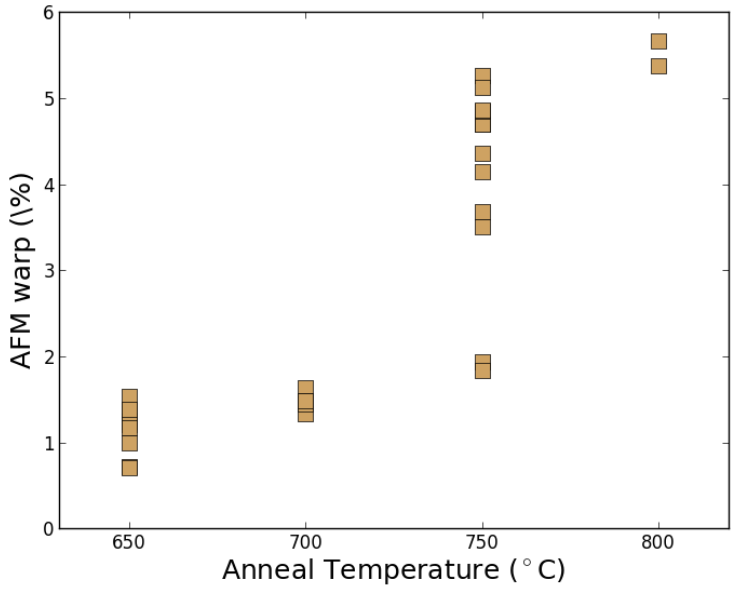

(a) Warp vs. annealing temperature

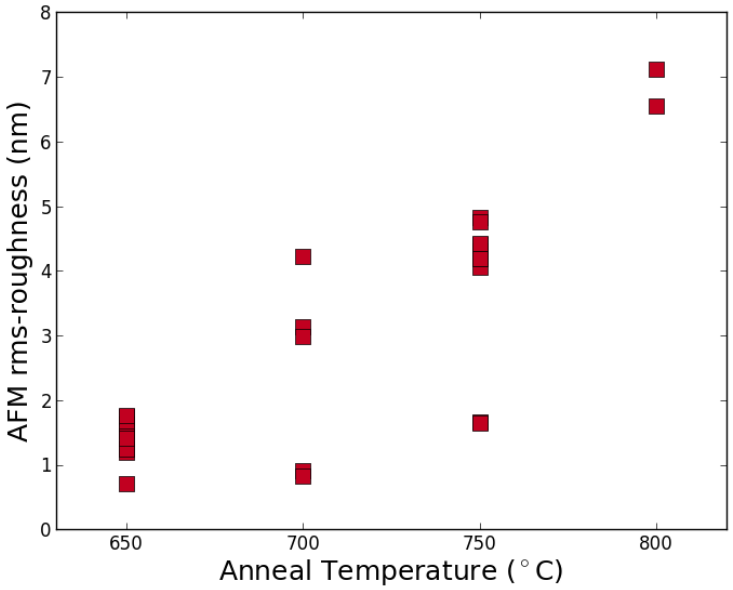

(b) rms-roughness vs annealing temperature

Figure 4.2: Top: Experimental data showing dependence of sample warp as a function of annealing temperature. Bottom: AFM experimental data showing surface roughness as a function of annealing temperature.

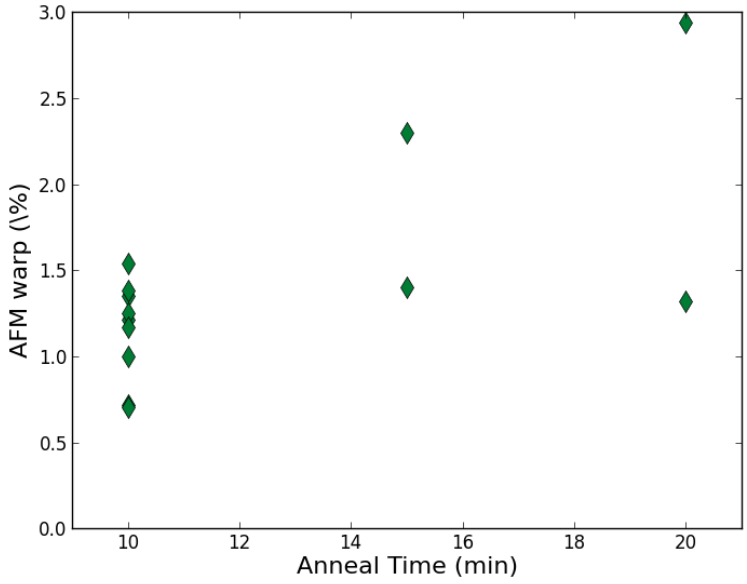

(a) Warp vs annealing time

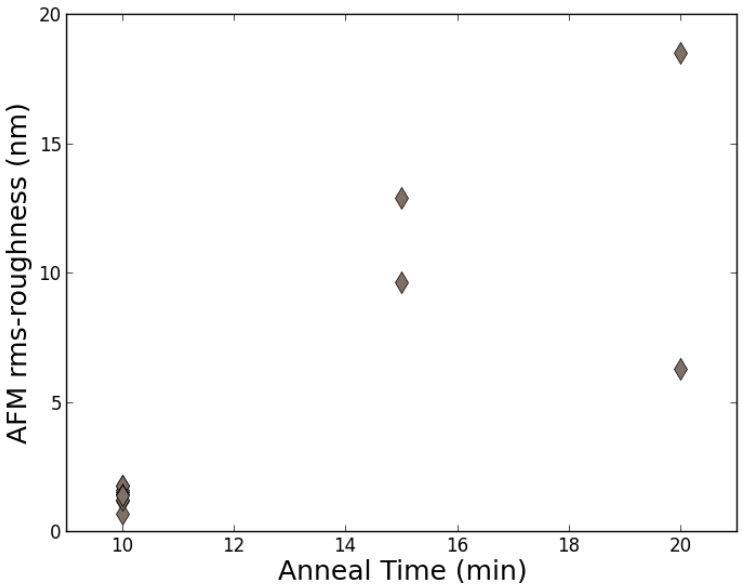

(b) rms-rougness vs annealing time

Figure 4.3: Top: Experimental data showing dependence of sample warp as a function of annealing time. Bottom: AFM experimental data showing surface roughness as a function of annealing time.

4.1.2 XRR experiments

XRR was applied to study processing parameters for several reasons. XRR is a very similar technique to NR, it provides a means of characterization of sample parameters which can be compared to AFM, and offers a means of quantifying warp due to processing parameters. Samples which were investigated by AFM were also investigated through XRR. A table of XRR data collection parameters is found in table 3.2 and is repeated here in table 4.2. As was explained in the Methods section XRR data were collected in two ways as the author developed the skill-set to change the beam intensity. Those different methods of data collection are highlighted in table 4.2 in the scan type column, where Continuous implies one beam intensity throughout the measurement and Split implies the beam intensity was increased when the reflected intensity was low enough such that an increase in incident intensity would not overwhelm the detector.

Table 4.2: Table of samples characterized through XRR for cathode fabrication parameter determination

Condition	anneal temp (°C)	anneal (min)	spin rate (rpm)	scan window ($\AA^{-1}$)	Scan type
Anneal Temp	650	10	3750	0-0.478	Continuous
	700	10	3750	0 - 0.569	Split
	750	10	3750	0 - 0.569	Split
	800	10	3750	0 - 0.255	Split
Anneal Time	650	10	3750	0 - 0.455	Continuous
	650	15	3750	0 - 0.437	Continuous
	650	20	3750	0 - 0.504	Continuous
Spin Rate	650	10	3000	0 - 0.569	Continuous
	650	10	3500	0 - 0.572	Split
	650	10	3750	0 - 0.498	Split

Plots of those datasets from the samples listed in table 4.2 are found in figures 4.4, 4.5, and 4.6. It should be noted that in the case of the spinning speed comparison the original sample was fractured and a new sample was made. While the processing parameters were the same it is obvious that there are differences in the platinum thickness due to using a different wafer from which a square was diced and used as the substrate.

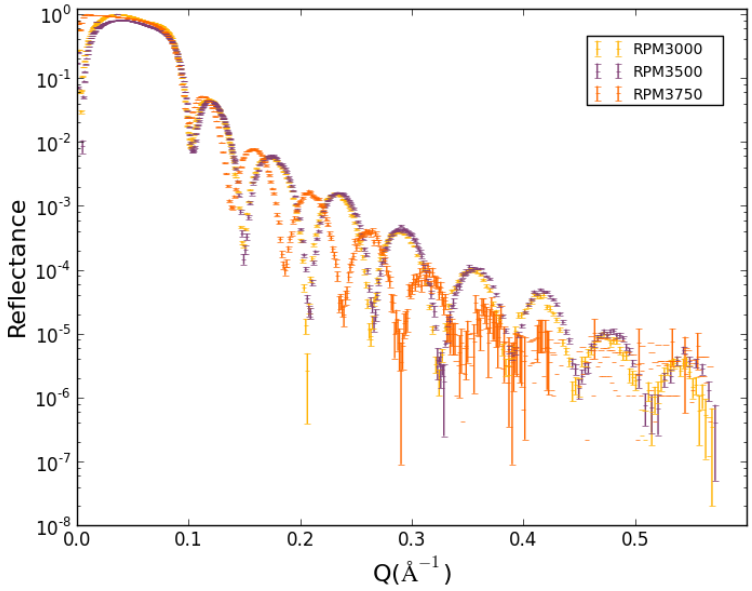

(a) XRR from spinning speed

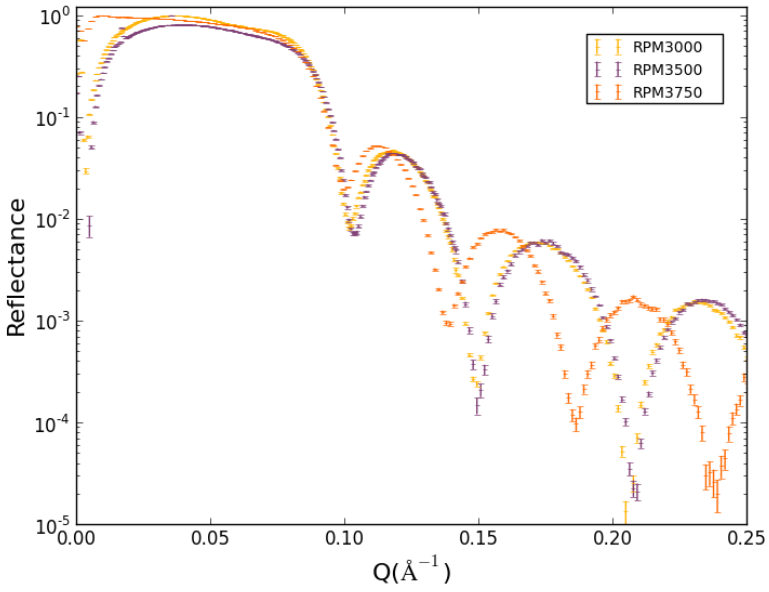

(b) XRR near critical edge

Figure 4.4: Reduced XRR data highlighting the change in reflectivity due to various spinning speeds. Top: Showing the full range of those reflected data for spinning speeds 3000 rpm, 3500 rpm, and 3750 rpm. Bottom: Highlighting the critical edge for those data.

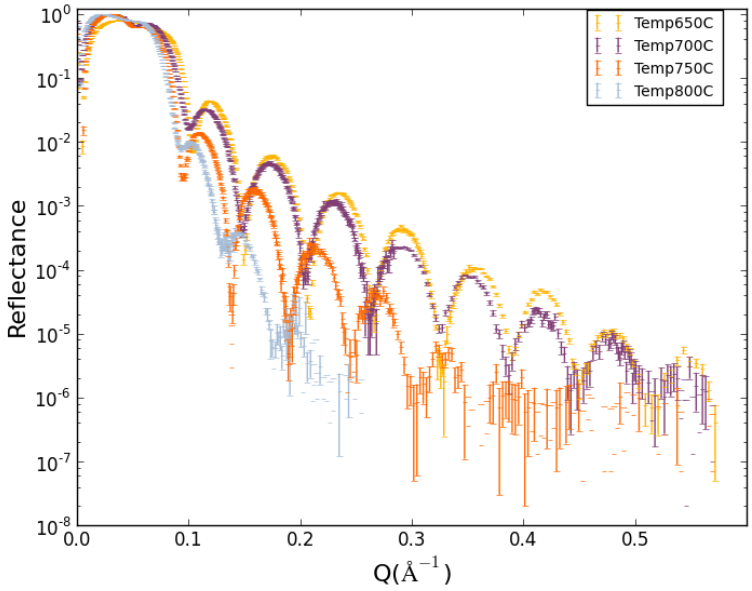

(a) XRR from annealing temperature

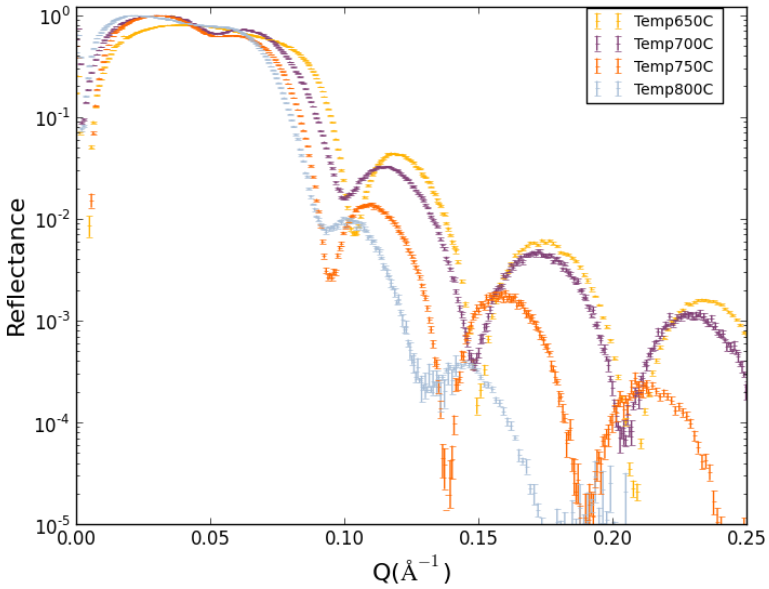

(b) XRR near critical edge

Figure 4.5: Reduced XRR data highlighting the change in reflectivity due to annealing temperature. Top: Showing the full range of those reflected data for temperatures 650 °C, 700 °C, 750 °C, and 800 °C. Bottom: Highlighting the critical edge for those data.

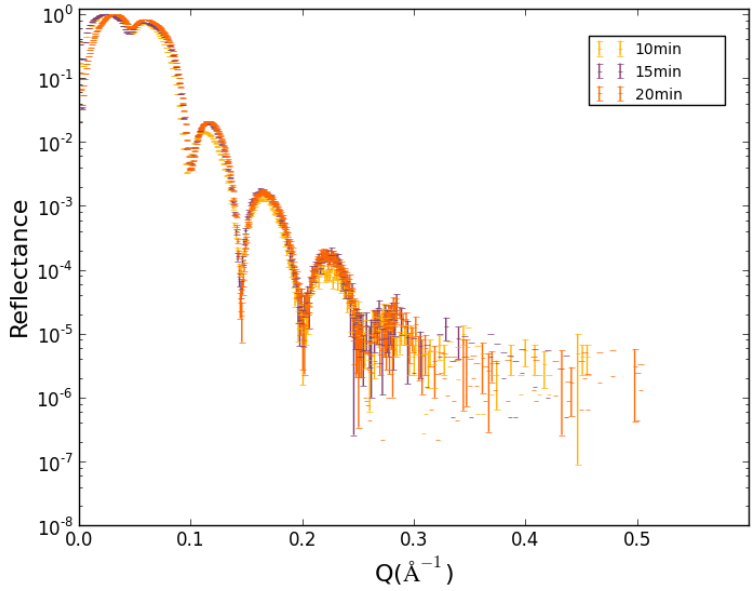

(a) XRR from anneal time

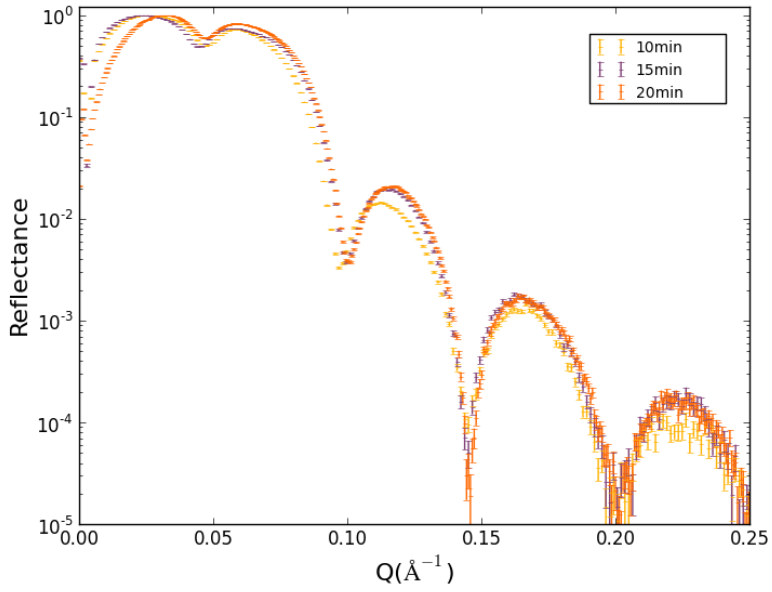

(b) XRR near critical edge

Figure 4.6: Reduced XRR data highlighting the change in reflectivity due to annealing time. Top: Showing the full range of those reflected data for annealing times 10 min, 15 min, and 20 min. Bottom: Highlighting the critical edge for those data.

Figures 4.4, 4.5, and 4.6 show generally similar results as those AFM results. In the spinning speed results it is obvious the 3750 rpm sample had poorer performance,

but this is likely an outlier as it was prepared at a different time and with a different substrate stock. It is obvious in the temperature comparison that the 650 °C sample had the best performance. The time comparison shows little information about which sample has better performance, however these data are collected in a limited range and AFM results indicate the roughness of the surface layer is significantly greater at longer times than 10 minutes.

4.1.3 XPS experiments

XPS was applied to two samples prepared in the same manner as the samples used for NR experiments. XPS is used to inspect the oxidation state of the Mn 2p3/2 peak in addition to examining the rough composition of the samples. Figure 4.7 shows the XPS spectra for both samples in the binding energy range 35 eV to 1200 eV. Lithium is not highlighted on these spectra as it is only very slightly removed from the Mn 3p peak and can not be easily observed. These samples exhibit similar O/Mn at% ratios of (O:Mn) 2.41 and 2.42. For pure $LiMn_2O_4$ this ratio should be 2:1, however it is observed in figure 4.7 that there is a significant contribution from carbon between 15-22 % of the total detected emission peaks. It is known (77; 78; 5) that $LiMn_2O_4$ annealed in air forms a lithium carbonate surface layer. The carbon used to form this carbonate likely comes from atmosphere or residual from decomposition of precursor materials.

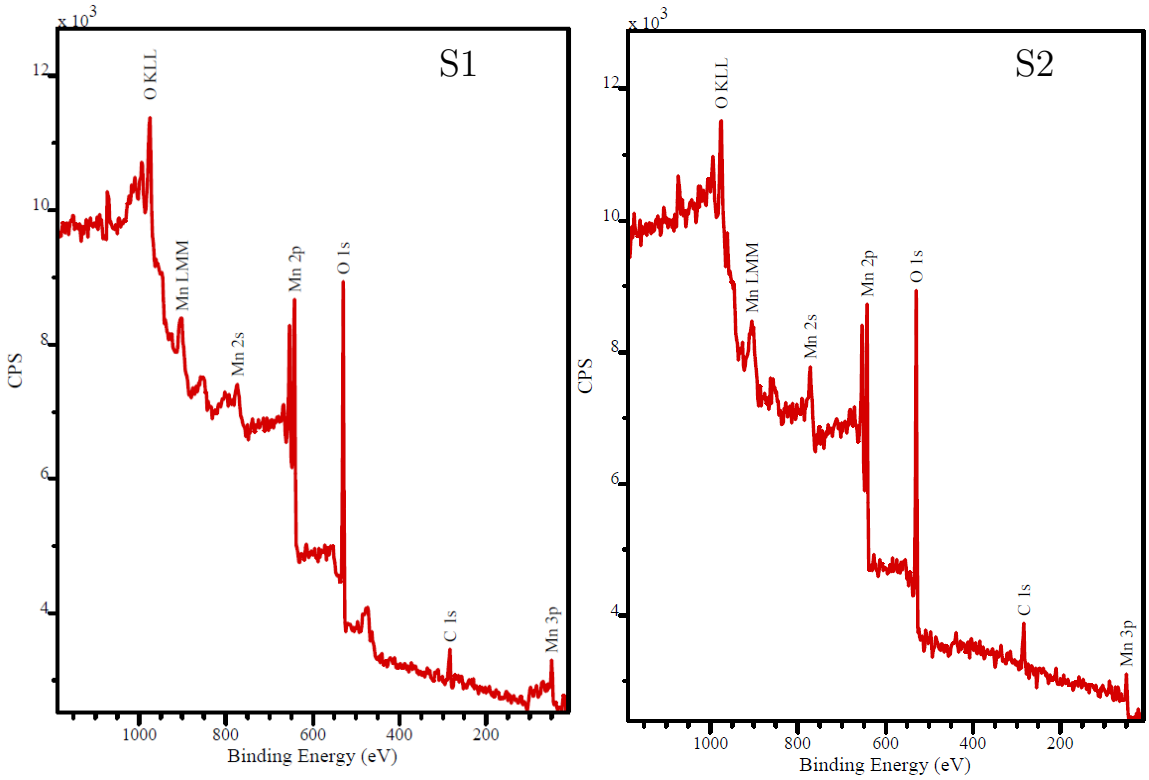

Figure 4.7: XPS spectra for two samples prepared in the same manner as the samples used for NR experiments.

As was discussed in section 2.2.3.1 the oxidation state of Mn in $LiMn_2O_4$ is very important. To explore the oxidation state a high-resolution XPS spectra was collected around the Mn 2p3/2 peak. This peak is typically used to investigate the oxidation state of Mn (97; 98), however fitting one peak to each oxidation state of Mn is incorrect as Mn exhibits multiplets in the 2p state (99; 100). Each sample Mn 2p3/2 peak is fit with Mn^{2+}, Mn^{3+}, Mn^{4+} multiplets. For the Mn 2p3/2 emission each oxidation state emits multiple photoelectrons nominally separated around 1 eV. Due to the large number of peaks required to simulate the multiplets the position of each multiplet peak are held to reported values for MnO (Mn^{2+}), Mn_2O_3 (Mn^{3+}), and MnO_2 (Mn^{4+})

with an 0.1 eV window to allow some movement of the peak position. This assumption is thought to be valid as reported peak positions from literature are within 0.1 eV from two sources (99; 100). From literature (100) each oxidation state contains between 5 and 6 multiplets to fully describe the Mn 2p3/2 peak. In this work only the first four multiplets are used to examine the Mn 2p3/2 peak for oxidation state as the peaks at higher binding energies are much smaller intensity than the primary photoelectron emissions and contribute little to the overall intensity. In addition to limiting the peak positions to reported values the FWHM of the Gaussian(70%)-Lorentzian(30%) curve used to describe each multiplet was limited to the range 0.8 eV to 1.8 eV. These limits reflect the range reported in literature to describe these multiplets (99; 100).

CasaXPS software are used to fit these mutliplets to the Mn 2p3/2 peak. Figure 4.8 shows the fitted Mn 2p3/2 peaks for both samples. Tables 4.3 and 4.4 provide the fitted parameters for the multiplet peaks. These results show there are three oxidation states of Mn present in the cathode layer. The cathode is composed of $\sim$ 29% MnO, and the contribution from Mn^{3+} and Mn^{4+} are not equivalent showing approximately 7% excess Mn^{4+}. The average oxidation state of the Mn^{3+}/Mn^{4+} mixture is 3.55+ which is slightly above the desired 3.5+.

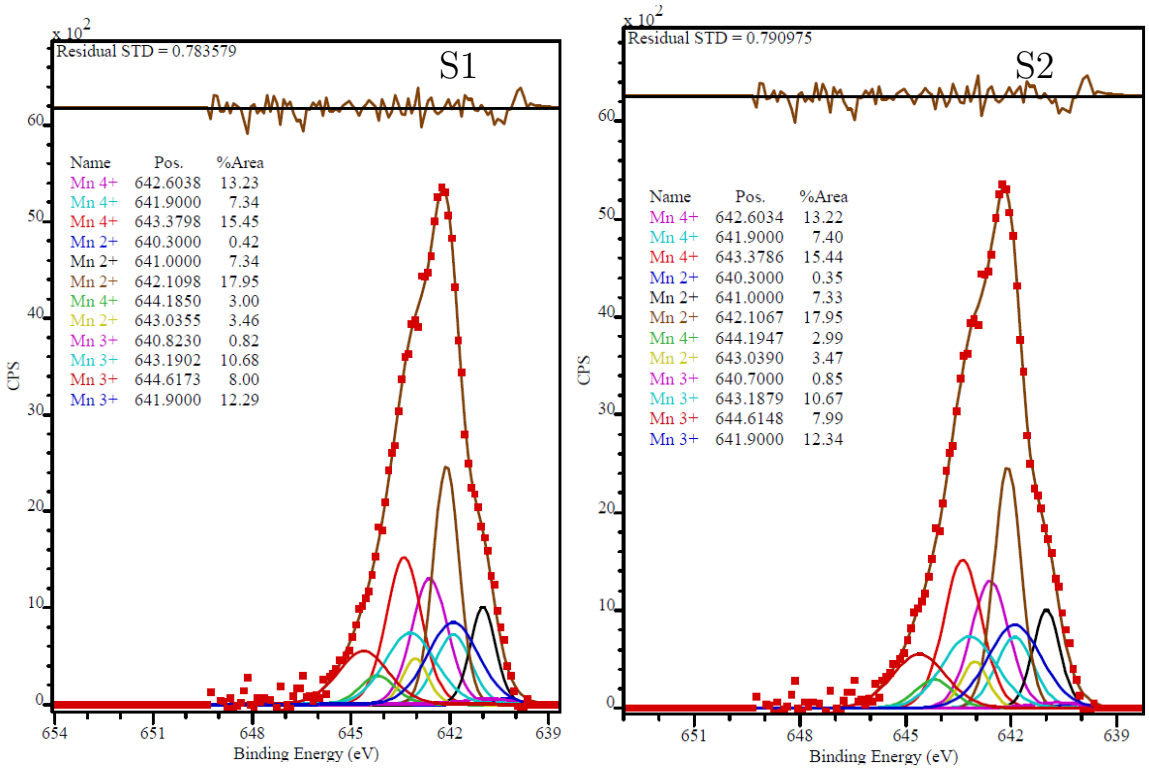

Figure 4.8: XPS spectra for two samples showing the Mn 2p peaks.

Table 4.3: Table of fitted Gaussian-Lorentzian peaks to the Mn 2p3/2 peak on S1 for cathode layer characterization on sample spun at 3750 rpm, and annealed for 10 min at 650 °C.

State	BE (eV)	Area	State	BE (eV)	Area	State	BE (eV)	Area
Mn^{2+}	640.3	46.7	Mn^{3+}	640.7	114.9	Mn^{4+}	641.9	996.6
	641.0	986.7		641.9	1662.1		642.6	1781.6
	642.1	248.4		643.2	1438.1		643.5	2081.1
	643.0	467.1		644.8	1077.7		644.1	402.8
FWHM (eV)	0.90			1.8			1.26	
% Total		29.1%			31.9%			39.1 %

Table 4.4: Table of fitted Gaussian-Lorentzian peaks to the Mn 2p3/2 peak on S2 for cathode layer characterization on sample spun at 3750 rpm, and annealed for 10 min at 650 °C.

State	BE (eV)	Area	State	BE (eV)	Area	State	BE (eV)	Area
Mn^{2+}	640.2	56.6	Mn^{3+}	640.8	110.9	Mn^{4+}	641.9	988.6
	641.1	988.3		641.8	1655.3		642.7	1782.9
	642.1	2417.4		643.1	1439.2		643.4	2082.1
	643.0	465.9		644.6	1079.2		644.2	404.8
FWHM (eV)	0.91			1.8			1.26	
% Total		29.2%			31.8%			39.0 %

The oxygen O1s peak is investigated in both samples for an assessment of the oxygen bound states. Figure 4.9 shows the O1s XPS spectra for both samples include the curve fits. It is apparent there are two modes present, one at 528.7 eV and one at 530.5 eV. When comparing against literature these energies are lower by approximately 1 eV than is expected (101). However, the shape of the emission is in-line with what should be expected and it is entirely possible there is a small offset in the collected results due to charging effects on the sample surface which can bias the calculated binding energy.

The O1s peak at 528.7 eV is related to the O^{2-} ion from the manganese oxide, and the peak at 530.5 eV is related to the contamination species present (101). Comparing the %area for these two curves indicates that the surface sampled by XPS is composed of ∼36% surface species and ∼64% $LiMn_2O_4$. XPS is capable of probing depths up to 8-10 nm, where as the cathode layer is on the order of 15-16 nm. As no platinum is observed in these XPS spectra it is unlikely that the entire cathode layer is being probed via XPS and therefore that estimation does not necessarily reflect the entirety of the sample composition.

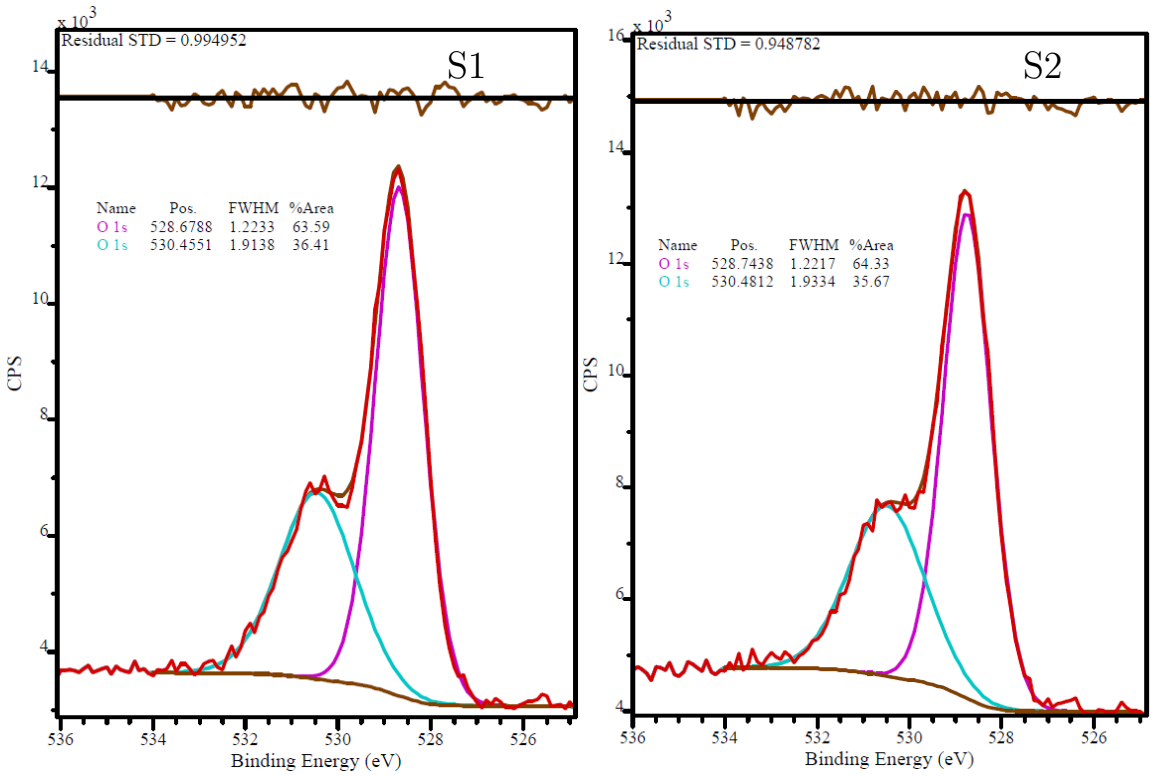

Figure 4.9: XPS spectra for two samples showing the O1s peak along with a two-curve fit. The peak positions are approximately 1 eV lower than reported values (101), which is likely due to a charging effect offset which is observed as a shift to lower binding energy than the true value

These XPS results indicate the samples investigated are generally composed of $LiMn_2O_4$ with some addition of a surface layer such as lithium carbonate. The Mn oxidation state is approximately 3.55+ around the expected 3.5+ for $LiMn_2O_4$ and the O1s peak is in line with literature for the bound O^{2-} ion. These results provide confidence that the preparation process does produce the desired material, but also includes a significant impurity phase.

4.1.4 Electrochemical measurements

The electrochemical response of samples made through this process are investigated for their electrochemical performance. Presented here are two such tests, first an example of the electrochemical performance of these $LiMn_2O_4$ thin films are prepared on a square test wafer. Next the performance of a sample tested in the NR electrochemical cell with a lithium electro-deposited anode is explored. These results show the characteristic electrochemical performance of $LiMn_2O_4$ and in conjunction with XPS highlight the sample preparation process produces the correct material for investigation with NR.

4.1.4.1 Small test wafer

A test wafer prepared in the same manner as NR samples was prepared and attached to a glass slide as described in section 3.6 of this work. A glass fiber filter paper is used as a separator, a small thin strip of lithium metal is sandwiched between two pieces of filter paper to act as the reference electrode, and a strip of lithium metal is used as an anode. The anode is sandwiched to the filter paper and cathode through another glass slide. This sandwich is fed into a 50 ml centrifuge tube and 10 ml of 1M $LiClO_4$ in 2:1 EC:DMC is pipetted into the bottom of the tube. The sample is cycled between 3600 and 4400 mV 126 times at 5 mV/s.

The first and last CV cycles are shown in figure 4.10. These curves show electrochemical behavior which is very consistent with the expected electrochemical response for $LiMn_2O_4$ as shown in figure 2.7. It should be noted that there is an additional reaction at 3700 mV which only occurs on the charging step. This trend increases with the first few cycles before decaying significantly. One way to investigate this behavior is to estimate the background and electrolyte breakdown contributions through the BV equation as described in equation 3.23.

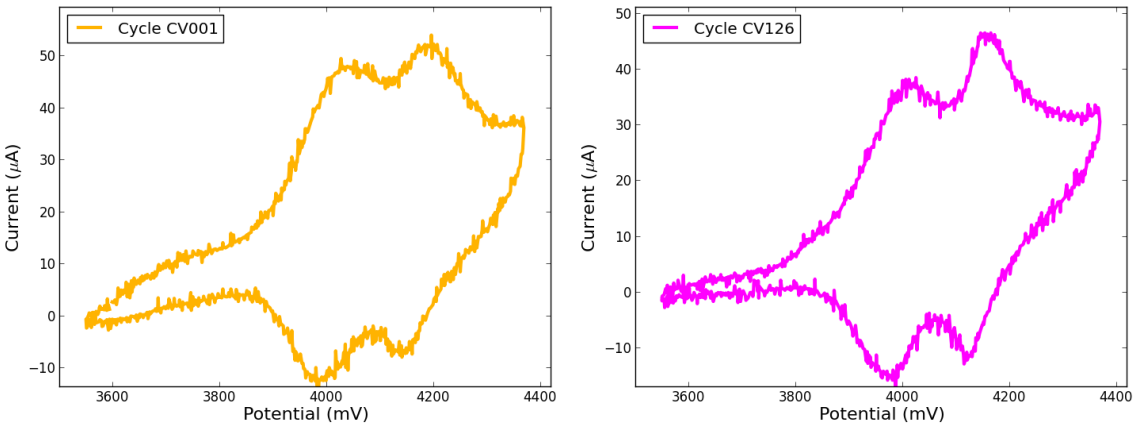

Figure 4.10: CV curves for the first and last cycle of a small test wafer prepared in the same manner as NR samples. CV curves were collected in the voltage range of 3600 to 4400 mV at 5 mV/s

In order to fit the BV equation to estimate background current the regions which represent background must be selected. In this case it is assumed that below 3650 mV and above 4350 mV satisfy this assumption. Throughout these regions the charging and discharging currents are averaged to find a centerline which provides a consistent dataset to fit equation 3.23. Charging current is defined as a positive voltage ramp, and discharging current is defined as a negative voltage ramp. Figure 4.11 shows two examples of these fits to raw data. In the CV004 case there is a small contribution to the averaged currents from the additional reaction around 3700 mV. It should be noted again here that the BV fit to estimate the background is only a first-order approximation. It is not expected to reflect exactly the background contribution, however it does allow an estimation and should be reviewed with that in mind.

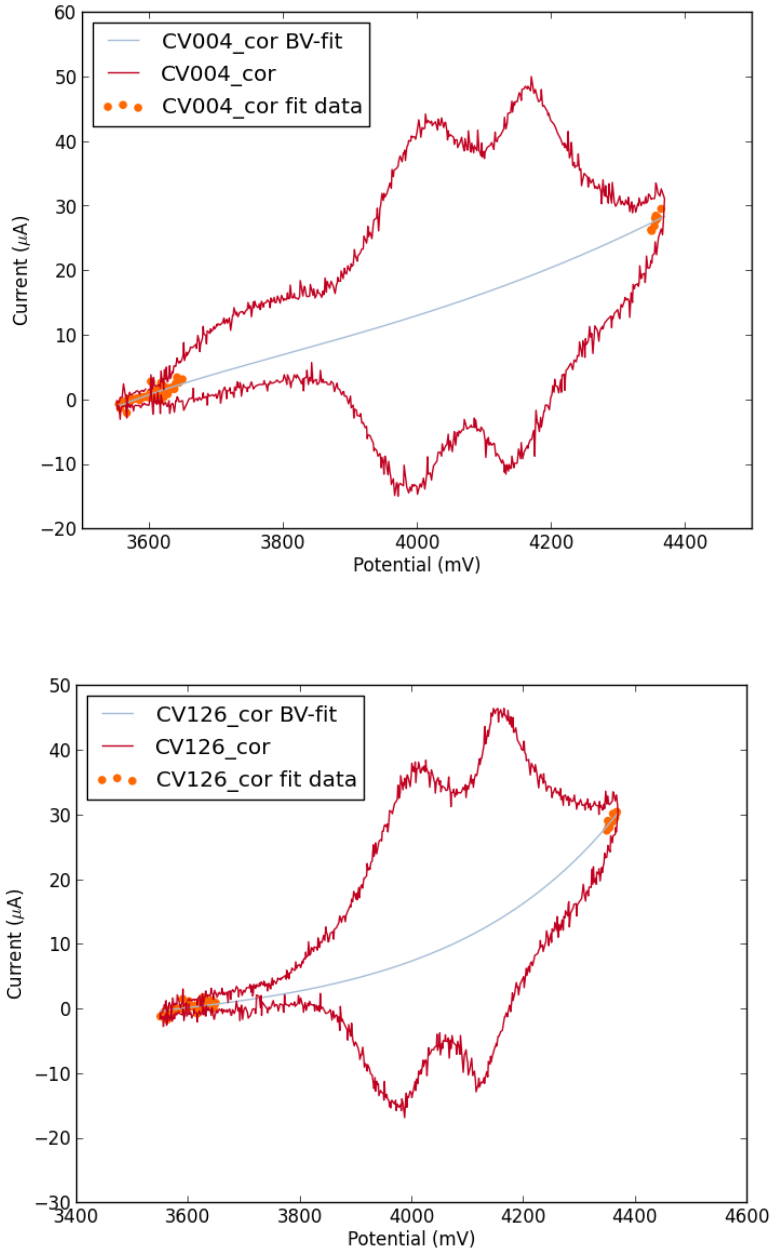

Figure 4.11: Example of two CV curves with a fitted BV line which is used to determine roughly the contribution of electrolyte breakdown and charging to the measured current. The voltage window used for averaging current values are below 3650 mV and above 4350 mV. Equation 3.23 is used to fit those data.

Through roughly estimating the capacitive and electrolyte breakdown currents a comparison between the corrected charging and discharging currents may be made. The fitted BV curve for each CV cycle is subtracted from the charging current and

added to the discharging current. Examples of this process are shown for two CV cycles in figure 4.12. It should be noted that the CV011 was chosen for comparison because it shows a significant additional current due to an unknown reaction.

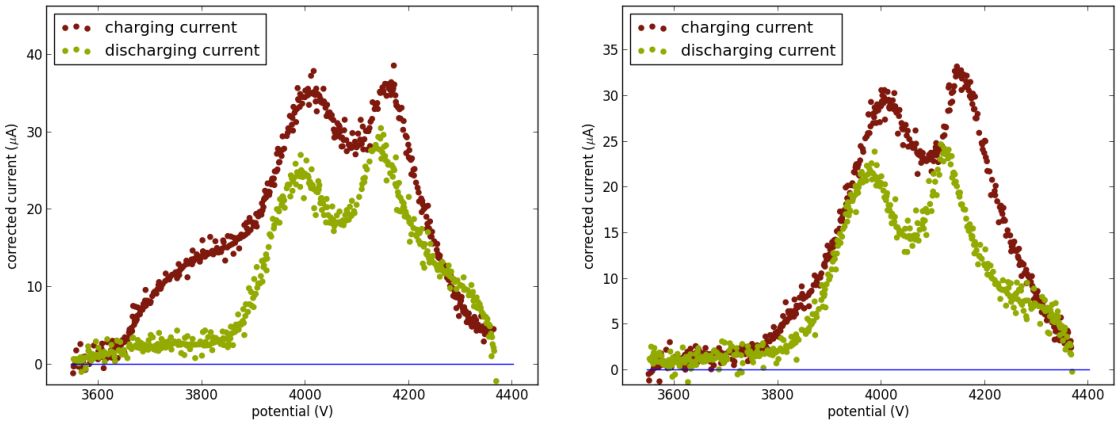

Figure 4.12: Example of two CV curves with background charging and breakdown current subtracted. The discharging current sign is made positive for ease of comparison. Left: (CV011) It can be observed that the CV011 curve shows a significant additional current from an unknown reaction pathway. Right: (CV126)

Integrating the corrected charging and discharging currents provides insight into the additional reaction shown in figure 4.12. Figure 4.13 shows the integrated charging and discharging currents. It is apparent in figure 4.13 that the additional current contribution initially increases in magnitude then gradually decays. It is interesting to note that the integrated discharging current is generally constant. This implies that the same amount of lithium is re-intercalated into the cathode each cycle indicating the sample is operating consistently. Conversely, the integrated charging current suggests that there is some additional process occurring when lithium is transported to the anode.

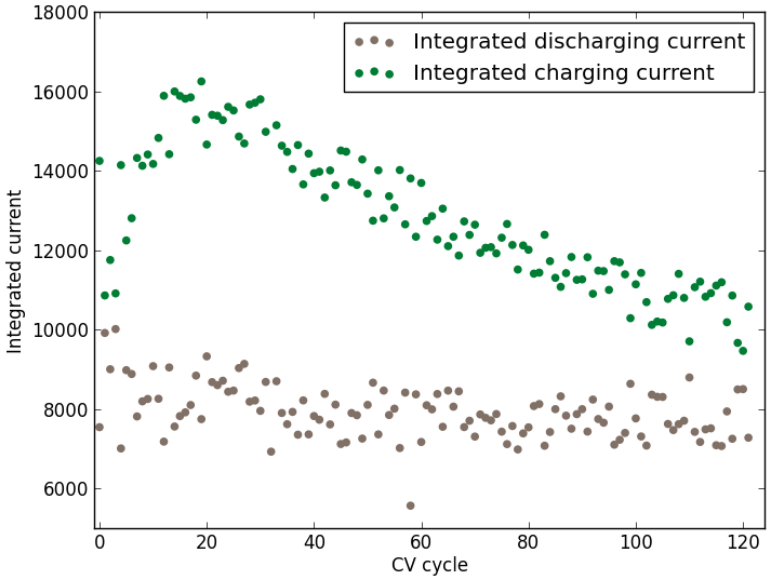

Figure 4.13: Integrated charging and discharging current values for the small test wafer as a function of CV cycle. The difference between the charging and discharging integrated currents are attributed to the current contribution from the unknown reaction pathway as described in figure 4.12

These data from the small test wafer exhibit characteristic $LiMn_2O_4$ electrochemical performance. There is an additional electrochemical feature which remains unknown. It was shown that the integrated discharging current remained roughly constant throughout cycling. The sample performance showed little degradation throughout the CV cycles indicating the sample preparation process results in acceptable electrochemical operation.

4.1.4.2 Full-cell test

To ensure the NR sample cell is capable of exhibiting characteristic electrochemical behavior testing with complete cells were performed. The results shown here are from a sample which was produced in the same batch as those used for NR measurements. Additionally the lithium anode was produced subsequently to those used for the NR measurements. The electrolyte used in this test was 1 M $LiClO_4$ in 1:1 EC:DMC.

Upon injection of electrolyte into the cell the open circuit potential is monitored for about a half hour to inspect the starting open circuit potential. Figure 4.14 shows those initial open circuit data where it can be observed that the potential is decaying with time.

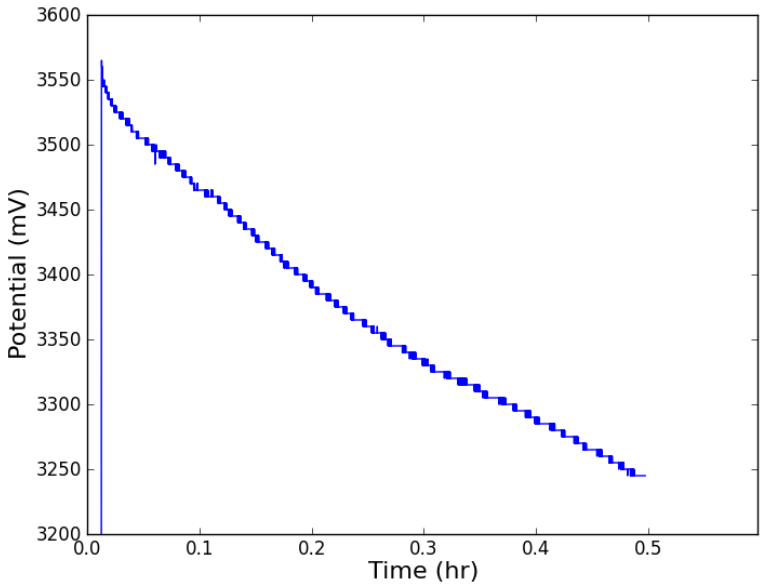

Figure 4.14: Open circuit potential vs time for the full-cell test following electrolyte injection and prior to any electrochemical cycling. The voltage resolution in this mode on the potentiostat is 5 mV.

Following the short open circuit time the cell was cycled twice at 5 mV/s from 3200 mV to 4450 mV shown in figure 4.15. The first cycle was using a current resolution window which was too large and subsequently poorly resolved current data were collected. The cell was cycled again after changing the current resolution window.

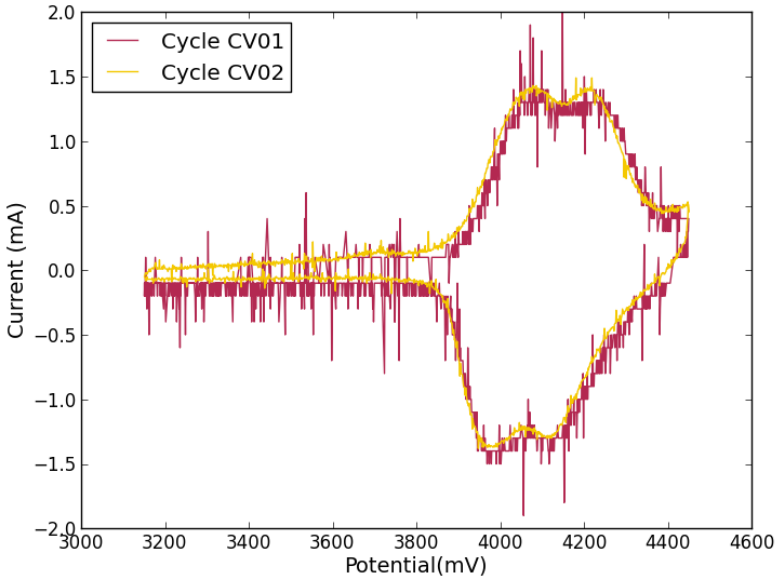

Figure 4.15: Test cell first two CV curves from 3200 to 4450 mV at 5 mV/s. The potentiostat current resolution window was too large for the first CV cycle and is the cause of those very noisy data.

Following the first two CV cycles the cell was left at open circuit for a little more than 6 hours. Those open circuit data are shown in figure 4.16 and it can be observed that the initial potential decay reaches a plateau around 2800 mV for almost 5 hours indicating a change in phase throughout this region. A relatively constant background current (figure 4.17) is observed throughout this open circuit window which is the cause of the potential decay. It is believed that this current and decay in cell potential is related to self-discharge of $LiMn_2O_4$ which is known to spontaneously intercalate lithium to form $Li_2Mn_2O_4$ as discussed in section 2.2.3.3.

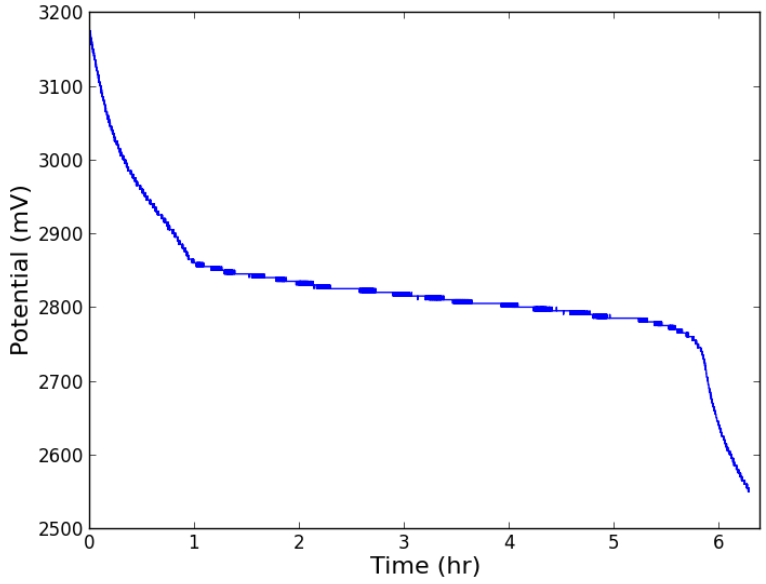

Figure 4.16: Open circuit potential vs time for the full-cell test following two CV cycles.

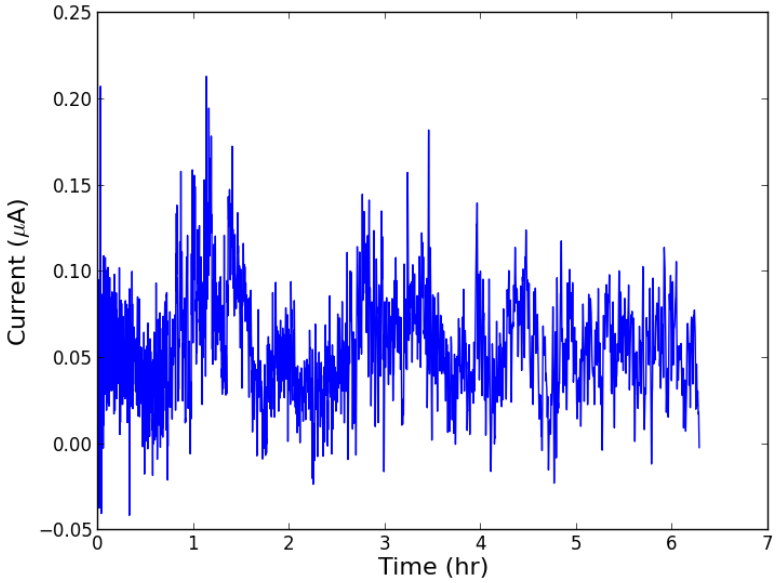

Figure 4.17: Current vs time at open circuit during the full-cell test following two CV cycles.

After sitting at open circuit for 6 hours the cell is cycled once at 5 mV/s from 3150 to 4450 mV. It can be observed in figure 4.18 that there is a significant additional

feature in the CV cycle whose origin is unknown. Given the previous supposition that the cathode was experiencing a phase change this additional feature can be explained by assuming it is due to the changing phase.

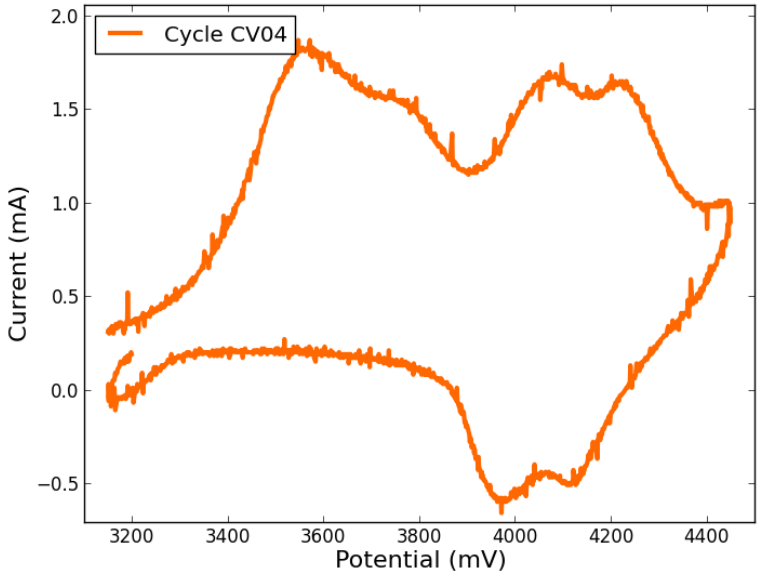

Figure 4.18: CV cycle collected following the second open circuit period of 6 hours. Data are collected at 5 mV/s from 3150 to 4450 mV.

Subsequently the cell is held at 3150 mV for seven hours to test the cell ability to maintain electrochemical performance over long potential hold periods. Figure 4.19 shows the measured current throughout the potential hold. The source of the current observed while holding the potential at 3150 mV is unknown.

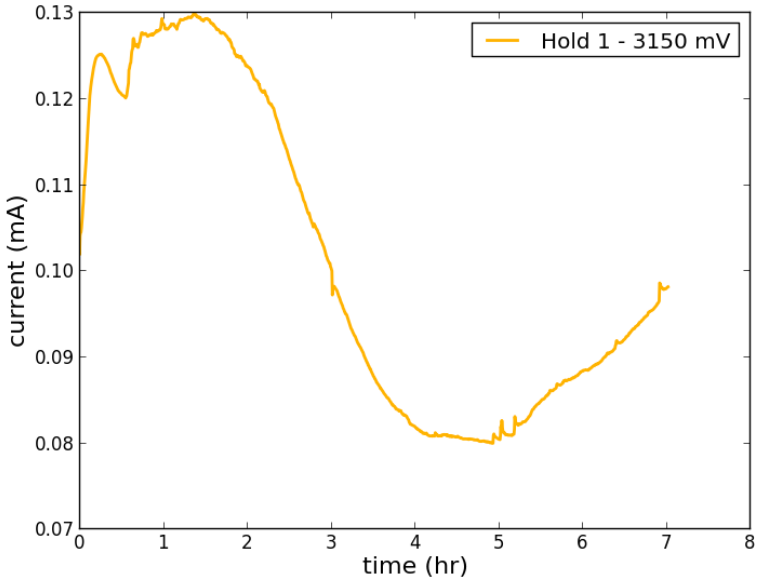

Figure 4.19: First potential hold at 3150 mV for the test cell following the fourth CV cycle.

Following a potential hold at 3150 mV for seven hours the sample is cycled once at 5 mV/s from 3150 to 4450 mV. In figure 4.20 a significant feature in the CV curve occurs at low potentials. This is potentially due to a lithium intercalation toward forming $Li_2Mn_2O_4$; however, the typical onset potential for that reaction occurs around 2800 mV which is ∼400 mV lower than the observed onset potential.

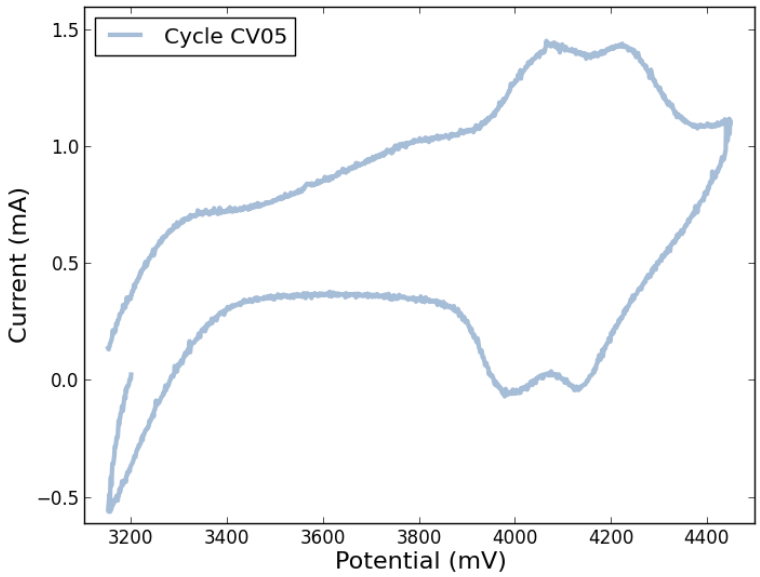

Figure 4.20: CV cycle collected following the first potential hold at 3150 mV for 7 hours. Data are collected at 5 mV/s from 3150 to 4450 mV

After the fifth CV cycle the cell is again held at 3150 mV for 6.5 hours. Figure 4.21 shows the measured current throughout the potential hold. The observed current shows the same general trend as the first potential hold current response. Following the second potential hold a CV cycle is collected from 3150 mV to 4450 mV at 5 mV/s. Figure 4.22 shows the sixth CV cycle in addition to cycle five in order to compare the response. It is observed in figure 4.22 that the general shape of the curves are similar, but there is a significant current offset in the CV05 case.

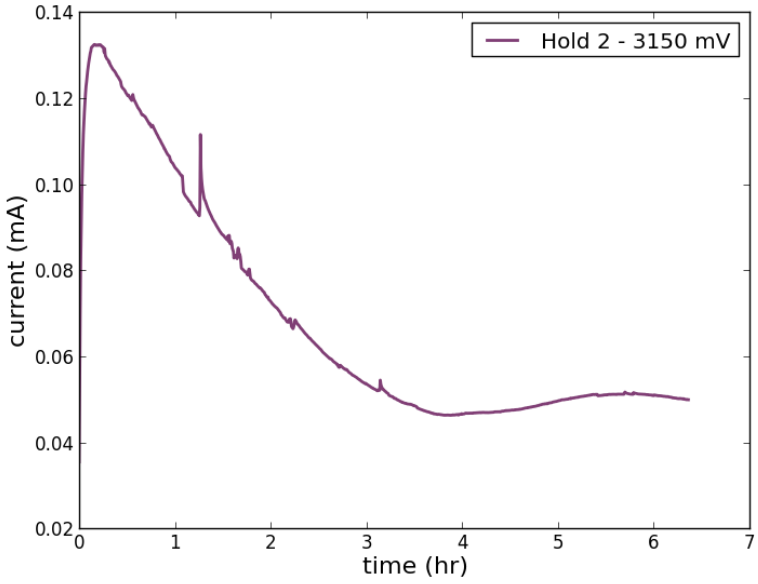

Figure 4.21: Second potential hold at 3150 mV for the test cell following the fifth CV cycle.

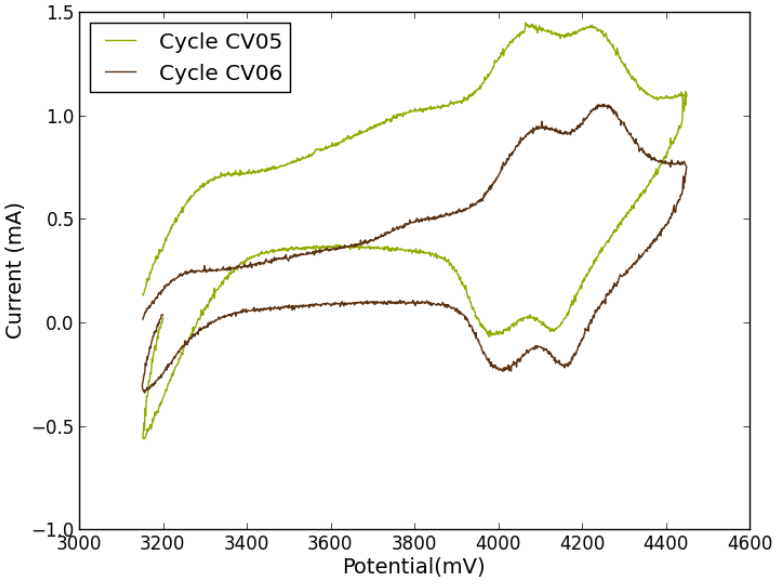

Figure 4.22: CV cycles 5 and 6 both collected between 3150 mV and 4450 mV at 5 mV/s. These CV show comparable response except CV05 shows a positive current offset.

Following the sixth CV cycle the cell is held at 3150 mV for 11 hours. The

current measured throughout this potential hold step is found in figure 4.23. The initial behavior of the measured current throughout this potential hold step generally follows that of the previous potential holds but also shows further oscillatory behavior than the previous holds. Upon completion of the potential hold the cell is cycled twice at 1 mV/s and once at 5 mV/s. The first 1 mV/s cycle experienced a significant background current and overloaded the current resolution range and will not be shown here. CV cycle 8 at 1 mV/s and CV cycle 9 at 5 mV/s are shown in figure 4.24. The noisy signal for CV 8 is due to a poor current resolution. The measured current is in a poor range where it is too large for a smaller current resolution and would experience overload such as in CV 7. Additionally the measured current is too low for the resolution window used and the result is a noisy signal. For this reason CV 9 was collected at 5 mV/s to increase the measured current to an acceptable range.

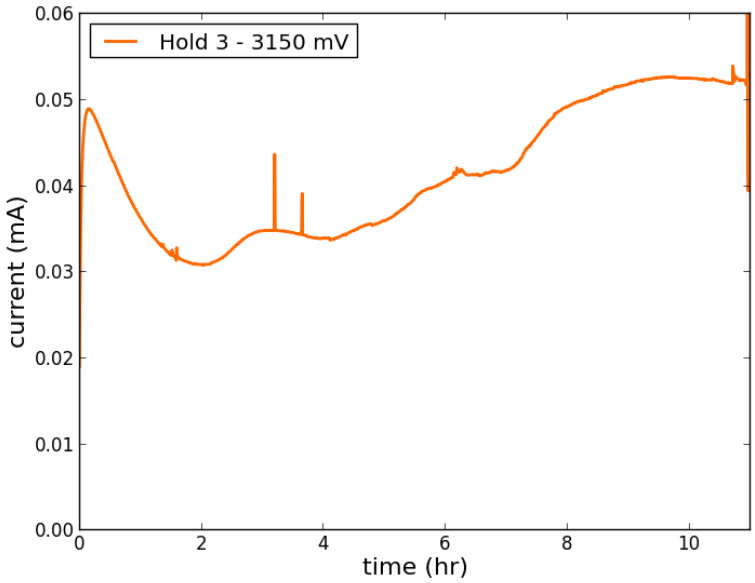

Figure 4.23: Third potential hold at 3150 mV for the test cell following the sixth CV cycle.

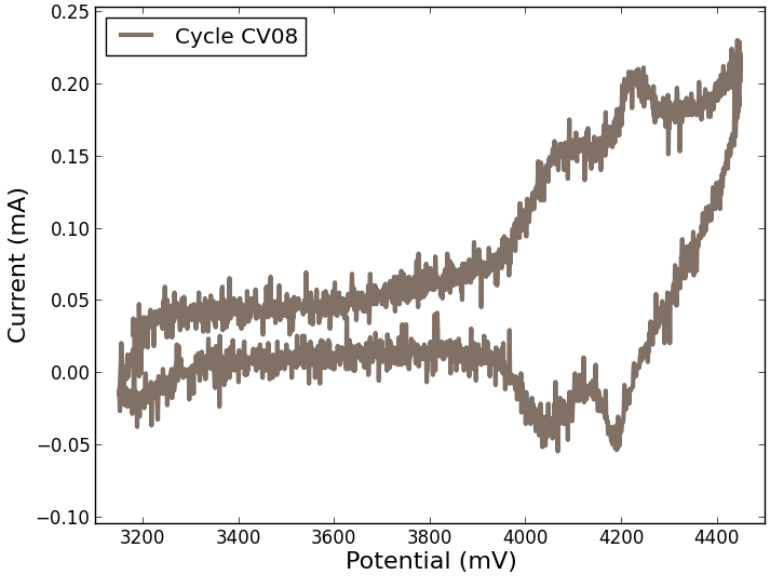

(a) CV cycle 8: 1 mV/s

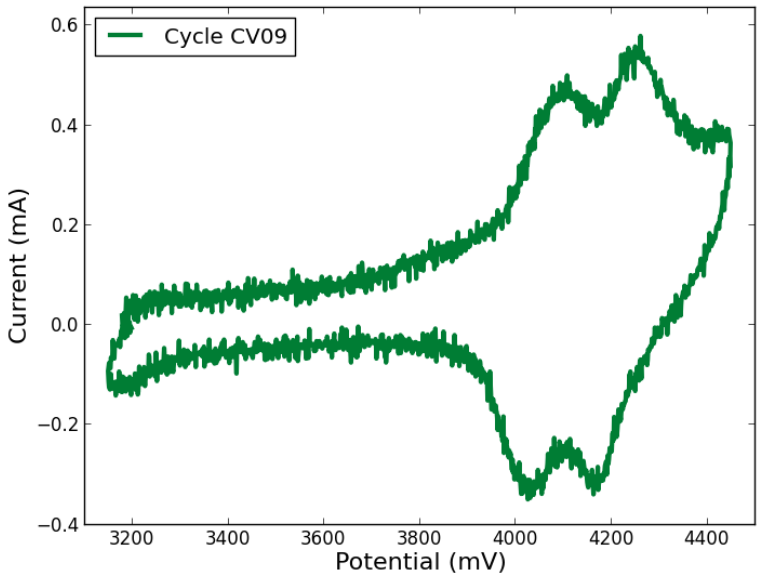

(b) CV cycle 9: 5 mV/s

Figure 4.24: CV cycles 8 and 9 collected at 1 mV/s and 5 mV/s respectively from 3150 to 4450 mV

Following CV cycle 9 the cell is held at 3180 mV for almost 3 hours. Figure 4.25 shows the current response for this potential hold. Those measured current are comparable to the response from previous potential holds. Figure 4.26 shows three

CV cycles collected at 5 mV/s from 3150 to 4450 mV following the potential hold at 3180 mV. CV cycles 10 and 11 were collected just following the potential hold at 3180 mV, whereas CV cycle 12 was collected following approximately an hour at open circuit after the end of CV cycle 11. The additional peak in CV 12 around 3100 mV on the charging step is due to de-intercalating lithium from a $Li_2Mn_2O_4$ phase. From this additional peak we can deduce that there is some fraction of the sample which has converted to the $Li_2Mn_2O_4$ phase.

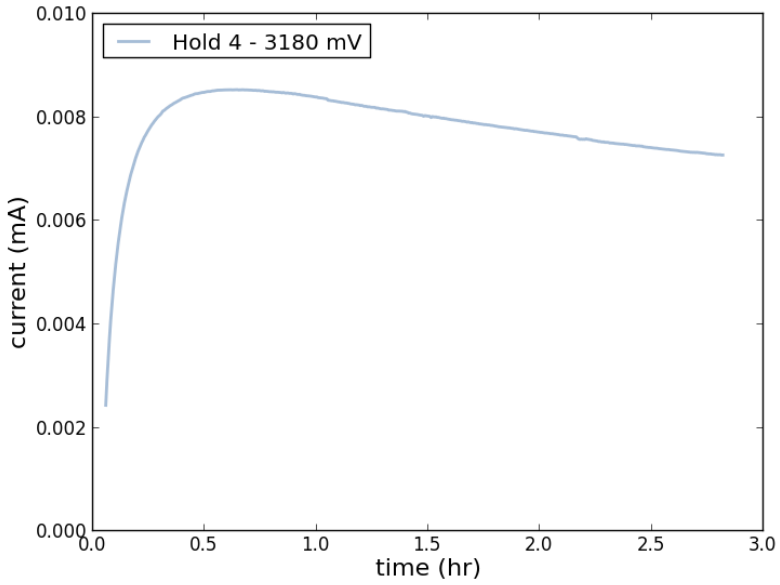

Figure 4.25: Fourth potential hold at 3180 mV for the test cell following the ninth CV cycle.

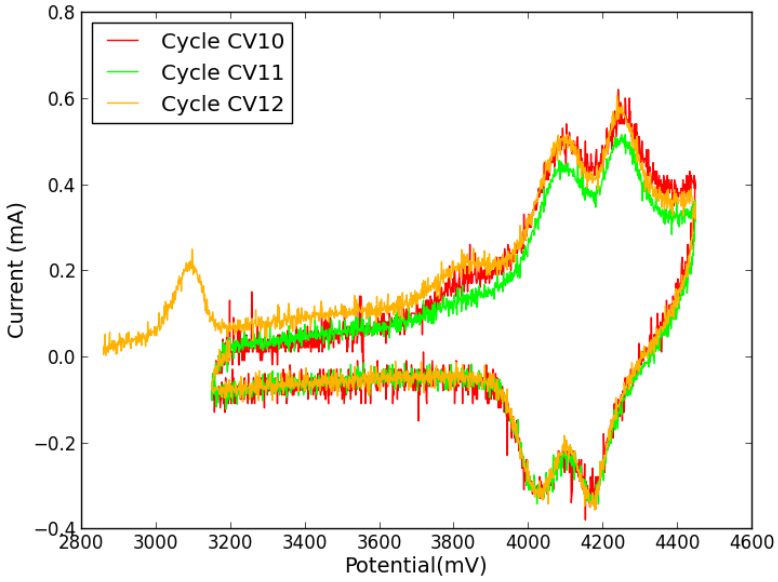

Figure 4.26: CV cycles 10 through 12 both collected at 5 mV/s. These CV are show comparable response to previous CV cycles. CV 12 was collected following an open circuit period of approximately 1 hour. The peak at 3100 mV in the CV 12 cycle is characteristic of $Li_2Mn_2O_4$.

Subsequent potential hold steps and CV cycles show similar behavior as those previously shown. Figure 4.27 shows four of the last 10 CV cycles collected at 5 mV/s from 3150 to 4450 mV. CV 43 was collected just following an 8 hour potential hold step. It is obvious from figure 4.27 that the sample cell is still operating very consistently. However, it should be noted that when comparing CV 2, CV 6, and CV 52 in figure 4.28 there is a significant decrease in overall measured current at the onset potentials.

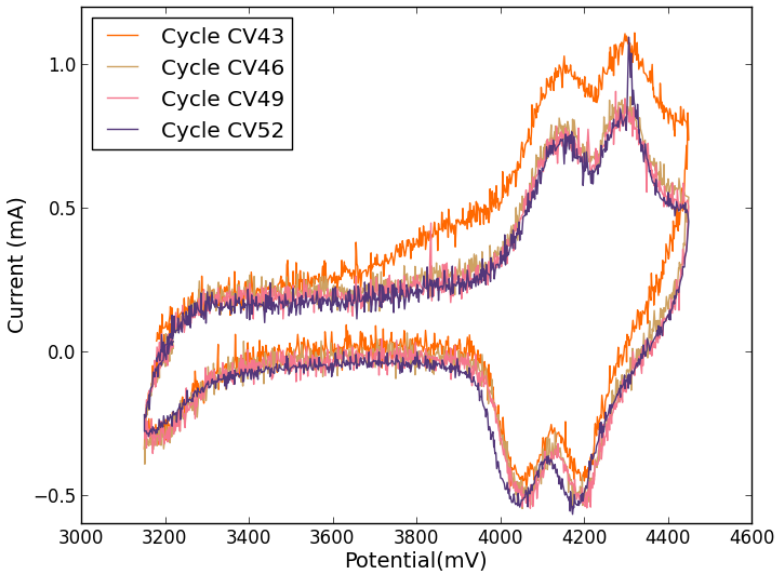

Figure 4.27: CV cycles 43, 46, 49, and 52 collected between 3150 and 4450 mV at 5 mV/s. These CV show comparable response to previous CV cycles.

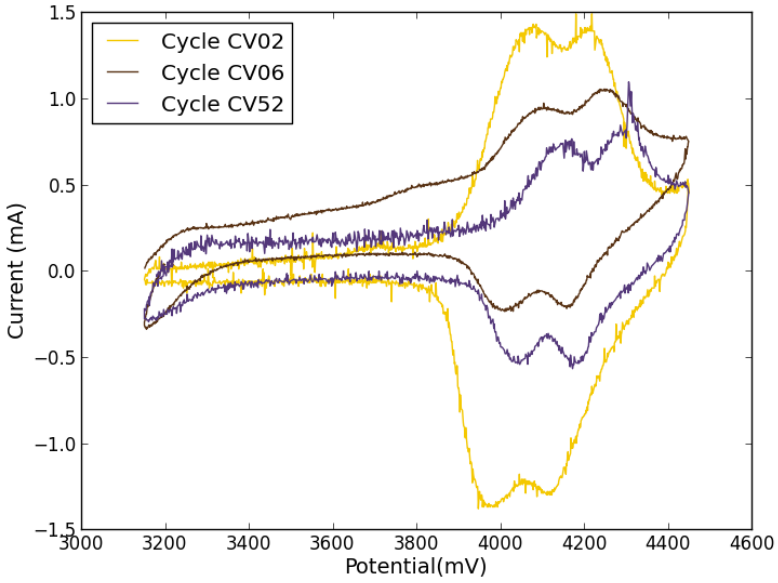

Figure 4.28: Comparing CV cycles 2, 6 and 52 collected between 3150 and 4450 mV at 5 mV/s. The difference in electrochemical response between these three CV cycles highlights the loss of capacity realized throughout the full-cell test.

These test cell results show that the electrochemical cell designed for NR work

operates with characteristic electrochemical behavior as $LiMn_2O_4$. Throughout these and other tests it was determined that sitting at an open circuit state is severely detrimental to the health of the cell. It is suggested that while sitting at an open circuit for extended periods of time leads to self-discharge of the cell and subsequent transition to $Li_2Mn_2O_4$. It was shown that this electrochemical cell is capable of exhibiting expected electrochemical response and may be used to explore the electrolyte/cathode interface through NR.

4.2 Lithium electro-deposition

Lithium electro-deposition was carried out using a 1 M solution of lithium perchlorate in a 2:1 mixture of EC:DMC as the electrolyte solvent. The deposition wafer as was described previously in section 3.2 and is composed of 100 nm SiO_2 / 7.5 nm Ti / 100 nm Cu thin films on a 5 mm thick, 100 cm diameter silicon wafer. The targeted current for deposition was 23 mA.

Prior to deposition a voltage scan at 5 mV/s from open circuit to well below zero volts vs. Li is used to estimate the potential required to achieve the desired deposition current. This process is necessary due to the fluctuation as the wafer rotates at $\sim$100 rpm. As stated in section 3.2, the current is not stable while the sample is spinning. The voltage can be controlled but the registered current through the cathode connection is quite noisy. This is likely due to both the wafer not rotating perfectly perpendicular to the lithium metal source and additional current from graphite rubbing against the copper rotating electrical connection. Figure 4.29 shows the voltage scan for both anodes used in these NR experiments. The first anode wafer showed approximately 23 mA around -750 mV vs Li/Li^+, whereas the second anode wafer showed approximately 23 mA around -1500 mV vs. Li/Li^+. The difference is likely due to using the same lithium metal as an ion source for both depositions. It is expected that the lithium metal source would develop a significant surface layer from

the excessive stripping which should occur at 20's of mA. A subsequent deposition of another test anode was performed with a fresh lithium metal source and was found to exhibit similar response to that of the sample which was deposited at -750 mV vs Li/Li^+.

Figure 4.30 shows current vs time for the Open Circuit experiment anode deposition. The voltage was set to -750 mV, however the measured average voltage over the deposition period was -742 mV. Data are collected approximately every 200 ms, and are averaged over two seconds. A Coulombic cutoff was used to stop the deposition after 400 C charge was passed. This value was selected to deposit approximately 700 nm of lithium across the surface. This value is determined by assuming every section of the wafer passes over the lithium metal source for the same extent of time. Another assumption is that the deposited material is fully dense. It is likely these two assumptions are only loosely valid, but the object is to deposit enough lithium that the anode can be assumed to be an infinite supply of lithium when opposite the thin-film cathode.

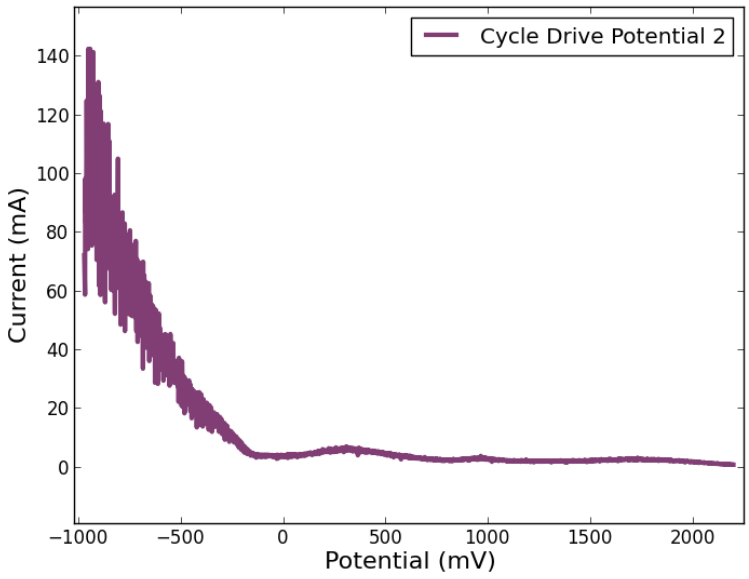

(a) OCV anode voltage scan

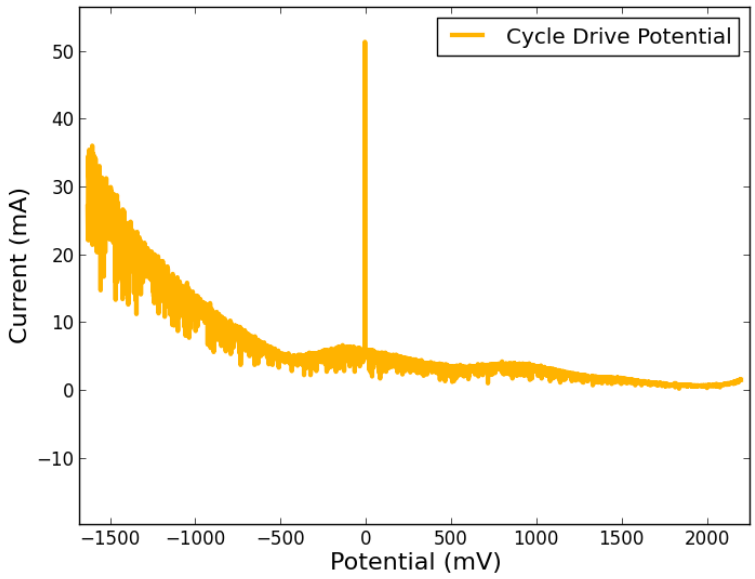

(b) Potential hold anode voltage scan

Figure 4.29: Voltage scan of anode wafers prior to Li electro-deposition of 1 M $LiClO_4$ in a 2:1 (v:v) mixture of EC:DMC. Top: First electro-deposited anode wafer 5 mV/s voltage scan from Cu OCV. The voltage which generally corresponded to 23 mA was determined to be ∼-750 mV. Bottom: Second electro-deposited anode wafer with 5 mV/s voltage scan from Cu OCV. The voltage which generally corresponded to 23 mA was determined to be ∼-1500 mV

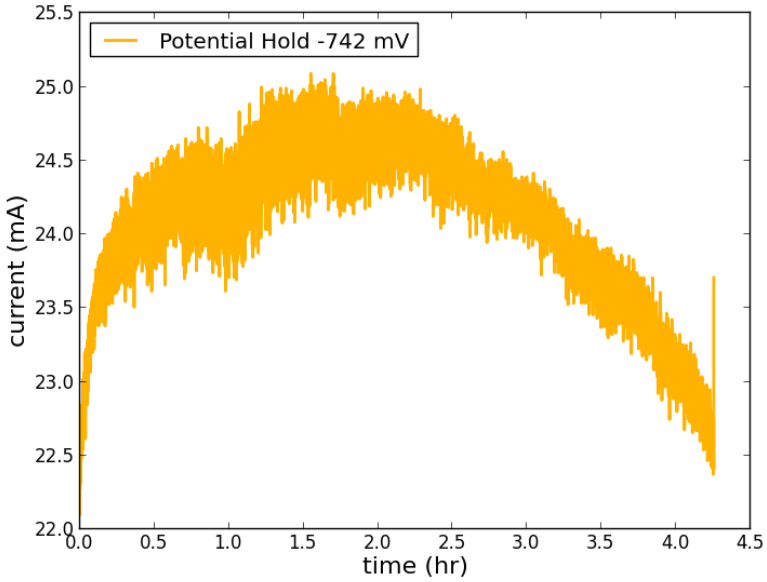

Figure 4.30: Averaged current vs time for OCV anode through Li electro-deposition at -750 mV. Average voltage is determined by averaging all measured voltages throughout the deposition process. It is apparent that current is not entirely stable throughout the deposition process.

Figure 4.31 shows current vs time for the potential hold anode deposition. The voltage was initially set to -1500 mV, but was observed to be about 5 mA below what was desired. The voltage was increased to -1750 mV which initially showed current around 23 mA, but subsequently increased throughout the deposition to a maximum around 35 mA. This is an indicator that the quality of the lithium metal source was degraded.

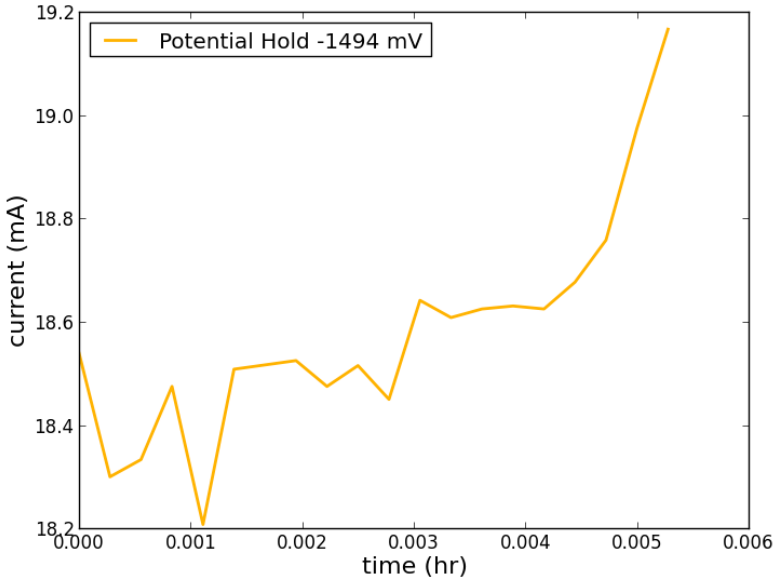

(a) Li electro-deposition at -1500 mV for potential hold anode

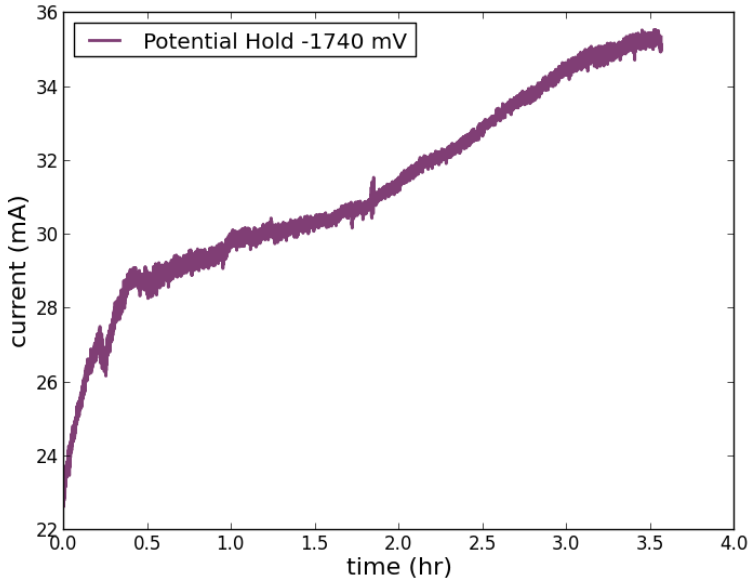

(b) Li electro-deposition at -1750 mV for potential hold anode

Figure 4.31: Li electro-deposition current vs time for potential hold anode at -1500 and -1750 mV Top: Current vs time for Li electro-deposition at -1500 mV. The measured current was below the desired value and therefore the process was stopped and the deposition voltage increased. Bottom: Current vs time for Li electro-deposition at -1750 mV. The starting current was around 23 mA, but subsequently increased throughout the deposition to a maximum around 35 mA.

An example of the surface area coverage of the deposition for the potential hold anode is shown in figure 4.32. Figure 4.32 shows very uniform coverage on the wafer surface. The glossy appearance is due to dried EC covering the wafer. The external ring of bare copper is a result of the wedge radius machined into the polyethylene which defines the lithium source footprint. This area is not exposed line-of-sight to the lithium source and therefore no deposition occurs. Similarly the water jetted holes have a region around which no deposition occurs. This is assumed to be due to perturbation in the electrolyte flow in this area causing a turbulence which prevents deposition. The center is observed to have significant dendritic buildup. This is expected and is a trait exhibited by all deposited wafers. This can be explained by the lack of movement while on the axis of rotation. This apparatus is thought to inhibit dendritic buildup by action of a shear force on the surface of the wafer by the electrolyte. At the very center and close to it the shear of the electrolyte is minimal and does not prevent dendrite formation. This area is removed carefully by direct spray of DMC through a pipette, wiping with a Kimwipe, and rinsing with DMC multiple times. The goal is to remove as much loose lithium as is possible to prevent short-circuiting in the full-cell.

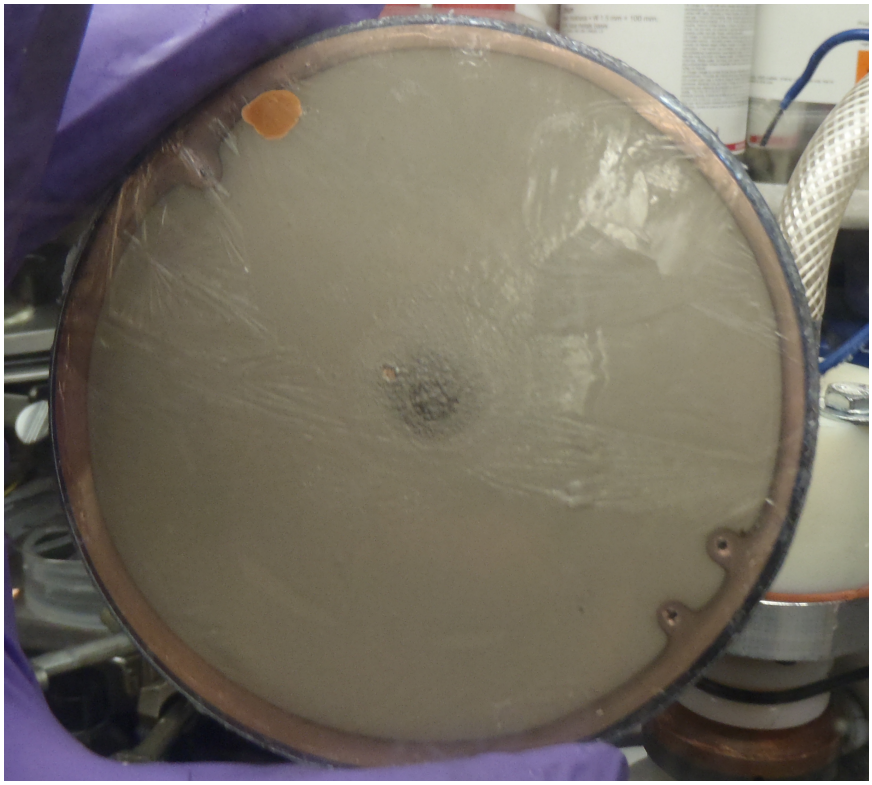

Figure 4.32: Example of electro-deposited lithium anode coverage from the potential hold anode. The deposition parameters are ∼100 rpm wafer rotation, -1750 mV voltage vs Li/Li^+, 400 C deposition cutoff. The outer copper ring is due to lack of line-of-sight to the lithium source wedge. The central buildup of dendritic lithium is a result of small angular velocity when near the axis of rotation.

4.3 NR sample characterization

NR samples were made using the previous recipe where it was decided the ideal processing parameters in the space investigated was 3750 rpm spinning speed, 650 °C annealing temperature, and 10 minutes anneal time. Two samples were investigated through AFM to examine the surface morphology to provide an estimate to compare against XRR results. The sample used for the OCV-experiment showed an average rms-roughness of 1.8 nm and a warp of 0.60%. The sample used for the potential hold experiment showed an average rms-roughness of 0.69 nm and a warp of 0.22%. Figure 4.33 shows height-profile data from these AFM investigations for both samples. The

OCV-experiment sample has a larger roughness and warp than the potential hold sample, but the sample roughness is within acceptable levels for NR. Additionally while the potential hold sample shows no observable features on the surface of the wafer, the OCV-experiment sample shows both some particulate on the surface and evidence of pinhole defects from the spinning process.

Following AFM the samples were then investigated through XRR to compare with NR for characterization prior to introducing the anode and electrolyte. Figure 4.34 shows the reduced XRR data for the OCV-sample. It should be noted that the fringes featured in the reflectivity profile are generally a result of the strongly scattering platinum. In fact the fringe near the A) marker in figure 4.34 is on the critical edge for platinum and is an interference directly related to the cathode layer. This is highlighted here and will be mentioned again to remind the reader that this fringe is of significant importance when fitting these results for the most accurate representation of the cathode layer. An additional note on these figures showing reflectivity are the lack of error bars on some points at higher Q. The lack of these bars are due to the uncertainty being on the order of the reflectivity and therefore when plotting as a log the location of the lower error bar would be at a negative value which is undefined. In these cases the plotting tool only plots the upper hat for the uncertainty and leaves out the line connecting the point.

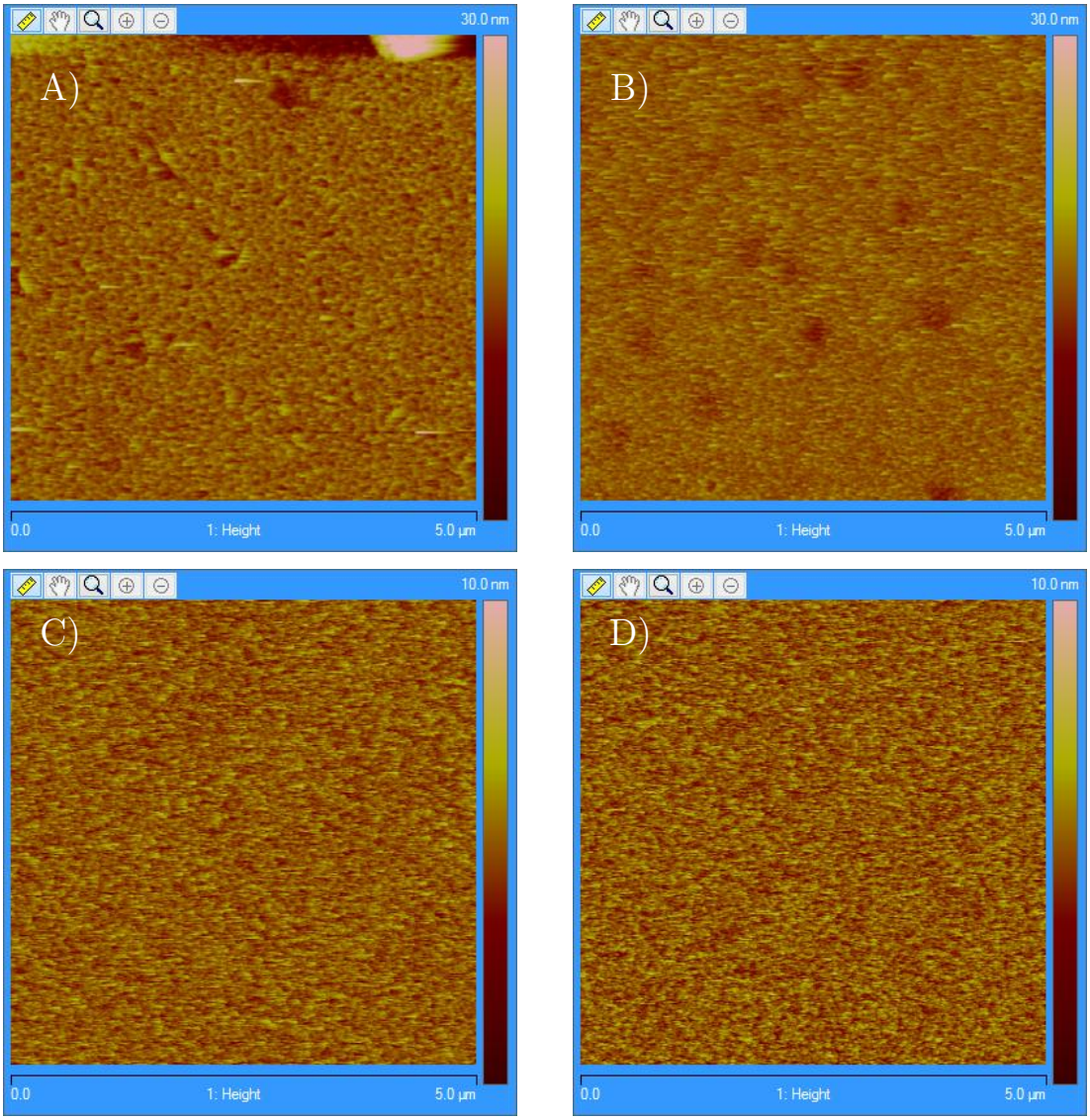

Figure 4.33: AFM height profiles for the OCV-sample (Top row) and the potential hold sample (Bottom row). A: OCV-sample height profiles showing a small particulate on the surface in the upper right hand corner (rms-roughness: 2.2 nm/warp: 0.631%). B: OCV-sample height profile showing pin-hole defects (rms-roughness: 1.41 nm/warp: 0.576%). C: Potential hold sample showing no observable features (rms-roughness: 0.64 nm/warp: 0.182%). D: Potential hold sample showing no observable features (rms-roughness: 0.74 nm/warp: 0.267%).

The XRR results for the potential hold sample are shown in figure 4.35. These results are very similar to those in figure 4.34 which is as expected given the processing parameters were consistent. It is noted that the fringe spacing for the OCV sample is

slightly wider which indicates the platinum layer is thinner for that sample. It should also be noted that there is greater definition in the fringe associated with the cathode layer near low-Q. This is readily observable in the R*Q^4 data near low-Q where the rapid change in slope occurs.

Following XRR, NR was used on the cathode samples prior to introduction of electrolyte to have a direct comparison to those XRR results. Figures 4.36 and 4.37 show those reduced NR results for the OCV-sample and potential hold sample respectively. There are two significant fringes which can be observed in these figures. The large fringes are associated with the strongly scattering platinum layer, the smaller fringes intermixed on those platinum fringes correspond to the SiO_2 layer. The impact of the $LiMn_2O_4$ layer is not easily directly observable, but its influence is greatest below Q $\leq 0.1\ \mathring{A}^{-1}$.

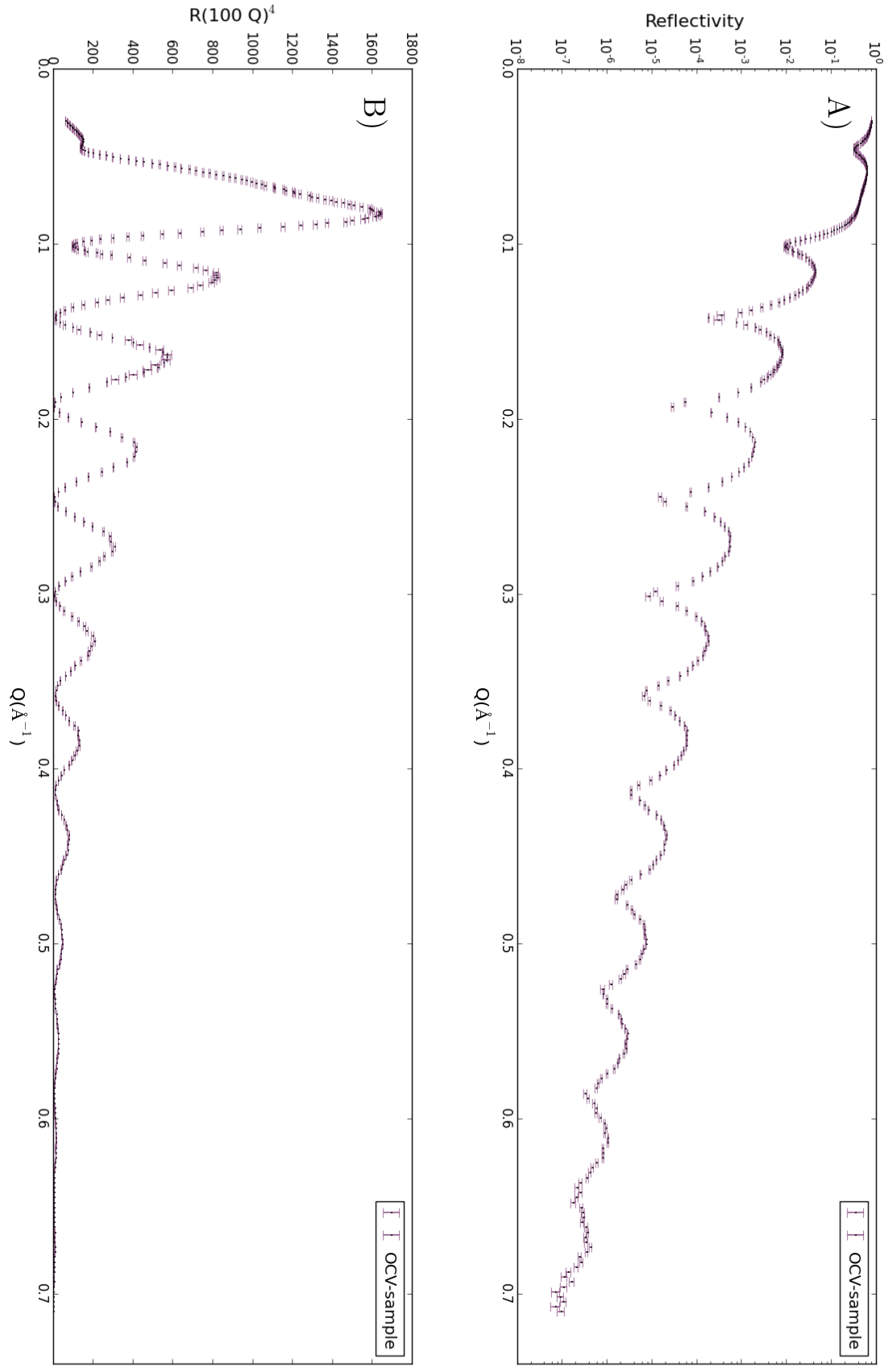

Figure 4.34: XRR results for the OCV-sample in air. A) Log(R) vs Q. B) R*(100*Q)^4, this form is used to examine the critical edge since it occurs at the first maximum.

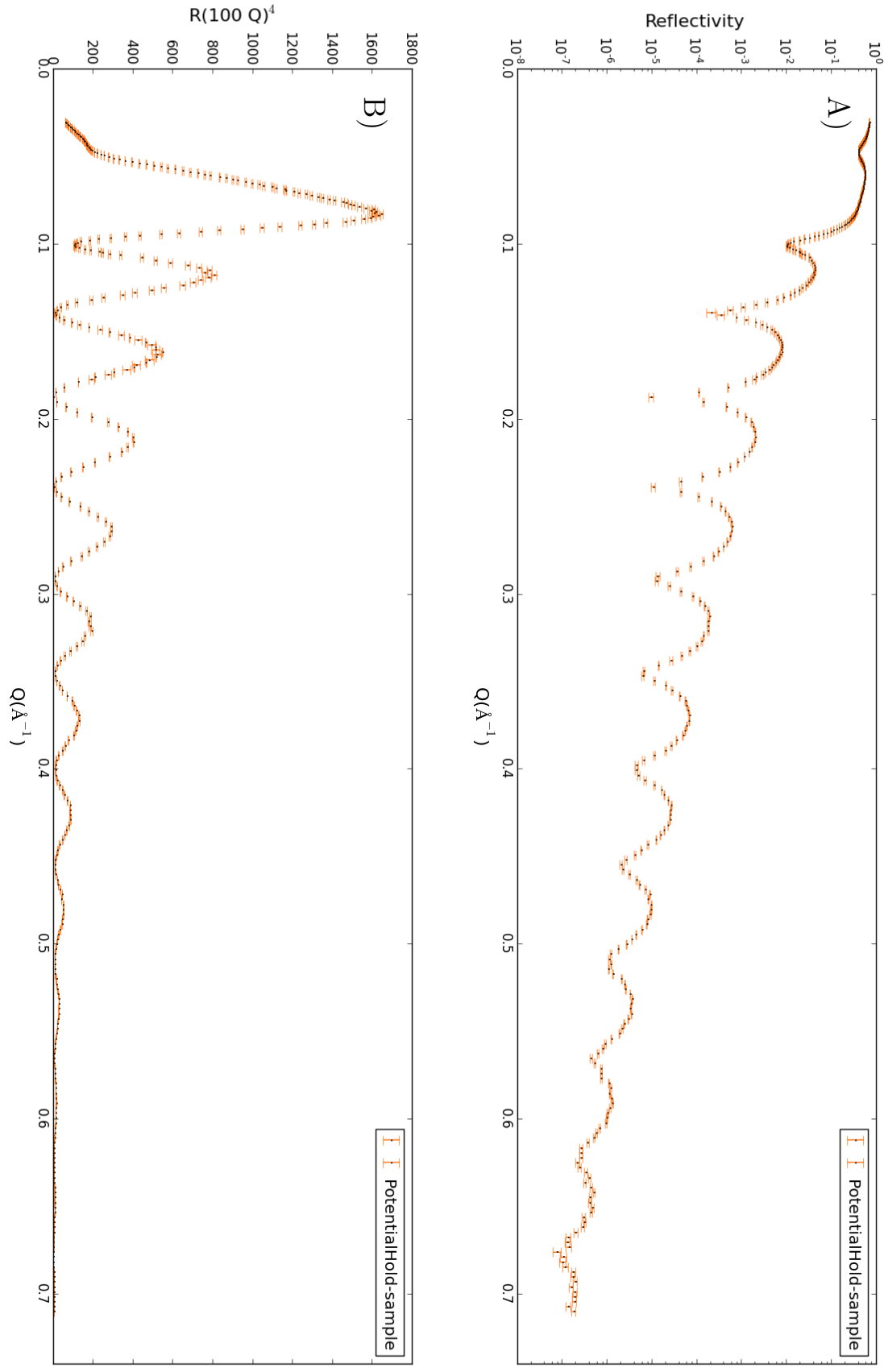

Figure 4.35: XRR results for the potential hold-sample in air. A) Log(R) vs Q. B) R*(100*Q)^4, this form is used to examine the critical edge since it occurs at the first maximum.

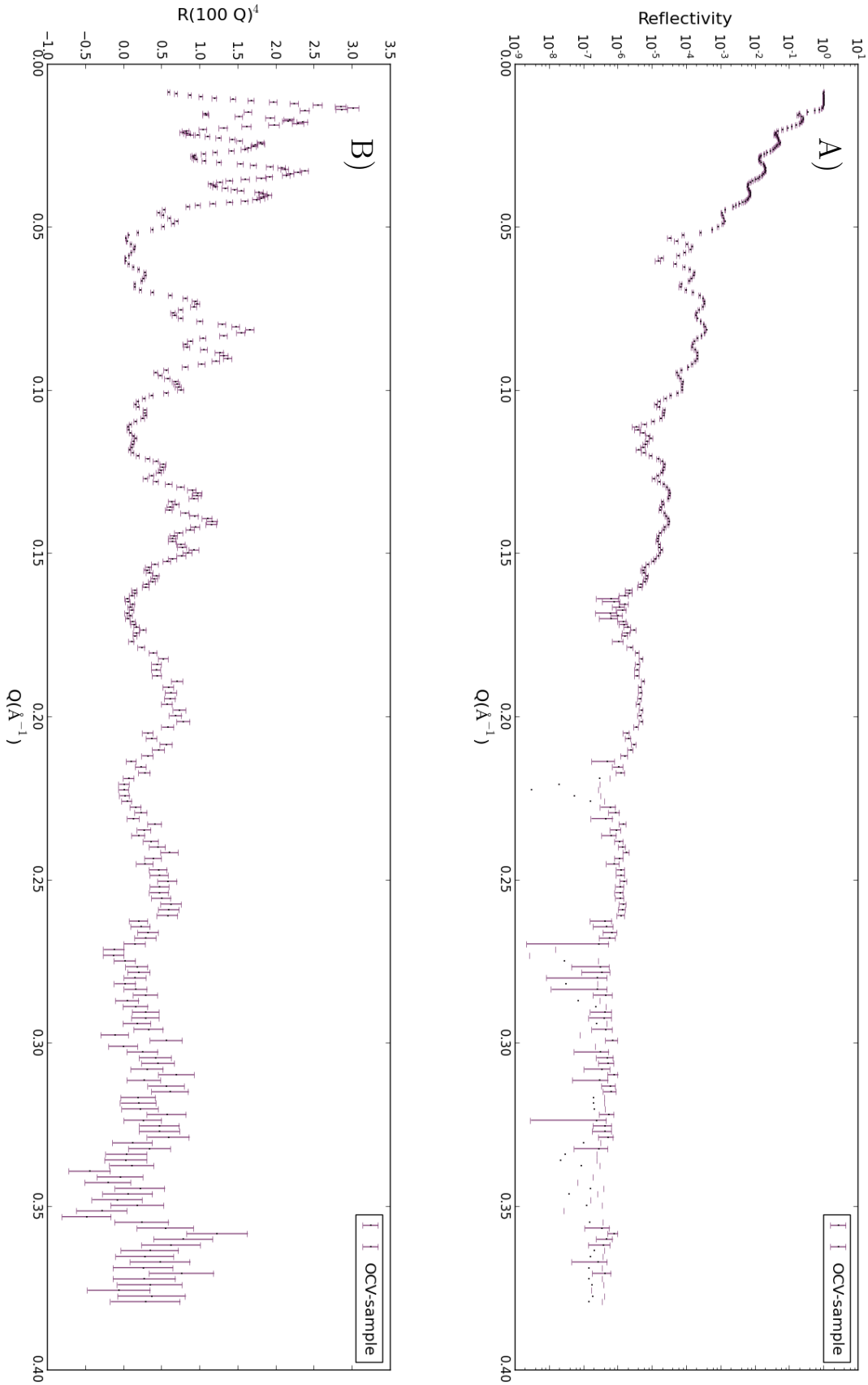

Figure 4.36: NR results for the OCV-sample in air. A) Log(R) vs Q. B) R*(100*Q)^4, this form is used to examine the critical edge as it occurs at the first maximum.

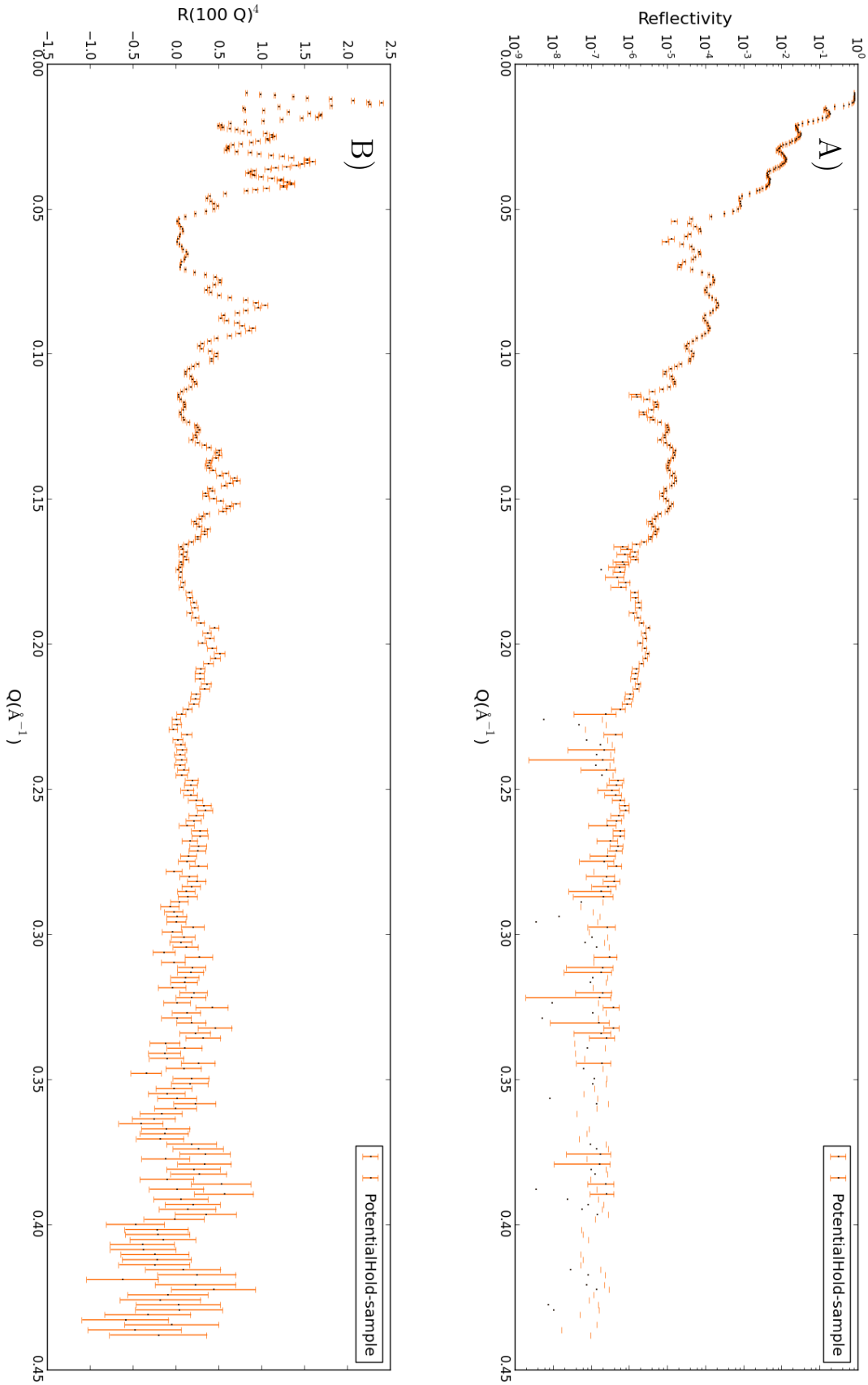

Figure 4.37: NR results for the potential-sample in air. A) Log(R) vs Q. B) R*(100*Q)^4, this form is used to examine the critical edge as it occurs at the first maximum.

4.4 NR results

This section provides reduced NR datasets for all electrochemical conditions on both the open-circuit and potential hold samples. A comparison of each dataset collected at every electrochemical condition is included to highlight which datasets may be combined for further analysis. First the open-circuit sample NR data are presented followed by the potential hold sample NR data.

4.4.1 OCV NR experiment

4.4.1.1 Introduction of electrolyte

Following the injection of electrolyte (1M $LiClO_4$ in 1:1 EC:DMC (v/v)) into the NR cell, potential and current are monitored through the potentiostat via a GPIB interface with a specially written LabView controller. The ADC in the potentiostat is triggered approximately every 41 milliseconds where those data are averaged over a 30 second window. Figure 4.38 shows the potential and current as a function of time. There is a constant 60 μA background current throughout the experiment. This current and the trend in the observed potential indicates a change in the cathode material and phase.

Figure 4.39 shows the first and second NR datasets collected while maintaining the cell at open circuit. Figure 4.40 shows the third and fourth NR datasets while maintaining open circuit. Figure 4.41 shows the normalized difference for the second and first NR datasets as well as the third and second NR datasets as determined through equation 3.9. Figure 4.42 shows the normalized difference between the fourth and third NR datasets while at open circuit.

Figure 4.41 shows substantial changes in the sample between the first and third NR datasets. These indicate that the potential vs time results observed in figure 4.38 exhibit a phase transformation in the cathode layer. Conversely there is little

change between the third and fourth NR datasets. Since stability in those NR data is observed between the third and fourth NR measurements, those data are combined and reduced for further analysis.

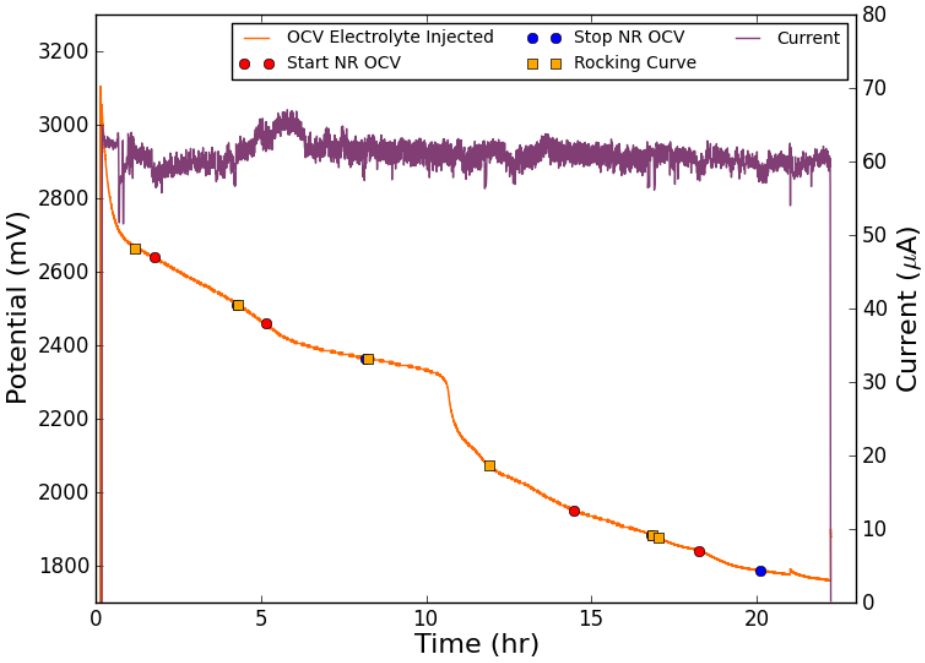

Figure 4.38: Current and potential as a function of time following injection of electrolyte, leaving the NR cell at an open circuit condition. Markers indicate start of NR measurement, stop of NR measurement for one dataset, and locations of rocking curves.

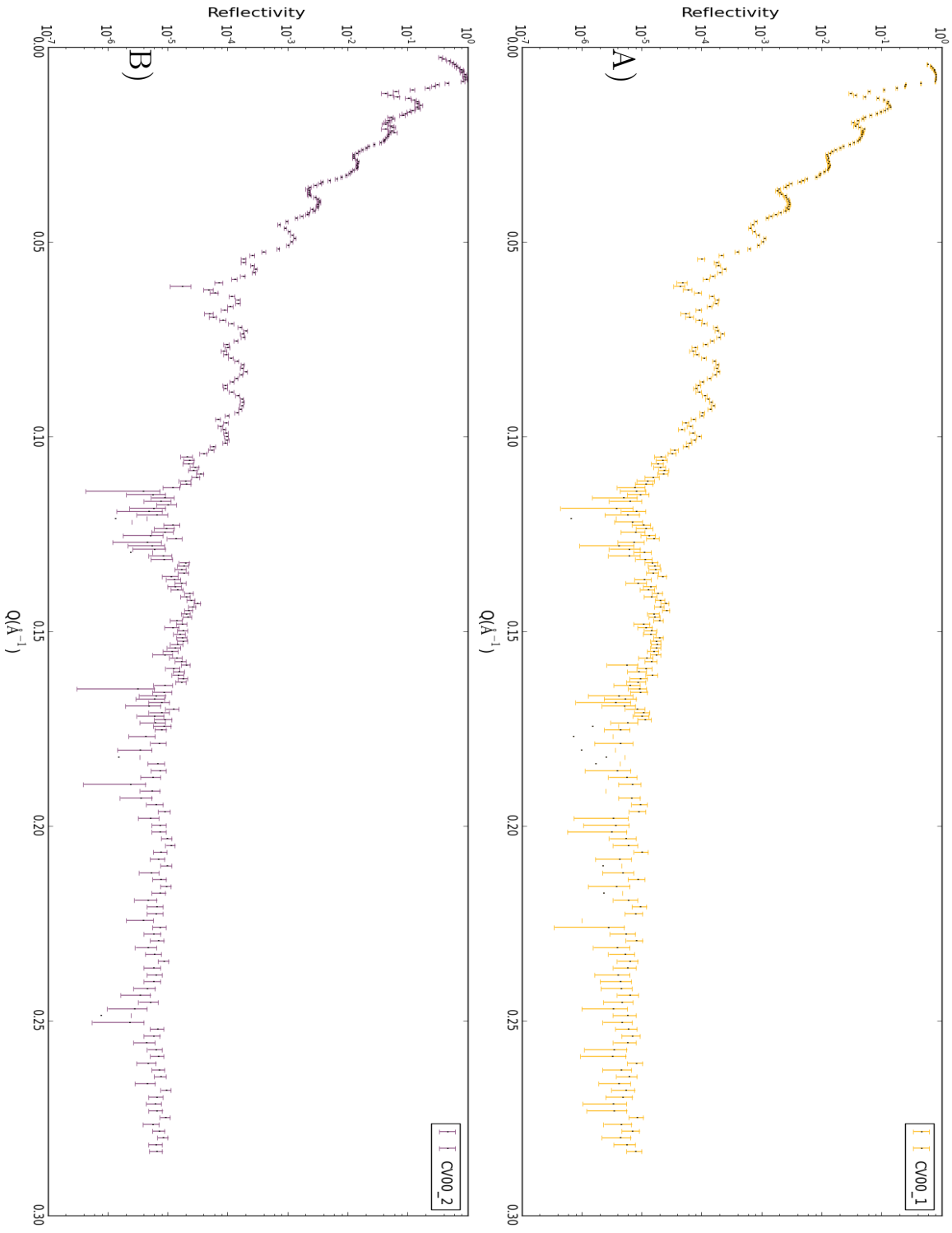

Figure 4.39: Reduced NR results for the sample at open circuit showing the first and second datasets. A) First dataset, B) Second dataset

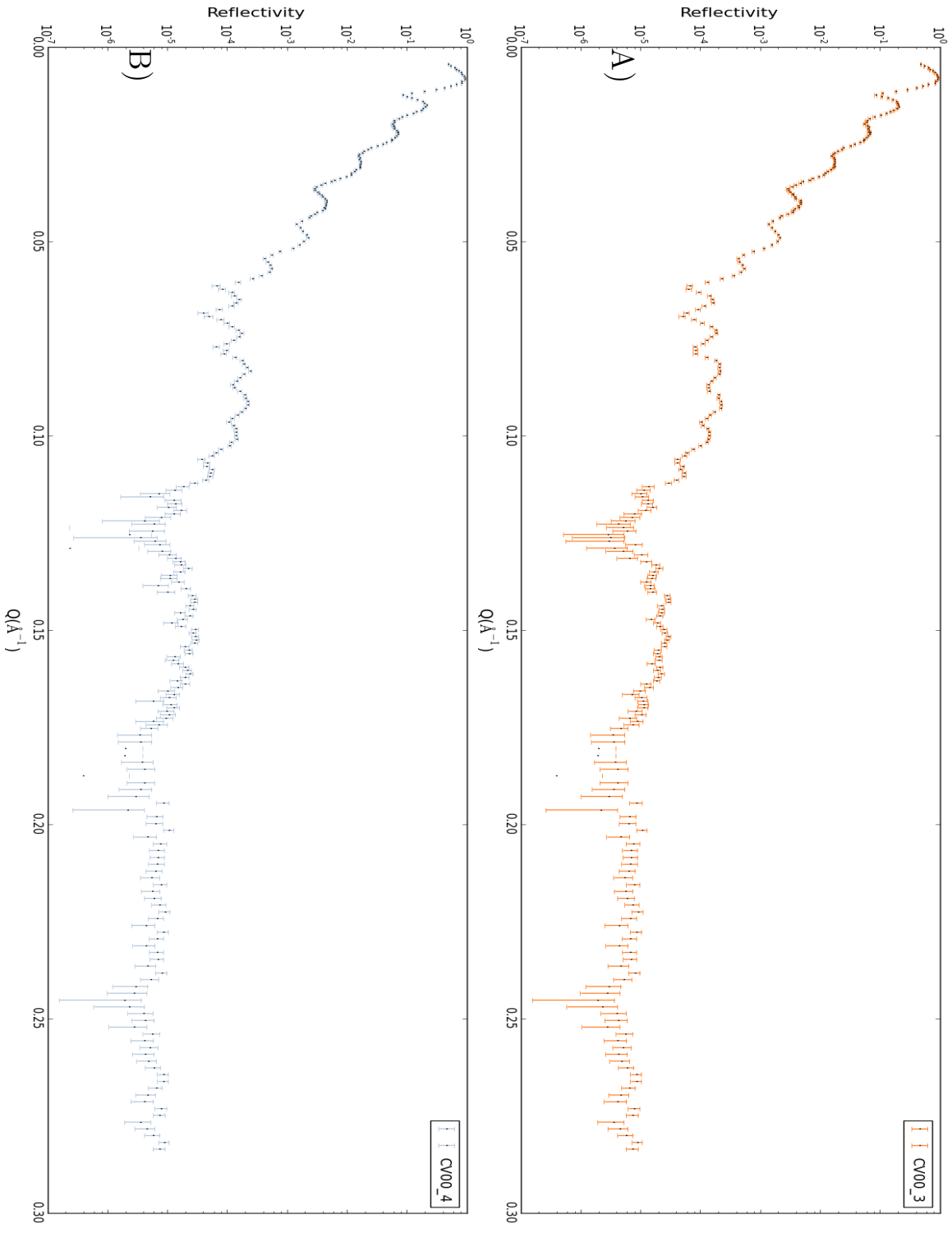

Figure 4.40: Reduced NR results for the sample at open circuit showing the third and fourth datasets. A)Third dataset, B) Fourth Dataset

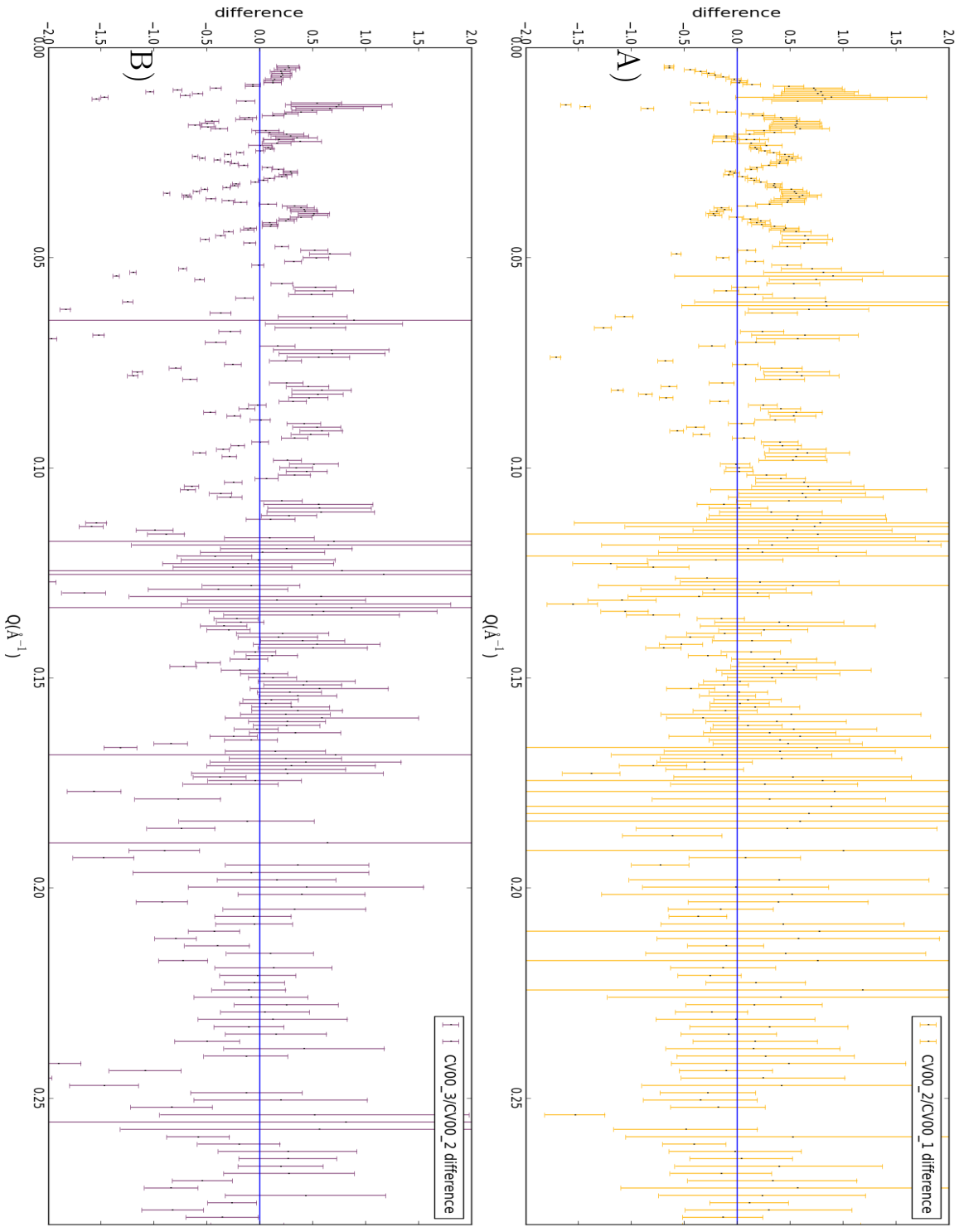

Figure 4.41: Normalized difference between first/second and third/second NR datasets collected while the sample was at open circuit prior to any electrochemical cycling. A) Normalized difference between first and second NR dataset. B) Normalized difference between second and third NR datasets.

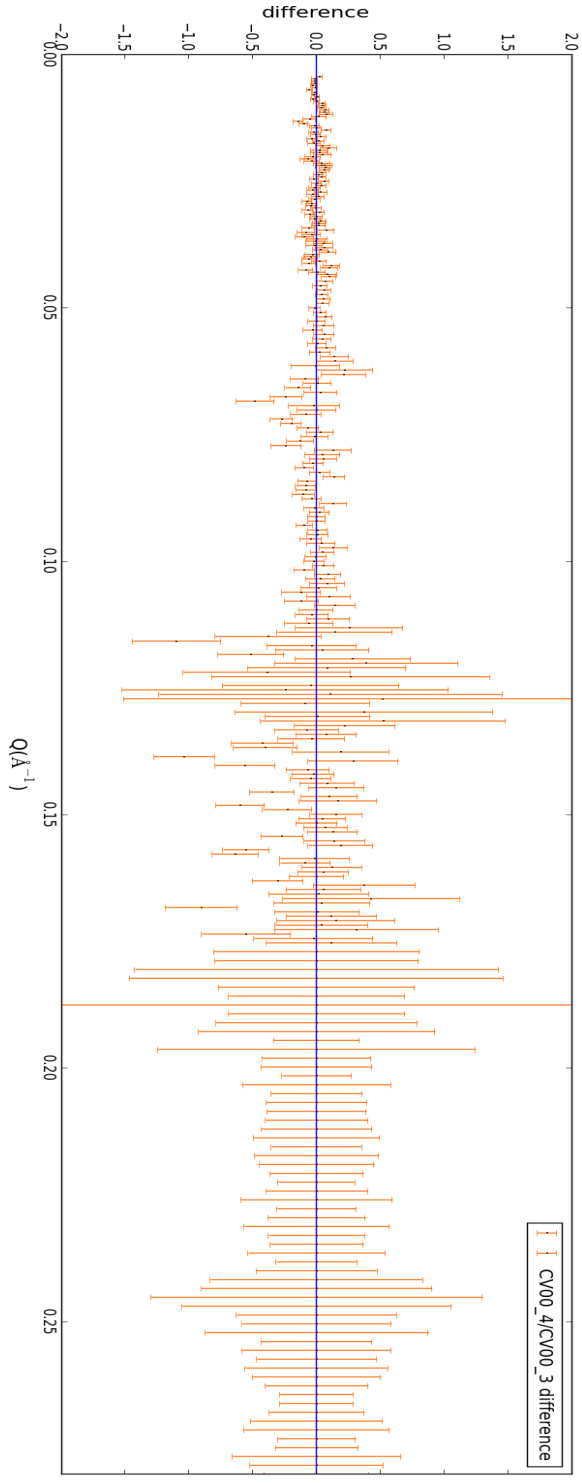

Figure 4.42: Normalized difference between fourth and third NR datasets collected while the sample was at open circuit prior to any electrochemical cycling.

4.4.1.2 Following 1 CV cycle

After 22.5 hours at open circuit following electrolyte introduction the NR cell is cycled one time at 5 mV/s between 1850 mV to 4500 mV and the cycle is stopped at 3300 mV. Figure 4.43 shows the CV data where no observed features correspond to the expected $LiMn_2O_4$ characteristic response.

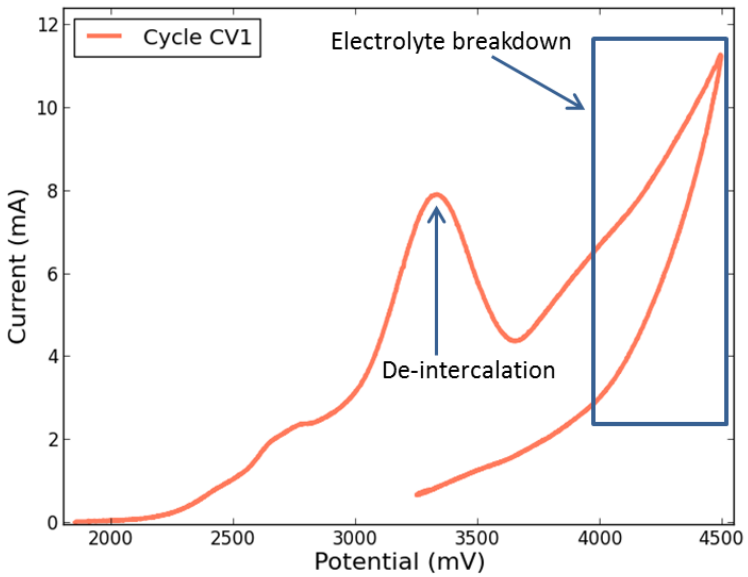

Figure 4.43: First CV curve for sample at open circuit for 22.5 hours from 1850 mV to 4500 mV and stopping at 3300 mV at 5 mV/s. The only significant observed onset potential is in the electrochemical region which is related to the deintercalation of 1 Li^+ from $Li_2Mn_2O_4$. The large positive tail is a result of electrolyte breakdown on the anode and charging effects.

Following the CV cycle the sample is again returned to open circuit and is left at open circuit while collected NR data. Figure 4.44 shows the current and potential of the NR cell as a function of time throughout the NR measurements. Comparing against figure 4.38 it is apparent that the final plateau of potential is very similar indicating the sample phase change was nearly complete before the first CV cycle. Additionally the observed current is very similar to that which was observed prior to the first CV cycle.

Figure 4.45 shows the collected reduced NR datasets taken in the regions indicated by the markers in figure 4.44. Further, figure 4.46 shows the normalized difference between the first NR dataset taken following one CV cycle and the last NR dataset taken before the CV cycle. Figure 4.46 shows the normalized difference between the second and first NR datasets taken following the first CV cycle. It is obvious from figure 4.46 that a significant change in the sample occurred through the one CV cycle. Those NR data which were collected following one CV cycle show little change between the collected data and are combined for further analysis.

Following these NR results further CV cycles show significantly reduced electrochemical reaction peaks and a large electrolyte breakdown current. It was decided to end the open circuit experiment and begin the experiment where the sample potential is held constant throughout the NR data collection period.

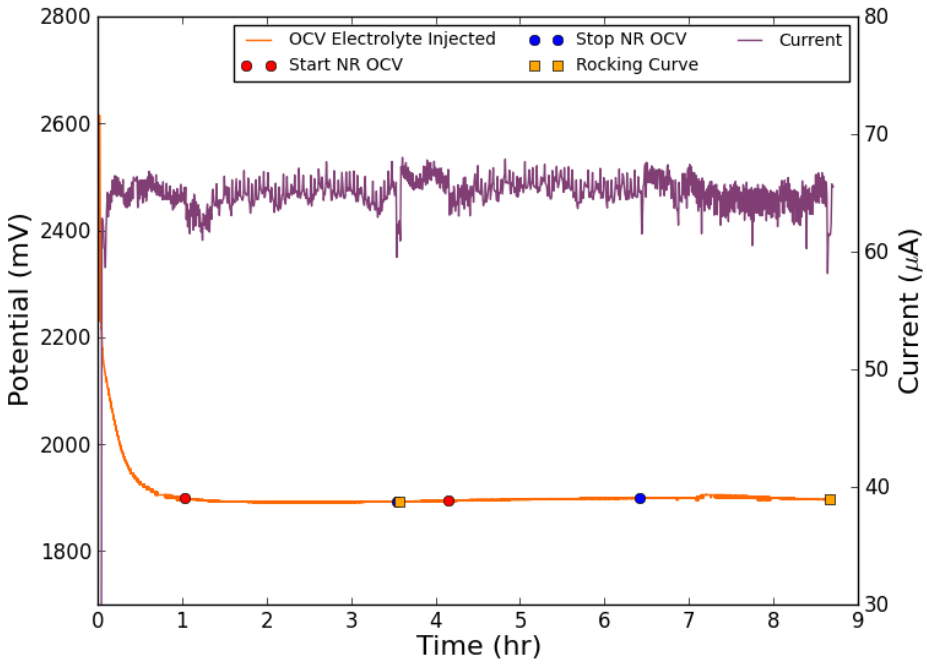

Figure 4.44: Current and potential as a function of time following one CV cycle, leaving the NR cell at an open circuit condition. Markers indicate start of NR measurement, stop of NR measurement for one dataset, and locations of rocking curves.

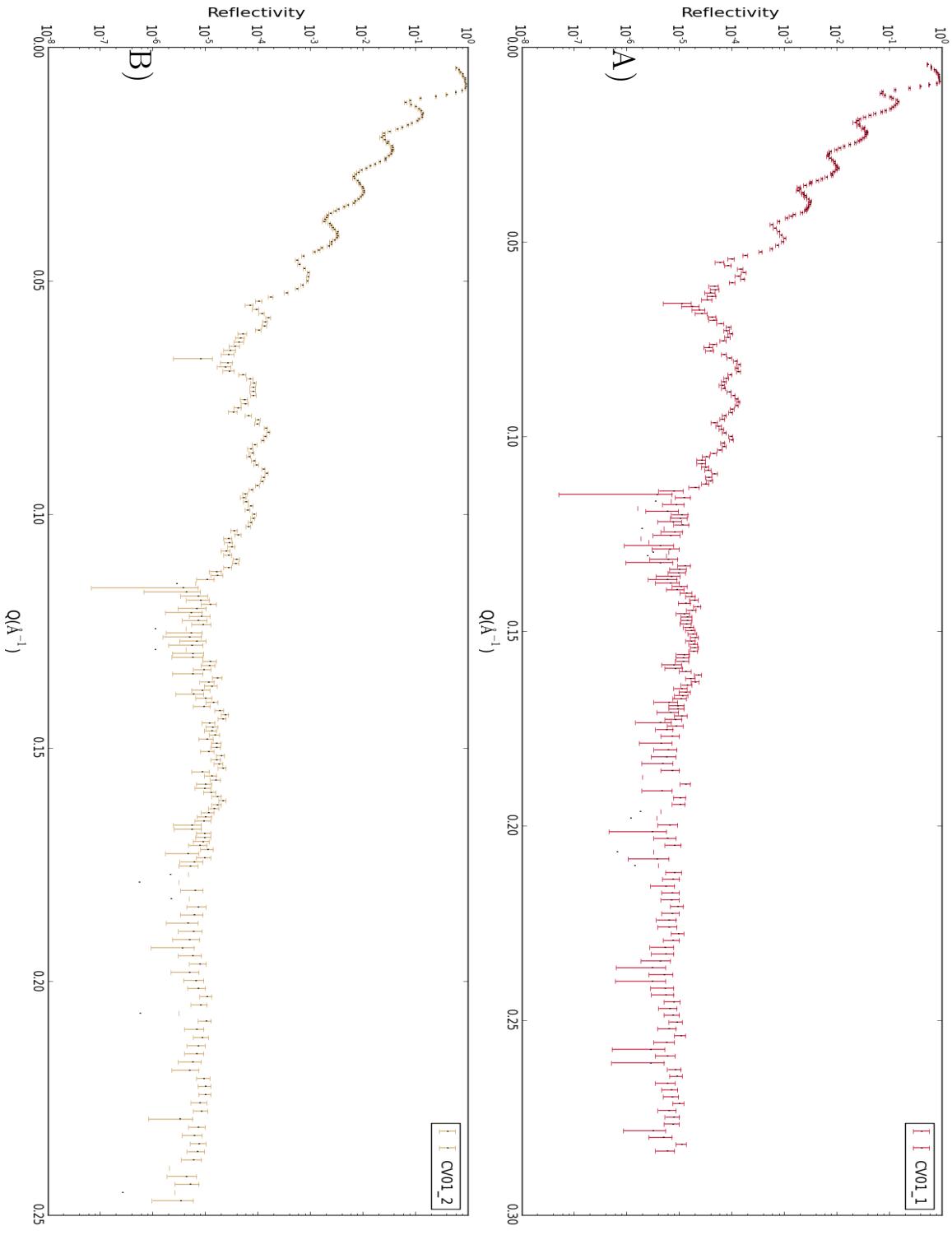

Figure 4.45: First and second reduced NR datasets at open circuit following one CV cycle at 5 mV/s. A)First dataset, B) Second Dataset

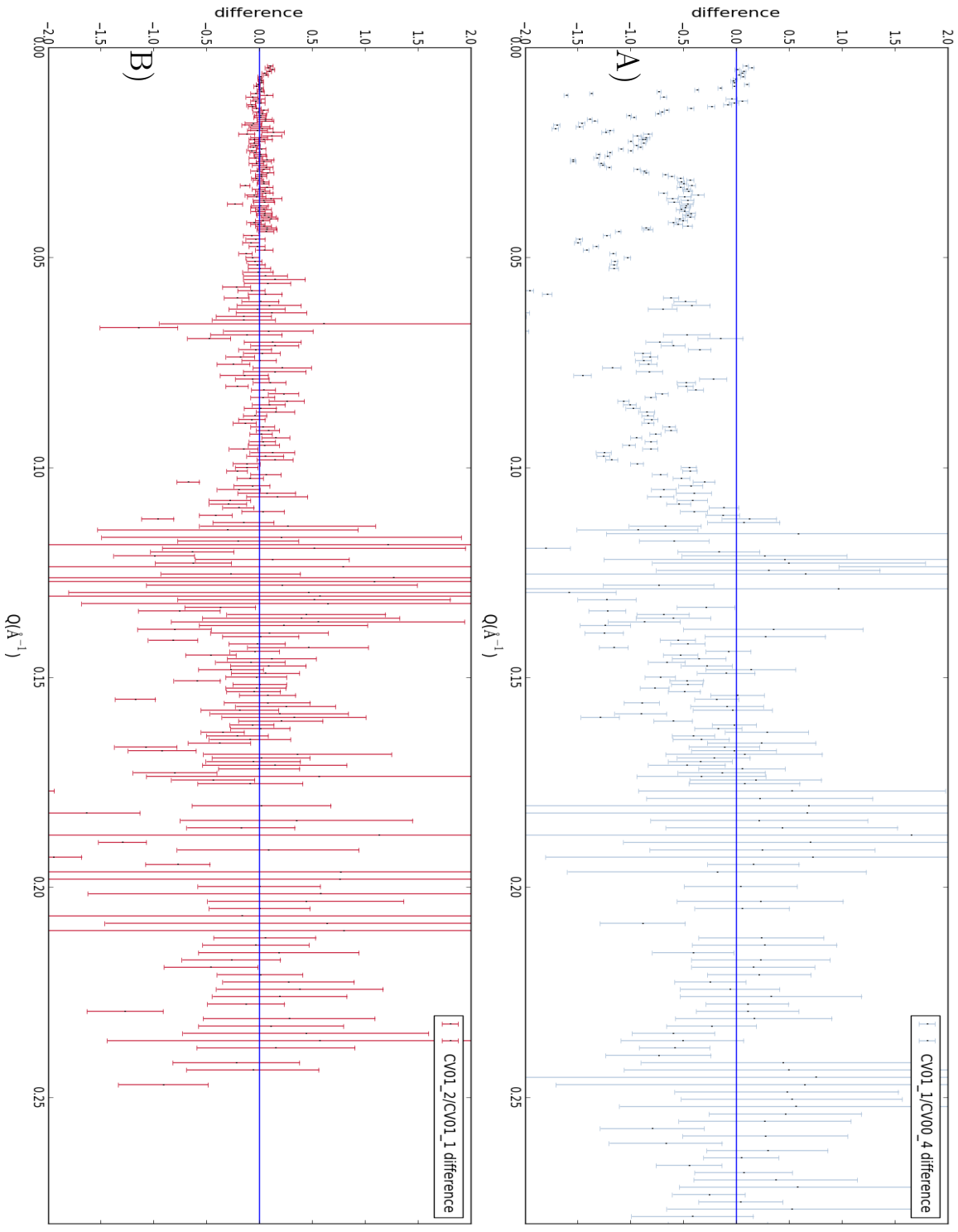

Figure 4.46: Normalized difference between first reduced NR dataset following 1 CV cycle and last NR dataset prior to electrochemical cycling and second/first NR datasets collected following 1 CV cycle while the sample was at open circuit. A) Normalized difference first NR dataset following 1 CV cycle and last NR dataset prior to electrochemical cycling. B) Normalized difference between first and second NR datasets following 1 CV cycle.

4.4.2 Potential hold NR experiment

4.4.2.1 Introduction of electrolyte

Upon injection of electrolyte the cell potential was held at 3300 mV to prevent excessive breakdown of the cathode layer. Figure 4.47 shows the recorded current as a function of time along with markers indicating where NR data and rocking curves were collected. There is a significant current while holding the potential at slightly above the open circuit potential for $LiMn_2O_4$ (3200 mV). Figures 4.48 and 4.49 show NR data throughout the first hold at 3300 mV prior to any electrochemical cycling. A total of four NR scans covering the same angular region from 0.1° to 6.48° were collected to ensure the final combined reduced dataset only contains datasets without any differences within uncertainty. Figures 4.50 and 4.51 show the normalized difference of the datasets as determined from equation 3.9.

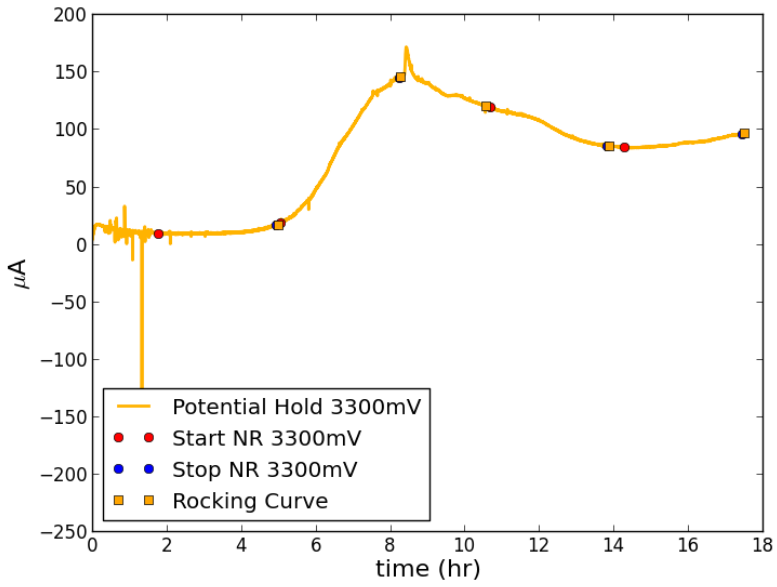

Figure 4.47: Current as a function of time while holding potential at 3300 mV for the potential hold sample following introduction of electrolyte. Markers indicate start and stop of NR data collection throughout the Q-range along with markers associated with location of rocking curves.

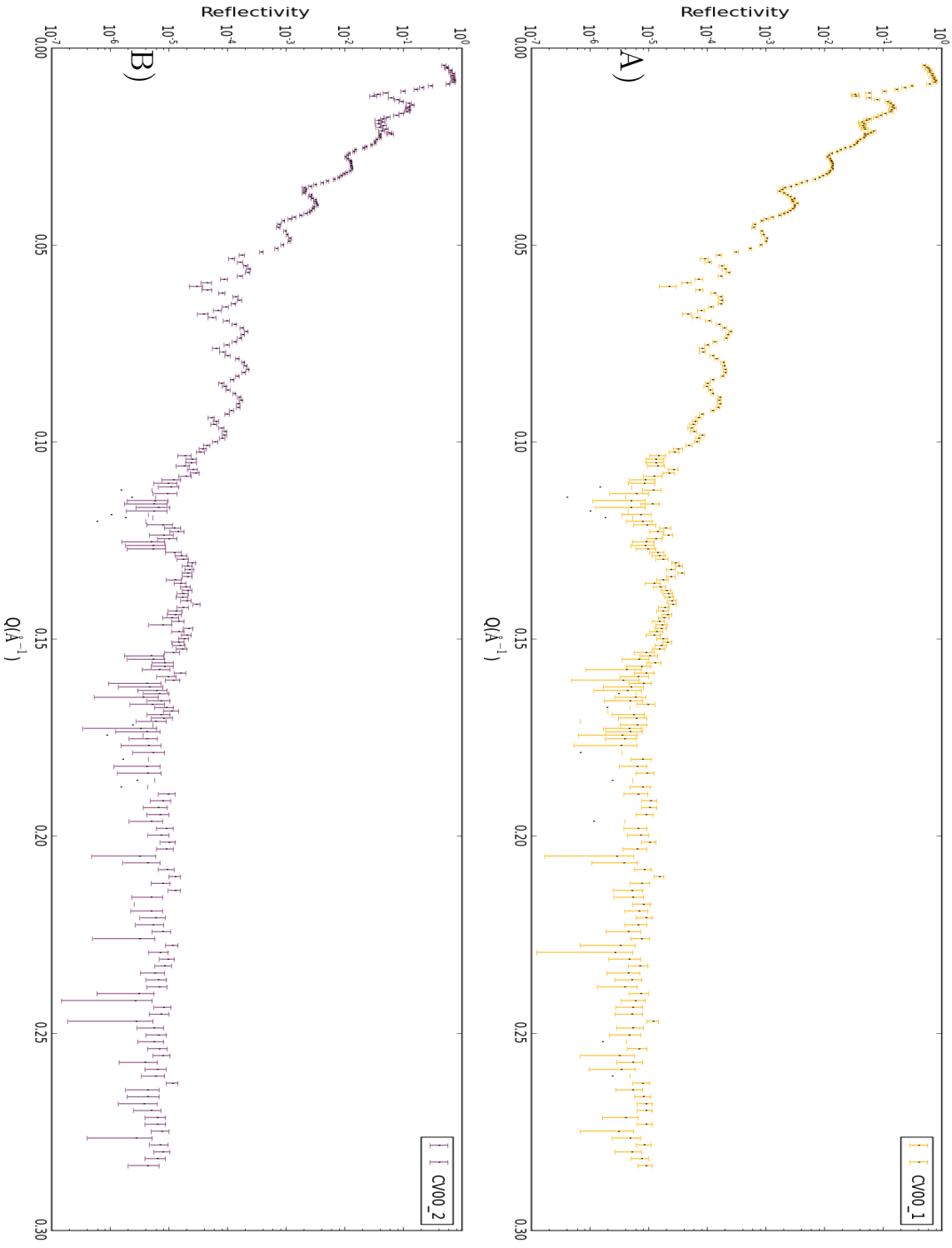

Figure 4.48: NR results for the potential hold sample following electrolyte injection at 3300 mV prior to any electrochemical cycling. A)First dataset, B) Second Dataset

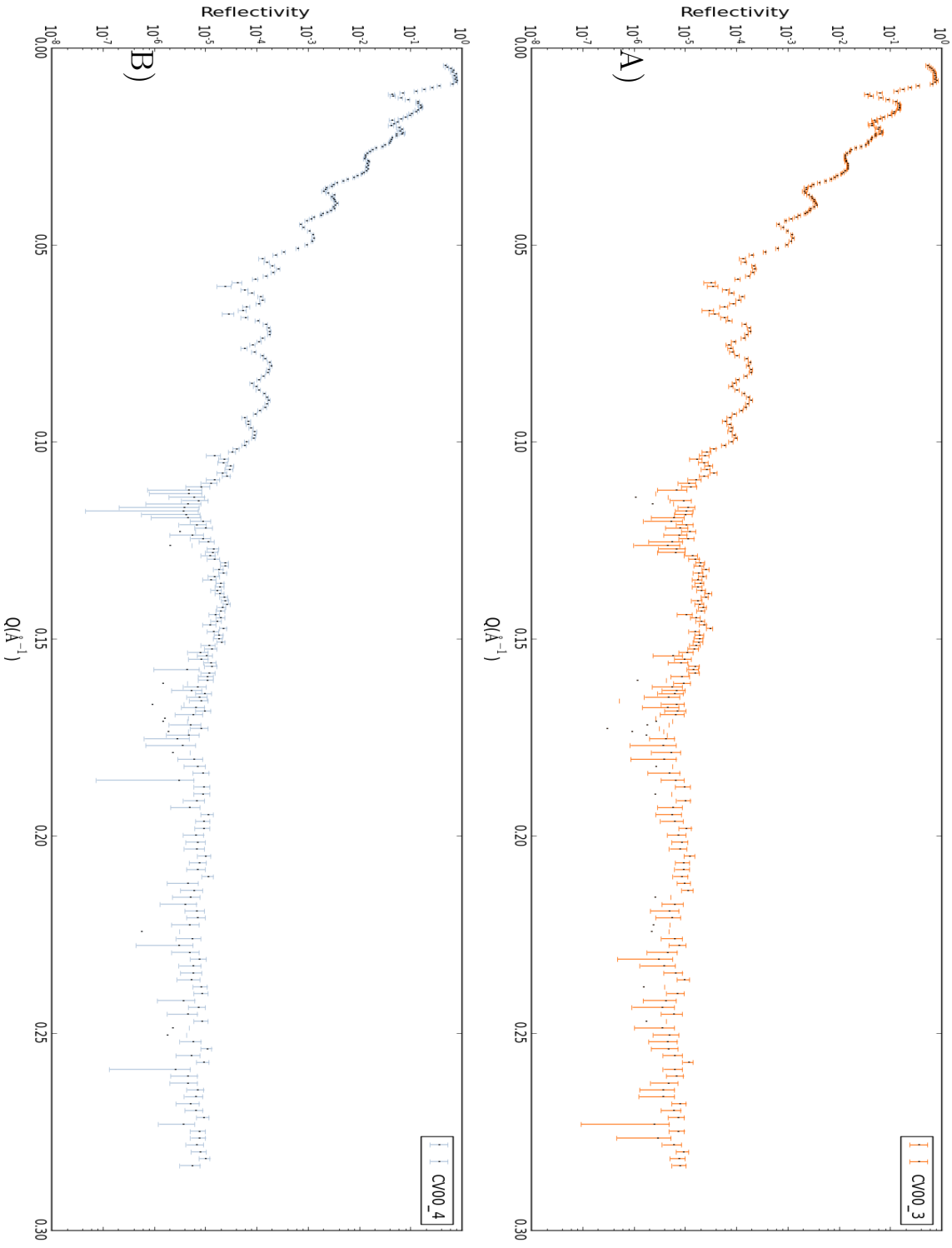

Figure 4.49: NR results for the potential hold sample following electrolyte injection at 3300 mV prior to any electrochemical cycling. A)Third dataset, B) Fourth Dataset

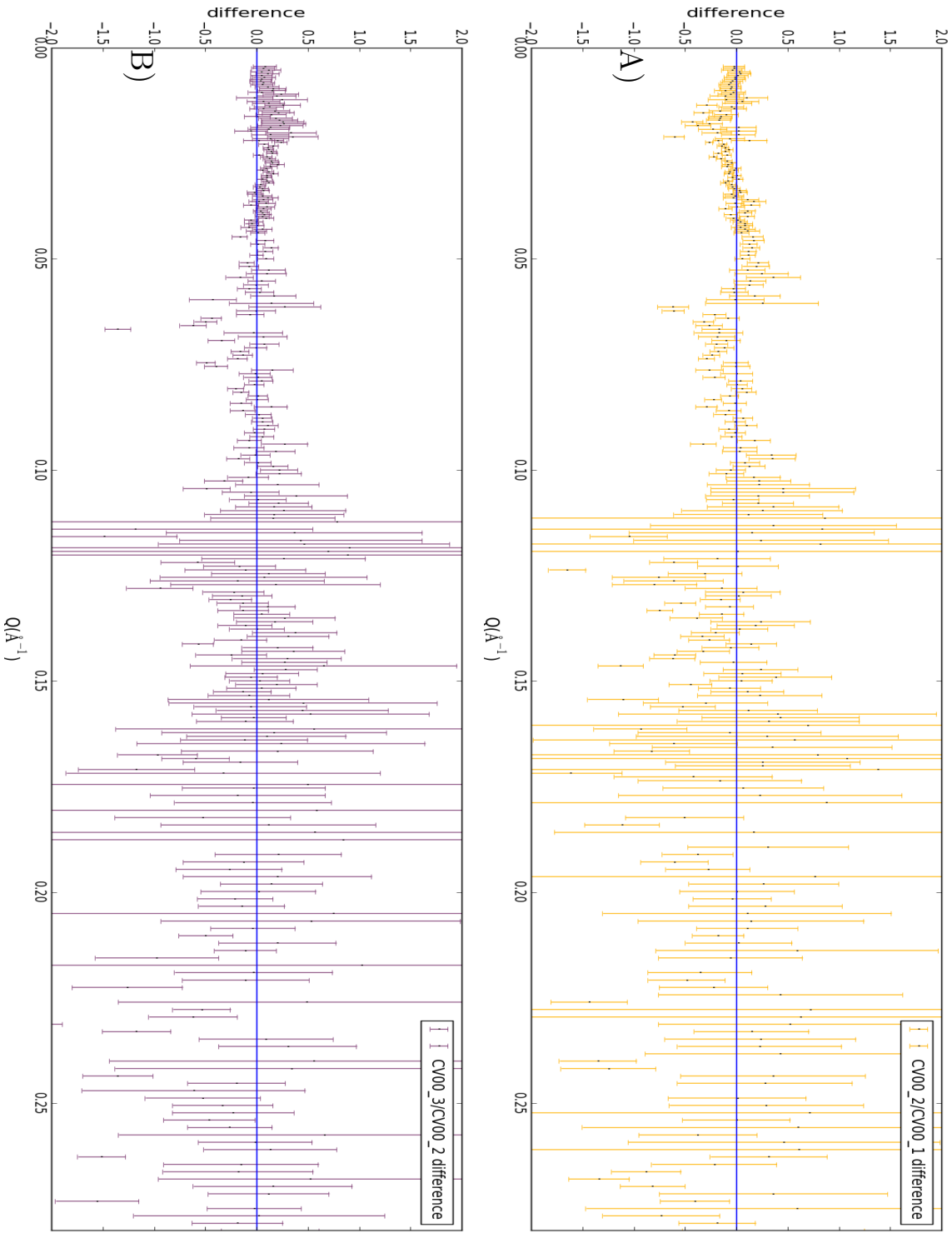

Figure 4.50: Normalized difference between first/second and third/second NR datasets collected while holding the cell voltage at 3300 mV prior to any electrochemical cycling. A) Normalized difference between first and second NR. B) Normalized difference between first and second NR datasets.

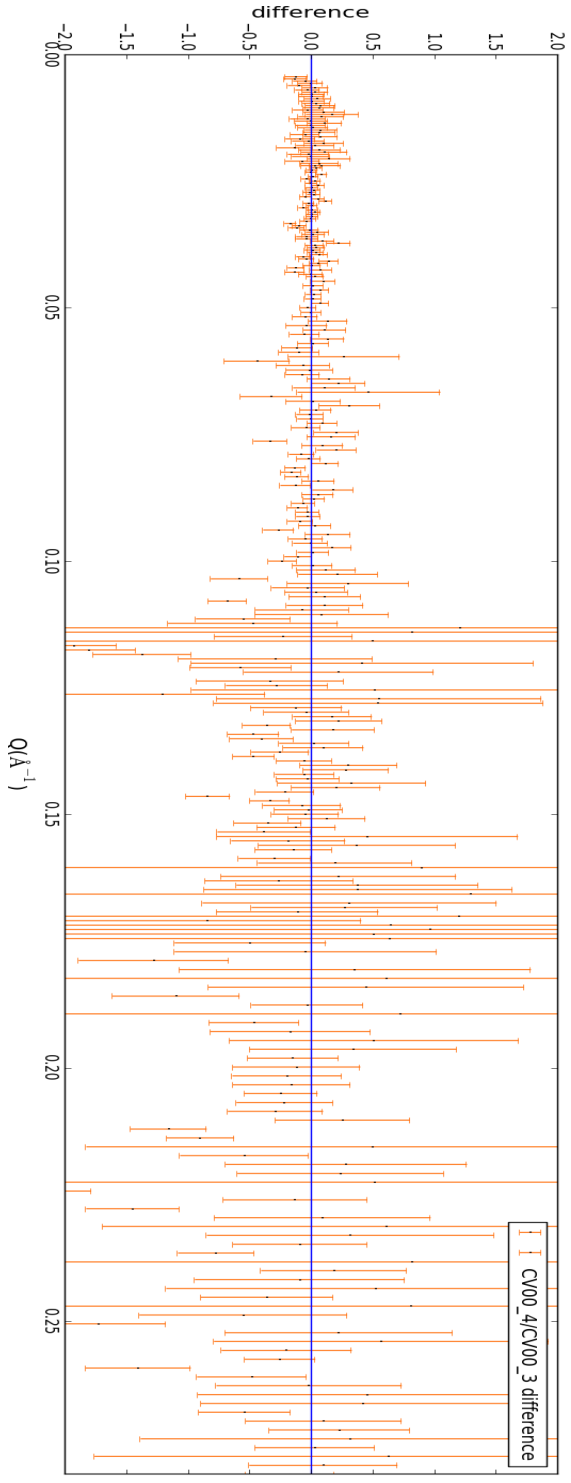

Figure 4.51: Normalized difference between fourth and third NR datasets collected while holding the cell voltage at 3300 mV prior to any electrochemical cycling

4.4.2.2 Following 3 CV cycles

After holding potential for almost 18 hours the cell was cycled three times between 3300 mV and 4500 mV. Figure 4.52 shows the CV curves which exhibit some characteristic response of $LiMn_2O_4$. The large positive tail in the CV curve is due to both charging and electrolyte breakdown which decreases as the cycles continue. The intercalation/de-intercalation peaks shown in figure 4.52 highlight a polarization effect where the onset potential is skewed by the existence of an interfacial layer which is known to exist on both electrodes and can impact the electrochemical response.

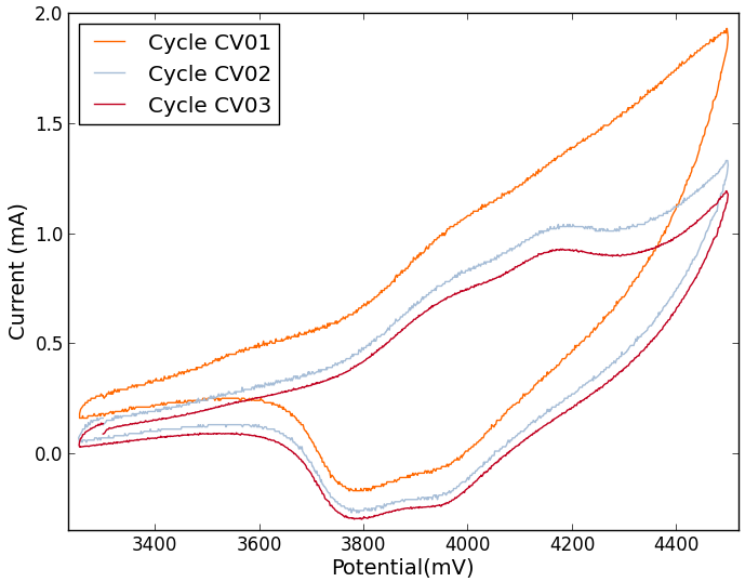

Figure 4.52: CV curves acquired at 5 mV/s from 3300 mV to 4500 mV. CV curves show characteristic $LiMn_2O_4$ response. Large positive tail is a result of electrolyte breakdown and charging effects. Peaks are shifted from the expected onset potential which is a result of large polarization due to interfacial resistance on the anode or cathode or both.

Following the three CV cycles the sample is again held at 3300 mV throughout NR data collection. Figure 4.53 shows the current response from the cell while being held at 3300 mV. There is an initial stabilization followed by significant current increase and indications of some shorting or lack of contact between the electrodes. Markers

on figure 4.53 show where NR data collection started and stopped. Figure 4.54 shows the reduced NR datasets collected following 3 CV cycles while holding potential at 3300 mV. Figure 4.55 shows the normalized difference calculated from equation 3.9 between the first reduced NR dataset following 3 CV cycles and the last NR dataset prior to electrochemical cycling. Figure 4.55 also shows the normalized difference between the second and first NR datasets following 3 CV cycles.

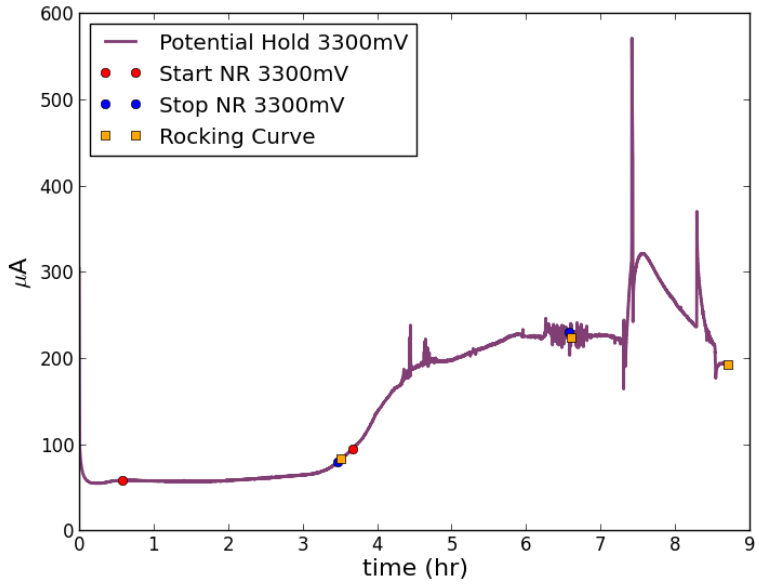

Figure 4.53: Current as a function of time while holding potential at 3300 mV for the potential hold sample following three CV cycles at 5 mV/s. Markers indicate where NR data collection starts, stops, and when rocking curves for alignment occur. Current spikes indicate poor state of health in the cell indicating shorting or poor connection between the electrodes.

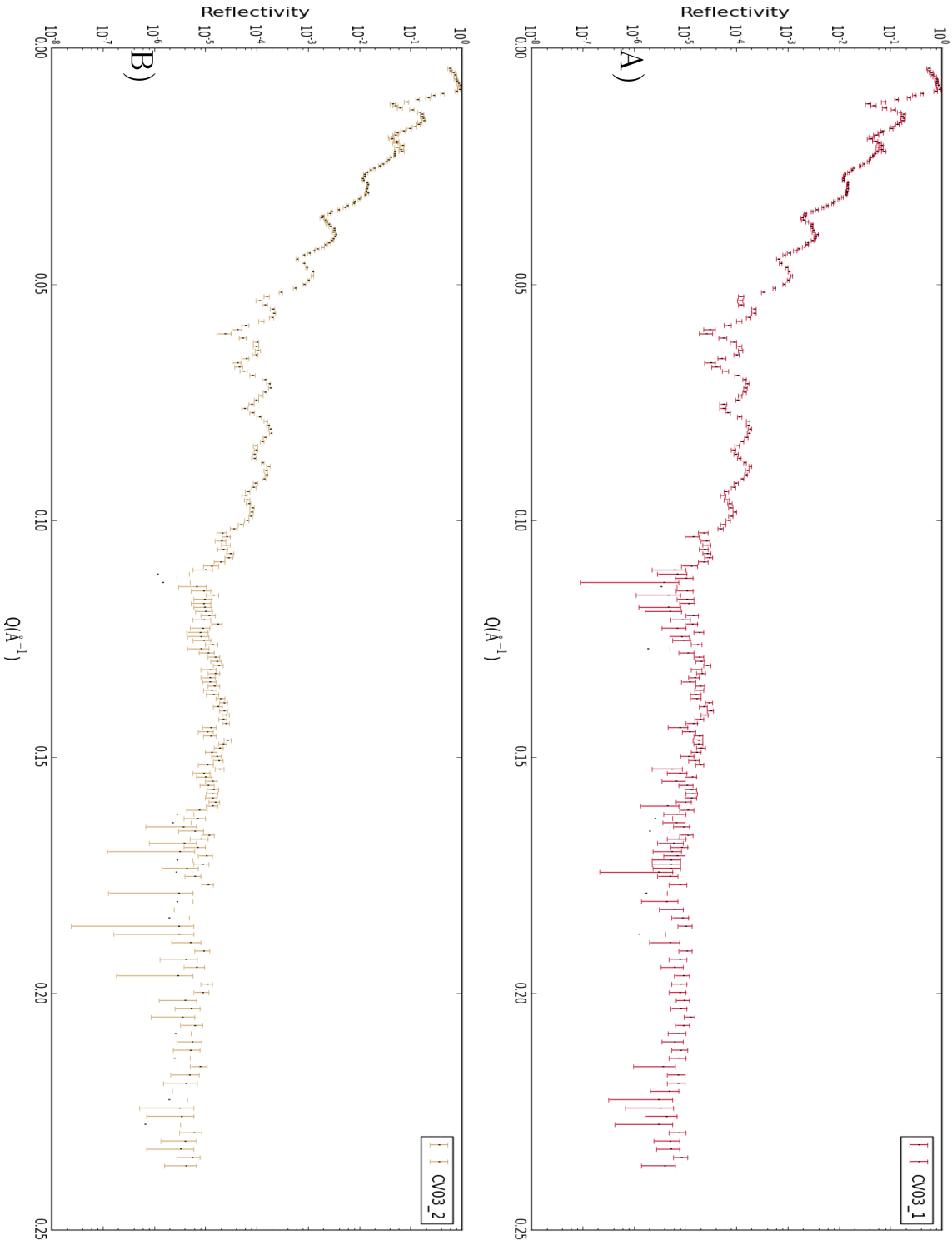

Figure 4.54: NR results for the potential hold sample following three CV cycles at 5 mV/s. A)First dataset, B) Second Dataset

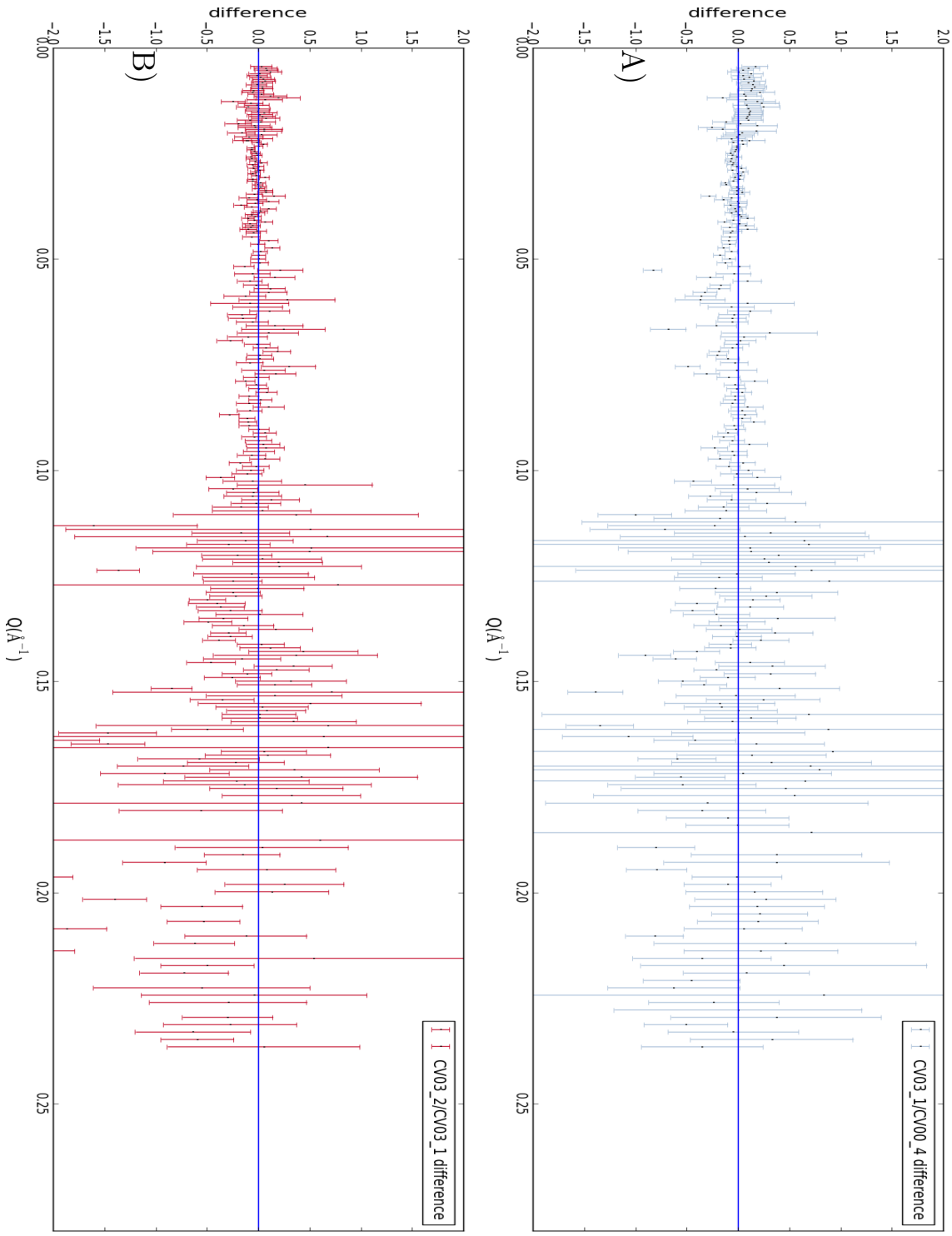

Figure 4.55: Normalized difference between first reduced NR dataset following 3 CV cycles and last NR dataset prior to electrochemical cycling and second/first NR datasets collected following 3 CV cycles while holding the cell voltage at 3300 mV. A) Normalized difference first NR dataset following 3 CV cycles and last NR dataset prior to electrochemical cycling B) Normalized difference between first and second NR datasets following 3 CV cycles.

4.4.2.3 Following 13 CV cycles

Following a nine hour potential hold at 3300 mV the cell is cycled 10 times. The first seven cycles were through a voltage window between 3300 mV and 4500 mV. The next cycle was between 3300 mV and 4700 mV to examine whether an increase in voltage would show a potential onset. As it was observed that the peak when discharging shifted to lower voltages it would be expected that the polarization would also affect the charging peak. Significant transient behavior in the eighth cycle provided motivation to reduce the upper voltage window. On the ninth cycle between 3300 mV and 4600 mV it appeared that the charging current had reached a maximum and might turn to a lower current right around the 4600 mV switch in voltage ramp. The observation provided impetus to increase the voltage window again to the range between 3300 mV and 4700 mV for the tenth cycle. The performance shown in these CV curves is worse than the first three cycles. Figure 4.56 shows those CV curves. The first CV highlighted at CV 4 in figure 4.56 shows significant noise and likely exhibits some shorting and open circuit effects. Those CV curves show a peak on the cathode side which shifts to lower potential as the cell is cycled. This peak shows similar behavior to the first three CV cycles.

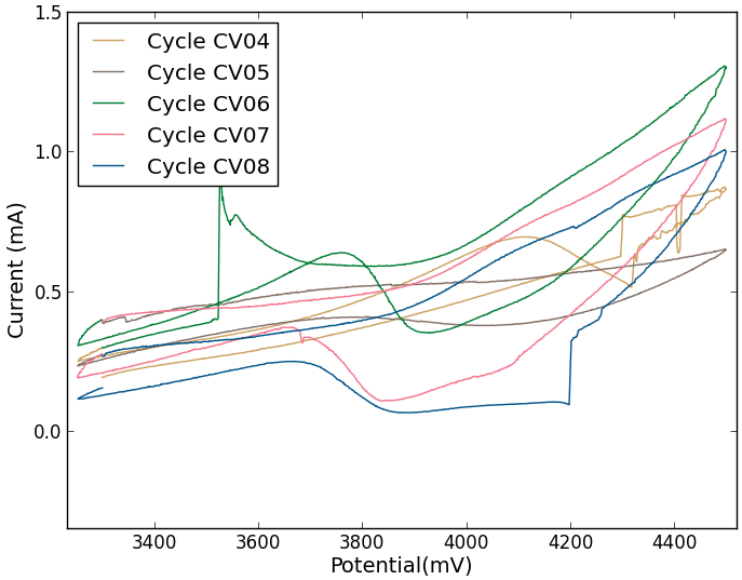

(a) CV cycles 04-08

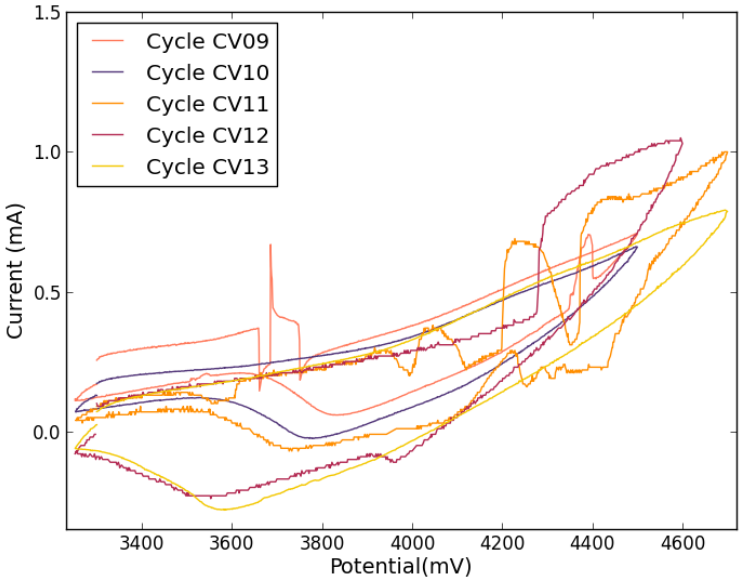

(b) CV cycles 09-13

Figure 4.56: CV data from cycle 4 through 13 for potential hold sample between 3300 mV and 4500 mV, 4600 mV, and 4700 mV. A) CV cycles between cycle 4 and cycle 8. Cycle 4 shows significant issues with cell performance. B) CV cycles between cycle 9 and cycle 14. Cycle 11 is not shown because it exhibited signs of a disconnected lead to the cell.

The cell was once again held at a potential of 3300 mV following the completion of

CV14. Figure 4.57 shows measured current vs time along with markers indicating the start and stop of NR data collection and when rocking curves were collected. Those current data show some short circuiting or loss of contact to the cell. The measured current is generally much lower than that of the previous potential hold steps. The trend is similar to that previously where a semi-plateau is followed by an increase in current.

Figure 4.58 shows the reduced collected NR data for two datasets collected at 3300 mV following 14 CV cycles. The normalized difference between the second NR dataset following three CV cycles and the first NR dataset following 14 CV cycles are shown in figure 4.59. Figure 4.59 also shows the normalized difference between the second and first NR datasets following 14 CV cycles.

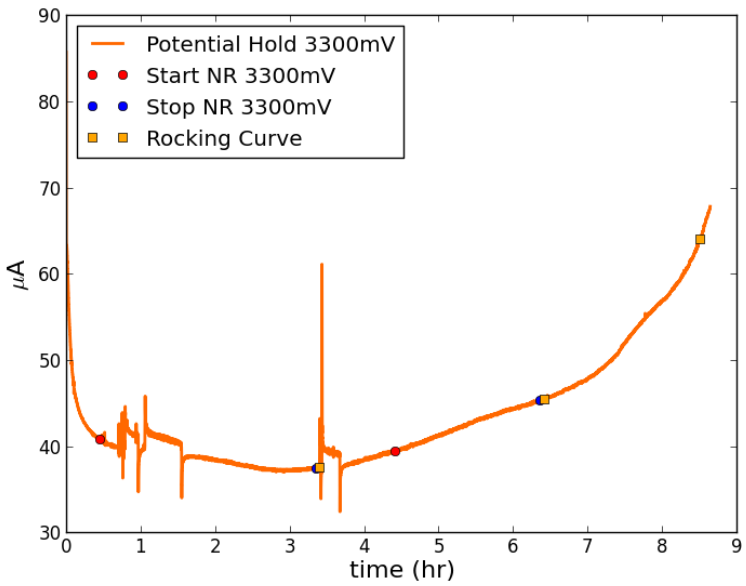

Figure 4.57: Current as a function of time while holding potential at 3300 mV for the potential hold sample following 14 CV cycles. Markers indicate start and stop of NR data collection throughout the Q-range along with markers associated with location of rocking curves.

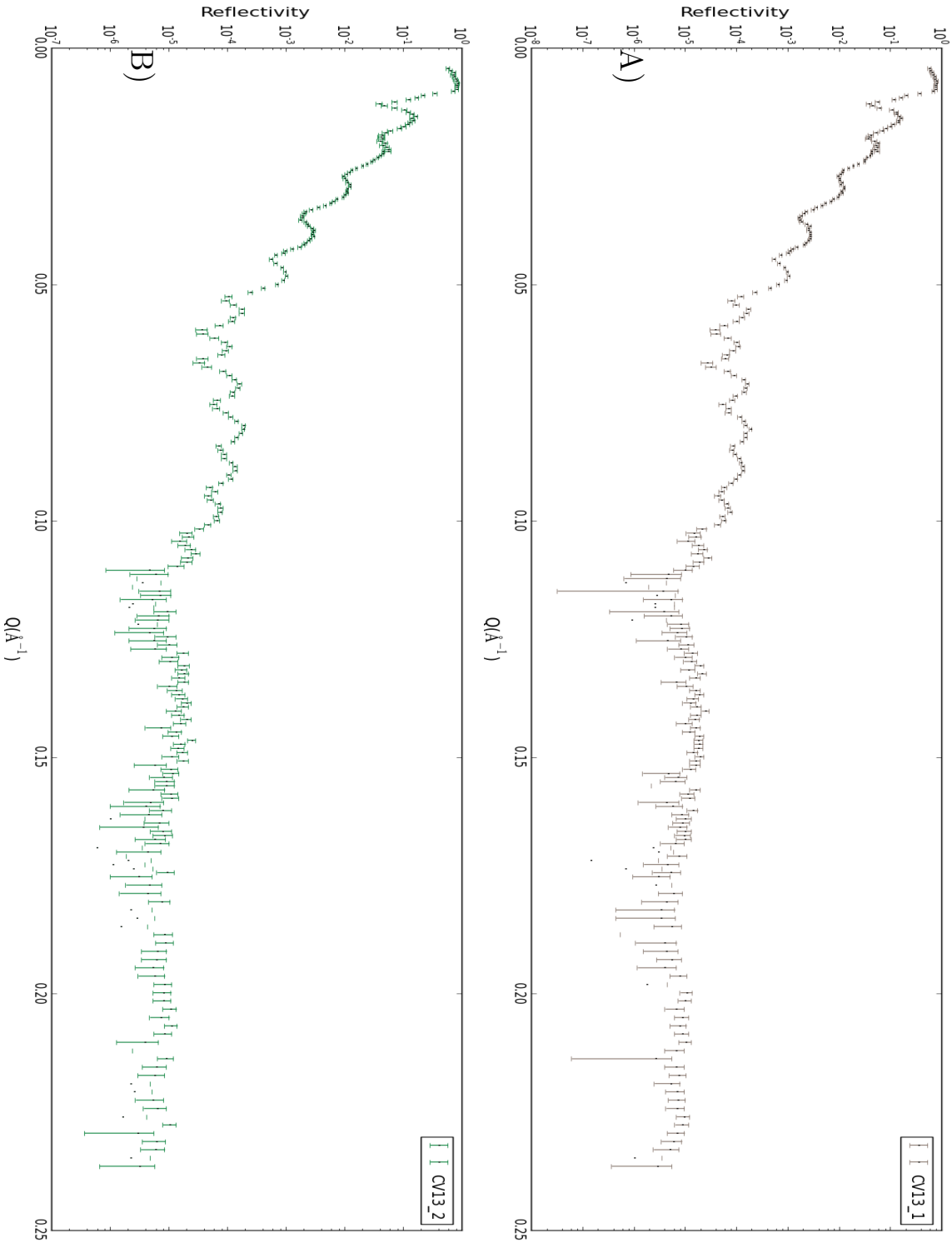

Figure 4.58: NR results for the potential hold sample following 14 CV cycles at 5 mV/s. A)First dataset, B) Second Dataset

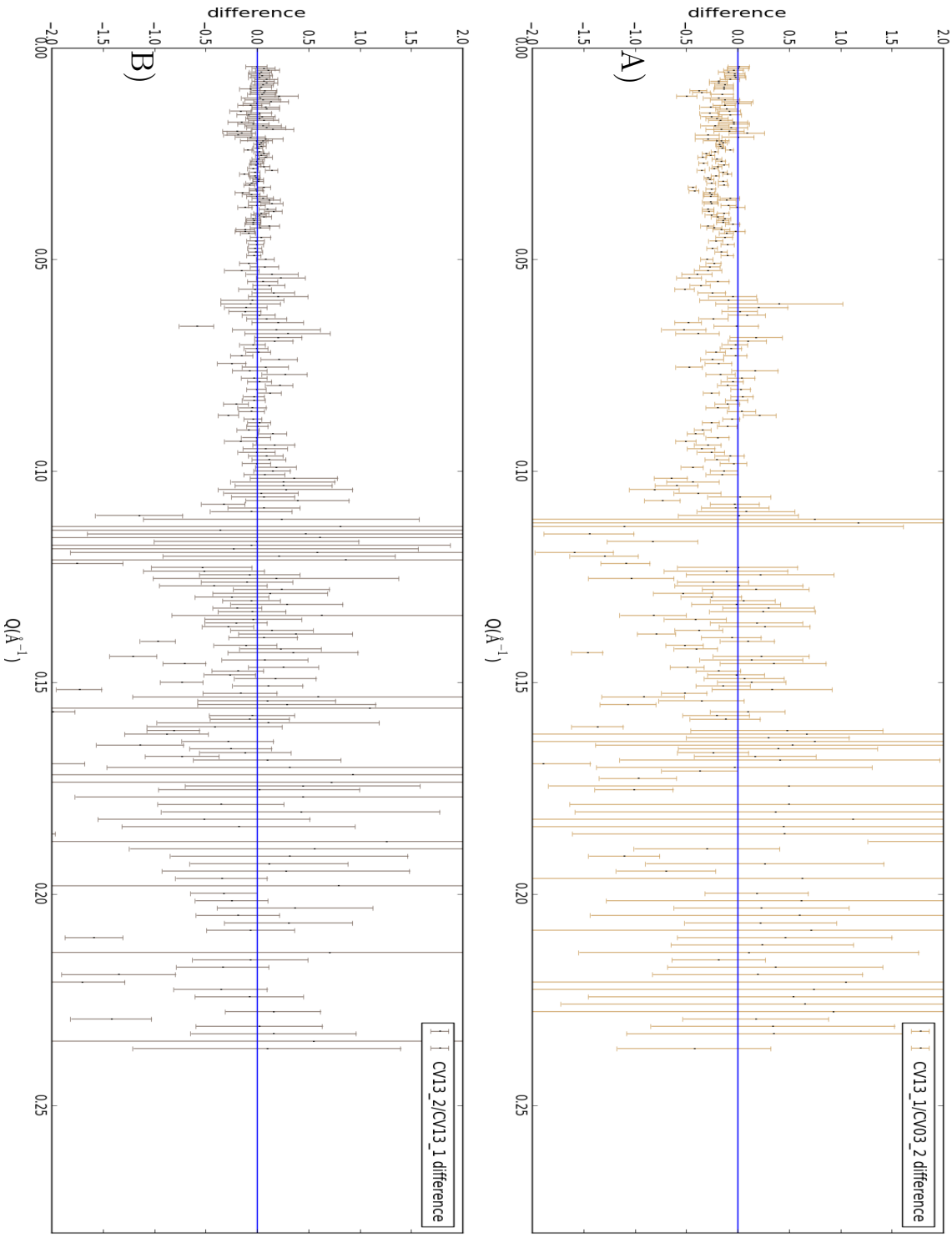

Figure 4.59: Normalized difference between first reduced NR dataset following 14 CV cycles and last NR dataset following 3 CV cycles, and second/first NR datasets collected following 14 CV cycles while holding the cell voltage at 3300 mV. A) Normalized difference first NR dataset following 14 CV cycles and last NR dataset following 3 CV cycles. B) Normalized difference between first and second NR datasets following 14 CV cycles.

4.4.2.4 Following 18 CV cycles

Following a eight and a half hour potential hold at 3300 mV the cell is cycled 4 times between 3300 mV and 4700 mV. Following the fourth cycle the voltage is ramped to 4700 mV and subsequently stopped at 4000 mV while discharging. The performance shown in these CV curves is improved from the previous ten cycles. Figure 4.60 shows those CV curves along with the voltage ramp to 4700 mV prior to holding at 4000 mV. These CV curves are well behaved compared to the previous 10 CV, and the large peak when discharging is observed and shifts to lower potential with cycling.

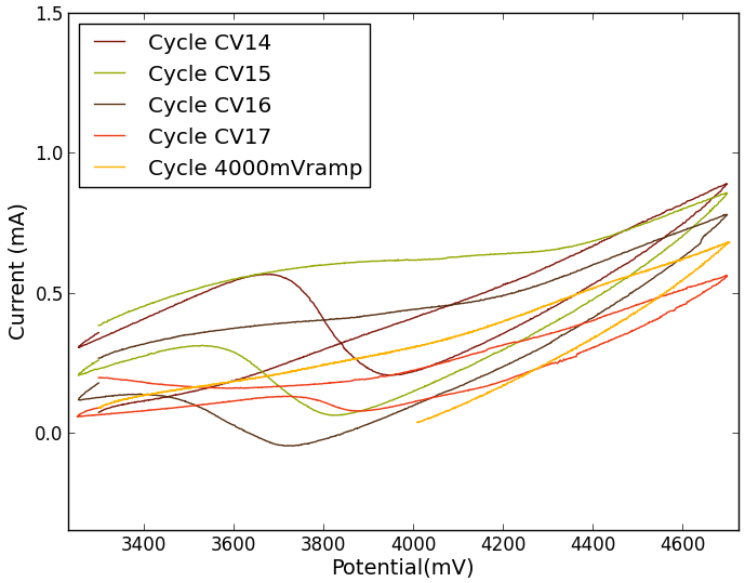

Figure 4.60: CV cycles 15 through 18 including a ramp to 4700 mV followed by a potential hold at 4000 mV following an eight and a half hour potential hold at 3300 mV.

Following the final ramp to 4700 mV the cell was held at a potential of 4000 mV to produce a partially delithiated cathode. Figure 4.61 shows measured current vs time along with markers indicating the start and stop of NR data collection and when rocking curves were collected. Those current data show generally decreasing current

hitting a plateau around 4 hours followed by an increase between hours 5 and 6 then decaying away again.

Figure 4.62 shows the reduced collected NR data for two datasets collected at 4000 mV following 17 CV cycles. The normalized difference between the second NR dataset following 14 CV cycles and the first NR dataset following 17 CV cycles are shown in figure 4.63. Figure 4.63 also shows the normalized difference between the second and first NR datasets following 17 CV cycles.

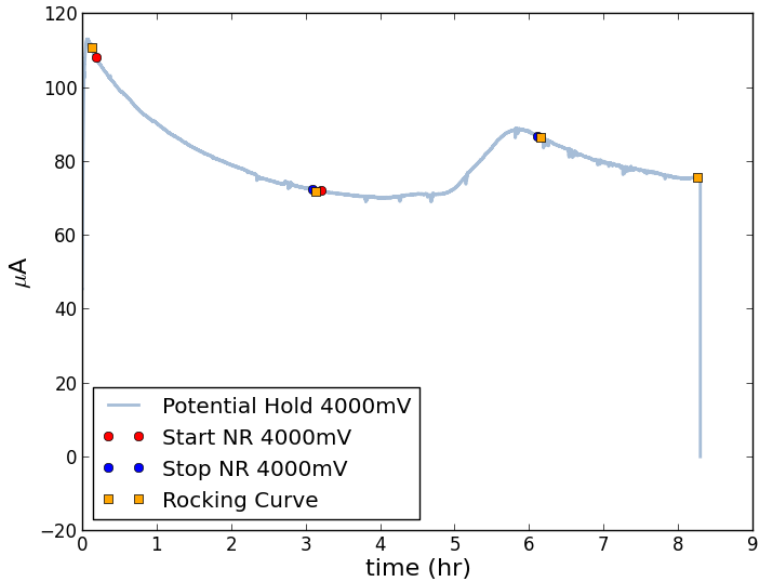

Figure 4.61: Current as a function of time while holding potential at 4000 mV for following 18 CV cycles. Markers indicate start and stop of NR data collection throughout the Q-range along with markers associated with location of rocking curves.

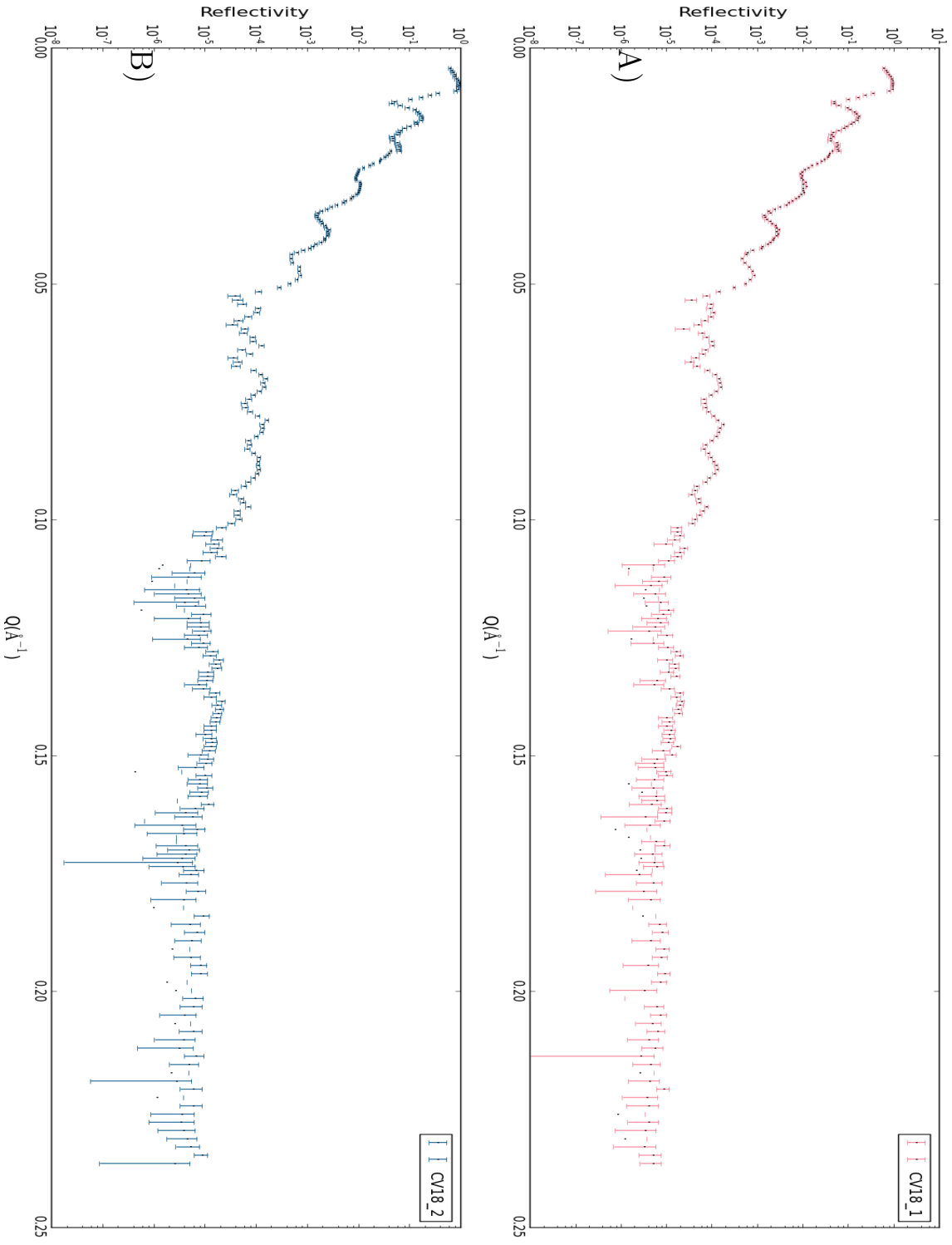

Figure 4.62: NR results for the potential hold sample held at 4000 mV following 17 CV cycles at 5 mV/s. A)First dataset, B) Second Dataset

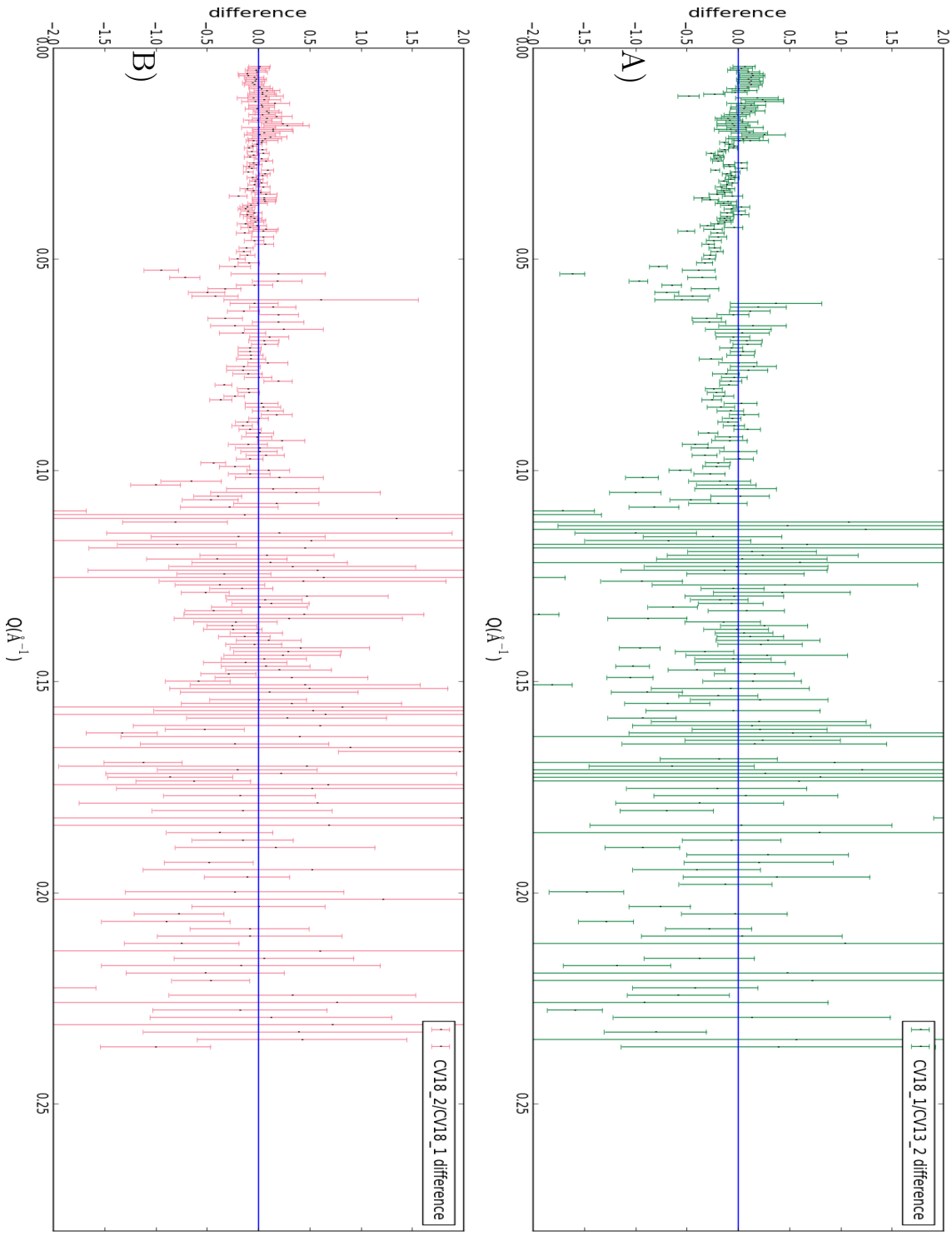

Figure 4.63: Normalized difference between first reduced NR dataset following 18 CV cycles and last NR dataset following 14 CV cycles, and second/first NR datasets collected following 17 CV cycles while holding the cell voltage at 4000 mV. A) Normalized difference first NR dataset following 17 CV cycles and last NR dataset following 14 CV cycles. B) Normalized difference between first and second NR datasets following 18 CV cycles.

4.4.2.5 Following 22 CV cycles

Following a eight an hour potential hold at 4000 mV the cell is cycled 4 times between 3300 mV and 4700 mV. Following the fourth cycle the voltage is ramped to 4700 mV and stopped at 4300 mV on the discharging step. Holding potential at 4300 mV is to study the cathode when lithium de-intercalation is maximized. Figure 4.64 shows those CV curves along with the voltage ramp to 4300 mV. These CV curves are well behaved and show a further decrease in the peak potential.

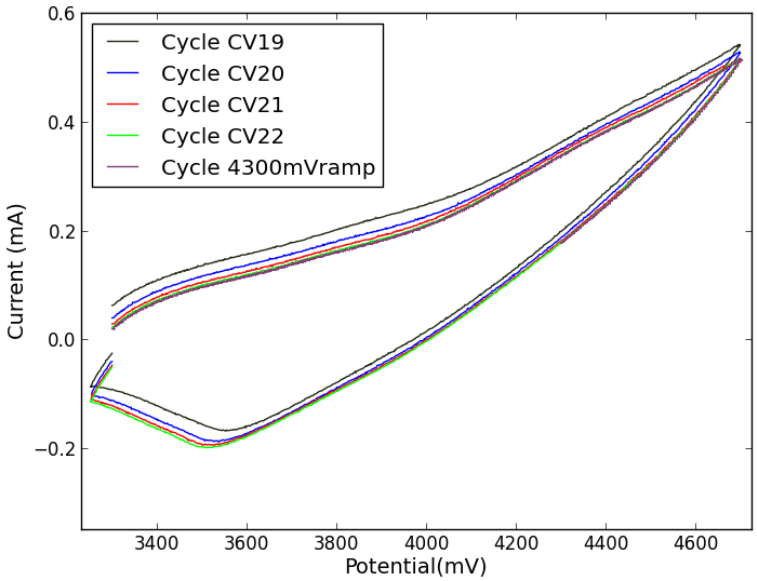

Figure 4.64: CV cycles 19 through 22 including a ramp to 4700 mV followed by a potential hold at 4300 mV following an eight and a half hour potential hold at 4000 mV.

Following the final ramp to 4700 mV the cell was held at a potential of 4300 mV to remove as much lithium from the cathode as is possible electrochemically. Figure 4.65 shows measured current vs time along with markers indicating the start and stop of NR data collection and when rocking curves were collected. Those current data show generally decreasing current throughout the potential hold step with some indications of shorting occurring between hours 7 and 8.

Figure 4.66 shows the reduced collected NR data for two datasets collected at 4300 mV following 22 CV cycles. The normalized difference between the second NR dataset following 17 CV cycles and the first NR dataset following 22 CV cycles are shown in figure 4.67. Figure 4.67 also shows the normalized difference between the second and first NR datasets following 22 CV cycles.

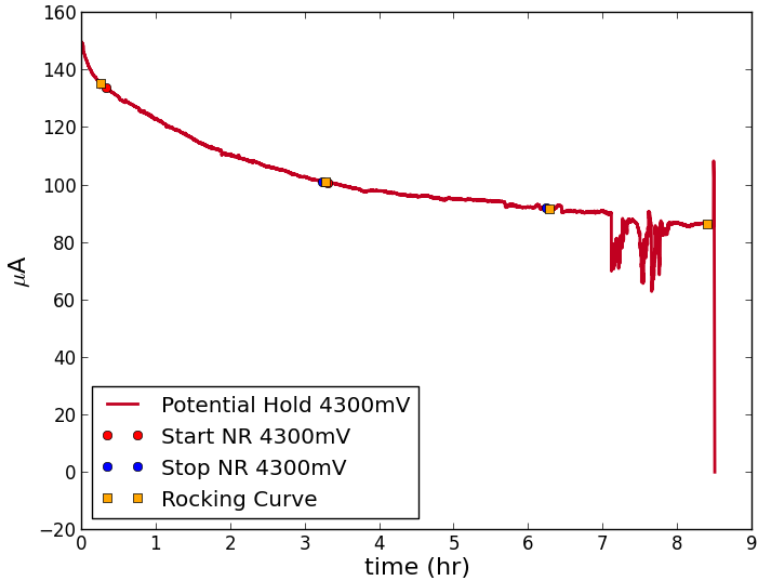

Figure 4.65: Current as a function of time while holding potential at 4300 mV for following 22 CV cycles. Markers indicate start and stop of NR data collection throughout the Q-range along with markers associated with location of rocking curves.

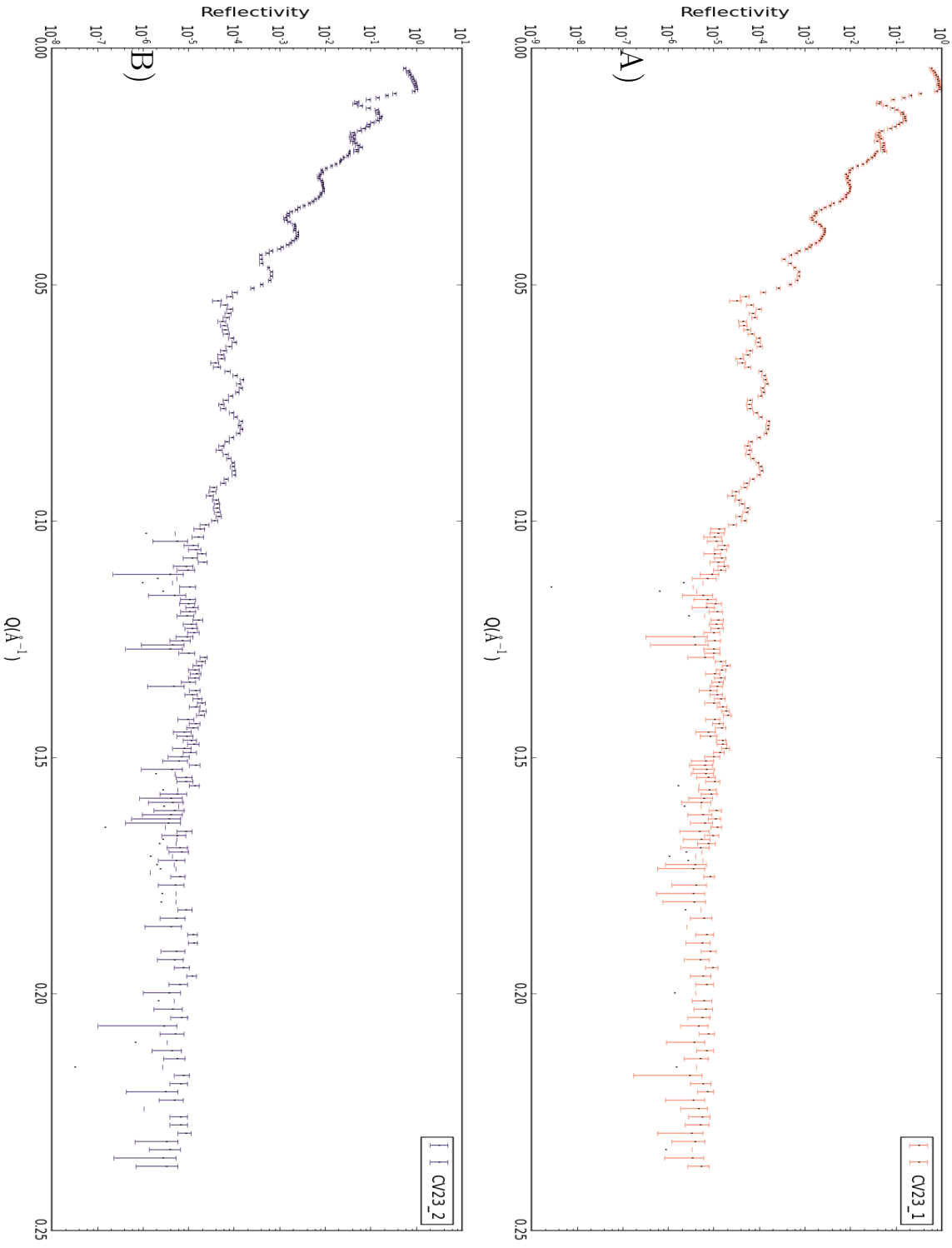

Figure 4.66: NR results for the potential hold sample following 22 CV cycles at 5 mV/s. A)First dataset, B) Second Dataset

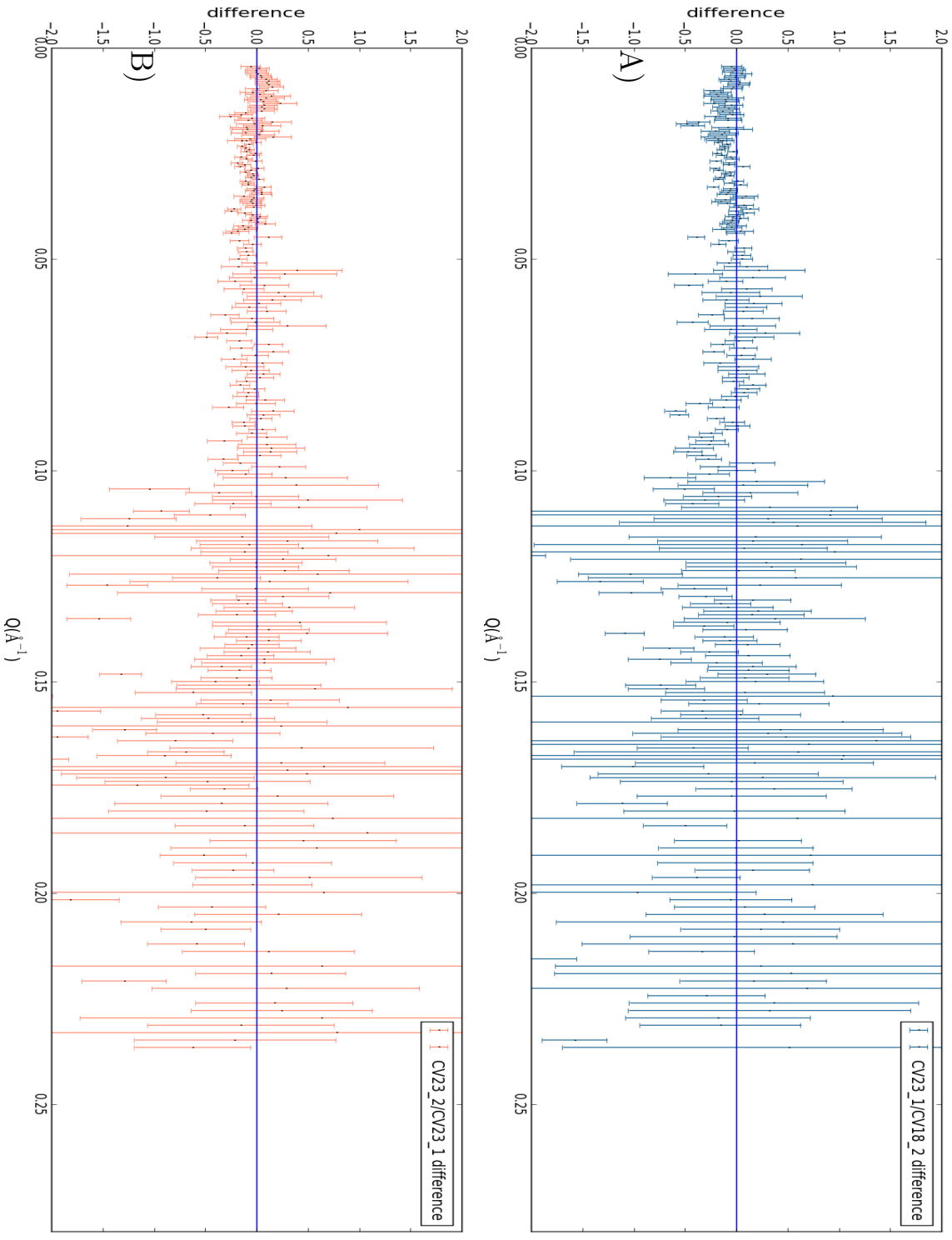

Figure 4.67: Normalized difference between first reduced NR dataset following 22 CV cycles and last NR dataset following 17 CV cycles, and second/first NR datasets collected following 22 CV cycles while holding the cell voltage at 4300 mV. A) Normalized difference first NR dataset following 22 CV cycles and last NR dataset following 17 CV cycles. B) Normalized difference between first and second NR datasets following 22 CV cycles.

4.5 Post-NR characterization

The NR samples sat following those NR work for approximately four months prior to any post-NR characterization. The sample cells were opened in a fume hood and rinsed in DMC several times to remove residual EC and $LiClO_4$ from the electrolyte solution. It was noted for both samples that there was some substantial delamination of the surface film. The sample was allowed to dry from the DMC wash. Three techniques are applied for post-NR analysis. XRR and XPS are applied to both NR samples, and SEM with Energy Dispersive x-ray Spectroscopy (EDX) is applied to the potential hold sample. A region of the sample which showed little delamination was used for XRR measurements on the cleaned-dried potential hold sample. Figure 4.68 shows images of both NR samples after rinsing in DMC.

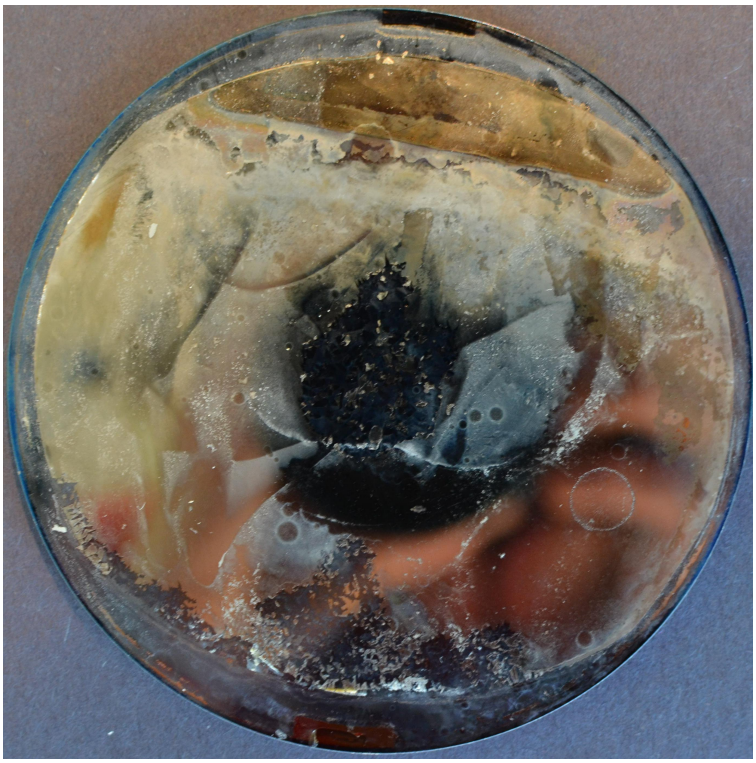

(a) OCP NR sample

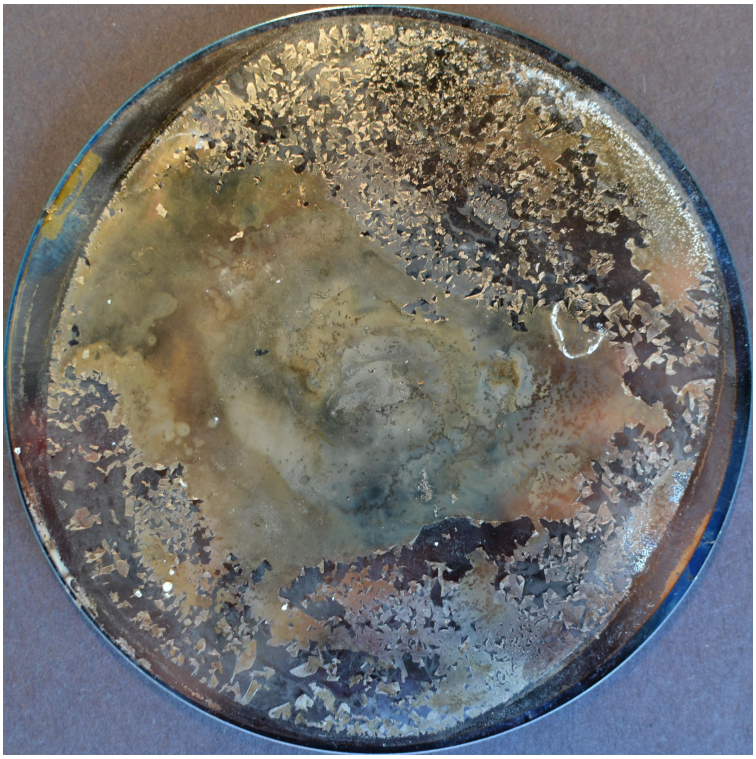

(b) Potential hold NR sample

Figure 4.68: Optical images of NR samples after the cells were dismantled and the wafers rinsed in DMC several times to remove EC and $LiClO_4$. a) Open circuit NR sample. The image shows a reflection of the individual taking the picture as the surface is very reflective. The discolored region at the top of the sample image is due to an air bubble forming in the top of the sample cell. b) Potential hold NR sample.

In order to perform SEM and XPS on these NR samples the sample thickness must be reduced. Both the XPS and SEM instruments are limited to a maximum sample thickness of 2 mm. An additional requirement for XPS is that the sample does not have a footprint greater than 2 cm x 2 cm. The sample wafers used for NR were 5 mm thick and were milled using a diamond coated 4 flute mill bit on a CNC-mill to remove 3 mm of material on the backside of the wafer in 0.005" increments. The milling process also allows the sample footprint to be selected. Figure 4.69 shows both the backside of the wafer when the sample is thinned to 2 mm prior to milling the footprint as well as a fully milled sample. It should be noted that the milling process produces significant silicon dust which is not combated throughout the process. Following milling the sample is rinsed in DMC to remove most of the silicon dust. It is possible and likely that nanoscale silicon particles are remaining on the surface. It is expected that any surface characterization performed following the milling will show silicon as a result of the milling process and dust production.

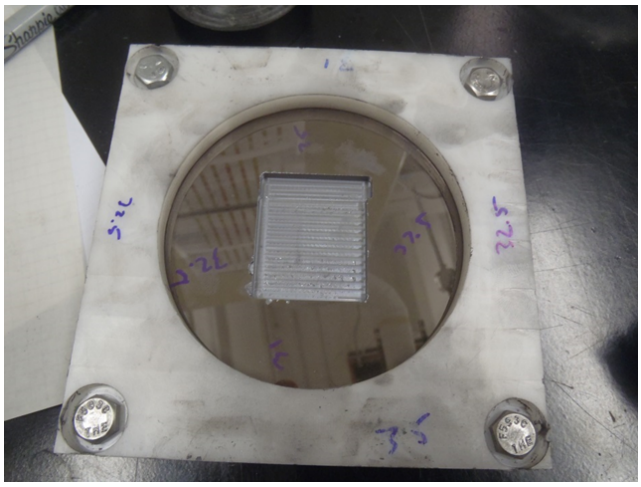

(a) Backside thinning

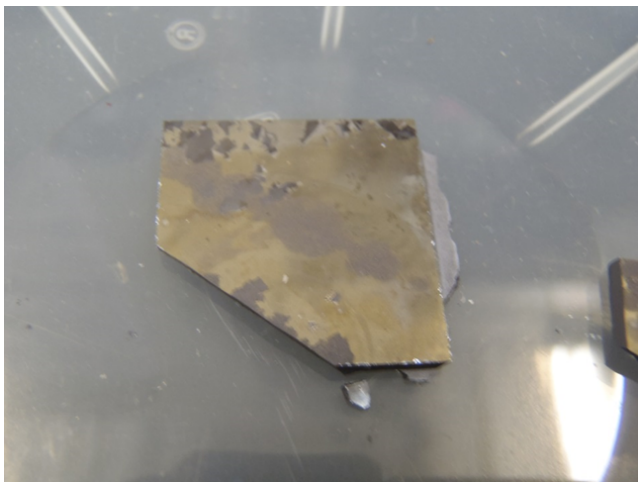

(b) Milled silicon sample top-view

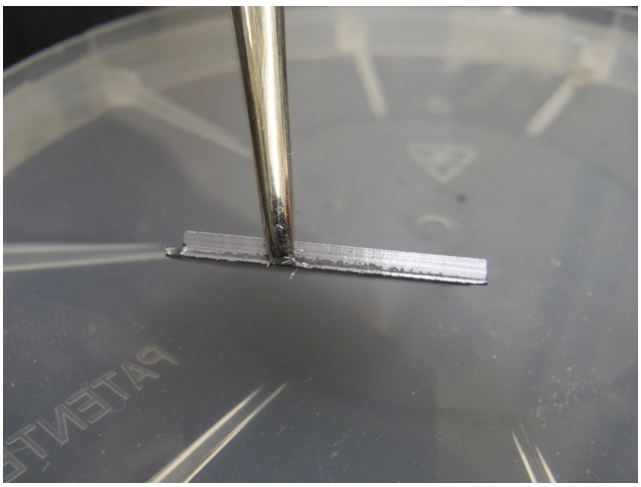

(c) Milled silicon sample side-view

Figure 4.69: Sample milling to reduce the footprint to 2 cm x 2 cm, and reduce the sample thickness to 2 mm. a) Showing the 4" diameter, 5mm thick sample in the holder used to thin the sample after the thinning process. b) Top-view of the milled potential hold sample. The corner missing from the square is due to the entire sample cracking when the wafer was flipped and re-inserted into the sample holder for milling. Dark spots on the sample surface are due to silicon dust as well as cathode delamination. c) A side view of the milled square showing ∼1.95 mm total thickness.

4.5.1 OCV Post-NR

4.5.1.1 XRR

XRR data were collected in the Q-range 0 $\mathring{A}^{-1} \leq 1.0638\ \mathring{A}^{-1}$. The reduced XRR data for this sample are shown in figure 4.70.

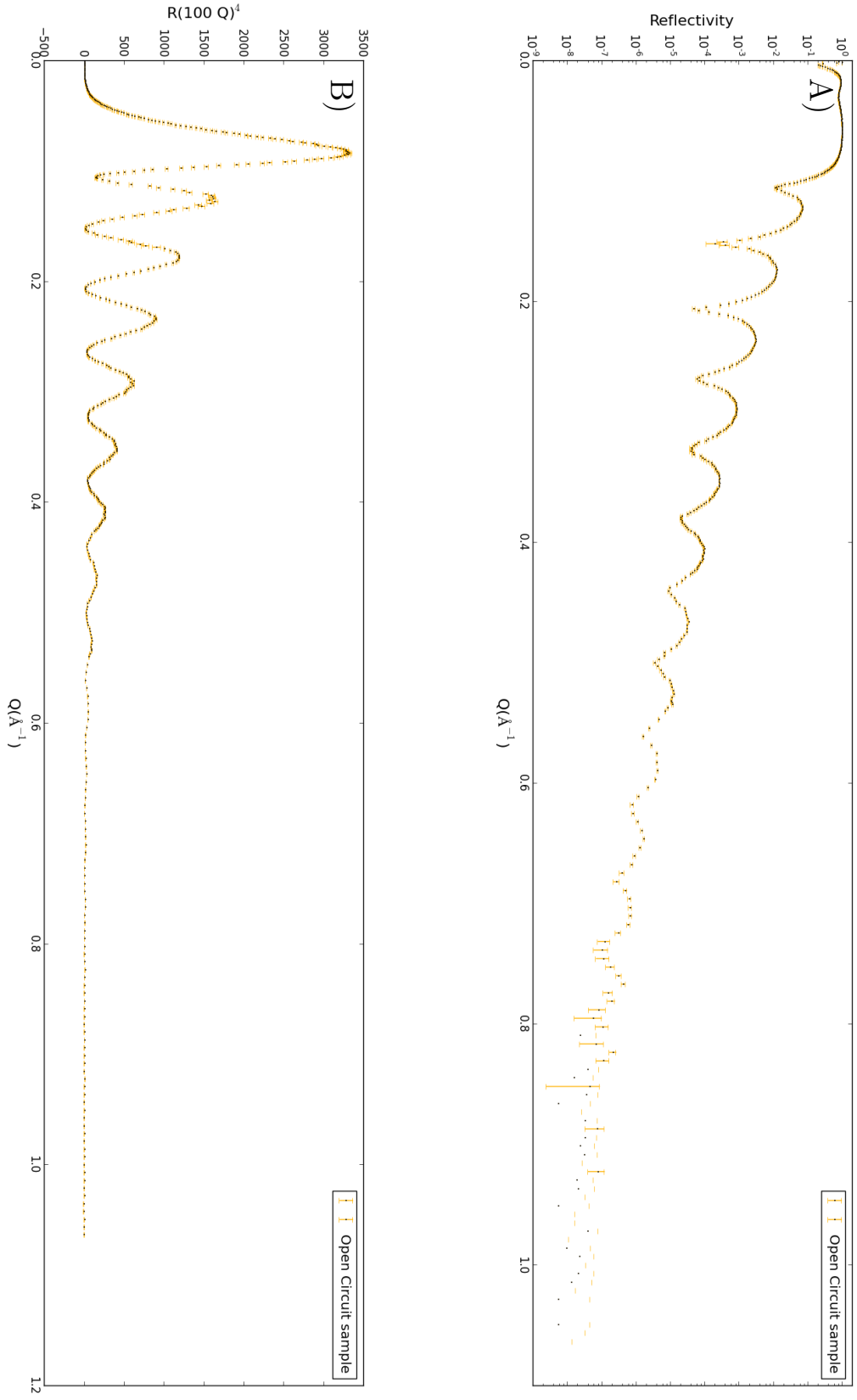

Figure 4.70: XRR results for the open circuit sample in air following NR and sitting for four months before the cell was disassembled and the sample rinsed multiple times in DMC. A) Log(R) vs Q. B) R*(100*Q)^4, this form is used to examine the critical edge as it occurs at the first maximum.

4.5.1.2 XPS

XPS was performed on two regions, a region with no delamination and a region with delamination. Scans of the full XPS range from 1200 eV to 0 eV were performed to elucidate general composition and are shown in figure 4.71. Higher resolution spectra of the Li 1s, C 1s, O 1s are collected to investigate the binding energies of C and O relative to literature reported energies for solid electrolyte species.

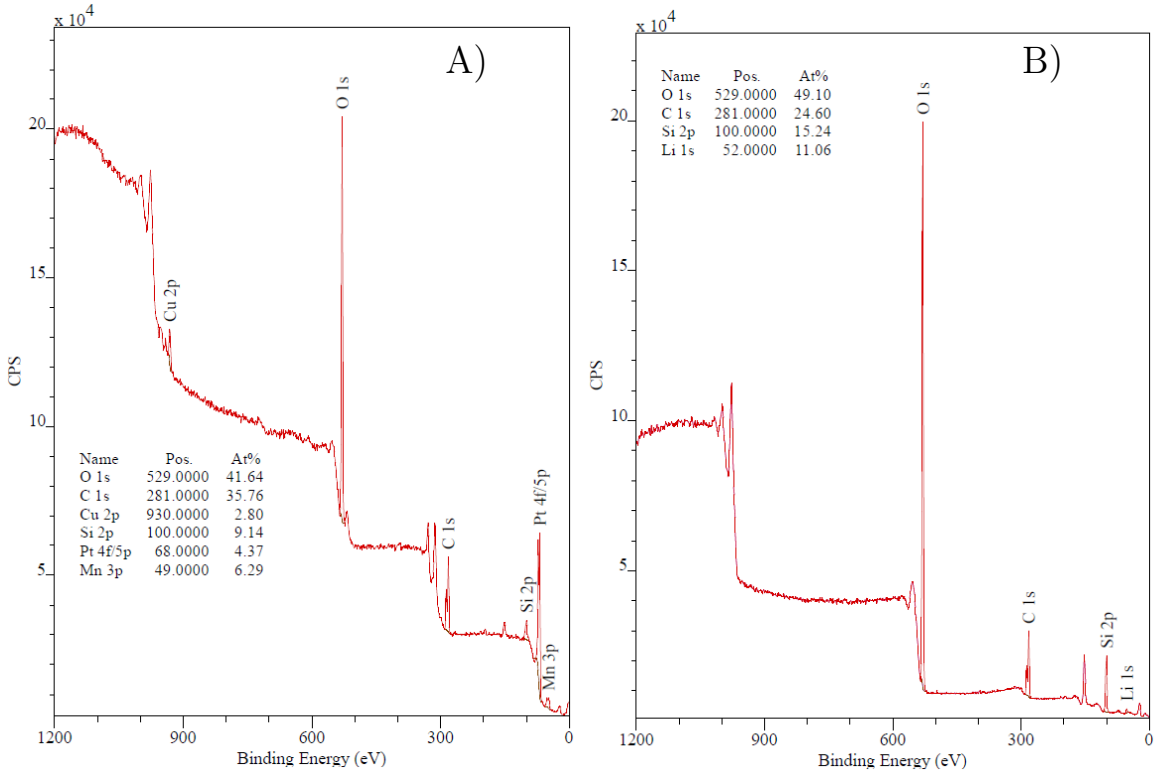

Figure 4.71: XPS spectra from 1200 eV to 0 eV on the open circuit sample in a region without delamination and a region with delamination. A) No delamination region , B) Delaminated region.

Figure 4.72 shows the Li 1s peak for the region without and with delaminated cathode layer. Figures 4.73 and 4.74 show the collected C 1s and O 1s emission lines.

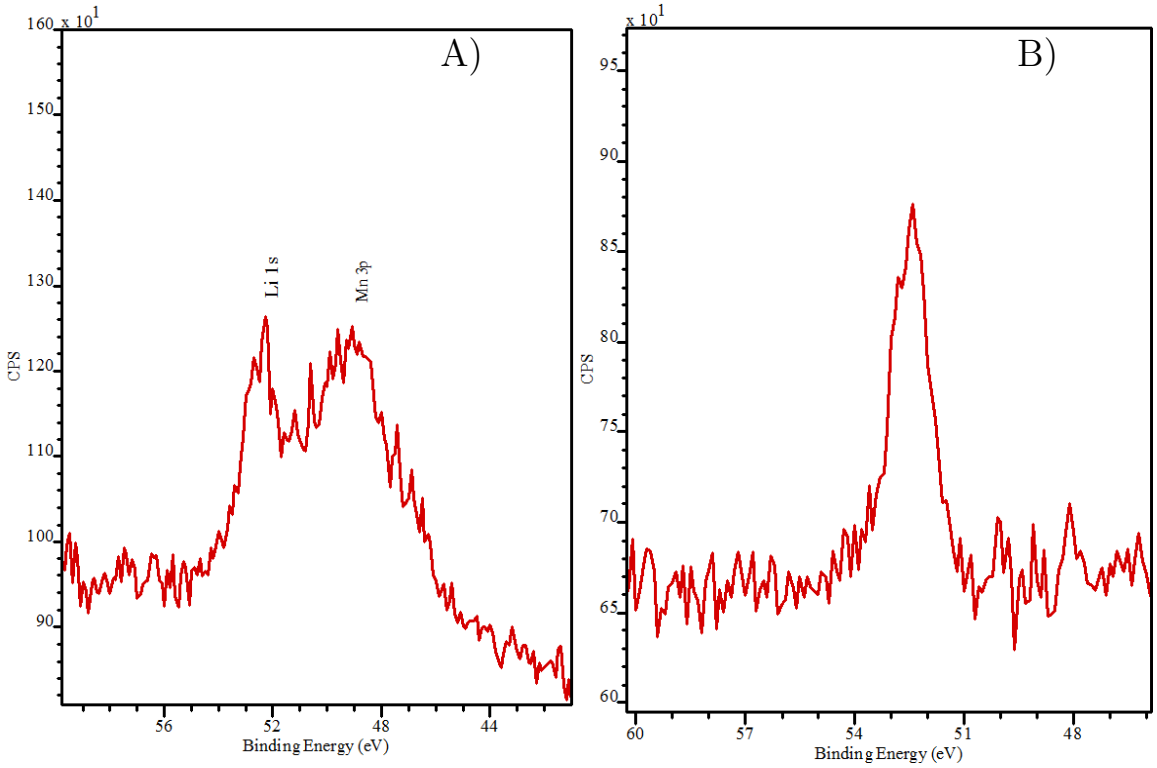

Figure 4.72: XPS spectra of Li 1s on the potential hold sample in a region without delamination and a region with delamination. A) No delamination region where Mn is present, B) Delaminated region where no Mn is present.

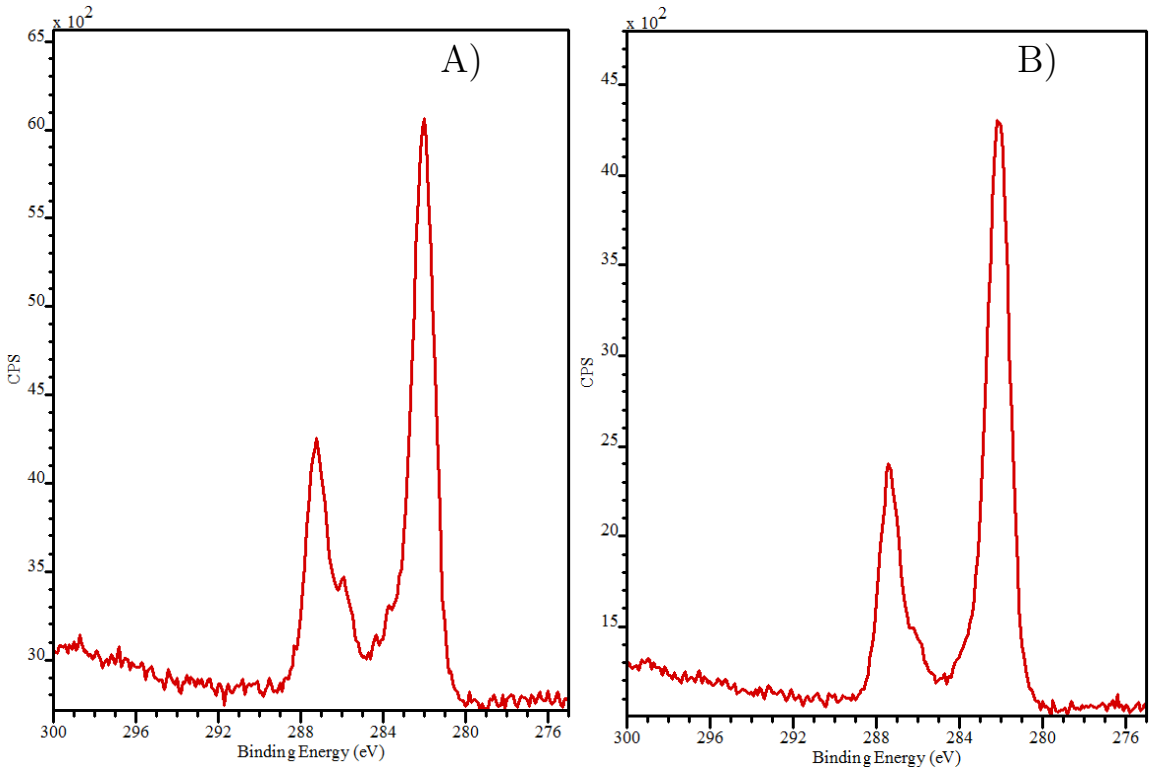

Figure 4.73: C 1s emission spectra on the open circuit sample in a region without delamination and a region with delamination. A) No delamination , B) Delaminated region.

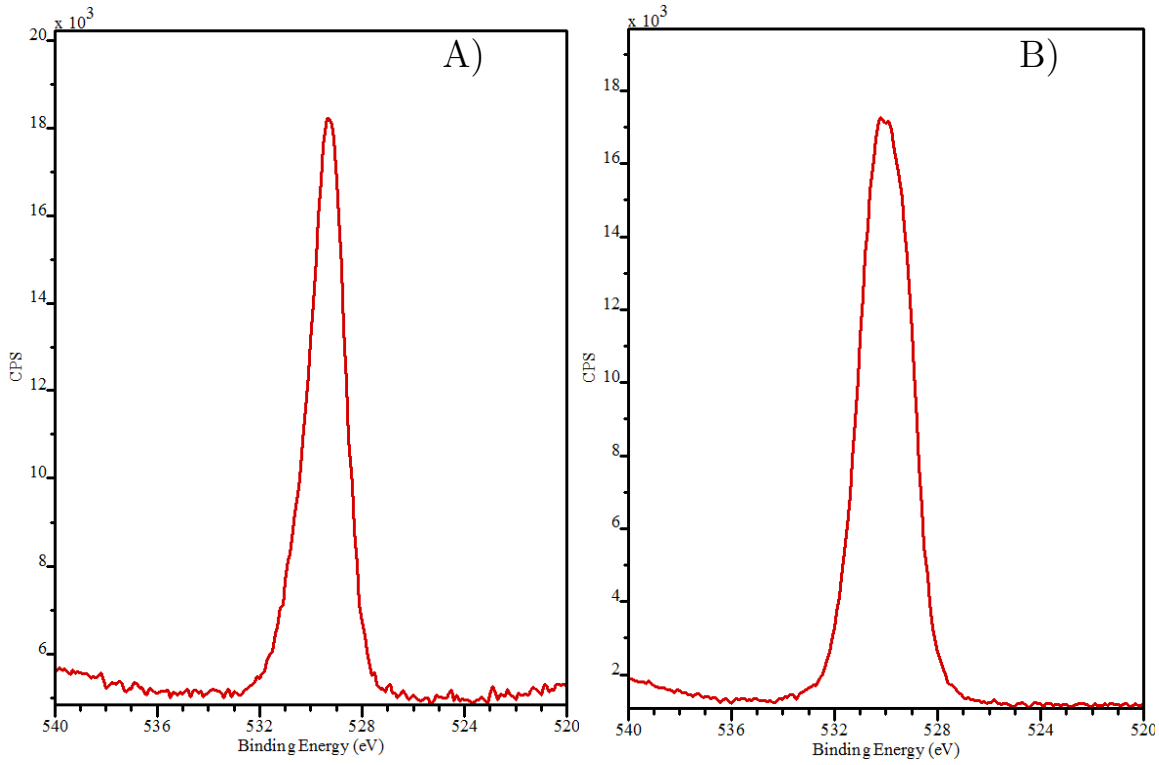

Figure 4.74: O 1s emission spectra on the open circuit sample in a region without delamination and a region with delamination. A) No delamination , B) Delaminated region.

4.5.2 Potential hold Post-NR

4.5.2.1 XRR

XRR data were collected in the Q-range 0 $\mathring{A}^{-1} \leq 1.007\ \mathring{A}^{-1}$. The reduced XRR data for this sample are shown in figure 4.75.

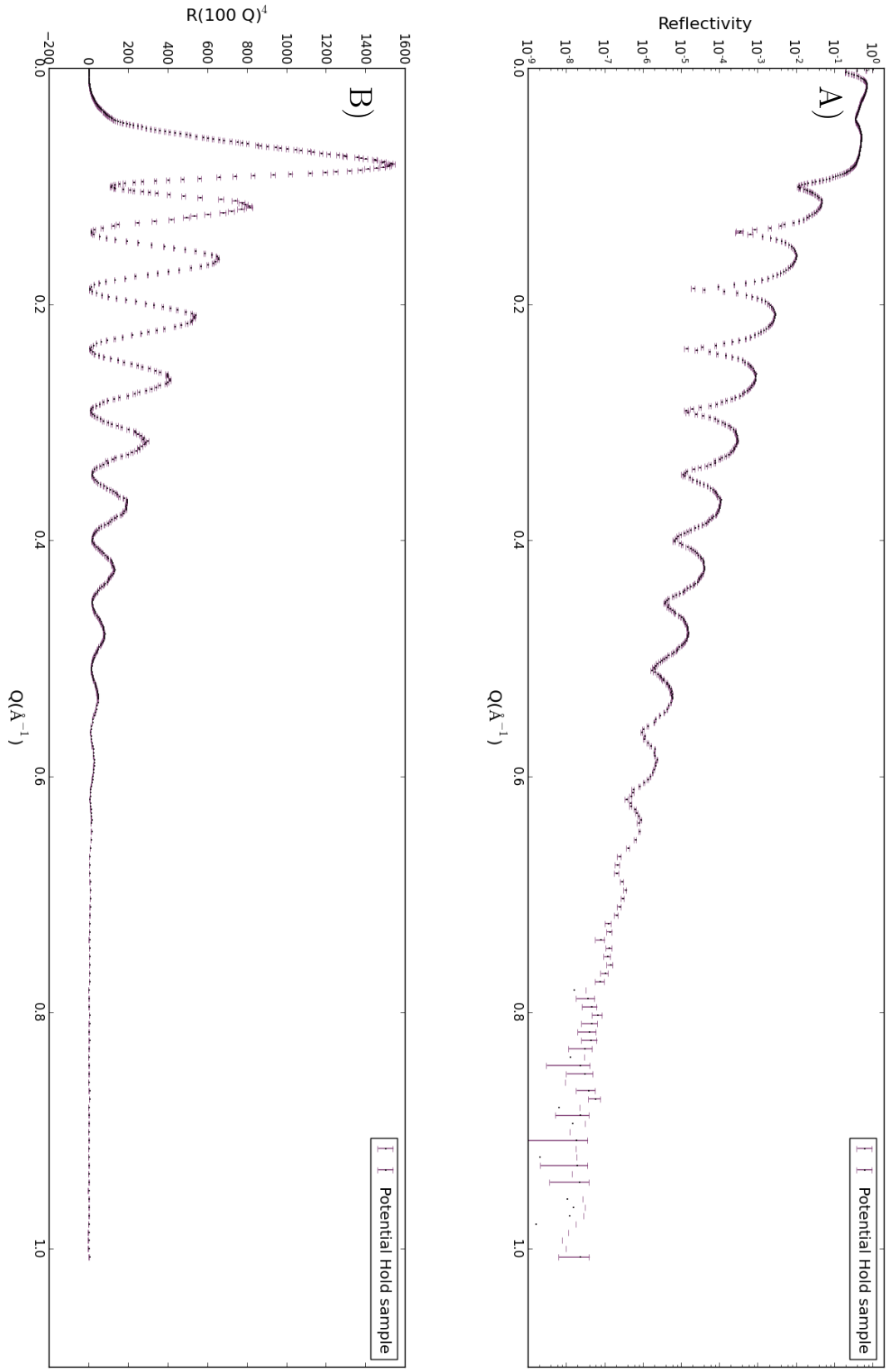

Figure 4.75: XRR results for the Potential Hold sample in air following NR and sitting for four months before the cell was disassembled and the sample rinsed multiple times in DMC. A) Log(R) vs Q. B) R*(100*Q)^4, this form is used to examine the critical edge as it occurs at the first maximum.

4.5.2.2 SEM

The potential hold sample surface was investigated through SEM and Energy Dispersive X-ray spectroscopy (EDX). SEM and EDX are used to not only visually inspect the surface but also to learn more about the delamination which occurs on the sample surface. Several regions were inspected through EDX to look at the differences between the cathode which is still adhered to the surface of the wafer, a region which is delaminated, and a delamination flake still attached at one end.

SEM images of a delaminated region at electron beam energies of 2 and 15 kV are shown in figure 4.76. The low beam energy is used to have a better contrast on the surface. This also reduces charging effects which are observed where delaminated film is still attached to the surface at one end. The improved contrast also brings to light a another film which is on the silicon throughout the cathode delaminated region. Boxes in figure 4.76 show locations where higher magnification images and EDX spectra are collected.

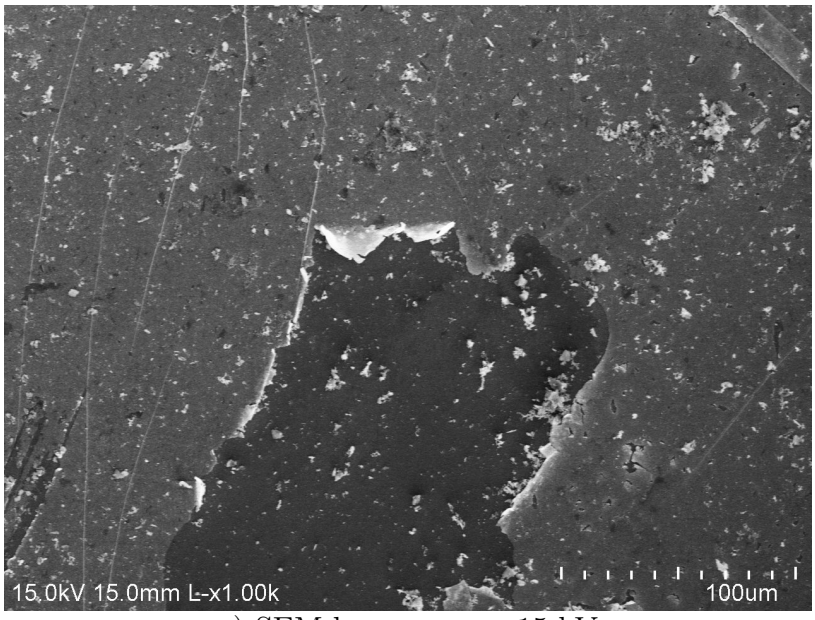

a) SEM beam energy 15 kV

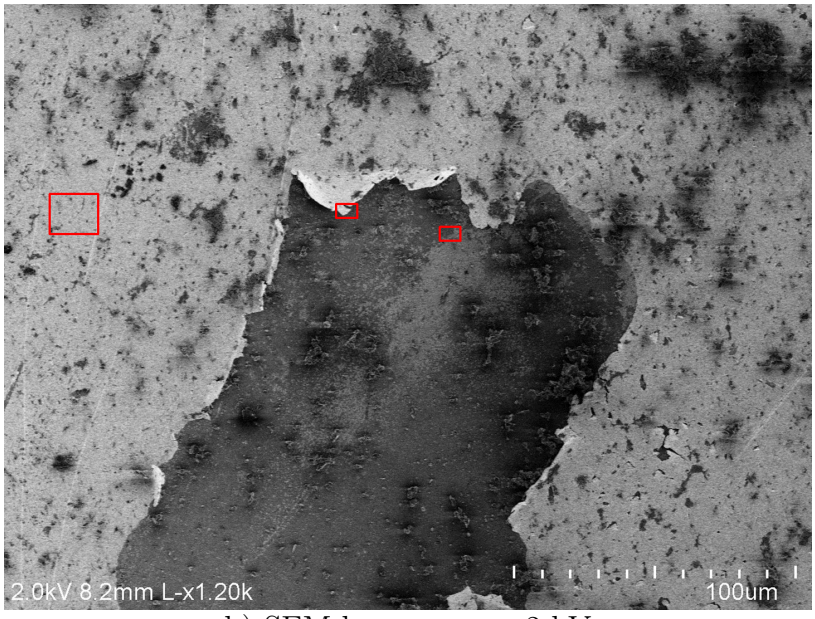

b) SEM beam energy 2 kV

Figure 4.76: SEM images showing a potential hold sample region of delamination at electron beam energies of 2 and 15 kV.

Those regions highlighted in figure 4.76 are magnified in figures 4.77, 4.78, and 4.79.

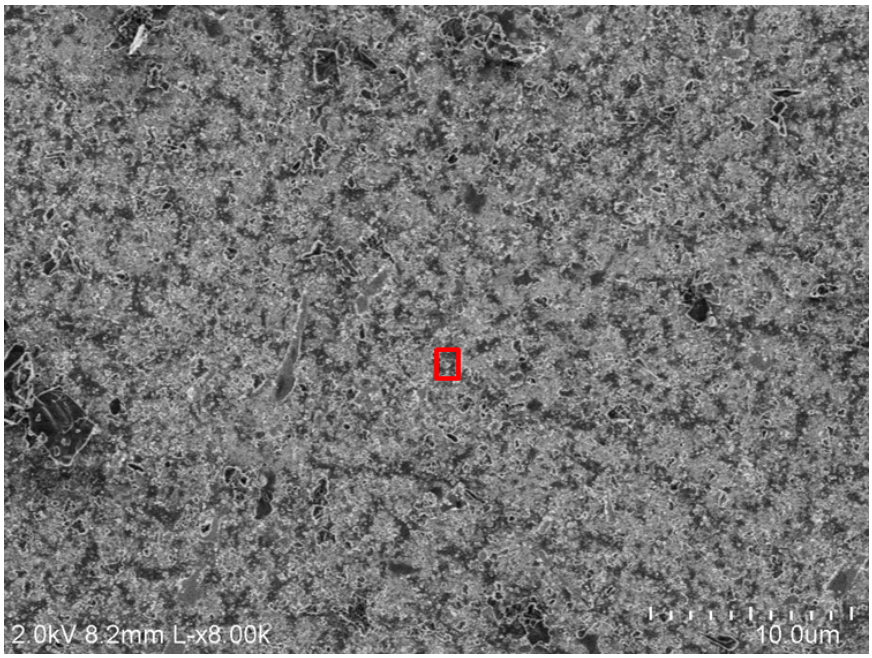

Figure 4.77: SEM image of potential hold sample surface from region 1 as shown in figure 4.76 collected at 2 kV. This image shows very little contrast is available on the surface of the cathode material.

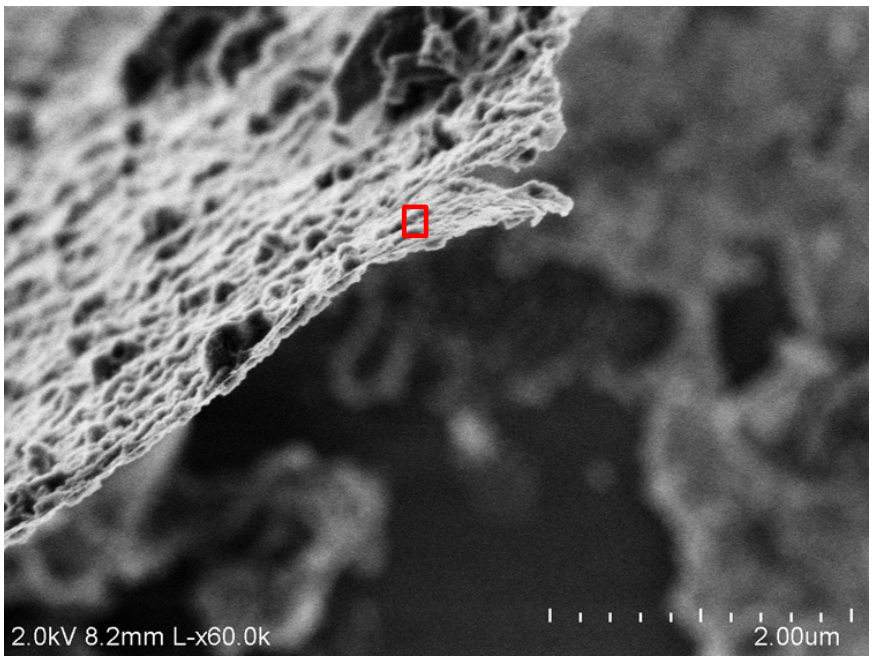

Figure 4.78: SEM image of potential hold sample surface from region 2 as shown in figure 4.76 collected at 2 kV. The image shows the very thin film along with significant buildup of additional material. The image appears to be very rough on both the top and bottom of the film. The box indicates a region which was explored through EDX.

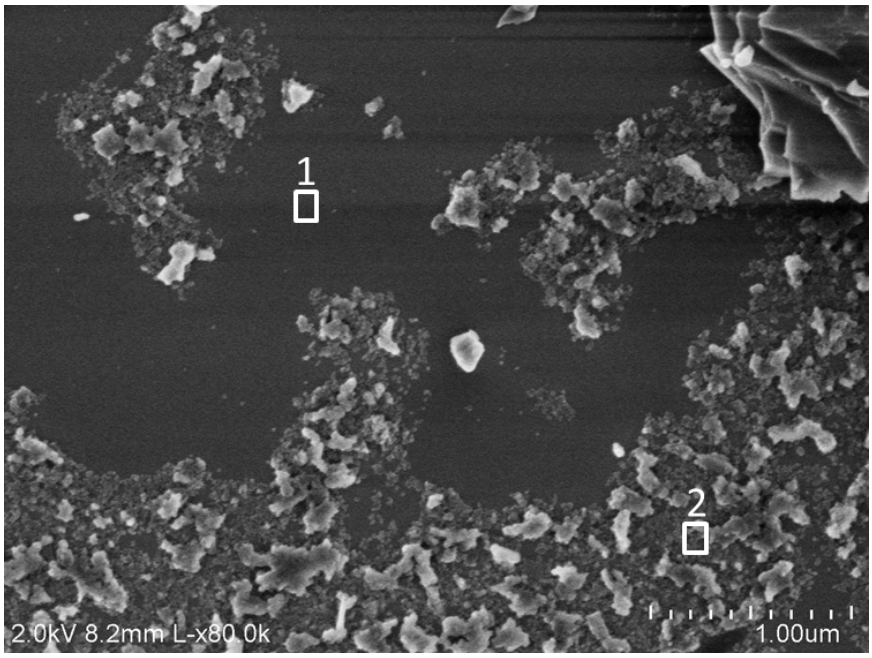

Figure 4.79: SEM image of potential hold sample surface from region 3 as shown in figure 4.76 collected at 2 kV. Very small grains can be observed on the surface which are coated with some very granular deposits. The boxes indicate where EDX data are collected

EDX data are collected from regions which are highlighted in figures 4.77, 4.78, 4.79. EDX spectra are shown in figures 4.80, 4.81, 4.82 where elemental energy shells are highlighted through vertical lines with labels. A summary table of these EDX spectra fitting results are provided in table 4.5.

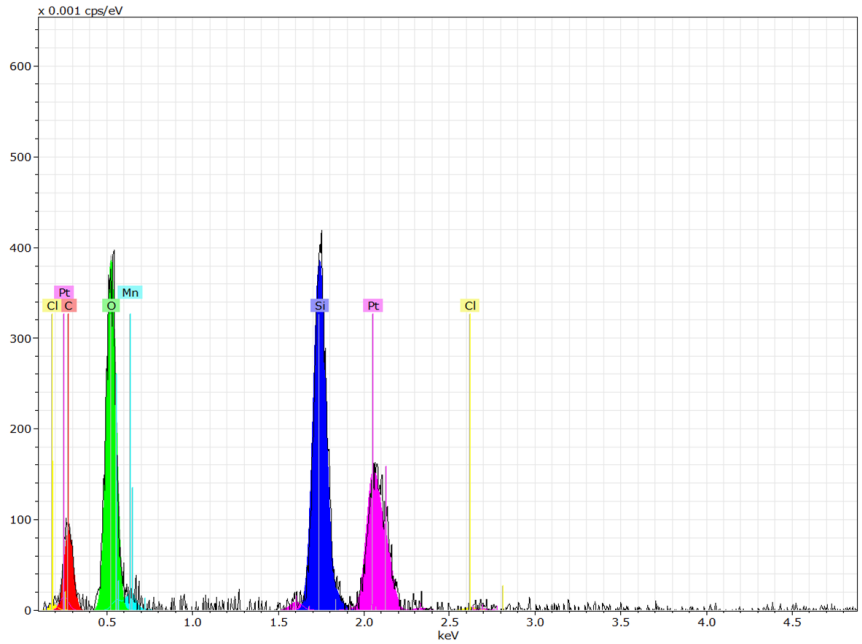

Figure 4.80: EDX spectra collected at 5 kV for a region highlighted in figure 4.77. This spectra shows the presence of all expected species wtih a small amount of Cl.

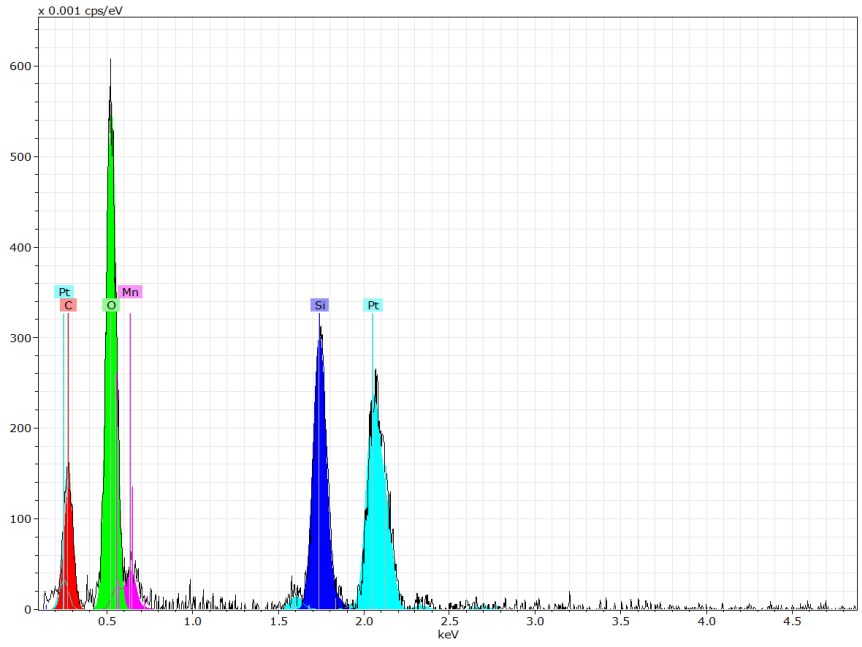

Figure 4.81: EDX spectra collected at 5 kV for a region highlighted in figure 4.78. These data show reduced Si signal and elevated Mn signal. The reduced Si signal is likely due to the distance of the delaminated flake to the surface and difficulty in collecting those characteristic x-rays.

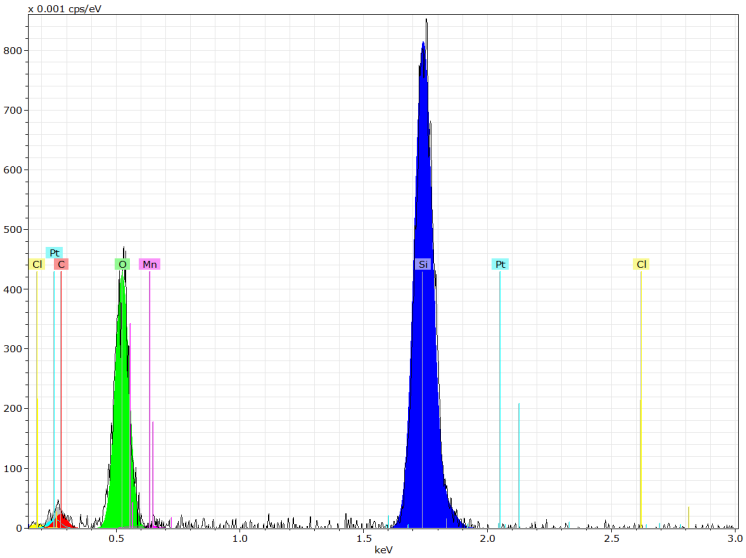

(a) Region 1 from figure 4.79

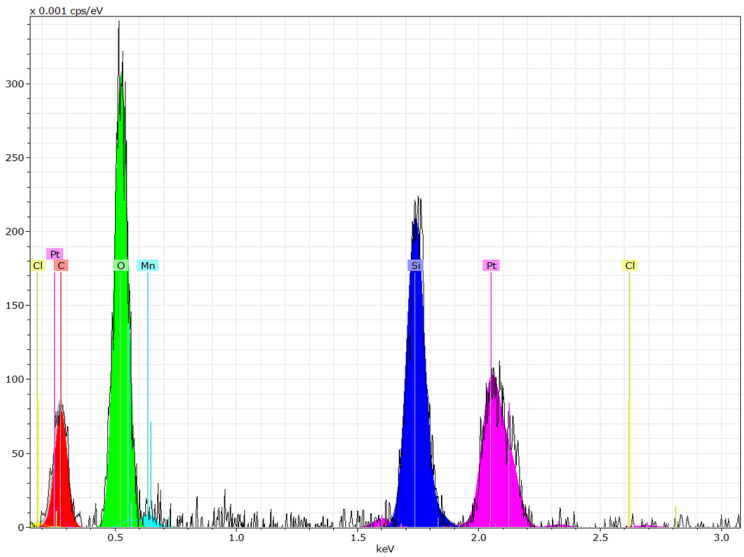

(b) Region 2 from figure 4.79

Figure 4.82: EDX spectra collected at 5 kV for two regions highlighted in figure 4.79. a) These spectra show no platinum signal but signficant O and Si signal indicating this region is primarily SiO_2. b) This spectra shows platinum signal but little to no Mn signal indicating the cathode layer is removed.

Table 4.5: EDX analysis results for spectra from figures 4.80, 4.81, 4.82.

Region	Pt (at%)	Mn (at%)	Si (at%)	O (at%)	C (at%)
Figure 4.80	4.94 ± 0.67	2.36 ± 1.18	37.42 ± 4.94	39.99 ± 10.45	14.84 ± 5.59
Figure 4.81	6.22 ± 0.76	4.20 ± 1.45	26.38 ± 3.23	46.54 ± 10.27	16.66 ± 4.95
Figure 4.82a	-	0.43 ± 0.48	59.06 ± 6.48	35.85 ± 9.65	4.66 ± 3.24
Figure 4.82b	4.57 ± 0.55	1.52 ± 0.75	31.21 ± 3.70	45.01 ± 9.35	17.68 ± 5.08

4.5.2.3 XPS

XPS was performed on two regions, a region with no delamination and a region with delamination. Scans of the full XPS range from 1200 eV to 0 eV were performed to elucidate general composition and are shown in figure 4.83. Higher resolution spectra of the Li 1s, Mn 3p, Mn 2p, C 1s, O 1s are collected to investigate the oxidation state of Mn, the content of Li relative to Mn, and the binding energies of C and O relative to literature reported energies for solid electrolyte species.

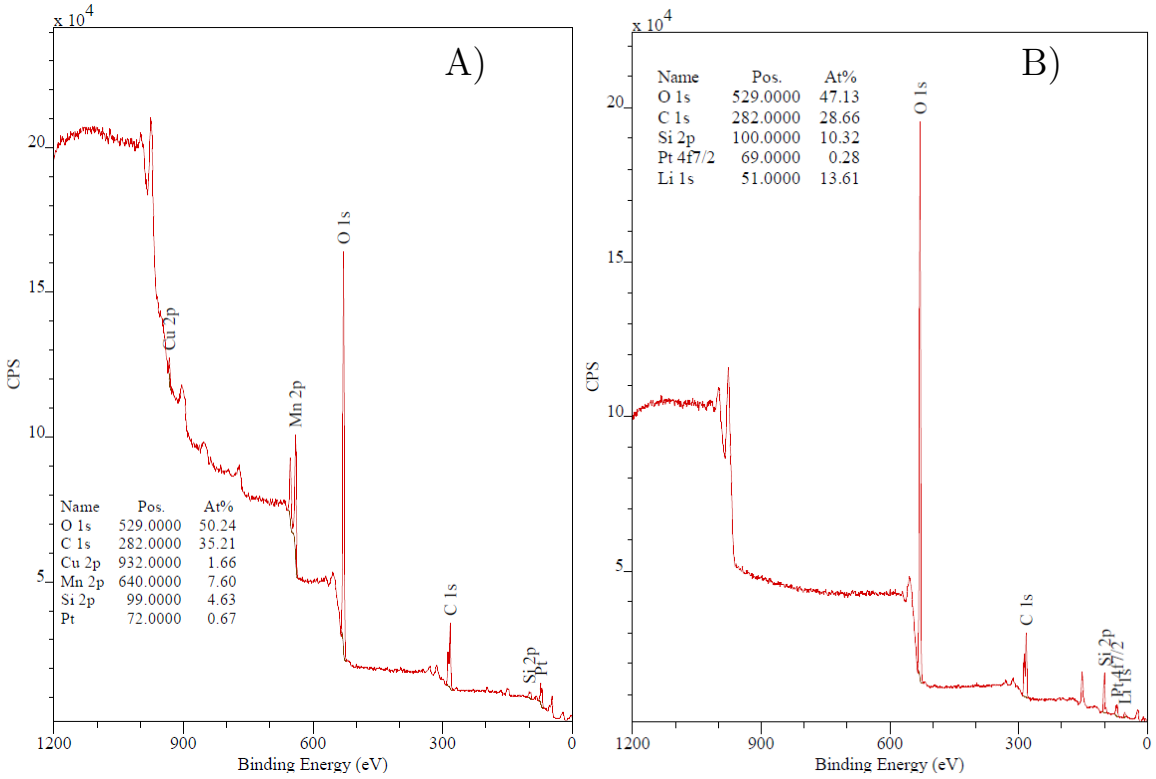

Figure 4.83: XPS spectra from 1200 eV to 0 eV on the potential hold sample in a region without delamination and a region with delamination. A) No delamination region where Mn is present, B) Delaminated region where no Mn is present.

Figure 4.84 shows the Li 1s peak for the region without and with delaminated cathode layer. It is obvious from the figure that the delaminated region shows no Mn content, which is also observed in figure 4.83. Figure 4.85 shows the collected XPS

data on the Mn 2p emission lines on the region without delamination. Figures 4.86 and 4.87 show the collected C 1s and O 1s emission lines.

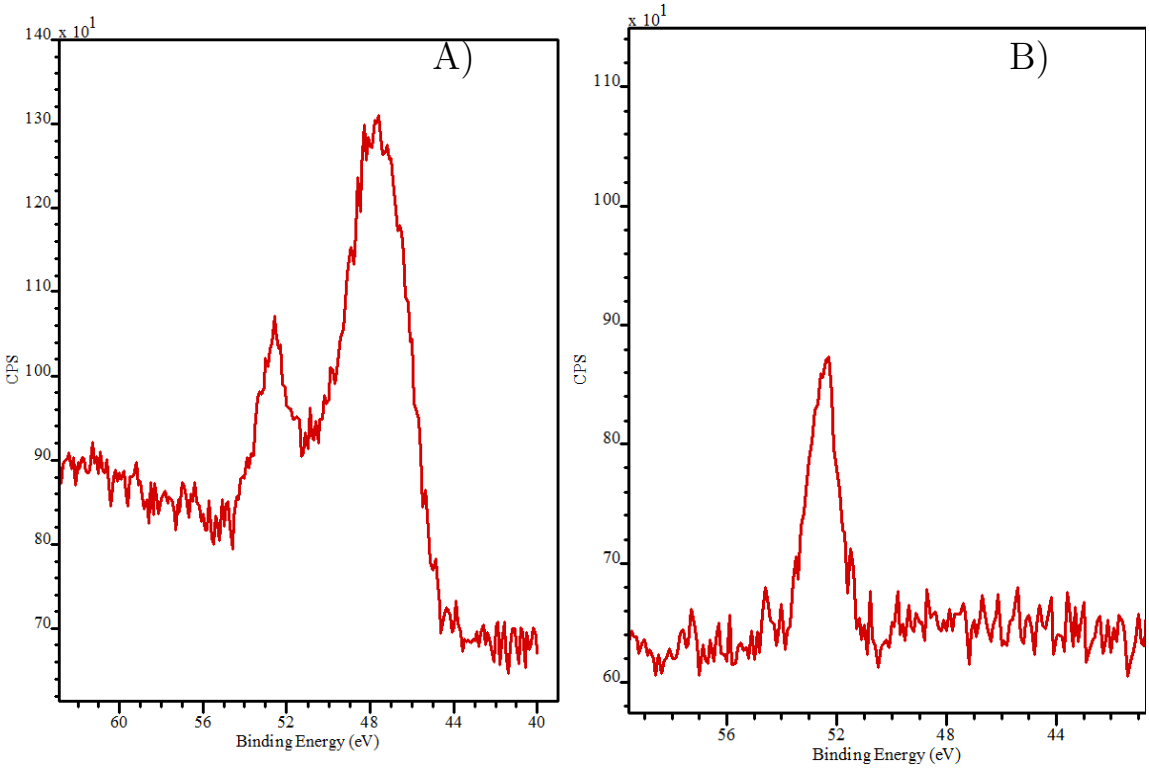

Figure 4.84: XPS spectra of Li 1s on the potential hold sample in a region without delamination and a region with delamination. A) No delamination region where Mn is present, B) Delaminated region where no Mn is present.

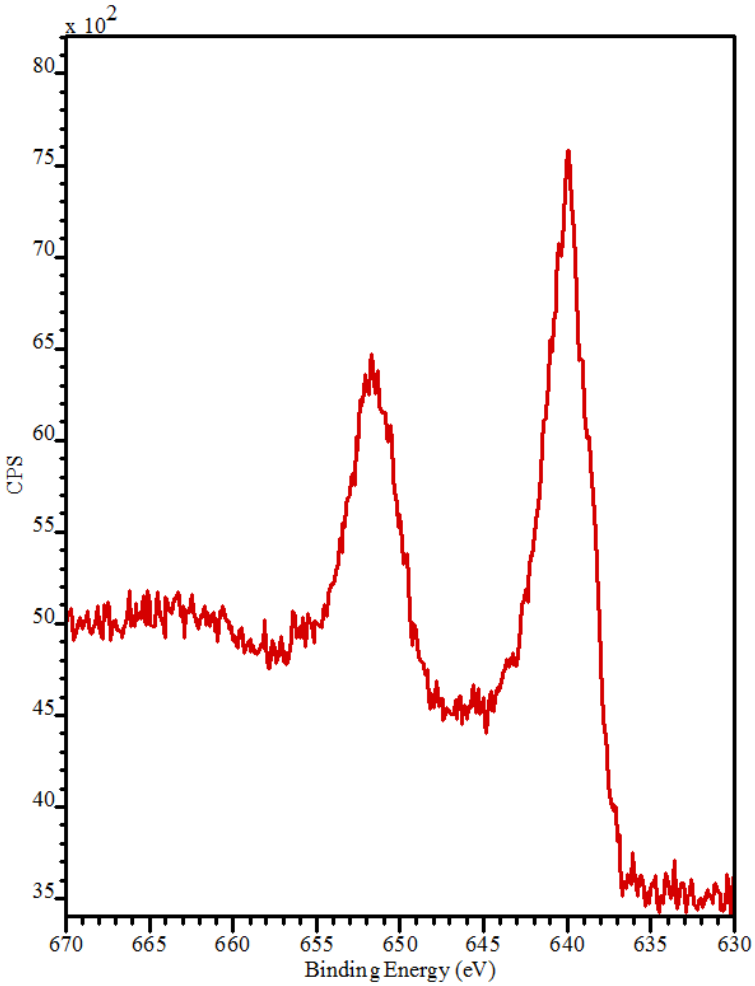

Figure 4.85: Mn 2p emission spectra for the potential hold sample following *in-situ* NR on a delaminated region.

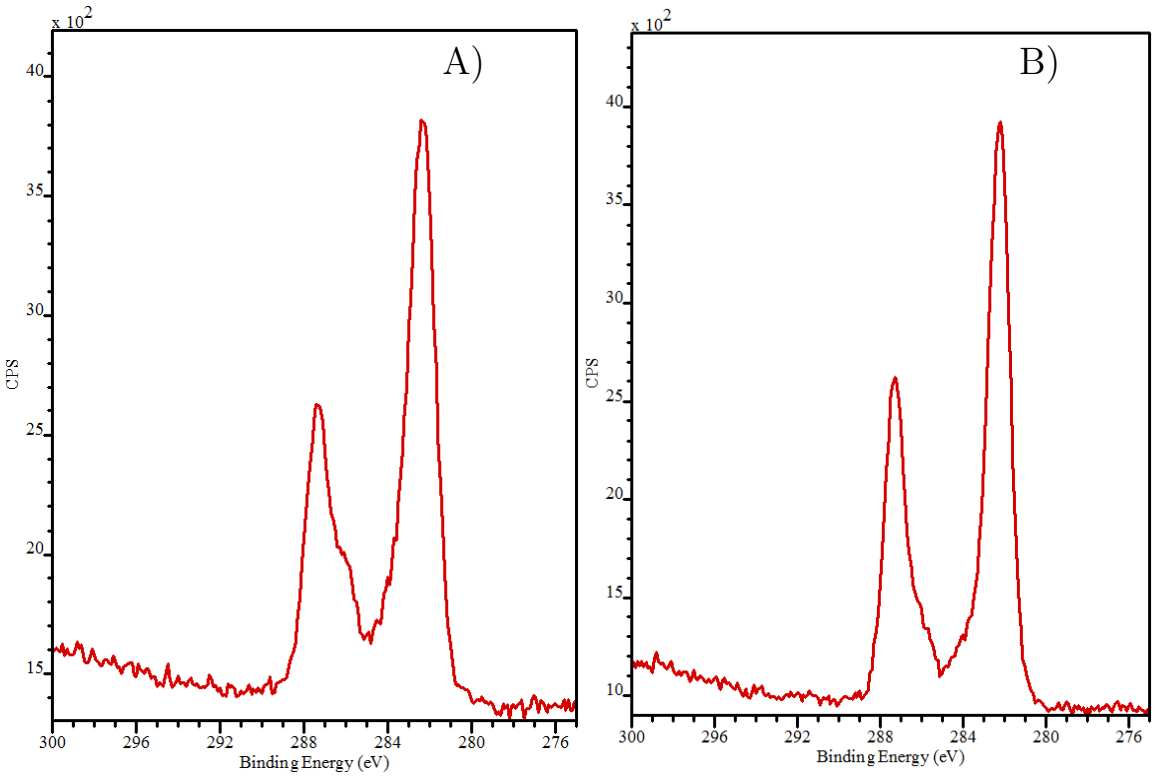

Figure 4.86: C 1s emission spectra on the potential hold sample in a region without delamination and a region with delamination. A) No delamination , B) Delaminated region.

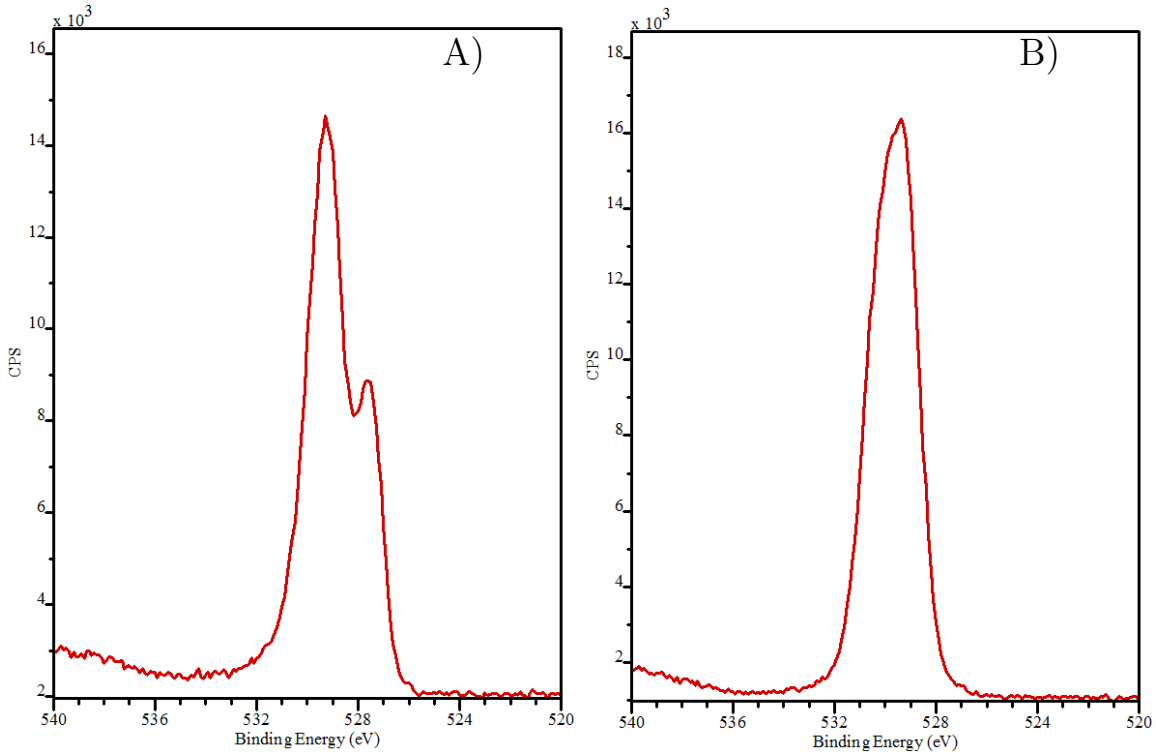

Figure 4.87: O 1s emission spectra on the potential hold sample in a region without delamination and a region with delamination. A) No delamination , B) Delaminated region.

CHAPTER V

Analysis

This chapter provides an analysis of data presented in the Results chapter. The chapter will first provide fitting results and analysis for those characterization XRR and NR experiments. Following the characterization analysis those NR data of the electrochemical cells with electrolyte will be discussed, a data correction applied, fitting results will be presented, and an analysis of those results will be discussed. Post-NR fitted XRR data will be presented and compared against those electrochemical cell NR data. Finally XPS results on those milled samples will be discussed.

5.1 Characterization Analysis

Those XRR and NR data from samples in air are fit to a model based upon equation 5.1.

$$Si/SiO_2/Pt/LiMn_2O_4/air \tag{5.1}$$

The initial starting values for each layer are listed in tables 5.1 and 5.2 for XRR and NR results respectively. The silicon, silicon dioxide, and platinum SLD's are held constant throughout the fitting process for XRR data. Similarly silicon and silicon dioxide SLD's are held constant while modeling NR results, but the platinum SLD is

allowed to vary. Allowing the Pt SLD to vary in XRR allows too much variation in the theta offset as those parameters are highly correlated meaning the effect of changing theta offset can result in very similar effects as changing the platinum SLD. It should be noted again that XRR and NR SLD values are different as the two techniques rely on different scattering centers where X-rays scatter off the electron shell and neutrons scatter from the nucleus.

As the platinum is deposited through a highly characterized sputtering deposition tool it was decided to set the platinum SLD constant at the bulk value. The starting thickness value for silicon dioxide is 500 $\mathring{A}$ which was the target thickness for the dry oxide furnace. The starting thickness of Pt is 100 $\mathring{A}$ which was the target deposition thickness on the sputter deposition tool. The starting thickness for $LiMn_2O_4$ is set to 150 $\mathring{A}$ which is derived from fitting previous testing sample XRR fits. The starting $LiMn_2O_4$ SLD for both NR and XRR are the bulk values, but are free to fit to a wide range of values.

Table 5.1: XRR characterization starting model.

Layer	thickness ($\mathring{A}$)	SLD ($10^{-6}\mathring{A}^{-2}$)	SLDi ($10^{-6}\mathring{A}^{-2}$)	Interface ($\mathring{A}$)
Si	-	20.1	0.458	5
SiO_2	500	18.8	0.243	5
Pt	100	136.1	13.36	5
$LiMn_2O_4$	150	33.2	2.289	25
Air	-	0	0	-

Table 5.2: NR characterization starting model.

Layer	thickness ($\mathring{A}$)	SLD ($10^{-6}\mathring{A}^{-2}$)	SLDi ($10^{-6}\mathring{A}^{-2}$)	Interface ($\mathring{A}$)
Si	-	2.07	0.00024	5
SiO_2	500	3.47	0.00011	5
Pt	100	6.36	0.0189	5
$LiMn_2O_4$	150	1.94	0.0038	25
Air	-	0	0	-

These models are applied to those collected XRR and NR data for both samples. As discussed in section 3.5.6 the software package Refl1D is used to fit a model to

those data through the maximum likelihood method. These models were fit using a population of 30, and 6000 steps of which the last 3000 are used to determine statistics of those fits. Figure 5.1 shows the fitted reflectivity profiles for the open circuit sample from XRR and NR methods in air.

Similarly figure 5.2 shows the fitted reflectivity profiles for the potential hold sample from XRR and NR methods in air. The models were fit using the same population, steps, and initial guesses as the open circuit sample.

The goodness-of-fit for both the XRR and NR fits for the potential hold sample were poorer than would normally be expected. In order to investigate the possibility of a two layers defining the $LiMn_2O_4$ film models were applied to both the open circuit and potential hold samples as in equation 5.2. Figures 5.3 and 5.4 show the XRR and NR fits from the model

$$Si/SiO_2/Pt/LMO_1/LMO_2/air \tag{5.2}$$

where LMO_1 and LMO_2 are considered to be separate layers within the $LiMn_2O_4$ film.

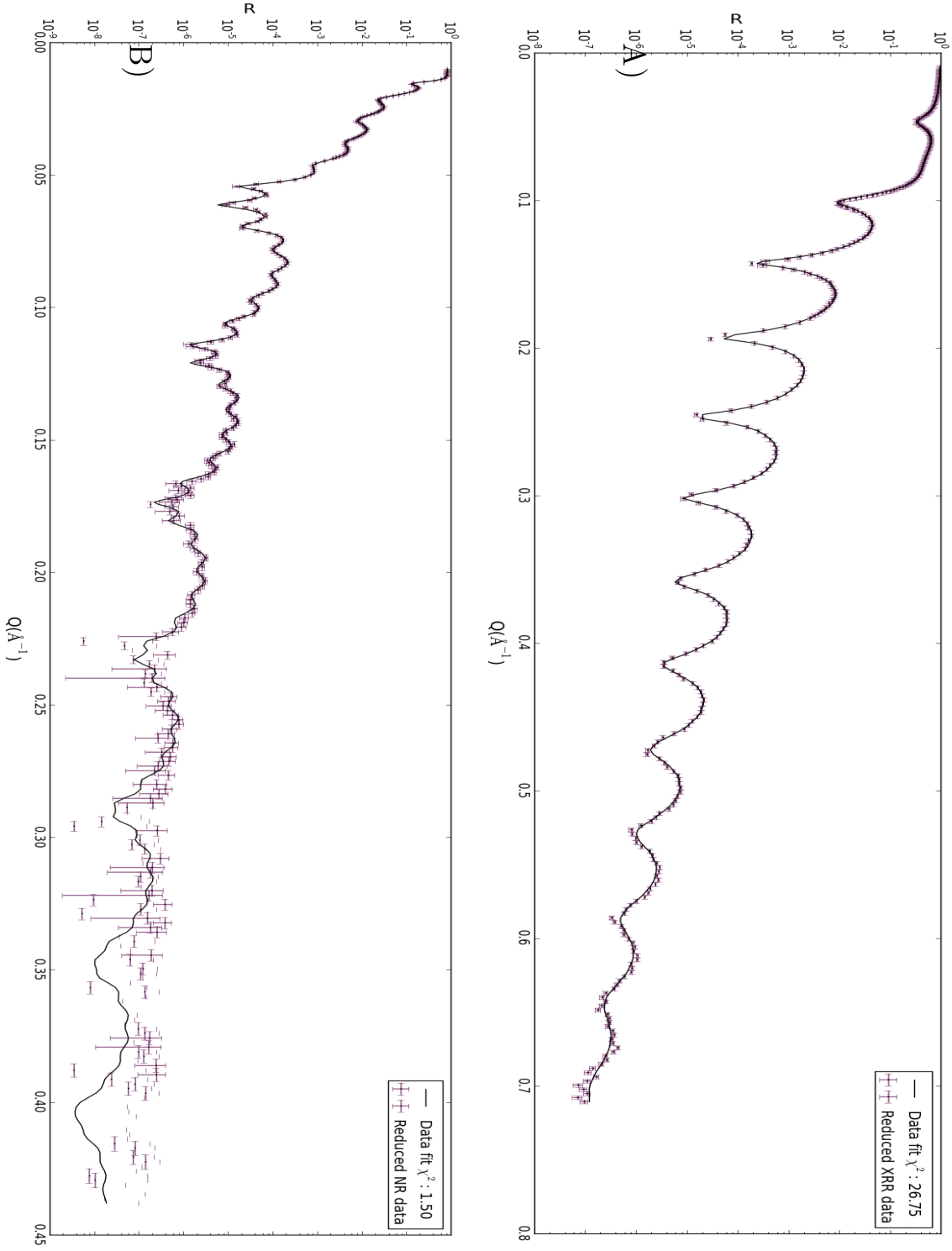

Figure 5.1: XRR and NR fits for the open circuit sample using one layer to represent the $LiMn_2O_4$ component. A) XRR data, B) NR data.

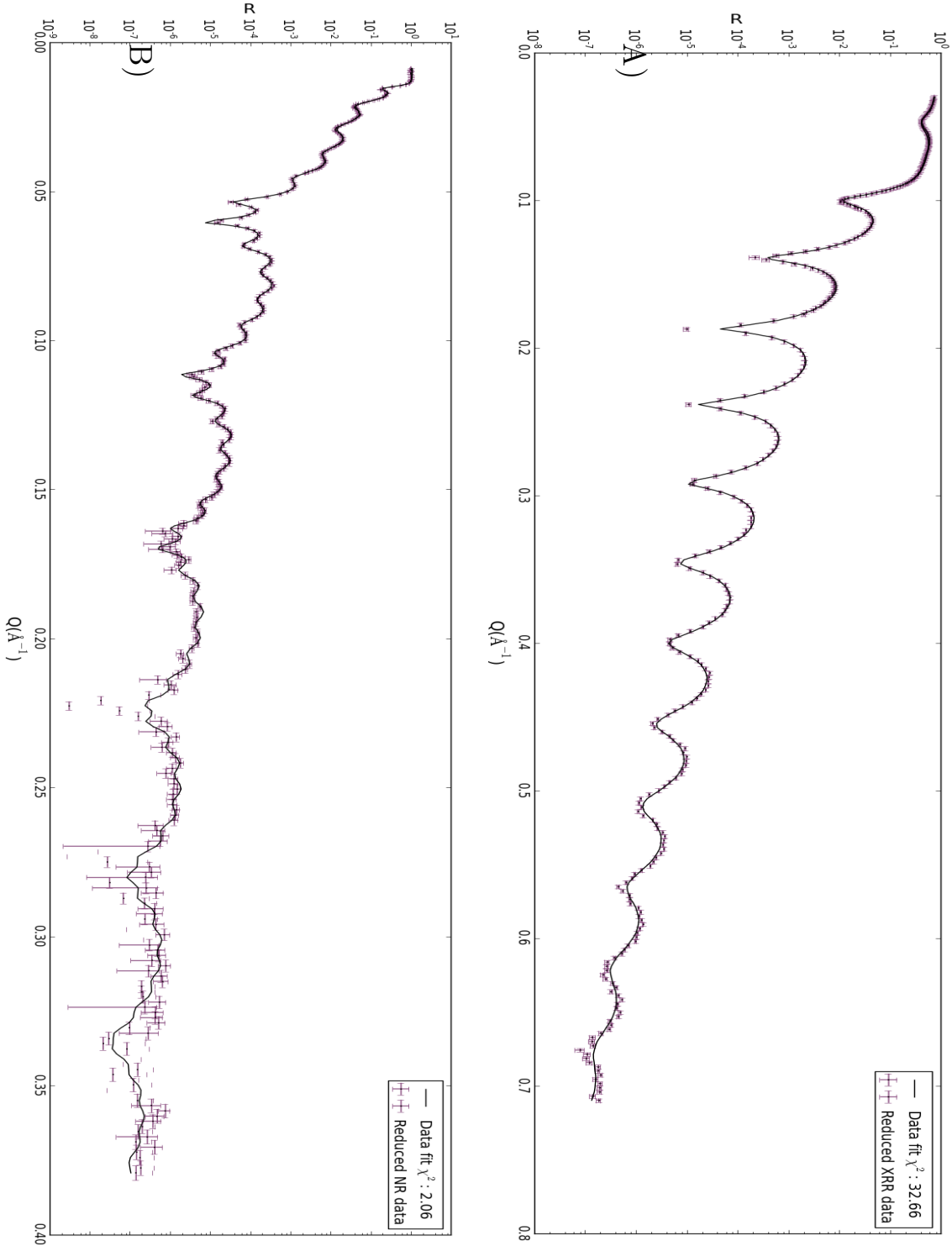

Figure 5.2: XRR and NR fits for the potential hold sample using one layer to represent the $LiMn_2O_4$ component. A) XRR data, B) NR data.

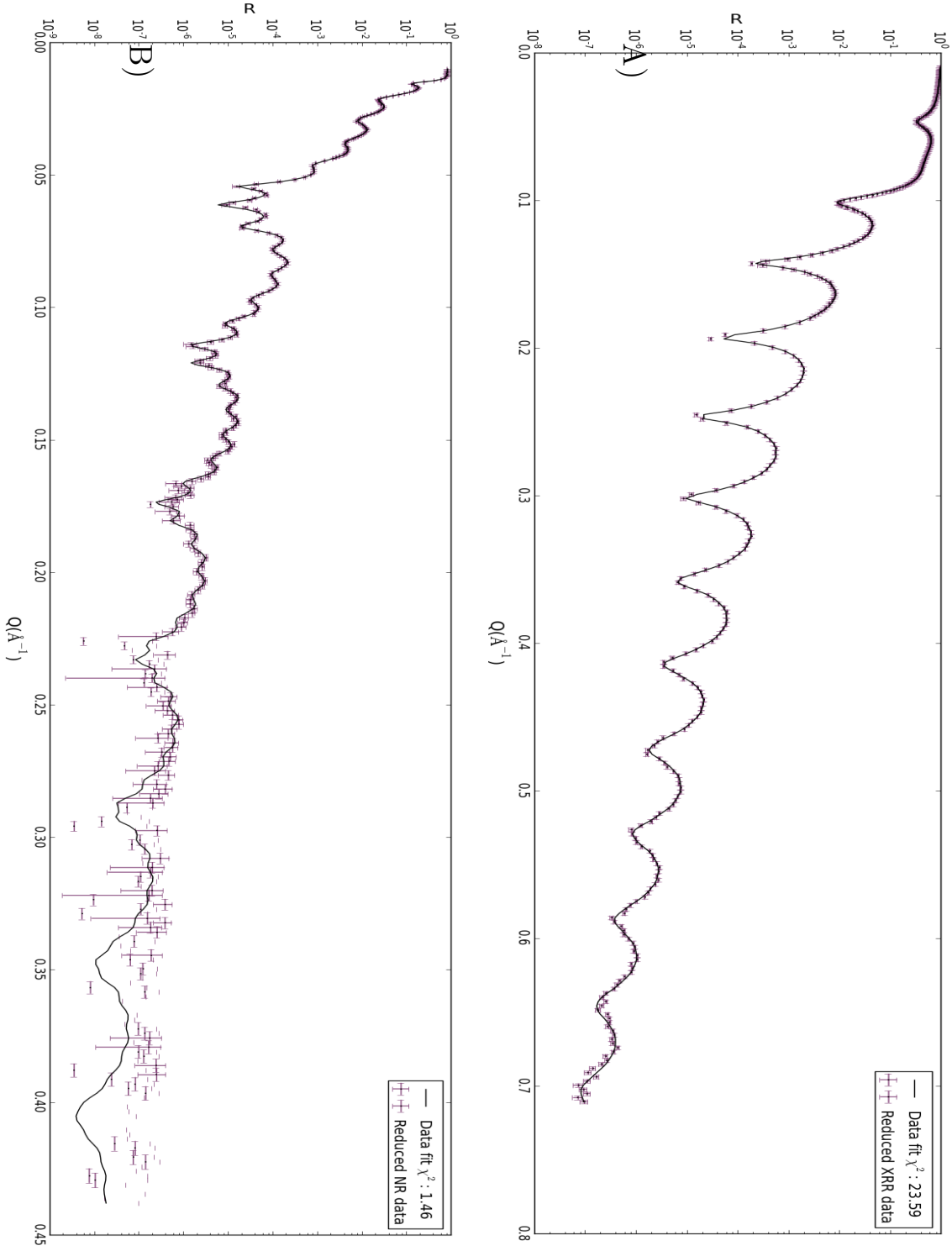

Figure 5.3: XRR and NR fits for the open circuit sample using two layers to represent the $LiMn_2O_4$ component. A) XRR data, B) NR data.

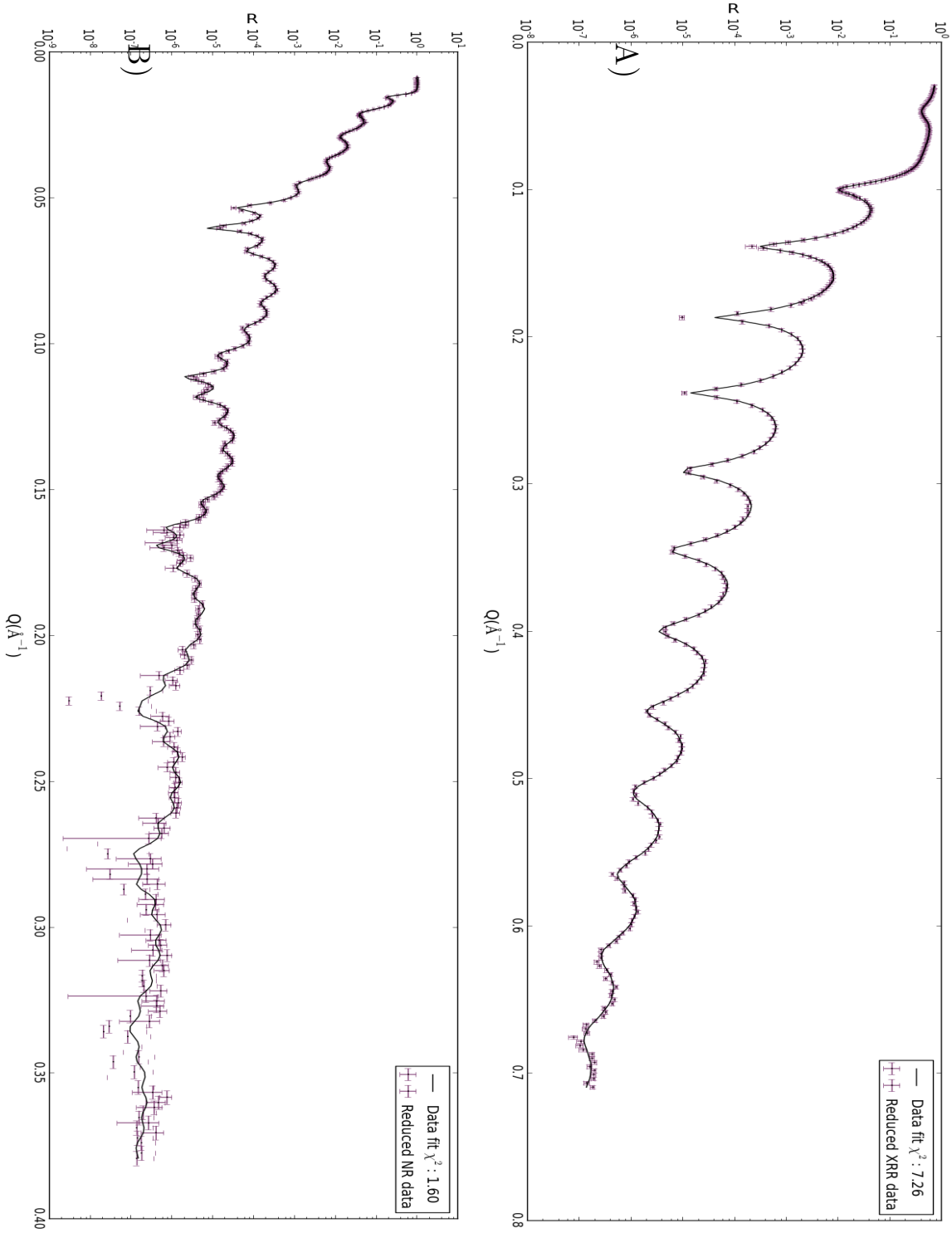

Figure 5.4: XRR and NR fits for the potential hold sample using two layers to represent the $LiMn_2O_4$ component. A) XRR data, B) NR data.

Figures 5.3 and 5.4 show the second layer can be used to arrive at better goodness-of-fits to both samples, but it is unclear which is necessarily better. The BIC from equation 3.11 as described in section 3.5.6 can be used to provide a determination of which model best describes these data by weighting the goodness-of-fit by the number of parameters used to arrive at those fits. Figure 5.5 shows the BIC values for both one and two layer models applied to the potential hold and open circuit sample XRR and NR results.

The BIC values for XRR and NR data for two-layers are substantially lower for the potential hold sample than the single layer BIC values. This is strongly indicative that the additional layer adds statistical certainty to the model. For the open circuit sample the BIC values show separation for the XRR data, but much less so than the potential hold sample. The NR BIC values for one and two layers on the open circuit sample are very similar with BIC's of 616.3 and 618.5. There could be justification to include the additional layer from XRR results, but the NR results strongly indicate that improvement in goodness-of-fit due to the additional layer does not add any statistical certainty to the fit and is therefore rejected. Two layers will be used to model the $LiMn_2O_4$ film in the potential hold sample, and one layer will be used in the open circuit sample.

The SLD profiles for the open circuit sample from XRR and NR fits are shown in figure 5.6. The SLD profiles presented in figure 5.6 include uncertainty in fitting parameters. SLD profiles in figure 5.6 are very similar and provide confidence in the model chosen. The SLD profiles for the potential hold sample from XRR and NR are shown in figure 5.7. These profiles show an interesting characteristic, namely that the first layer used to describe the $LiMn_2O_4$ film shows higher density in XRR, but lower density in NR. This can be attributed to a greater concentration of lithium in the layer as lithium has a negative scattering length. Additional lithium in XRR would raise the density in XRR, but due to the negative scattering length of lithium

for neutron scattering this manifests as a lower SLD.

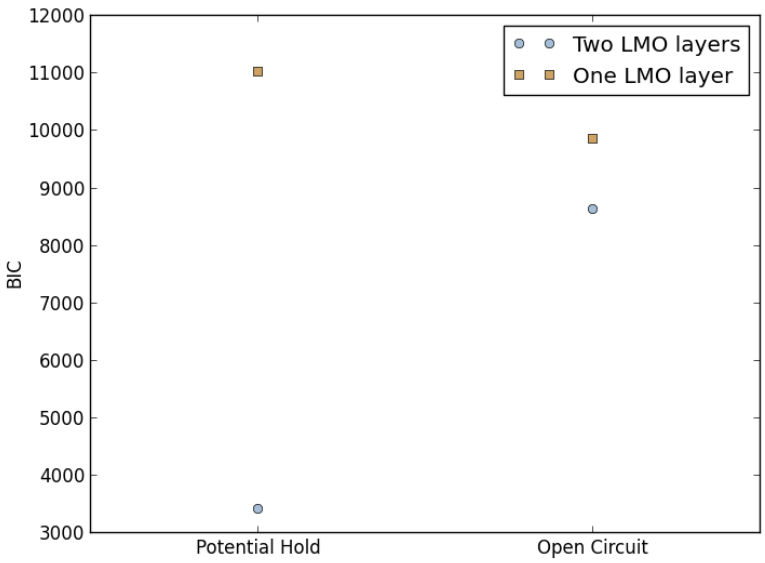

(a) XRR

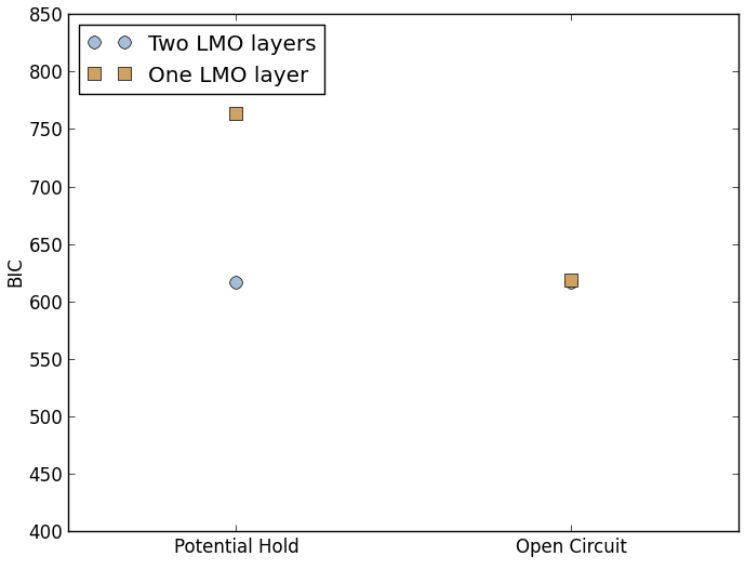

(b) NR

Figure 5.5: BIC values for models involving one and two layers which describe the $LiMn_2O_4$ film for NR and XRR fits on the Potential Hold and open circuit samples.

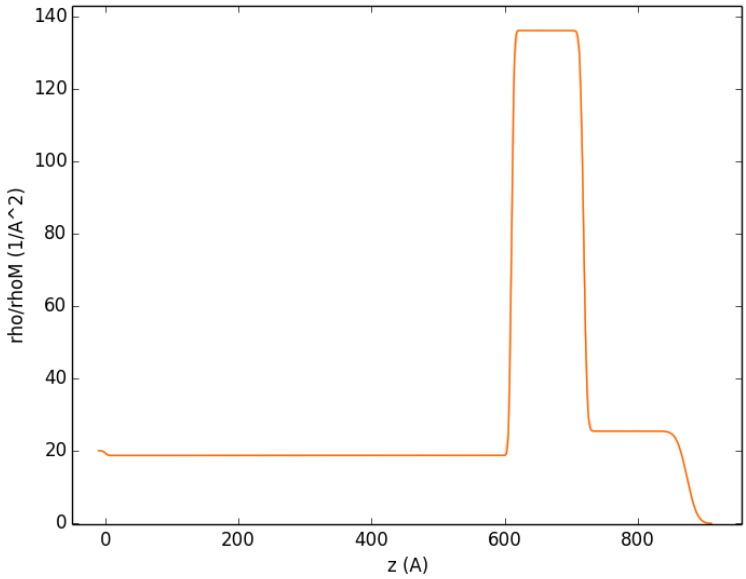

(a) XRR

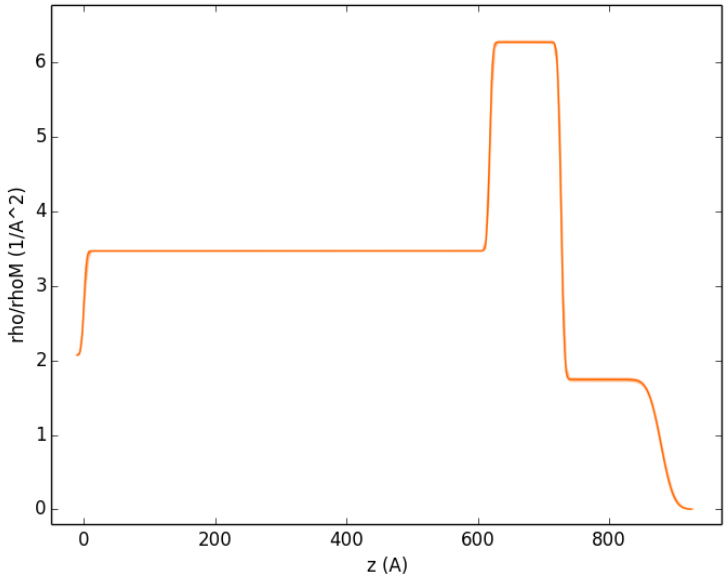

(b) NR

Figure 5.6: SLD profiles including uncertainty for XRR and NR for the open circuit sample. The uncertainty is given by shaded bands showing 1, 2, and 3 σ on all parameters given in the model. These models are very well behaved and those uncertainty bands are too small to observe.

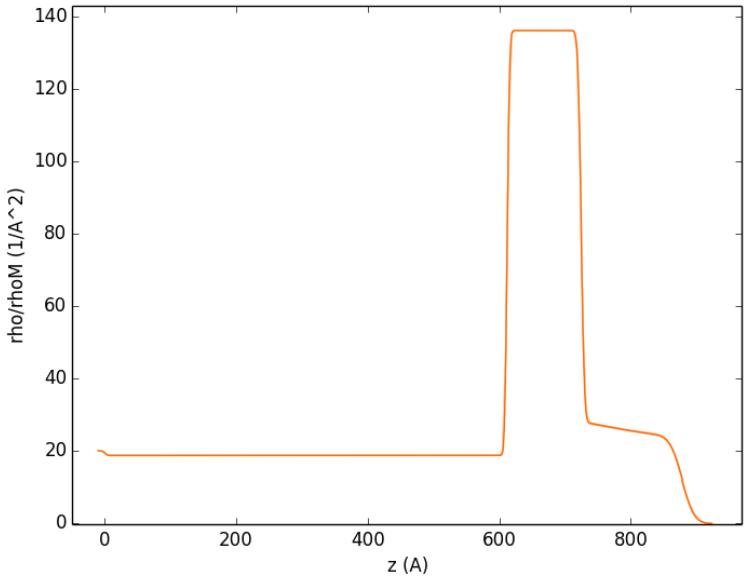

(a) XRR

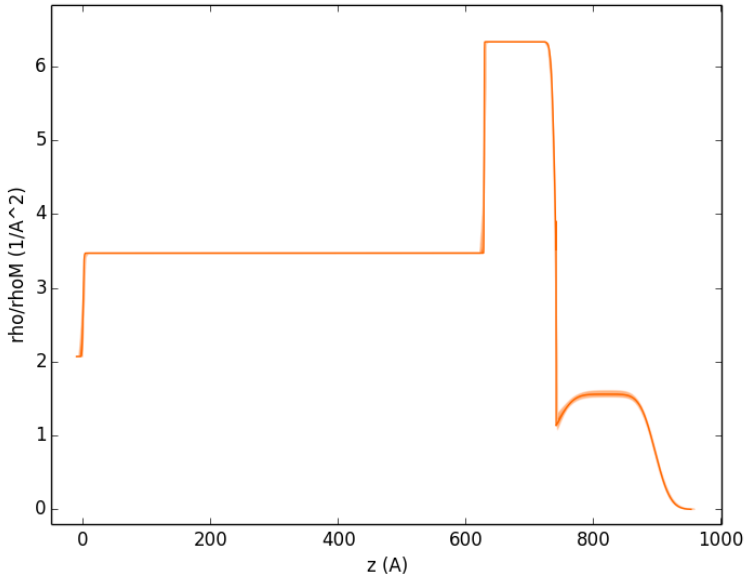

(b) NR

Figure 5.7: SLD profiles including uncertainty for XRR and NR for the potential hold sample. The uncertainty is given by shaded bands showing 1, 2, and 3 σ on all parameters given in the model. These models are very well behaved and those uncertainty bands too small to observe.

Figure 5.8 shows the residuals for XRR and NR fits on the open circuit sample. It should be noted that these residual figures show what appears to be a smearing effect at each datapoint. These residual plots are constructed from the same data which are used to generate the SLD profiles with uncertainty. Each Q value is actually composed of 50 residual values which represent the 3σ spread around the best fit value of the fit parameters. Figure 5.9 shows the XRR and NR residuals for the potential hold sample. The residual feature occurring at low-Q for the XRR fit of the open circuit sample indicates some part of the sample is not well modeled, but the overall residual bears a consistent deviation about the model. The residual for the fit to NR data on the open circuit sample shows no residual features. The same general comments can be made about the potential hold sample which also shows no significant errors in the models chosen.

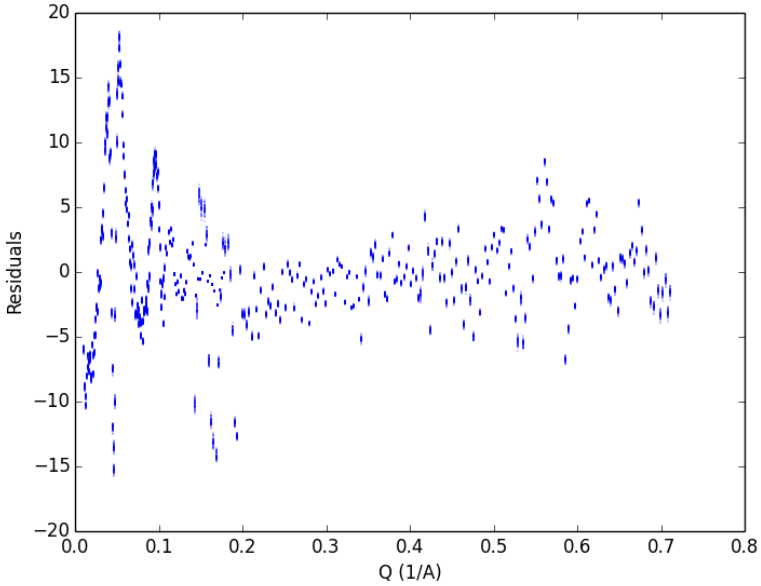

(a) XRR

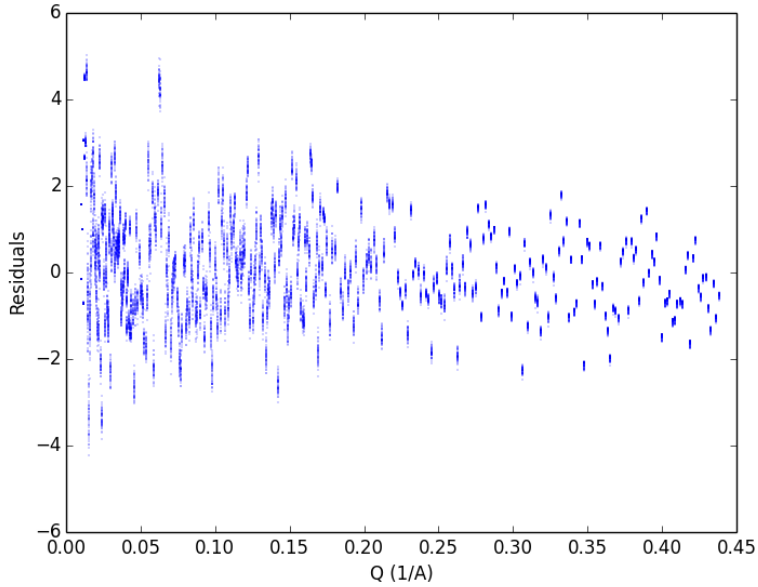

(b) NR

Figure 5.8: Residuals from XRR and NR fits for the open circuit sample. The residuals show no significant deviation from the flat trend expected from a good fit.

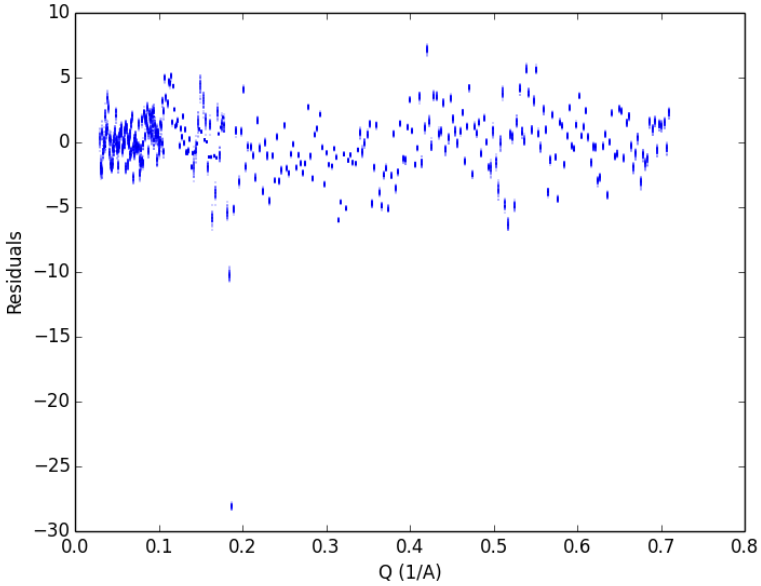

(a) XRR

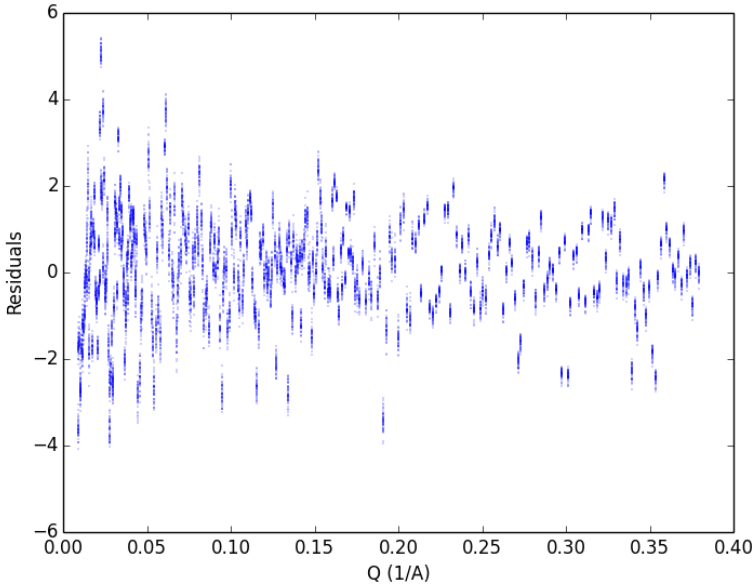

(b) NR

Figure 5.9: Residuals from XRR and NR fits for the potential hold sample. The residuals show no significant deviation from the flat trend expected from a good fit.

Tables 5.3 and 5.4 provide the fitted parameter values for the open circuit and potential hold samples in air. Those data in tables 5.3 and 5.4 highlight the general consistency between NR and XRR results for both samples. The oxide thickness

between NR and XRR for both samples show some deviation; however, the deviation is on the order of 1.5% and can be expected. For x-rays the contrast between the Si and SiO_2 layers is very small and therefore the contribution from that interface is very weak. For this reason the interface parameter is held constant for both sample XRR results. Neutrons however have a fairly significant contrast between the Si and SiO_2 layers and therefore it is realistic to fit the interface parameter.

Table 5.3: Open circuit sample XRR and NR in air. Parenthesis indicate uncertainty in fitted parameters. Parameters without uncertainty where held constant.

XRR				
Layer	thickness ($\mathring{A}$)	SLD ($10^{-6}\mathring{A}^{-2}$)	SLDi ($10^{-6}\mathring{A}^{-2}$)	Interface ($\mathring{A}$)
Si	-	20.1	0.458	3
SiO_2	609.96 (29)	18.8	0.243	2.9622 (32)
Pt	108.2255 (86)	136.1	13.36	4.0561 (54)
$LiMn_2O_4$	155.21 (11)	25.51 (27)	2.289	12.151 (86)
Air	-	0	0	-
Intensity: 1.01211 (44 Θ offset: 0.004715 (79) Background: $3.55*10^{-8}$ (42)				
NR				
Layer	thickness ($\mathring{A}$)	SLD ($10^{-6}\mathring{A}^{-2}$)	SLDi ($10^{-6}\mathring{A}^{-2}$)	Interface ($\mathring{A}$)
Si	-	2.07	0.00024	3.16 (58)
SiO_2	617.76 (21)	3.47	0.00011	3.82 (24)
Pt	108.720 (74)	6.33	0.0189	3.88 (15)
$LiMn_2O_4$	152.37 (27)	1.790 (11)	0.0038	15.81 (31)
Air	-	0	0	-
Intensity: 0.9774 (25 Θ offset: 0.00046 (15) Background: $1.20*10^{-8}$ (97)				

Table 5.4: Potential hold sample XRR and NR in air. Parenthesis indicate uncertainty in fitted parameters. Parameters without uncertainty where held constant. LMO_x are used to describe the first and second $LiMn_2O_4$ layers.

XRR				
Layer	thickness ($\AA$)	SLD ($10^{-6}\AA^{-2}$)	SLDi ($10^{-6}\AA^{-2}$)	Interface ($\AA$)
Si	-	20.1	0.458	3
SiO_2	611.9 (10)	18.8	0.243	2.9327 (33)
Pt	112.5111 (91)	136.1	13.36	3.9381 (64)
LMO_1	24.5 (21)	31.38 (18)	2.289	97.0 (21)
LMO_2	129.3 (20)	23.19 (12)	2.289	14.73 (19)
Air	-	0	0	-
$LiMn_2O_4$ total thickness: 153.78 (19) Intensity: 0.8997 (13) Θ offset: -0.004193 (84) Background: $1.27*10^{-8}$(41)				
NR				
Layer	thickness ($\AA$)	SLD ($10^{-6}\AA^{-2}$)	SLDi ($10^{-6}\AA^{-2}$)	Interface ($\AA$)
Si	-	2.07	0.00024	1.05 (62)
SiO_2	628.78 (22)	3.47	0.00011	0.70 (41)
Pt	112.771 (75)	6.418 (18)	0.0189	5.06 (23)
LMO_1	0.51 (42)	0.74 (11)	0.0038	21.2 (19)
LMO_2	154.98 (64)	1.562 (28)	0.0038	19.04 (48)
Air	-	0	0	-
$LiMn_2O_4$ total thickness: 155.72 (65) Intensity: 1.0419 (51) Θ offset: -0.00068 (29) Background: $6.1*10^{-8}$(27)				

From these models it is observed that the $LiMn_2O_4$ layer is not fully crystallized. Assuming the layer is composed of just $LiMn_2O_4$ the open circuit sample XRR results give a density which is 75.5% of the theoretical density, while NR results show a density which is 90.8% theoretical density. For the potential hold sample the two layers with a wide interface roughness between them make a simple comparison more difficult. Figure 5.10 shows a % theoretical density curve throughout the assumed pure $LiMn_2O_4$ layer for both the open circuit and potential hold samples. For the potential hold sample in figure 5.10 the $LiMn_2O_4$ layer is apparently larger for NR data which is a result of a larger observed surface roughness.

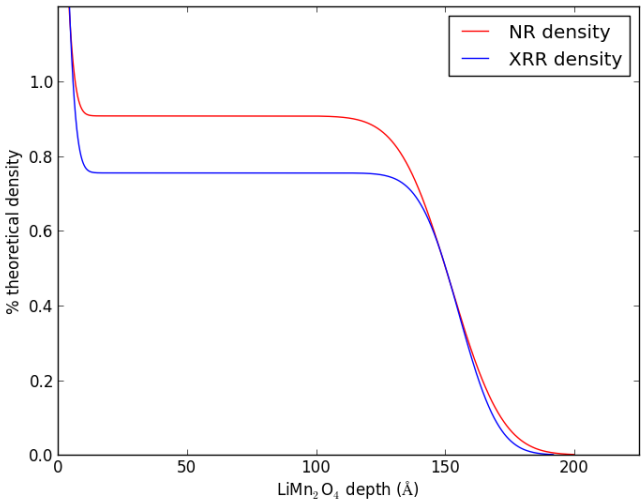

(a) Open circuit sample

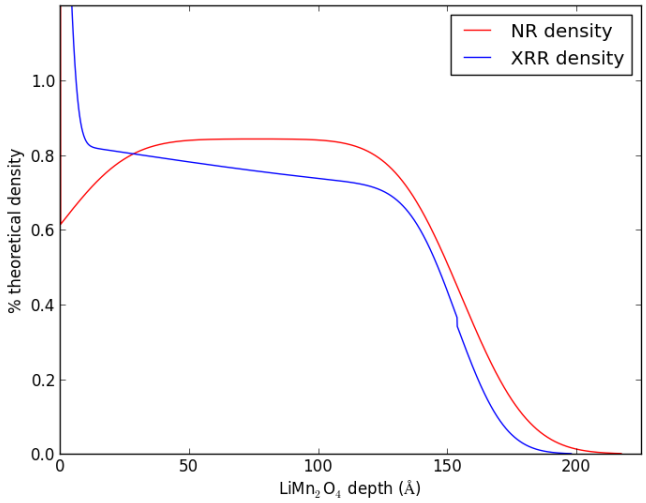

(b) Potential hold sample

Figure 5.10: $LiMn_2O_4$ layer % theoretical density as a function of layer depth for the open circuit and potential hold samples.

Figure 5.10 shows the assumption that the $LiMn_2O_4$ layer is pure $LiMn_2O_4$ is a poor assumption. It is known that $LiMn_2O_4$ has a Li_2CO_3 contaminant layer (77; 78; 5), however applying that knowledge is not straightforward in this case as the fraction which is Li_2CO_3 is unknown and the densification of both materials are also unknown. The deviation between these results will be addressed further in later

sections as more analysis requires more information than has so far been laid out.

5.2 Electrochemical Cell NR analysis

Prior to fitting these results to a model, an issue related to data reduction must be addressed. Both the open circuit sample and the potential hold sample exhibited poor reflectivity at low-Q which is attributed to warp effects on the sample. These effects are not entirely surprising given the rapid heat treatment to anneal the cathode film while preventing roughening. To correct for the loss of intensity due to warp a correction is applied which is described in section 3.5.7. The correction assumes below the critical edge the effect due to warp is a constant value, and after the critical edge the warp is a linear function of angle. This is not necessarily a perfect representation of warp, but it is assumed that warp is exacerbated at the radius of the sample wafer and diminished as the footprint becomes smaller on the sample surface.

For NR datasets on the open circuit sample the effect of warp is not as apparent as in the potential hold case which will be discussed. The slit-width in the low-Q angular range was set to 0.075 mm which better encompasses the warp effect than the 0.05 mm used in the potential hold case. The difference in slit-widths was due to efforts to produce a cleaner total reflection plateau than was initially observed. For the open circuit sample the same correction is applied to all datasets prior to combining those datasets for better statistics. Figure 5.11 shows corrected data along with the uncorrected data and the correction function. The effect of warp correction is essentially to raise the intensity in the total reflection region to 1 from nominally 0.9. This effect was initially ignored in these data; however, it was discovered that stable fitted solutions were not possible without the correction. Figures for corrections not shown here may be found in appendix A.

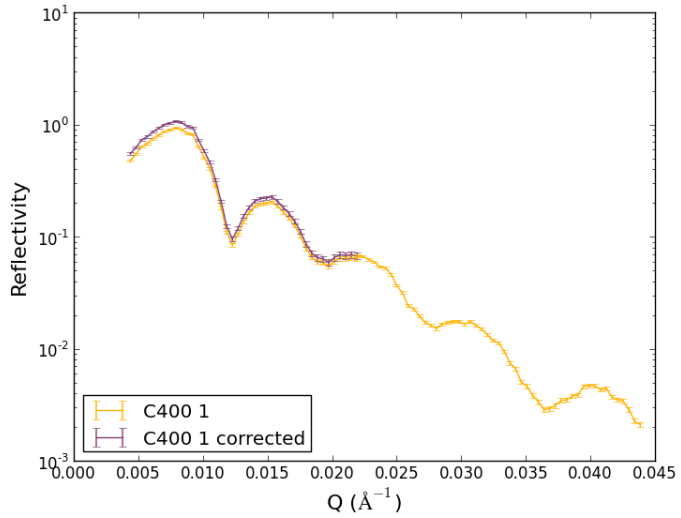

(a) First dataset following electrolyte introduction

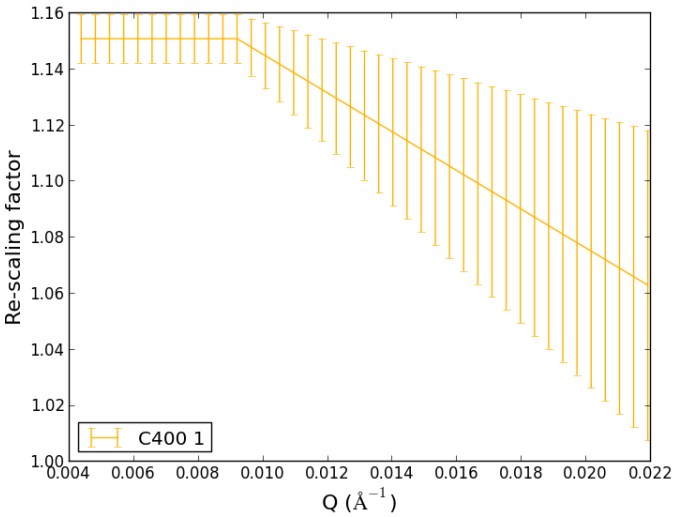

(b) Correction applied to first dataset following electrolyte introduction

Figure 5.11: Reduced NR dataset for potential hold experiment highlighting the discrepancy between the first two angular ranges.

For all NR datasets within the potential hold sample there are discontinuities between the first two angular regions. The angular regions are described in table 3.5. Two examples of this discontinuity are highlighted in figure 5.12 which shows an obvious discontinuity between the first two angular ranges within the dataset. The discrepancy between those two angular ranges are due to sample warp. The first

angular range uses a very tight slit set at 0.05 mm, whereas the second angular range uses a slit width of 0.2 mm. The significant difference in slit width means that at very low angles warp will deflect the part of the beam outside the slit width, but at larger slit widths the effect is less pronounced.

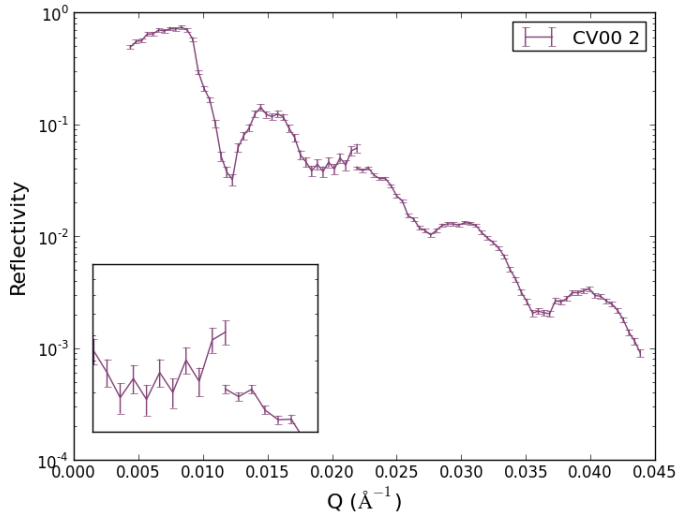

(a) Second dataset collected following electrolyte introduction

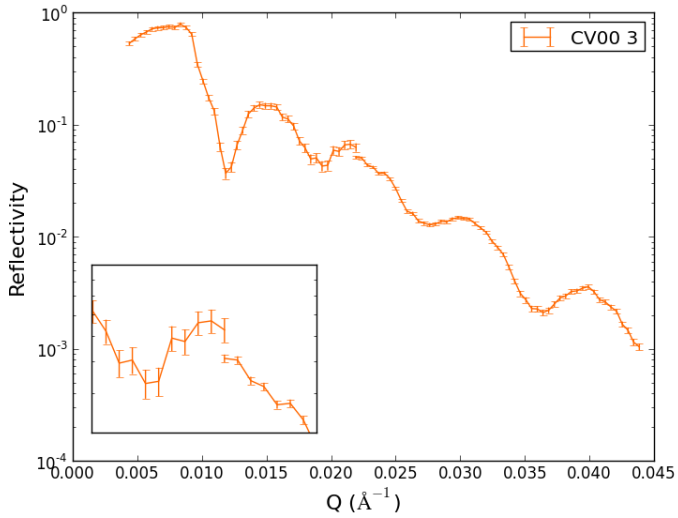

(b) Third dataset collected following electrolyte introduction

Figure 5.12: Reduced NR dataset for potential hold experiment highlighting the discrepancy between the first two angular ranges.

Figures 5.13 and 5.14 shows the correction function applied to those datasets from

figure 5.12 along with those corrected reflectivity data. Corrections for scans which are not shown here may be found in appendix B.

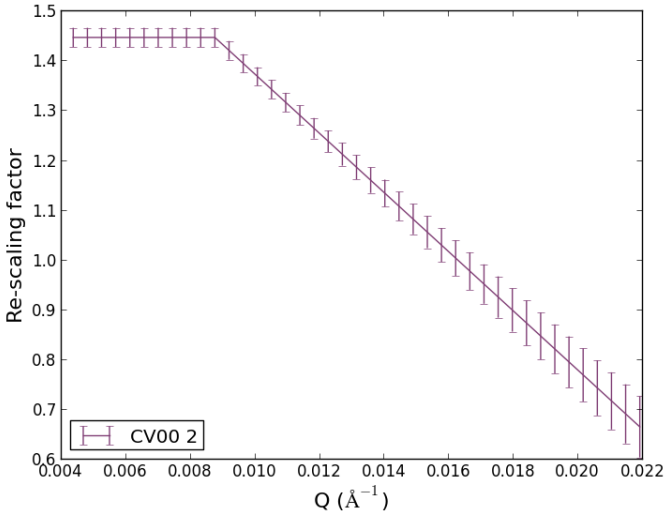

(a) Correction function applied to the second dataset from those data following electrolyte introduction.

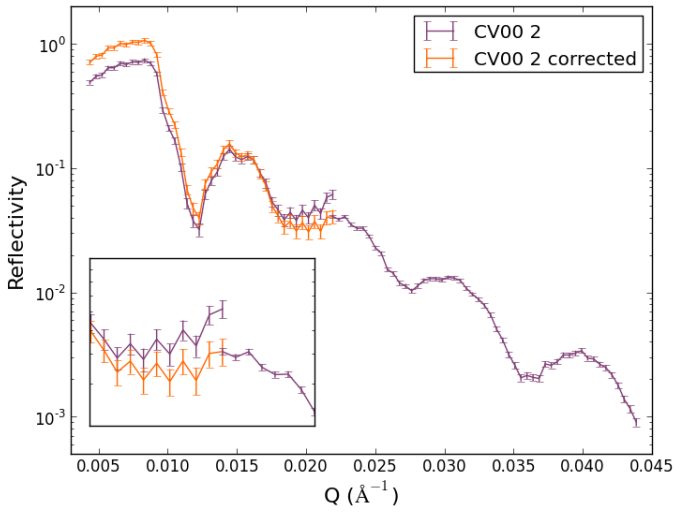

(b) Second dataset collected following electrolyte introduction with correction

Figure 5.13: Correction function and corrected reflectivity data for second dataset following electrolyte introduction for potential hold sample.

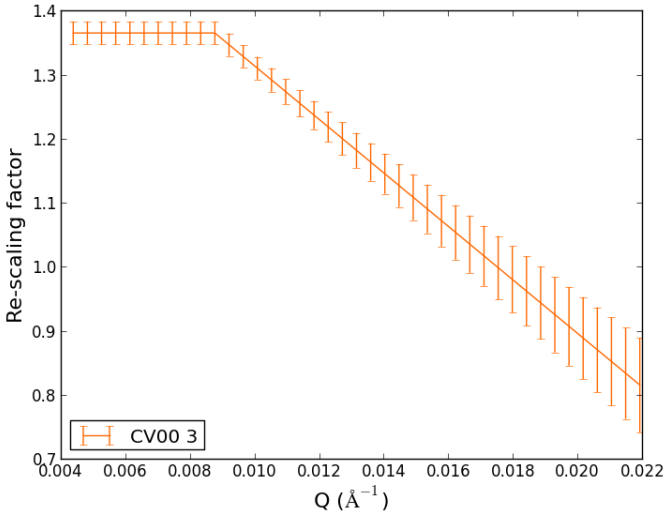

(a) Correction function applied to the third dataset from those data following electrolyte introduction

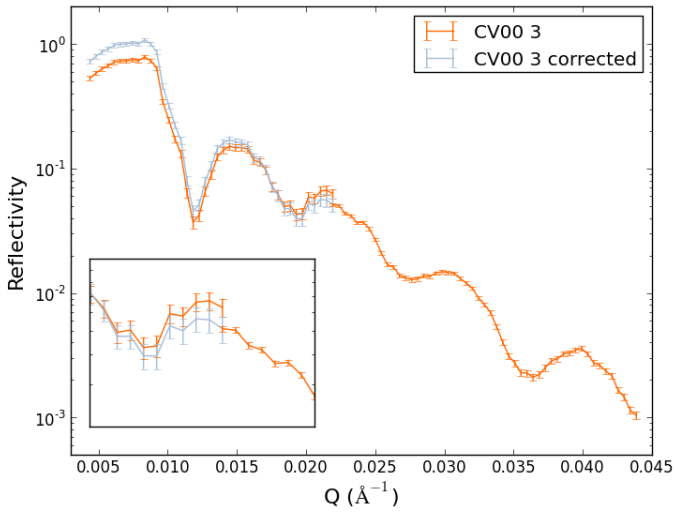

(b) Third dataset collected following electrolyte introduction with correction

Figure 5.14: Correction function and corrected reflectivity data for third dataset following electrolyte introduction for potential hold sample.

There are two interesting features which arise from this re-scaling analysis. The first that the maximum reflectivity of an NR dataset prior to correction vs Q where that maximum reflectivity occurs shows identical behavior to the maximum reflectivity vs scan as shown in figure 5.15. It is additionally interesting that the maximum

reflectivity as a function of position shows very similar behavior as a function of measurement point. The magnitude of change in Q between the first and last scan is on the order or 0.15° which is significant given the uncertainty in the position of the detector is ∼0.003°. This indicates some change in the sample thin-films which reduces the de-focusing effect highlighted by reflectivity being substantially less than unity to a focusing effect indicated through the reflectivity being greater than 1 in CV 26.

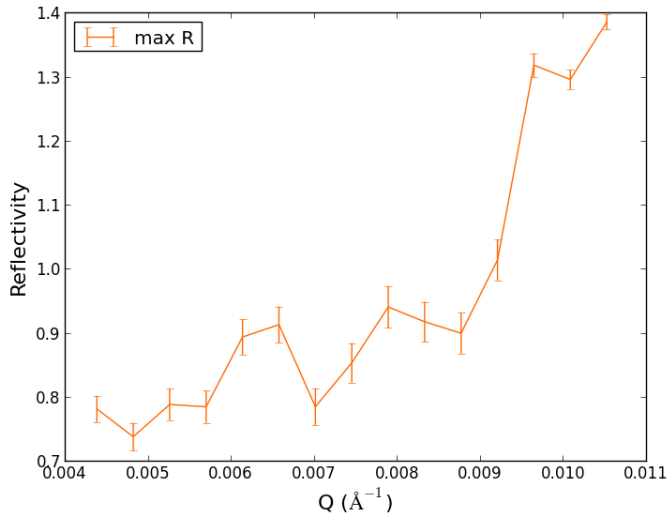

(a) Max R vs Q

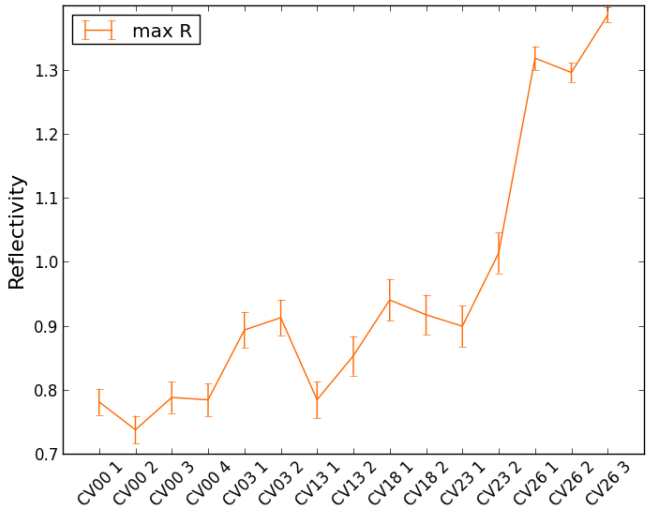

(b) Max R vs scan

Figure 5.15: a) Potential hold sample maximum reflectivity as a function of Q position of the maximum reflectivity and b) Potential hold sample maximum reflectivity as a function of cycle number. If no dependence upon cycling it would be expected that a) would be randomly distributed roughly around a few points in the critical edge and b) normally distributed around a common value.

The endpoint of the correction shows fair consistency with an average value of 0.742. Figure 5.16 shows the rescaling factor at the endpoint as a function of scan number. The consistency of the endpoint value indicates similar warp effects at that

position. The endpoint value less than unity indicates the reflectivity is focusing in this condition.

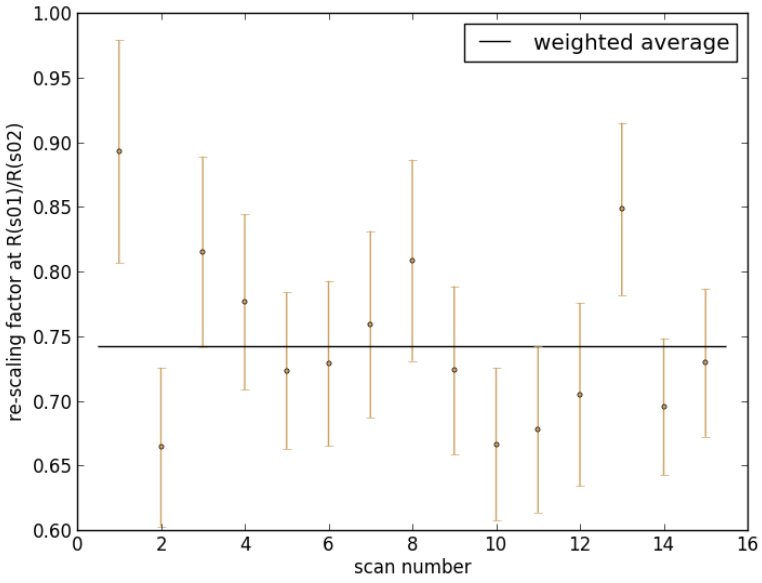

Figure 5.16: Endpoint as a function of scan highlighting consistent endpoint values. Consistency indicates warp at the footprint given by the incident angle remains relatively constant unlike the maximum reflectivity.

Following the application of a correction to each dataset, the datasets are combined where applicable and reduced. Those combined-reduced corrected data include an uncertainty which is based upon the square root of the corrected detector counts and is combined with the correction uncertainty after the reduction.

5.2.1 Open Circuit experiment

5.2.1.1 Electrolyte Injection

Data presented in the previous chapter on the open circuit sample prior to CV cycling are fit to a model as presented in equations 5.3 and 5.4. While the NR in-air results indicate only one cathode layer is required to adequately fit these data, using one layer in the model results in poor fits. Through allowing two-layers to define the

cathode more reasonable fitted results were achieved. The starting parameters for these models are drawn from the in-air characterization parameters with the exception of the electrolyte. The electrolyte starting SLD is estimated as $3.9*10^{-6}$ $\AA^{-2}$ from 10 ml of a 1:1 mixture of EC:DMC-d6 with 1.016 g $LiClO_4$ dissolved. The solution expands approximately 3.1 % upon dissolution of the electrolyte salt which is accounted for in the SLD estimation. The starting point for the SEI SLD in the model suggested in equation 5.3 is chosen as halfway between the electrolyte and LMO_2 layers, 100 $\AA$ thickness, and 40 $\AA$ interface. These values are very rough estimations, but also show the power of the Refl1D software. As the parameter space will be searched anyway the initial guess of the SEI layer parameters does not have much of an outcome on the final result as many of the other parameters are already well known. If the starting point does have an impact on the final fitted parameters it shows the fitting algorithm has not had a long enough period to probe the search space and should be re-run with a longer burn-in step.

$$Si/SiO_2/Pt/LMO_1/LMO_2/SEI/Electrolyte \tag{5.3}$$

$$Si/SiO_2/Pt/LMO_1/LMO_2/Electrolyte \tag{5.4}$$

Figure 5.17 shows the fitted results using both models applied to the open circuit sample data following electrolyte injection but prior to any electrochemical cycling. The fitted results indicate the model with an SEI layer is required in order to adequately describe the reflectivity data. Figure 5.18 shows the residual for these models applied to the open circuit data prior to electrochemical cycling. The model without an SEI appears to do an adequate job describing these data; however, in examining the SLD profile in figure 5.19 it becomes apparent that the model has arrived at an unrealistic result. Table 5.5 provides the fitted values for the model with SEI.

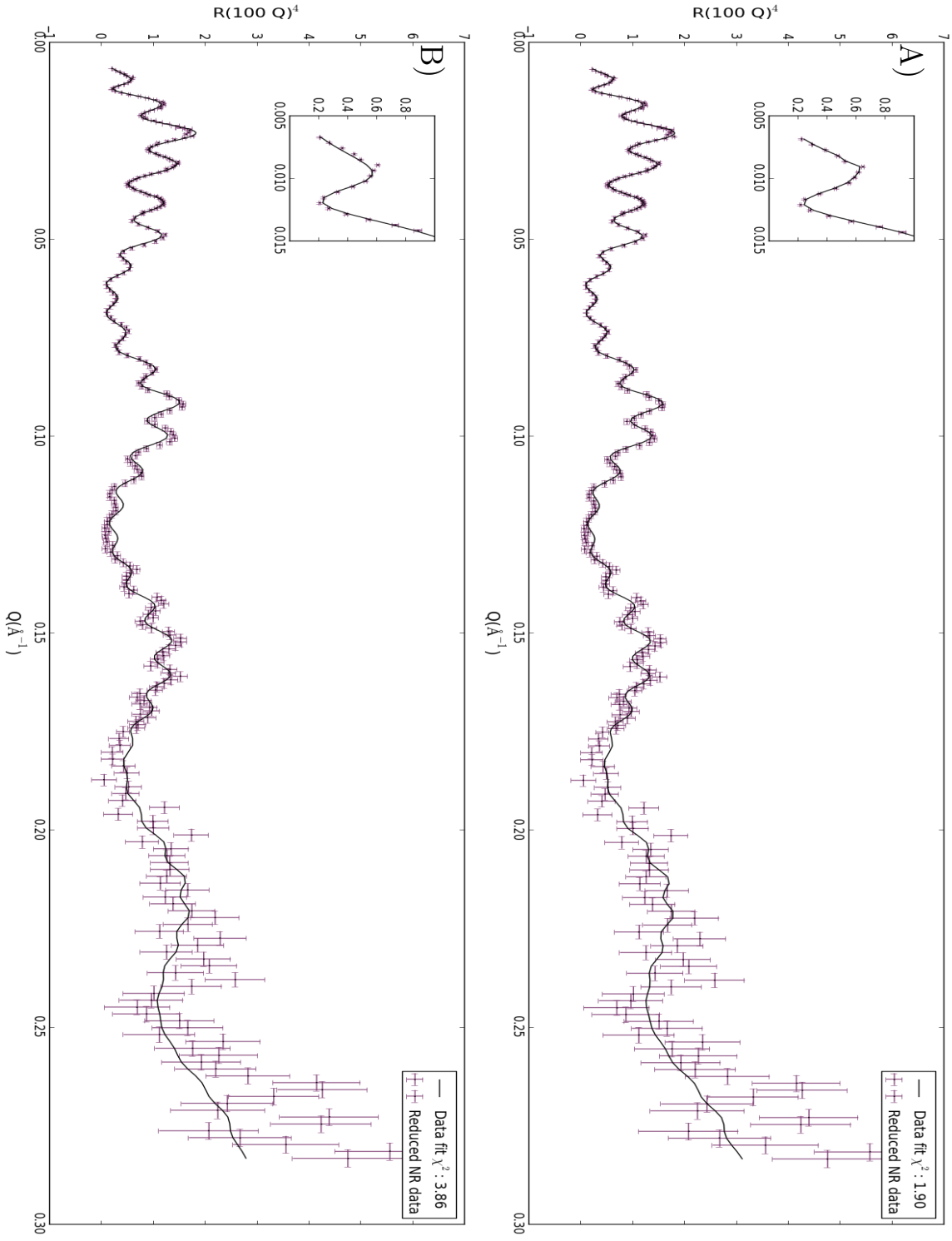

Figure 5.17: Fits to NR open circuit sample data with and without an SEI layer following electrolyte injection into the NR sample cell. A) With SEI layer, B) Without SEI layer.

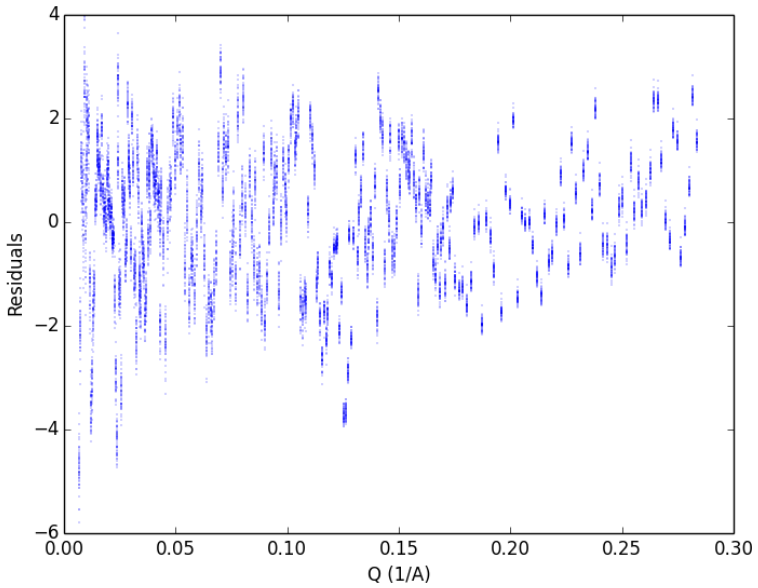

(a) With SEI

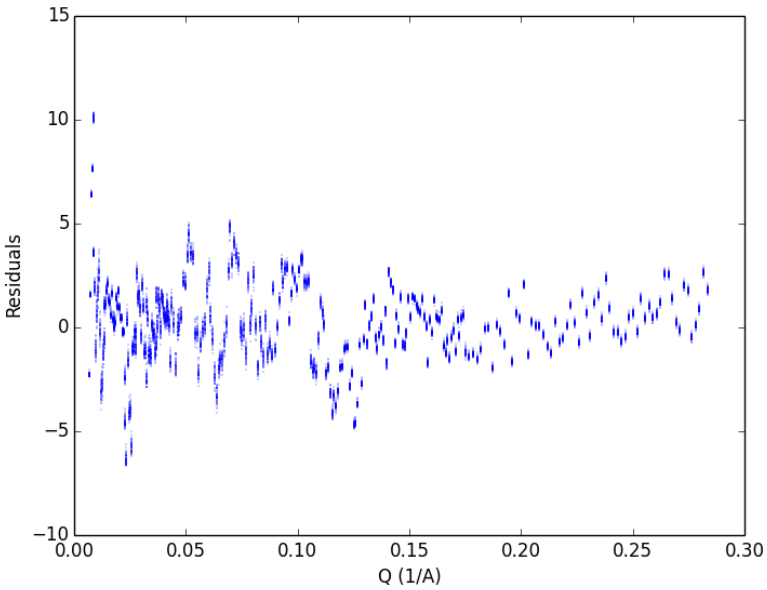

(b) Without SEI

Figure 5.18: Residuals from NR data fit to models with and without an SEI layer from the potential hold sample following electrolyte injection. Both residuals show good agreement with those data.

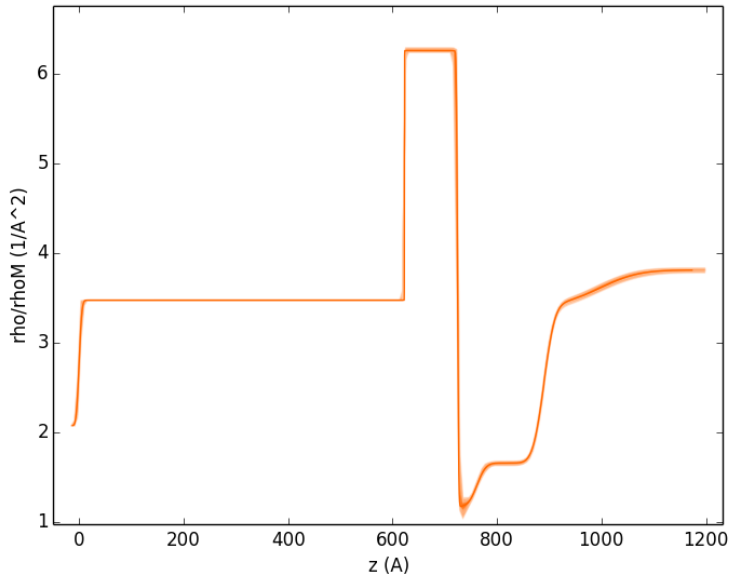

(a) With SEI

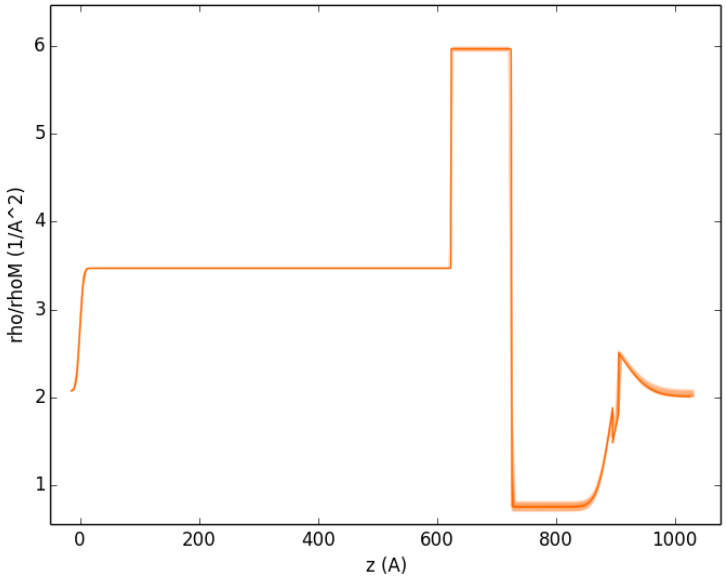

(b) Without SEI

Figure 5.19: SLD profiles including uncertainty for NR fits with and without an SEI layer to the open circuit sample following injection of electrolyte into the NR cell. The uncertainty is given by shaded bands showing 1, 2, and 3 σ on all parameters given in the model.

Table 5.5: Fitted NR results for the open circuit sample following electrolyte injection prior to any electrochemical cycling.

NR				
Layer	thickness ($\mathring{A}$)	SLD ($10^{-6}\mathring{A}^{-2}$)	SLDi ($10^{-6}\mathring{A}^{-2}$)	Interface ($\mathring{A}$)
Si	-	2.07	0.00024	3.5 (86)
SiO_2	622.69 (28)	3.47	0.00011	0.38 (21)
Pt	101.67 (15)	6.257 (12)	0.0189	1.67 (86)
LMO_1	36.3 (32)	1.141 (77)	0.0038	13.5 (28)
LMO_2	128.9 (31)	1.6495 (13)	0.0038	16.54 (52)
SEI	103.8 (31)	3.395 (39)	0.00917	60.0 (70)
Electrolyte	-	3.808 (10)	0.00917	-
$LiMn_2O_4$ total thickness: 165.24 (35) Intensity: 1.056 Θ offset: -0.00299 (57) Background: 319*10^{-8}(26)				

The fitted electrolyte SLD value in this case is about 0.1*10^{-6} $\mathring{A}^{-2}$ different from the estimate which is far enough to warrant an examination of the fitted result when the electrolyte SLD is held at the expected value of 3.9*10^{-6} $\mathring{A}^{-2}$. The result is generally the same between the models. The χ^2 for the model without holding the electrolyte SLD is 1.90 and has a BIC from equation 3.11 of 639.6. The χ^2 for the model holding the electrolyte SLD is 2.37 and has a BIC of 766.4, both of which indicate the freely varying electrolyte SLD value is more statistically significant.

The overall thickness of the cathode layer from air to electrolyte changes by 13 $\mathring{A}$ but the interface stays generally constant. This corresponds to around an 8.5% increase in layer thickness. The SLD change of the $LiMn_2O_4$ layer from the sample in air vs in electrolyte decreases instead of the expected increase from 1.744*10^{-6} $\mathring{A}^{-2}$ to 1.6495*10^{-6} $\mathring{A}^{-2}$. This change is unexpected since the porosity in the sample should lead to SEI formation within the cathode layer as well as on it which should lead to an increase in the cathode SLD.

The decrease is likely due to additional lithium in the structure from self-discharge. As discussed in section 2.2.3.3 self-discharge leads to the uptake of lithium into $LiMn_2O_4$ leading to the formation of $Li_2Mn_2O_4$. $Li_2Mn_2O_4$ exhibits a lower-SLD

due to the additional lithium which has a negative bound coherent scattering length.

Further information suggesting this is the case comes from the open-circuit voltage measurement throughout the experiment. These NR data were collected over half-way through the 22.5 hr open-circuit period where the measured voltage was below 2000 mV. This is in the same potential range as $Li_2Mn_2O_4$ (55).

Another way to roughly explore these results are to assume the difference between the SLD determined in air for the cathode layer and the theoretical value are open pores which is approximately 9.8%. If that fraction is open to the electrolyte then based upon the observed cathode layer coverage with an SEI the open pores should then also be filled with a SEI. A mixture of 9.8% SEI SLD and in-air SLD the expected cathode layer SLD in electrolyte would be $2.076*10^{-6}$ $\mathring{A}^{-2}$ which is much larger than the fitted value of $1.6495*10^{-6}$ $\mathring{A}^{-2}$. Based upon the previous supposition that the cathode layer experiences self-discharge the assumption is made that the cathode undergoes a phase change. We can estimate the SLD assuming a 6% (102) volume change due to the change of phase. The expected cathode SLD given a phase change to $Li_2Mn_2O_4$ would be $1.369*10^{-6}$ $\mathring{A}^{-2}$. If we add in the estimated 9.8% fraction composed of SEI the estimated cathode SLD is $1.701*10^{-6}$ $\mathring{A}^{-2}$ which is close to the observed fitted value of $1.6495*10^{-6}$ $\mathring{A}^{-2}$. This rough approximation provides some explanation as to why the layer SLD drops from the in-air case and is supported by literature showing the phase change occurs.

5.2.1.2 Following 1 CV cycles

Following one CV cycle the NR results showed significant change from prior to cycling. Models from equations 5.3 and 5.4 are applied to these data and are shown in figure 5.20. In this case the electrolyte SLD is held constant to the value fit for the electrolyte injection case. This is due to unreasonable fitted models if the electrolyte SLD is allowed to vary. From figure 5.20 it is observed that both models fit these

data with similar chi-square values. Further BIC values from these models a are 758.6 and 756.6 indicating the additional layer does not provide a statistical benefit to the resulting fit.

The fitted SLD profile with uncertainty as well as the residual for the model without an SEI can be found in figure 5.21. From figure 5.21 it appears that the interpretation of the two-layer structure does not represent two-layers in the cathode. The second cathode layer in the model is better represented by an SEI which transitions to the electrolyte over a very wide range. This result indicates that severe degradation of the cathode layer occurred in the one CV cycle.

The fitted SLD of the apparent cathode layer is $3.169*10^{-6}$ $\mathring{A}^{-2}$ which is significantly higher than the previous $1.6495*10^{-6}$ $\mathring{A}^{-2}$. This change indicates excessive breakdown of the cathode layer. This is further highlighted by the very thick SEI layer which has a lower-SLD of $2.899*10^{-6}$ $\mathring{A}^{-2}$. The cathode layer also shows a large change in layer thickness, from $\sim$165 $\mathring{A}$ before the first CV cycle to $\sim$ 86 $\mathring{A}$ following the first CV cycle.

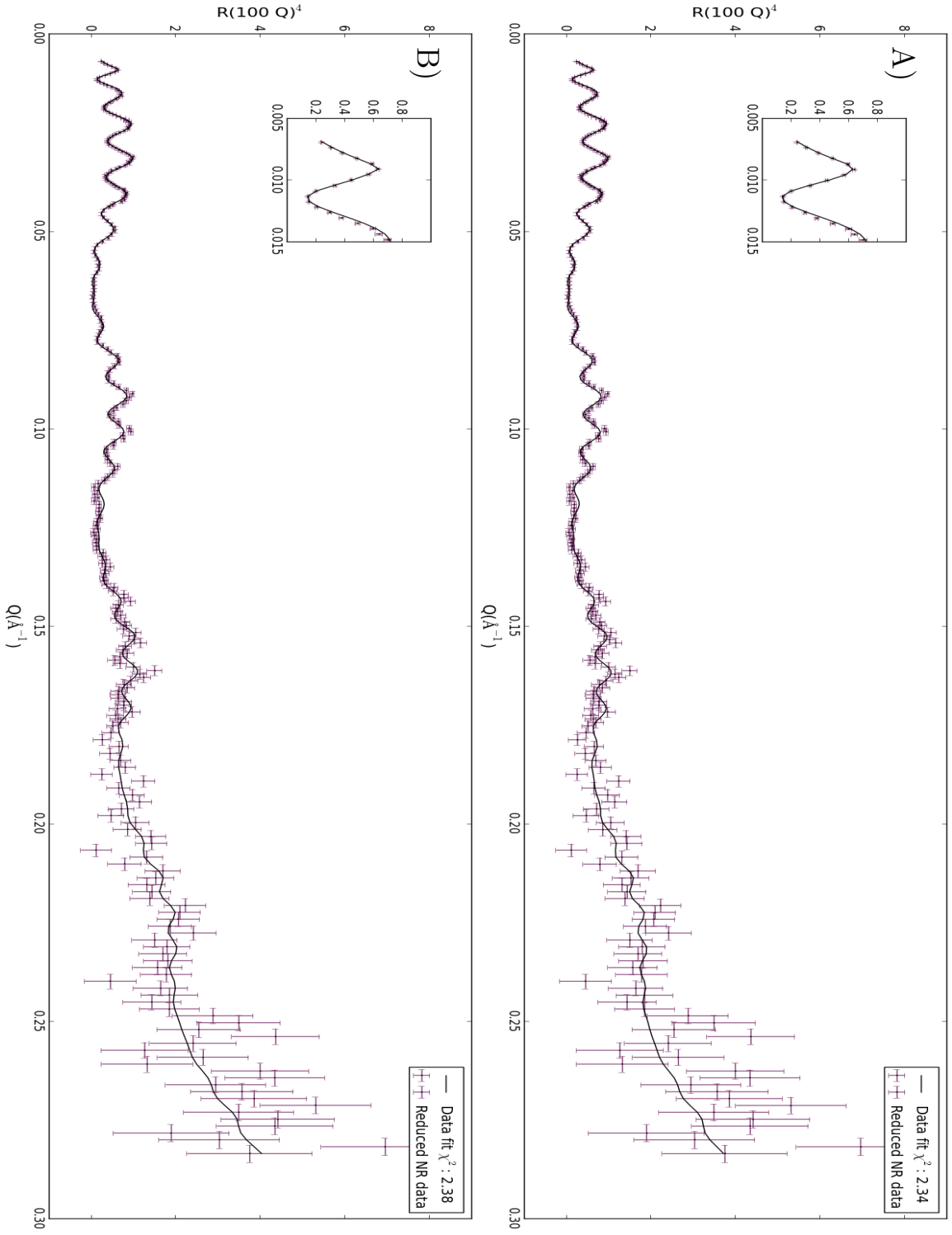

Figure 5.20: Fits to NR open circuit sample data with and without an SEI layer following one CV cycle. A) With SEI layer, B) Without SEI layer.

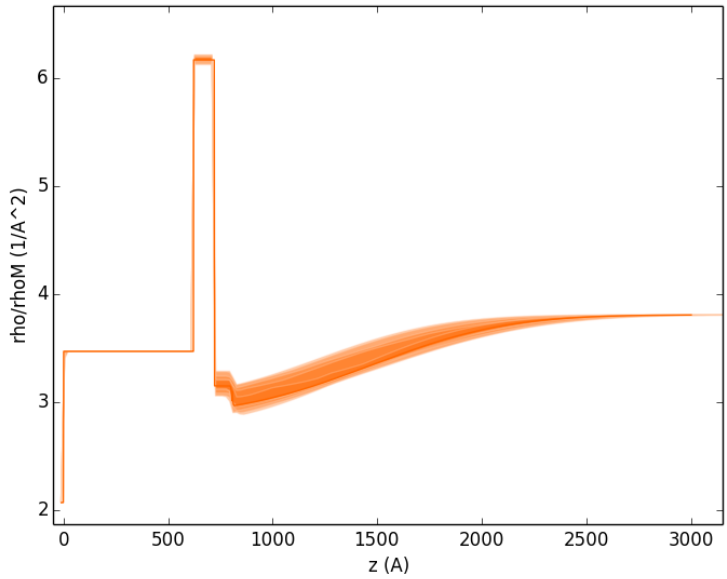

(a) SLD profile with uncertainty

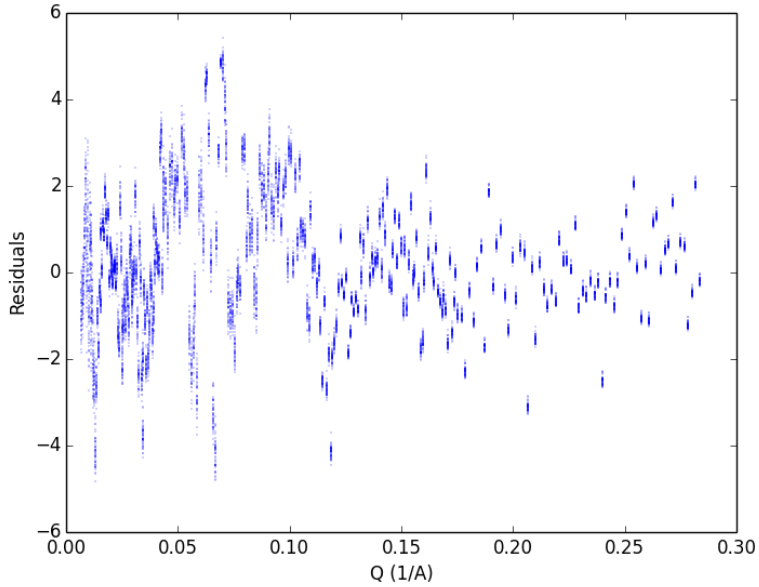

(b) CV1 fit residual

Figure 5.21: SLD profile with uncertainty and fit residual for the model fit to CV1 data using two layers to represent the region between the Pt layer and the electrolyte.

The breakdown of the cathode layer is not necessarily unexpected. The Jahn-Teller effect is known to cause breakdown of the crystal-structure because of the inability of the $LiMn_2O_4$ structure to handle the large volume change due to the effect.

Further $Li_2Mn_2O_4$ is known to decompose into Li_2MnO_3 and MnO, where the MnO is known to dissolve into the electrolyte. It was suggested in the electrolyte injection case that a phase change to $Li_2Mn_2O_4$ occurs. Following the one CV cycle it is observed that the attempt to remove lithium from this fractured cathode due to the Jahn-Teller effect leads to breakup of the cathode. This is an interesting observation as it suggests that formation of $Li_2Mn_2O_4$ at open circuit is very susceptible to breakup.

5.2.2 Potential hold experiment

5.2.2.1 Electrolyte Injection

Corrected-reduced NR data for the potential hold sample following electrolyte injection and prior to electrochemical cycling are fit to the models suggested in equations 5.3 and 5.4. Other models such as holding the platinum SLD constant were explored but were rejected due to poor fitting results and unrealistic fitting parameters. The starting parameters for these models are drawn from the in-air characterization parameters with the exception of the electrolyte. The electrolyte starting SLD is estimated as $3.9*10^{-6}$ $\AA^{-2}$ from 10 ml of a 1:1 mixture of EC:DMC-d6 with 1.016 g $LiClO_4$ dissolved. The solution expands approximately 3.1 % upon dissolution of the electrolyte salt which is accounted for in the SLD estimation. The starting point for the SEI SLD in the model suggested in equation 5.3 is chosen as halfway between the electrolyte and LMO_2 layers, 100 $\AA$ thickness, and 40 $\AA$ interface. These values are very rough estimations, but also show the power of the Refl1D software. As the parameter space will be searched anyway the initial guess of the SEI layer parameters does not have much of an outcome on the final result as many of the other parameters are already well known. If the starting point does have an impact on the final fitted parameters it shows the program has not had a long enough period to probe the search space and should be re-run with a longer burn-in step.

Figure 5.22 shows the fitted results as $R*(100*Q)^4$ when applying the models

given in equations 5.3 and 5.4. The Q vs RQ^4 format is used to compare these fits as it emphasizes the difference between these models in a more straightforward manner than Log(R) vs Q. The goodness-of-fit is relatively close (1.26 with SEI vs 1.81 without SEI). The insets in figure 5.22 show the first fringe fits much better when the model with SEI is applied. Residuals for these fits are found in figure 5.26 which show both models adequately fit these NR data.

Figure 5.24 shows the SLD profiles with uncertainty for both models applied to those data. It is obvious in figure 5.24 that the uncertainty in the SLD profile for the model with an SEI is lower than that for the model without an SEI layer. The fitted electrolyte SLD is much lower than the estimated value for the model without an SEI layer. The fitted electrolyte SLD is very close to the estimated SLD for the electrolyte SLD which provides some confidence in the validity of the SEI layer model.

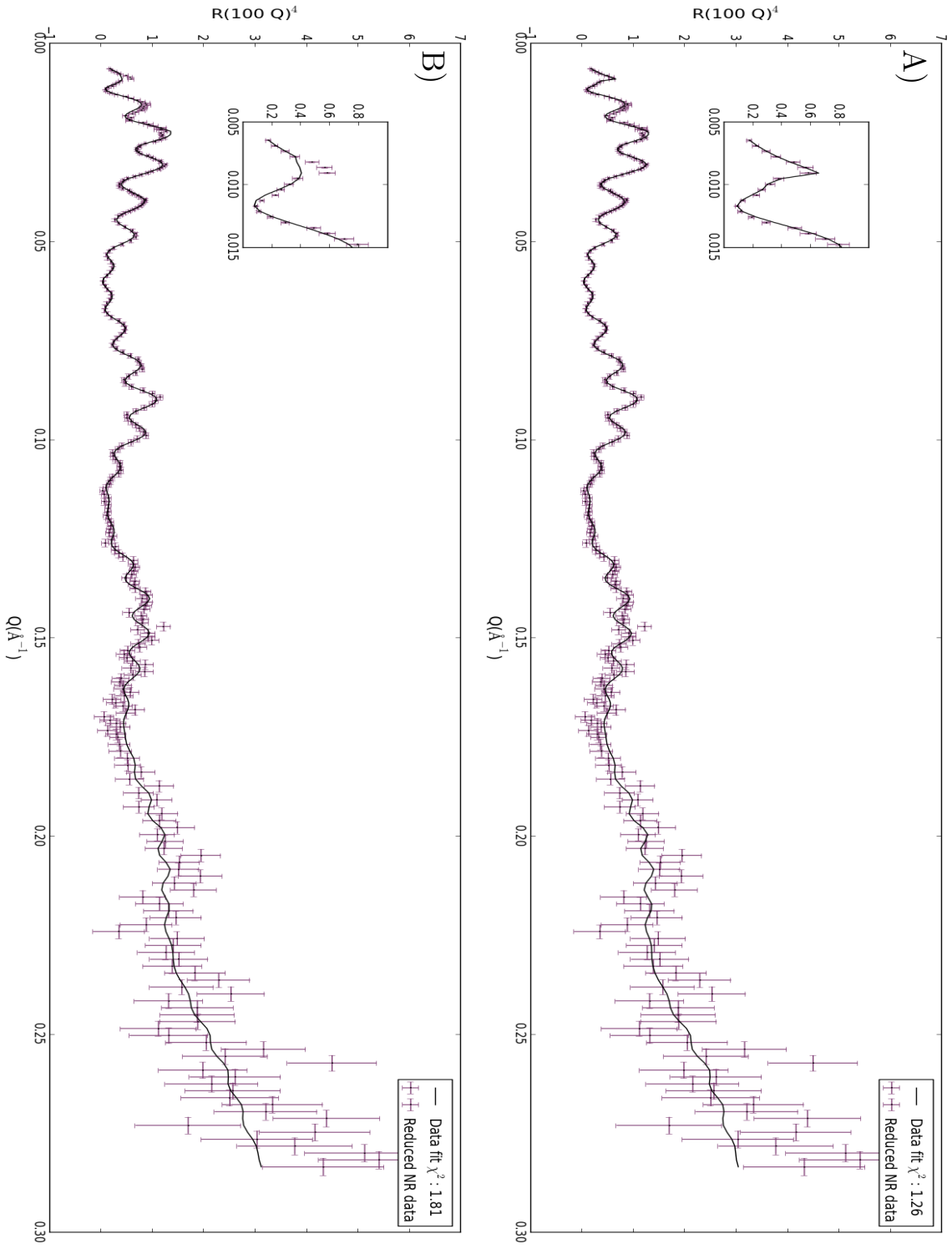

Figure 5.22: Fits to NR Potential hold sample data with and without an SEI layer following electrolyte injection into the NR sample cell. A) With SEI layer, B) Without SEI layer. Note the first fringe which is highlighted in the sub-plot shows the critical edge, where the model with SEI does a significantly better job reproducing the fringe.

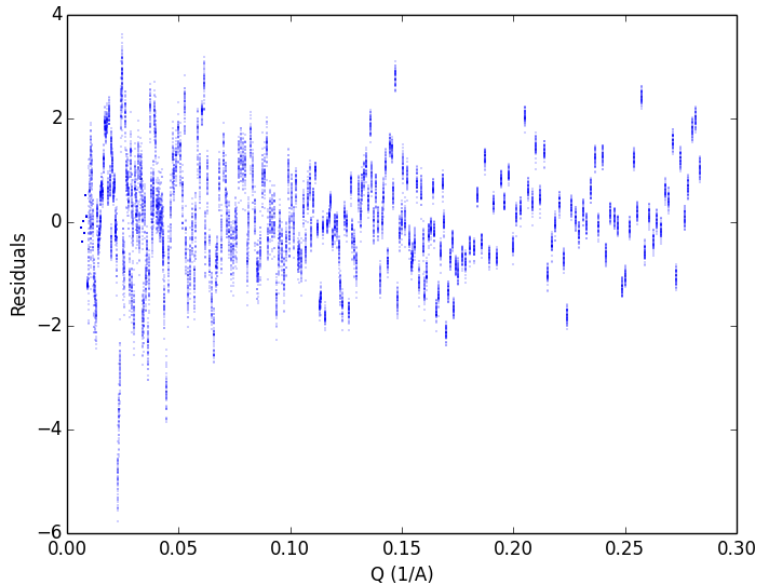

(a) With SEI

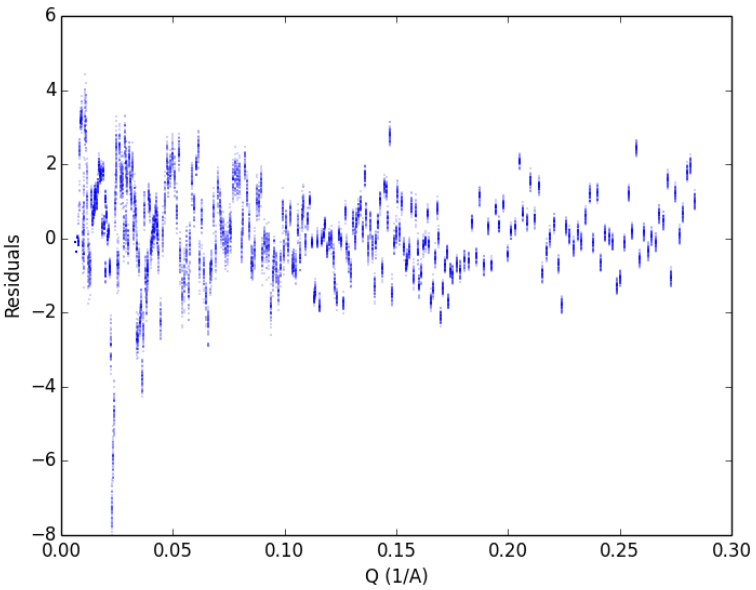

(b) Without SEI

Figure 5.23: Residuals from NR data fit to models with and without an SEI layer from the potential hold sample following electrolyte injection. Both residuals show good agreement with those data.

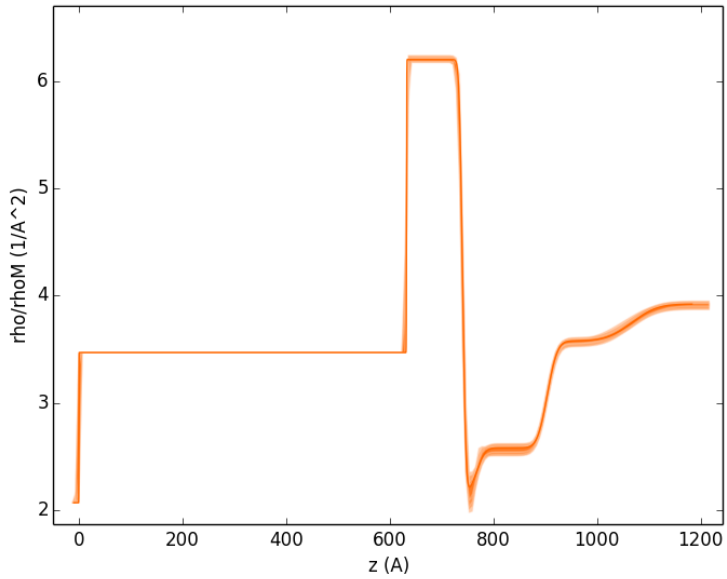

(a) With SEI

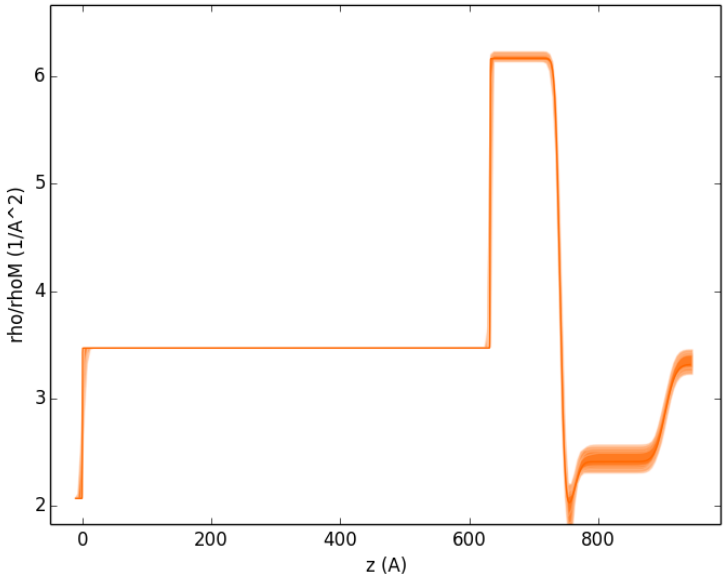

(b) Without SEI

Figure 5.24: SLD profiles including uncertainty for NR fits with and without an SEI layer to the potential hold sample following injection of electrolyte into the NR cell. The uncertainty is given by shaded bands showing 1, 2, and 3 σ on all parameters given in the model.

Table 5.6: Fitted NR results for the potential hold sample following electrolyte injection prior to any electrochemical cycling.

NR				
Layer	thickness ($\AA$)	SLD ($10^{-6}\AA^{-2}$)	SLDi ($10^{-6}\AA^{-2}$)	Interface ($\AA$)
Si	-	2.07	0.00024	1.41 (90)
SiO_2	632.06 (43)	3.47	0.00011	0.73 (47)
Pt	108.24 (47)	6.197 (16)	0.0189	5.50 (83)
LMO_1	24.5 (59)	1.99 (20)	0.0038	11.6 (52)
LMO_2	138.8 (56)	2.562 (29)	0.0038	15.3 (10)
SEI	163 (16)	3.565 (24)	0.00917	41.5 (42)
Electrolyte	-	3.911 (25)	0.00917	-
$LiMn_2O_4$ total thickness: 163.12 (90) Intensity: 1.0 Θ offset: -0.00273 (56) Background: 474*10^{-8}(26)				

5.2.2.2 Following 3 CV cycles

Following 3 CV cycles the cell is held at 3300 mV throughout NR data collection. These data use the same models applied to the dataset following electrolyte injection from equations 5.4 and 5.3. Figure 5.25 shows the fitted results as R*(100*Q)^4 to emphasize the critical edge. From figure 5.25 the model with an SEI does a much better job fitting the critical edge as seen in the inset on those plots. Similar to those data following electrolyte injection the residuals found in figure 5.26 show no significant features indicating poor fits.

Figure 5.27 shows the SLD profiles with uncertainty for both models applied to those NR data following three CV cycles. It is obvious in figure 5.27 that the uncertainty in the SLD profile for the model with an SEI is lower than that for the model without an SEI layer. The fitted electrolyte SLD is much lower than the estimated value for the model without an SEI layer. The fitted electrolyte SLD is very close to the estimated SLD for the electrolyte SLD which provides further confidence in the validity of the SEI layer model.

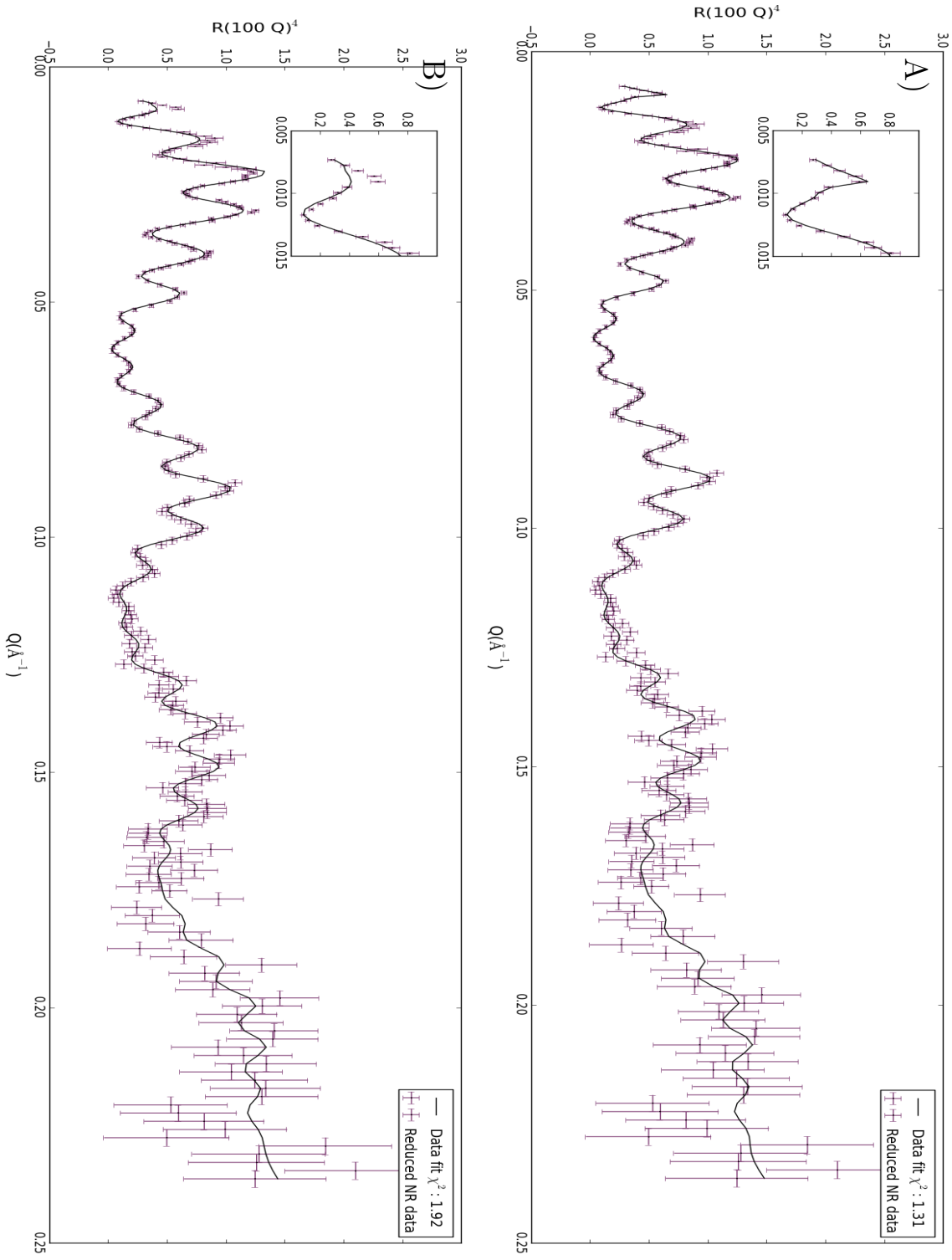

Figure 5.25: Fits to NR Potential hold sample data with and without an SEI layer following three CV cycles. The model with an SEI fits the critical edge much better than the model without an SEI. A) With SEI layer, B) Without SEI layer. Note the first fringe which is highlighted in the sub-plot shows the critical edge, where the model with SEI does a significantly better job reproducing the fringe.

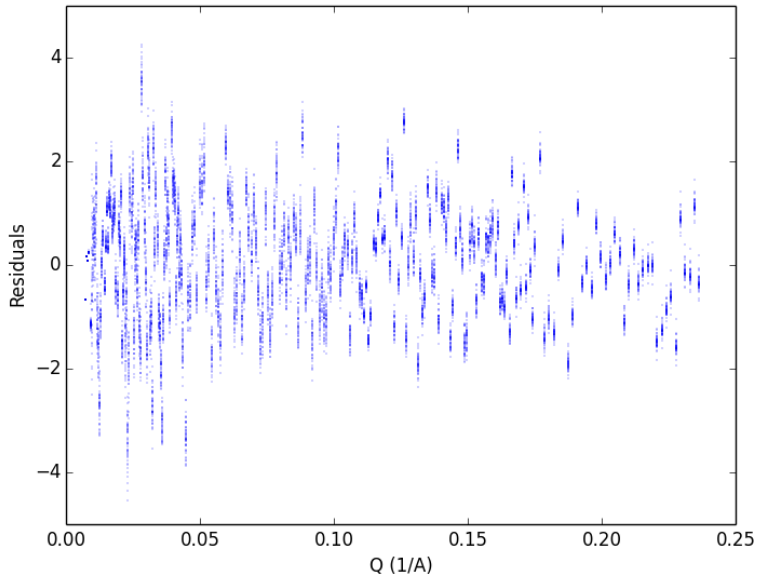

(a) With SEI

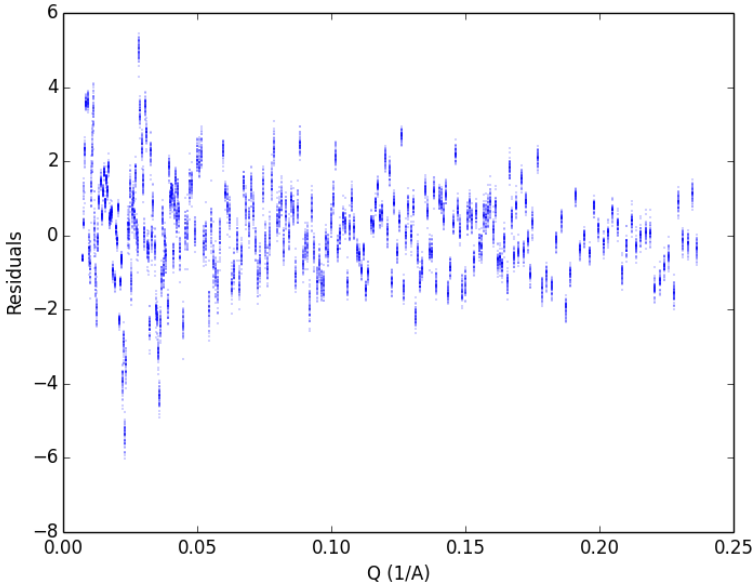

(b) Without SEI

Figure 5.26: Residuals from NR data fit to models with and without an SEI layer from the potential hold sample following three CV cycles. Both residuals show good agreement with those data.

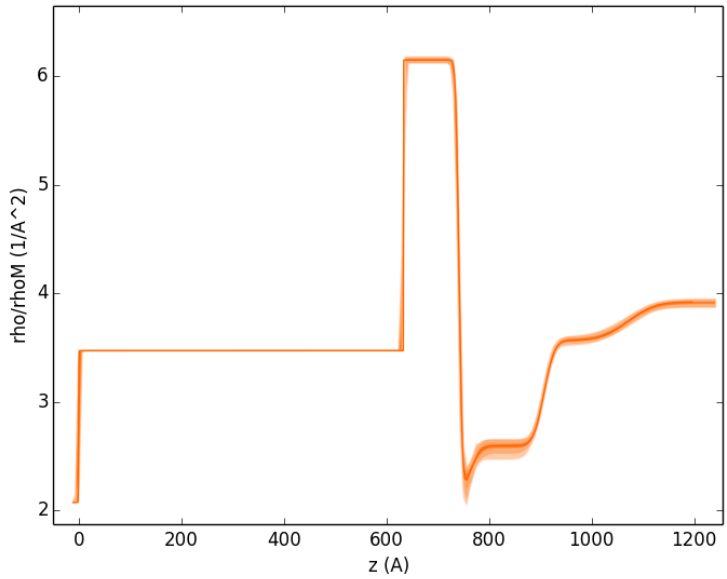

(a) With SEI

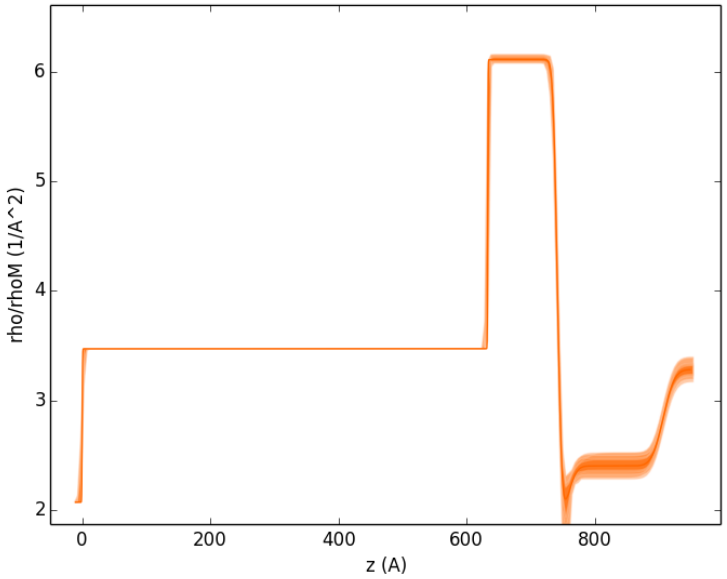

(b) Without SEI

Figure 5.27: SLD profiles including uncertainty for NR fits with and without an SEI layer to the potential hold sample following three CV cycles. The uncertainty is given by shaded bands showing 1, 2, and 3 σ on all parameters given in the model.

Table 5.7: Fitted NR results for the potential hold sample following 3 CV cycles.

NR				
Layer	thickness ($\mathring{A}$)	SLD ($10^{-6}\mathring{A}^{-2}$)	SLDi ($10^{-6}\mathring{A}^{-2}$)	Interface ($\mathring{A}$)
Si	-	2.07	0.00024	1.19 (78)
SiO_2	633.20 (42)	3.47	0.00011	1.02 (66)
Pt	108.22 (40)	6.152 (16)	0.0189	4.73 (92)
LMO_1	23.1 (75)	2.11 (21)	0.0038	16.3 (58)
LMO_2	142.6 (73)	2.593 (27)	0.0038	16.5 (10)
SEI	164.8 (51)	3.566 (21)	0.00917	43.5 (35)
Electrolyte	-	3.912 (19)	0.00917	-
$LiMn_2O_4$ total thickness: 163.12 (90) Intensity: 1.0 Θ offset: -0.00280 (53) Background: 456*10^{-8}(33)				

5.2.2.3 Following 13 CV cycles

Following 13 CV cycles the cell is held at 3300 mV throughout NR data collection. These data use the same models applied to the dataset following electrolyte injection from equations 5.4 and 5.3. Figure 5.28 shows the fitted results as R*(100*Q)^4 to emphasize the critical edge. From figure 5.28 the model with an SEI does a much better job fitting the critical edge as seen in the inset on those plots. Residuals from those fits are found in figure 5.29 and show little deviation which would indicate poor models.

Figure 5.30 shows the SLD profiles with uncertainty for both models applied to those NR data following thirteen CV cycles. It is obvious in figure 5.30 that the uncertainty in the SLD profile for the model with an SEI is lower than that for the model without an SEI layer. The fitted electrolyte SLD is much lower than the estimated value for the model without an SEI layer. The fitted electrolyte SLD is very close to the estimated SLD for the electrolyte SLD which provides further confidence in the validity of the SEI layer model.

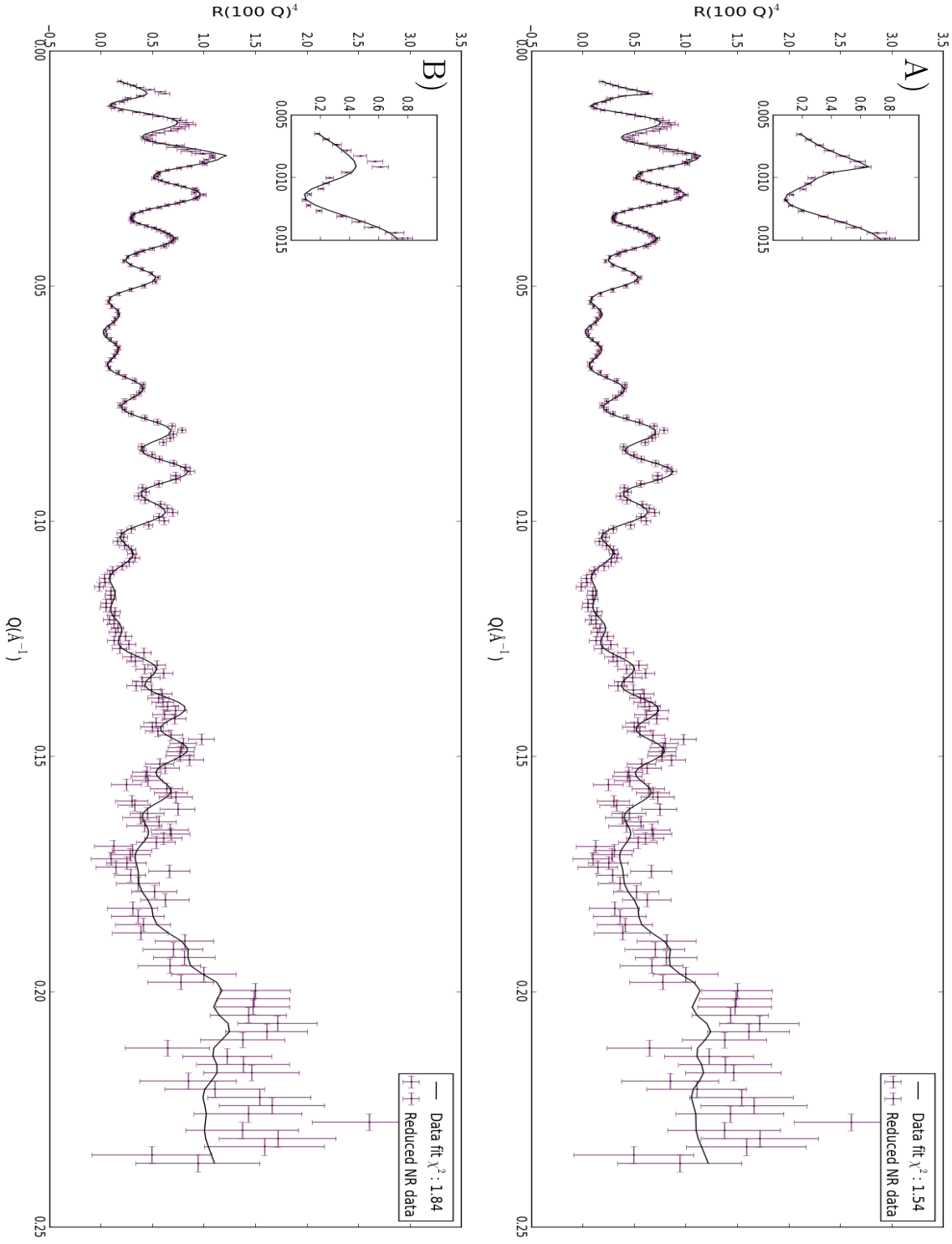

Figure 5.28: Fits to NR Potential hold sample data with and without an SEI layer following 13 CV cycles. The model with an SEI fits the critical edge much better than the model without an SEI. A) With SEI layer, B) Without SEI layer.

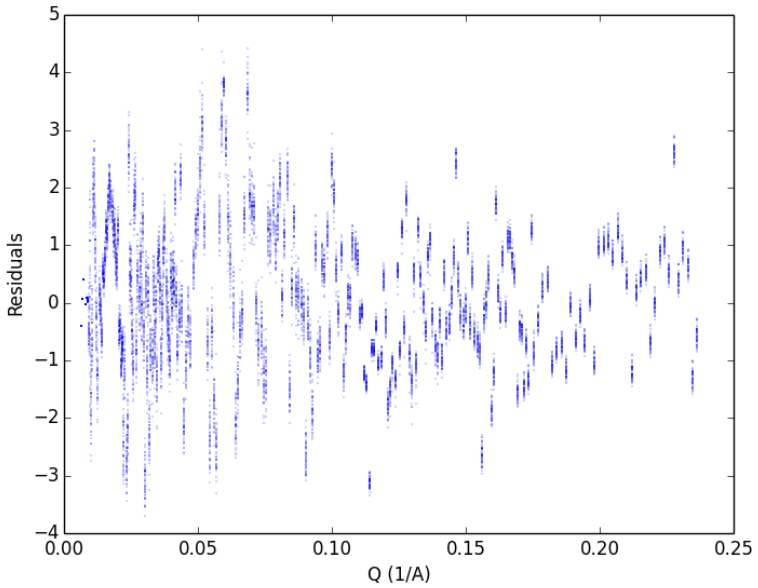

(a) With SEI

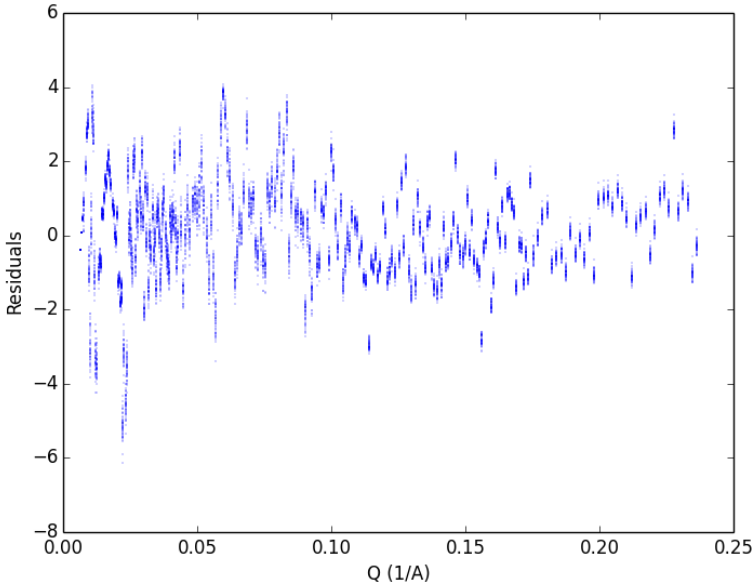

(b) Without SEI

Figure 5.29: Residuals from NR data fit to models with and without an SEI layer from the potential hold sample following 13 CV cycles. Both residuals show good agreement with those data.

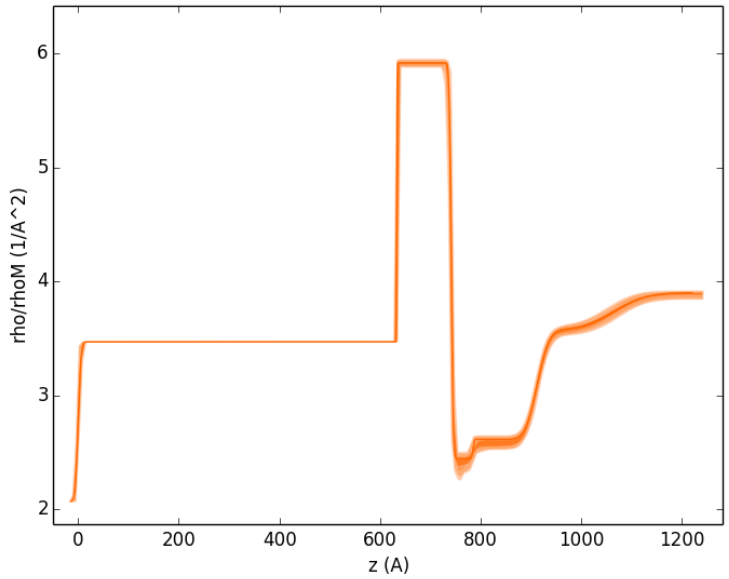

(a) With SEI

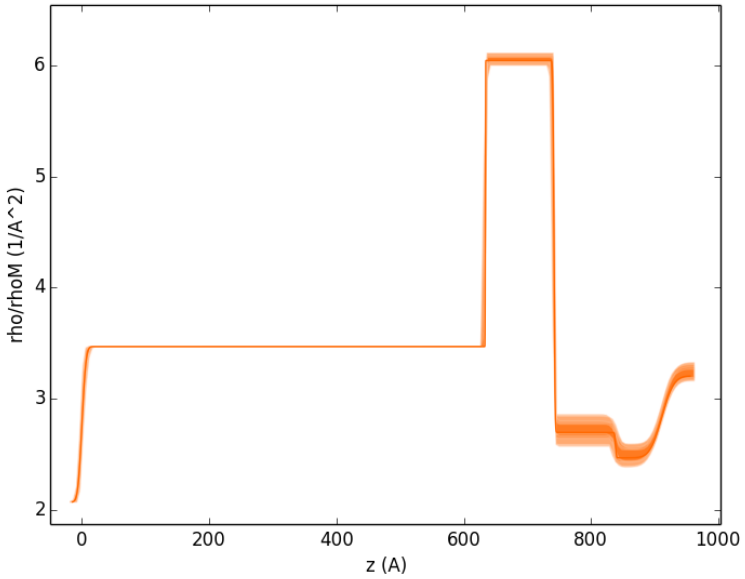

(b) Without SEI

Figure 5.30: SLD profiles including uncertainty for NR fits with and without an SEI layer to the potential hold sample following 13 CV cycles. The uncertainty is given by shaded bands showing 1, 2, and 3 σ on all parameters given in the model.

Table 5.8: Fitted NR results for the potential hold sample following 13 CV cycles.

NR				
Layer	thickness ($\mathring{A}$)	SLD ($10^{-6}\mathring{A}^{-2}$)	SLDi ($10^{-6}\mathring{A}^{-2}$)	Interface ($\mathring{A}$)
Si	-	2.07	0.00024	4.24 (68)
SiO_2	632.96 (48)	3.47	0.00011	0.71 (46)
Pt	108.36 (25)	5.916 (20)	0.0189	3.10 (10)
LMO_1	40.7 (84)	2.404 (77)	0.0038	8.1 (53)
LMO_2	129.7 (83)	2.594 (38)	0.0038	18.9 (12)
SEI	129.7 (83)	3.564 (30)	0.00917	51.5 (56)
Electrolyte	-	3.896 (23)	0.00917	-
$LiMn_2O_4$ total thickness: 170.37 (80) Intensity: 1.0 Θ offset: -0.00054 (62) Background: 402*10^{-8}(34)				

5.2.2.4 Following 18 CV cycles

Following 18 CV cycles the cell is held at 4000 mV throughout NR data collection. These data use similar models applied to the dataset following electrolyte injection but do not include a second layer to describe the $LiMn_2O_4$ film. The models used for this dataset are found in equations 5.6 and 5.5. Figure 5.31 shows the fitted results as R*(100*Q)^4 to emphasize the critical edge. From figure 5.31 the model with an SEI does a much better job fitting the critical edge as seen in the inset on those plots. Residuals from those fits are found in figure 5.32 and show little deviation which would indicate poor models.

$$Si/SiO_2/Pt/LiMn_2O_4/SEI/Electrolyte \tag{5.5}$$

$$Si/SiO_2/Pt/LiMn_2O_4/Electrolyte \tag{5.6}$$

Figure 5.33 shows the SLD profiles with uncertainty for both models applied to those NR data following 18 CV cycles. It is obvious in figure 5.33 that the uncertainty in the SLD profile for the model with an SEI is lower than that for the model without

an SEI layer. The fitted electrolyte SLD is much lower than the estimated value for the model without an SEI layer. The fitted electrolyte SLD is very close to the estimated SLD for the electrolyte SLD which provides further confidence in the validity of the SEI layer model.

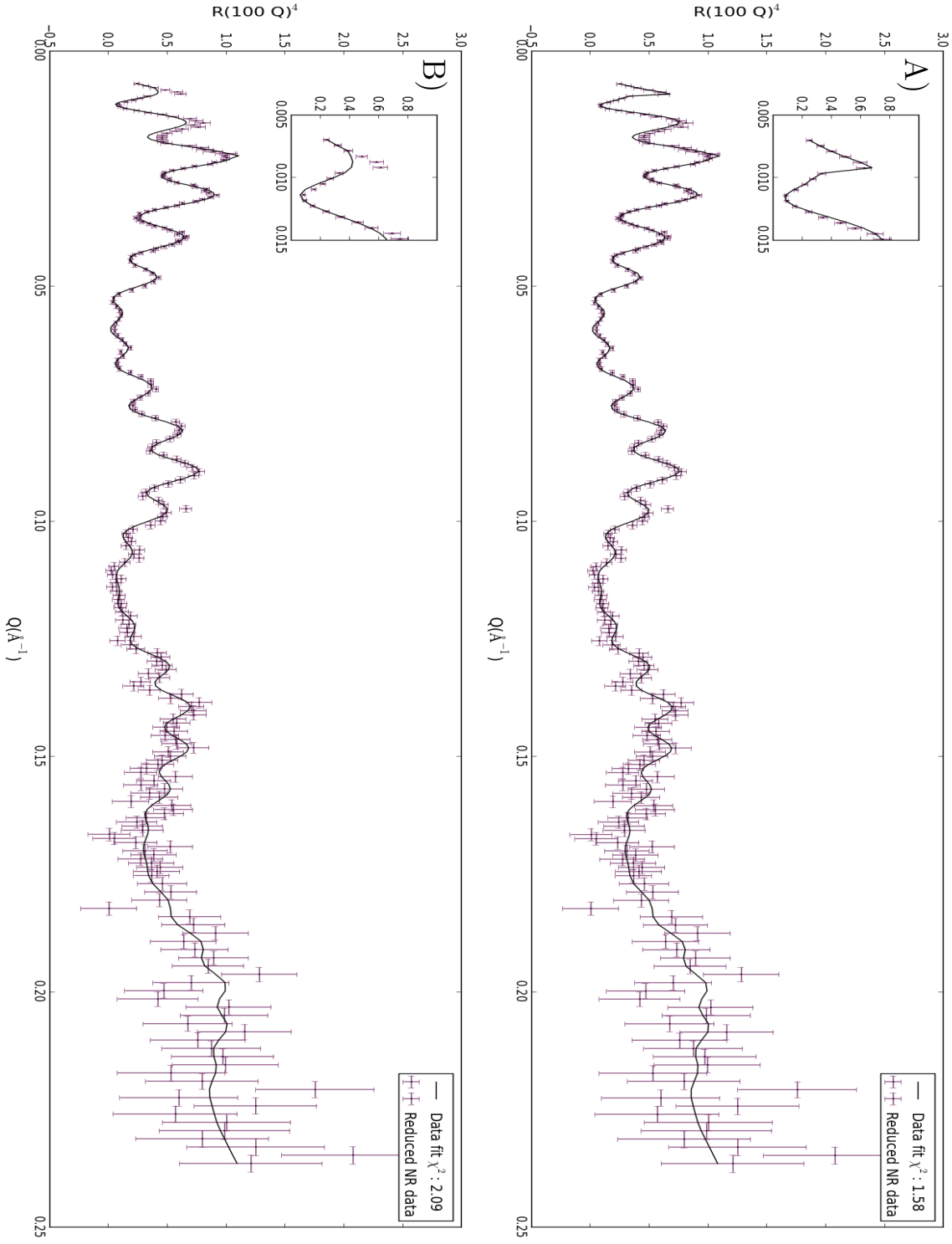

Figure 5.31: Fits to NR Potential hold sample data with and without an SEI layer following 18 CV cycles. The model with an SEI fits the critical edge much better than the model without an SEI. A) With SEI layer, B) Without SEI layer.

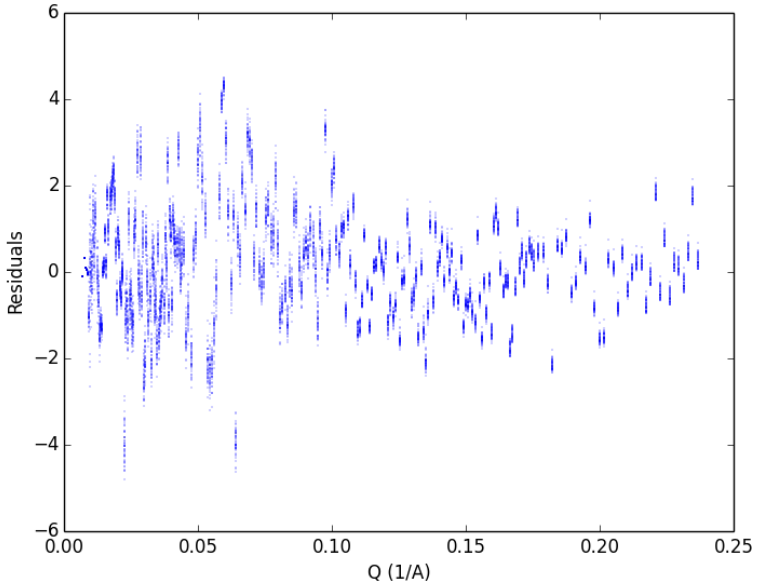

(a) With SEI

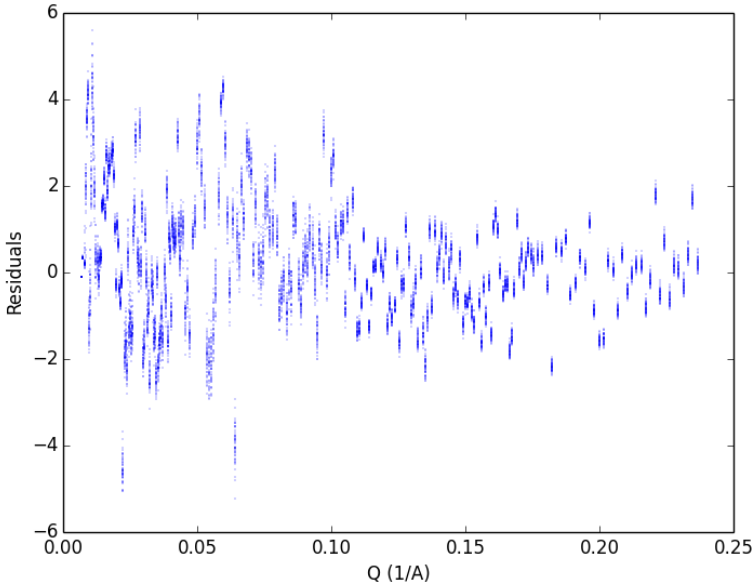

(b) Without SEI

Figure 5.32: Residuals from NR data fit to models with and without an SEI layer from the potential hold sample following 18 CV cycles. Both residuals show good agreement with those data.

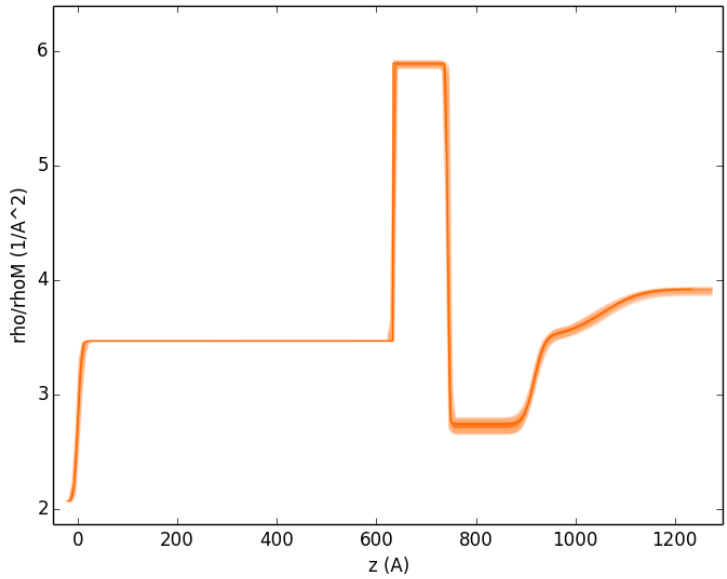

(a) With SEI

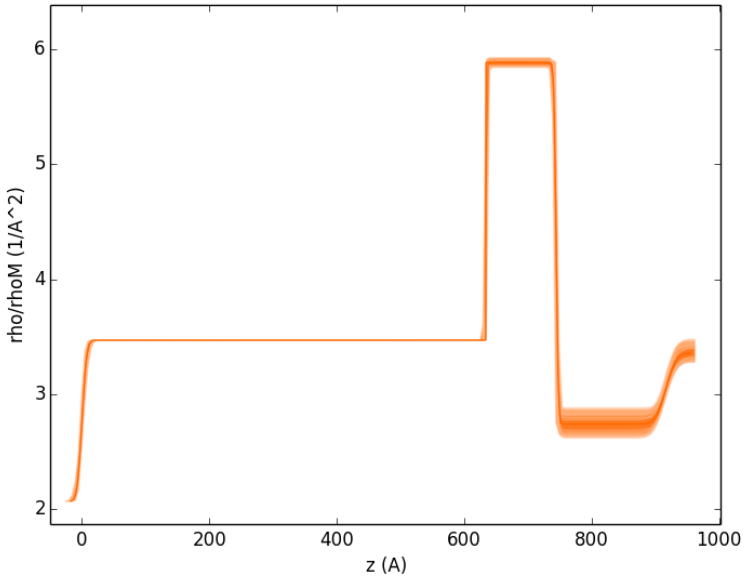

(b) Without SEI

Figure 5.33: SLD profiles including uncertainty for NR fits with and without an SEI layer to the potential hold sample following 18 CV cycles. The uncertainty is given by shaded bands showing 1, 2, and 3 σ on all parameters given in the model.

Table 5.9: Fitted NR results for the potential hold sample following 18 CV cycles.

NR				
Layer	thickness ($\mathring{A}$)	SLD ($10^{-6}\mathring{A}^{-2}$)	SLDi ($10^{-6}\mathring{A}^{-2}$)	Interface ($\mathring{A}$)
Si	-	2.07	0.00024	6.01 (81)
SiO_2	633.54 (49)	3.47	0.00011	0.72 (47)
Pt	110.26 (18)	5.884 (14)	0.0189	2.33 (85)
LMO	172.90 (91)	2.732 (33)	0.0038	17.2 (14)
SEI	137.2 (83)	3.503 (28)	0.00917	62.1 (60)
Electrolyte	-	3.916 (15)	0.00917	-
Intensity: 1.0 Θ offset: -0.00070 (60) Background: $352*10^{-8}$(29)				

5.2.2.5 Following 23 CV cycles

Following 23 CV cycles the cell is held at 4300 mV throughout NR data collection. These data use similar models applied to the dataset following 18 CV cycles as described by models 5.6 and 5.5. Figure 5.34 shows the fitted results as R*(100*Q)^4 to emphasize the critical edge. From figure 5.34 the model with an SEI does a slightly better job fitting the critical edge as seen in the inset on those plots. The model with SEI also does a better job fitting the second fringe in these data as opposed to the model without SEI which undershoots the second oscillation. Residuals from those fits are found in figure 5.35 and show little deviation which would indicate poor models.

Figure 5.36 shows the SLD profiles with uncertainty for both models applied to those NR data following 23 CV cycles. It is obvious in figure 5.36 that the uncertainty in the SLD profile for the model with an SEI is lower than that for the model without an SEI layer. The fitted electrolyte SLD is much lower than the estimated value for the model without an SEI layer. The fitted electrolyte SLD is very close to the estimated SLD for the electrolyte SLD which provides further confidence in the validity of the SEI layer model.

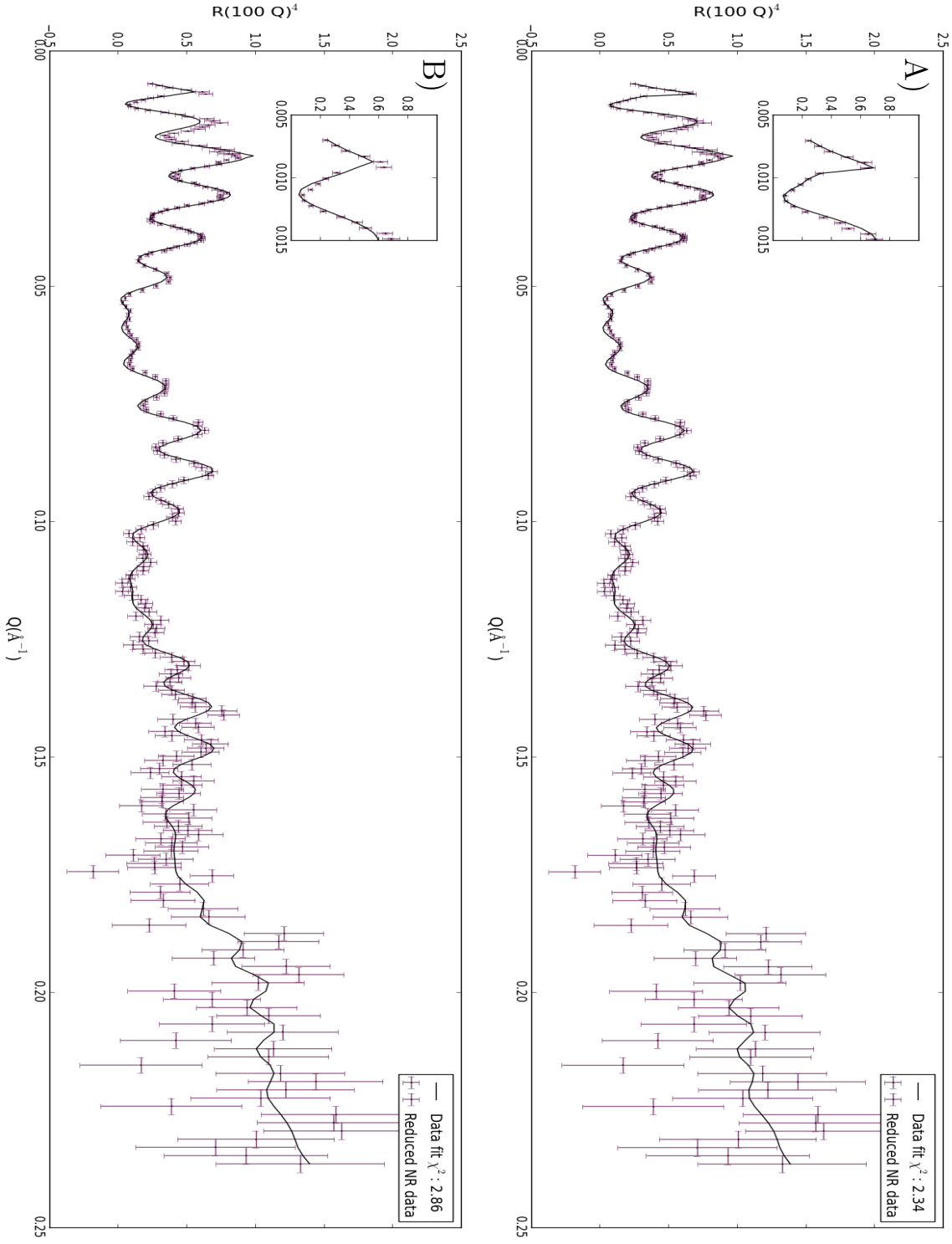

Figure 5.34: Fits to NR Potential hold sample data with and without an SEI layer following 23 CV cycles. The model with an SEI fits the critical edge better than the model without an SEI. In this case the improvement in critical edge fitting is less pronounced than previous datasets; however, the model with SEI also does a much better job fitting the second fringe indicating it is the better model. A) With SEI layer, B) Without SEI layer.

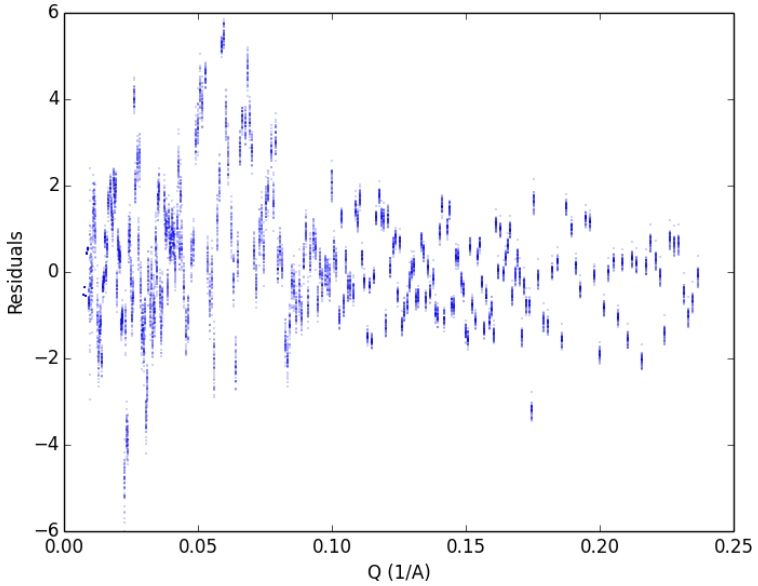

(a) With SEI

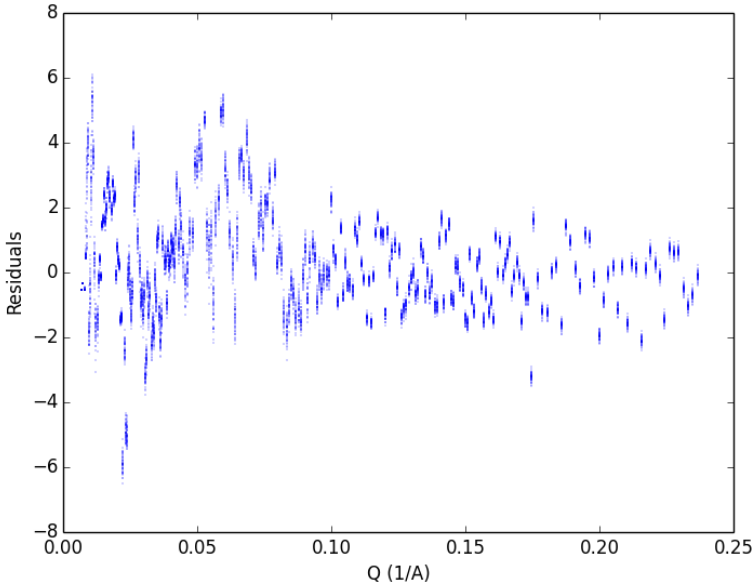

(b) Without SEI

Figure 5.35: Residuals from NR data fit to models with and without an SEI layer from the potential hold sample following 23 CV cycles. Both residuals show good agreement with those data.

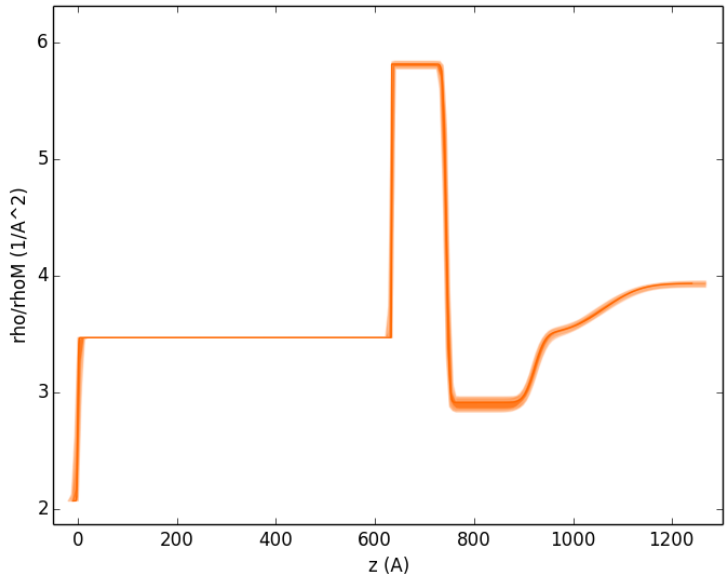

(a) With SEI

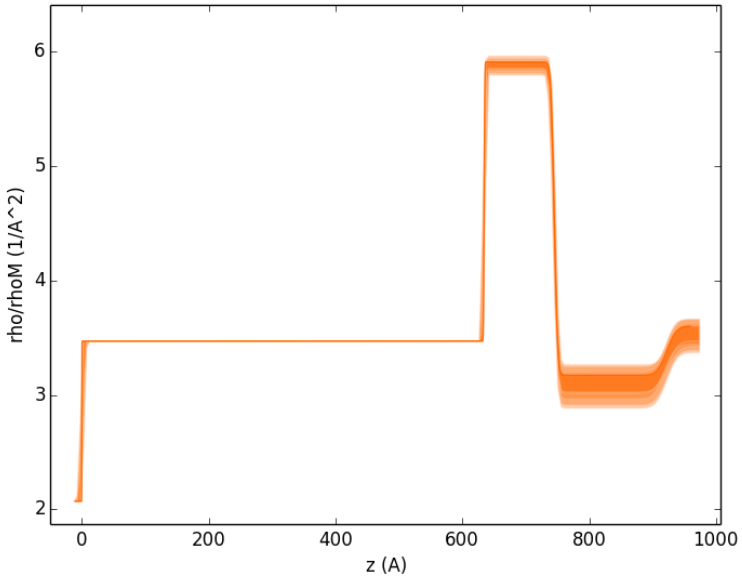

(b) Without SEI

Figure 5.36: SLD profiles including uncertainty for NR fits with and without an SEI layer to the potential hold sample following 23 CV cycles. The uncertainty is given by shaded bands showing 1, 2, and 3 σ on all parameters given in the model.

Table 5.10: Fitted NR results for the potential hold sample following 23 CV cycles.

NR				
Layer	thickness ($\mathring{A}$)	SLD ($10^{-6}\mathring{A}^{-2}$)	SLDi ($10^{-6}\mathring{A}^{-2}$)	Interface ($\mathring{A}$)
Si	-	2.07	0.00024	2.0 (12)
SiO_2	633.15 (50)	3.47	0.00011	0.74 (48)
Pt	110.62 (21)	5.818 (14)	0.0189	4.80 (51)
LMO	178.1 (13)	2.894 (34)	0.0038	17.9 (17)
SEI	136.7 (66)	3.492 (26)	0.00917	60.1 (49)
Electrolyte	-	3.933 (12)	0.00917	-
Intensity: 1.0 Θ offset: 0.00102 (62) Background: 437*10^{-8}(26)				

5.2.2.6 Following 26 CV cycles

Following 26 CV cycles the cell is held at 3300 mV throughout NR data collection. These data use similar models applied to the dataset following 18 CV cycles as described by equations 5.6 and 5.5. Figure 5.37 shows the fitted results as R*(100*Q)^4 to emphasize the critical edge. From figure 5.34 the model with an SEI does a slightly better job fitting these data as observed by the χ^2 however the better fit is not obvious in this case. Residuals from those fits are found in figure 5.38 and show an oscillating feature which may indicate the models do not represent these data as well as previous datasets.

Figure 5.39 shows the SLD profiles with uncertainty for both models applied to those NR data following 23 CV cycles. It is not obvious in figure 5.39 that either model is more defined than the other. The fitted electrolyte SLD is similar between those models and are close to the estimated SLD for the electrolyte SLD. These models are very similar, and the fitted SEI layer between the $LiMn_2O_4$ film could be encompassed by the additional roughness observed in the model without SEI.

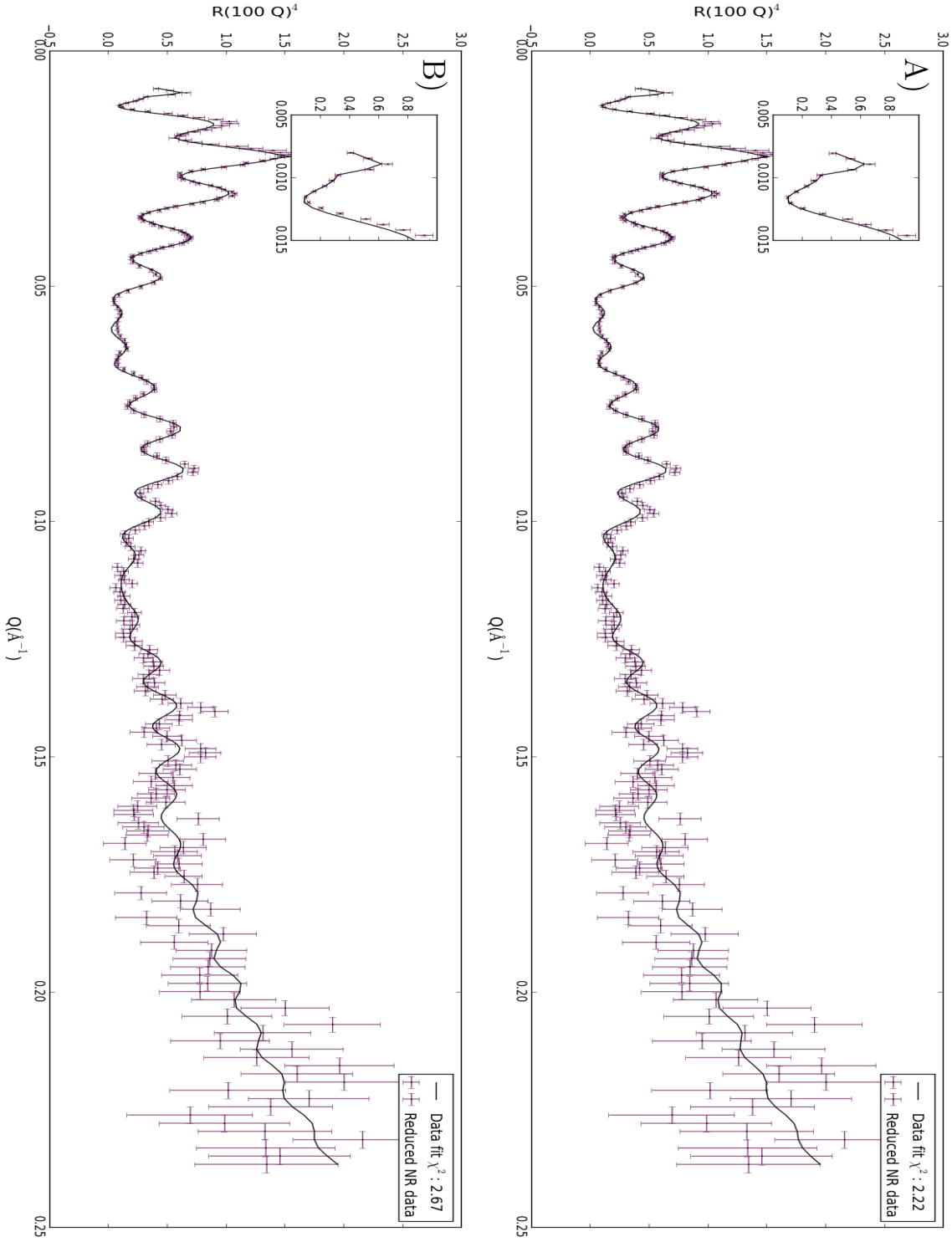

Figure 5.37: Fits to NR Potential hold sample data with and without an SEI layer following 26 CV cycles. The model with an SEI fits the critical edge better than the model without an SEI. In this case the improvement in critical edge fitting is less pronounced than previous datasets; however, the model with SEI also does a much better job fitting the second fringe indicating it is the better model. A) With SEI layer, B) Without SEI layer.

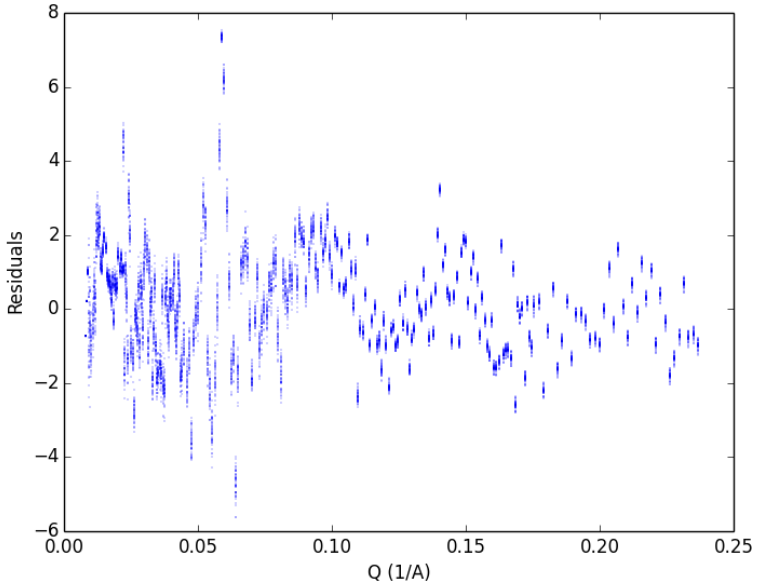

(a) With SEI

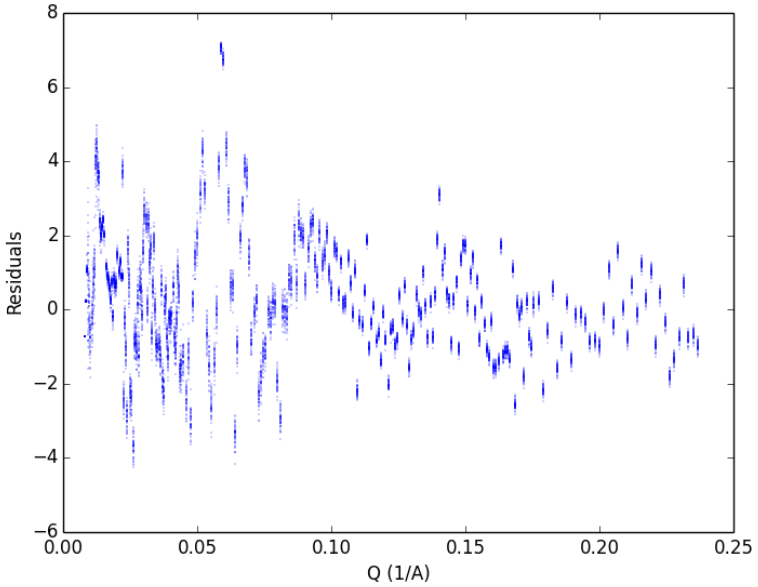

(b) Without SEI

Figure 5.38: Residuals from NR data fit to models with and without an SEI layer from the potential hold sample following 26 CV cycles. Both residuals show an oscillating feature which indicates the model does not fully represent these data.

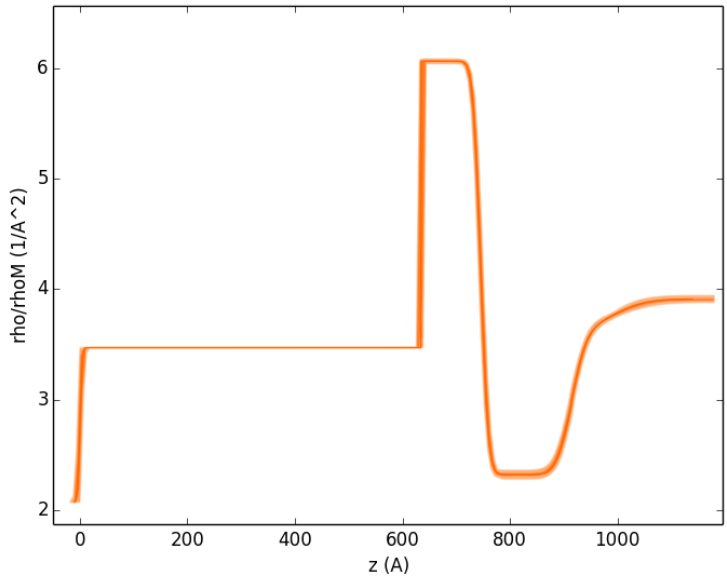

(a) With SEI

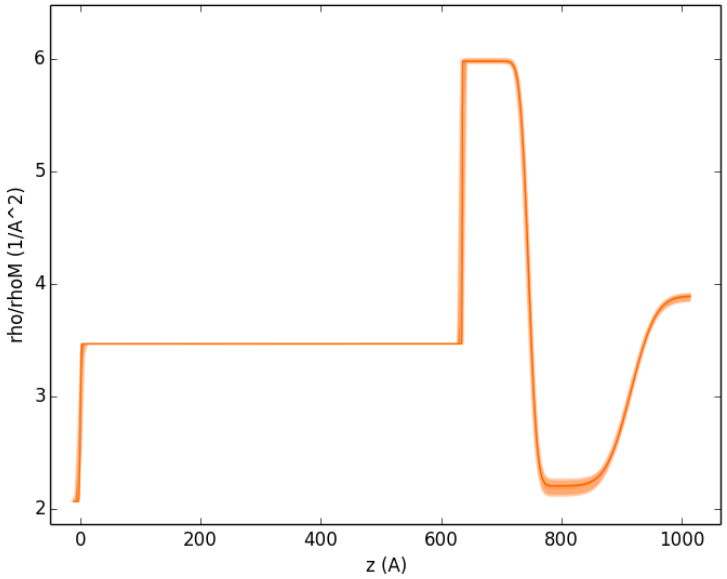

(b) Without SEI

Figure 5.39: SLD profiles including uncertainty for NR fits with and without an SEI layer to the potential hold sample following 26 CV cycles. The uncertainty is given by shaded bands showing 1, 2, and 3 σ on all parameters given in the model.

Table 5.11: Fitted NR results for the potential hold sample following 26 CV cycles.

NR				
Layer	thickness ($\mathring{A}$)	SLD ($10^{-6}\mathring{A}^{-2}$)	SLDi ($10^{-6}\mathring{A}^{-2}$)	Interface ($\mathring{A}$)
Si	-	2.07	0.00024	2.7 (12)
SiO_2	634.72 (42)	3.47	0.00011	0.57 (36)
Pt	111.09 (18)	6.063 (13)	0.0189	11.36 (24)
LMO	168.40 (91)	2.321 (20)	0.0038	22.9 (11)
SEI	75 (12)	3.595 (59)	0.00917	50.4 (78)
Electrolyte	-	3.907 (15)	0.00917	-
Intensity: 1.0 Θ offset: 0.00378 (51) Background: $575*10^{-8}$(24)				

5.2.2.7 Discussion of potential hold CV results

The CV data collected throughout the potential hold experiment indicate initially successful operation of a $LiMn_2O_4$ cathode. The first three cycles show very characteristic electrochemical performance. Figure 5.40 shows background-corrected charging and discharging currents for the first three CV cycles, where the background is estimated as described in section 2.5. These corrected CV cycles show the performance is generally consistent with additional current in the first CV cycle which is significantly reduced in subsequent cycles.

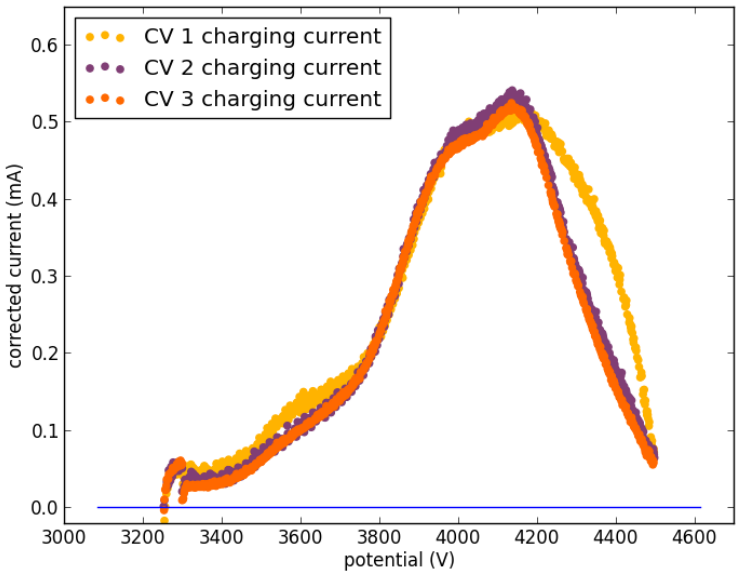

(a) Charging

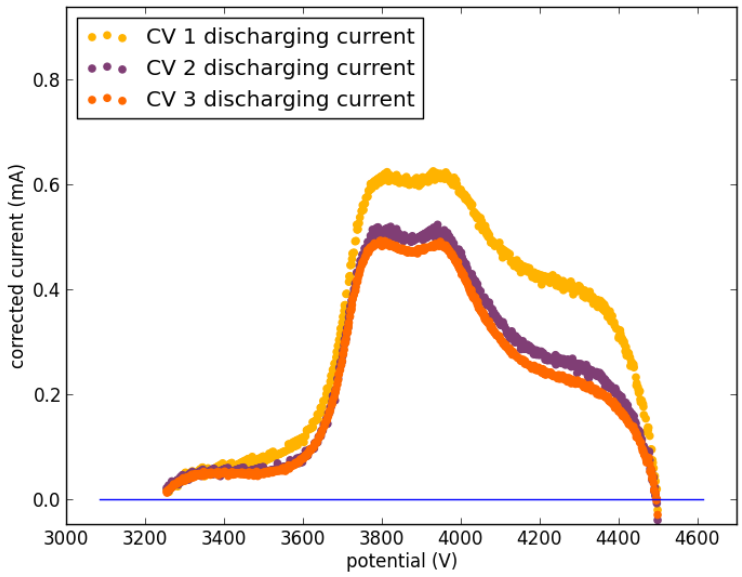

(b) Discharging

Figure 5.40: Background corrected CV data for charging and discharging current for the first three CV cycles on the potential hold sample.

Following these three CV cycles the collected CV data appear to be inconsistent with the expected performance. However, the stability of those fitted SLD values for the cathode layer indicate no significant change in the sample and therefore it should

be expected to operate normally. Figures 5.41 and 5.42 show 4th through 9th and 10th through 13th cycles respectively. The 4th through 8th cycles show some erratic behavior, but do show some characteristic behavior such as the 7th and 8th cycles in both the charging and discharging currents from figure 5.41. The 9th through 13th cycles show significant erratic behavior. This behavior may be due to poor electrical connection to the experimental cell. In many cases the measured current spikes or abruptly changes magnitude in a way which is not consistent with an onset potential.

Further cycles show similar erratic behavior and a shifting in onset potentials. The results shown in figures 5.40, 5.41, and 5.42 highlight the observation that the electrical connection likely is the mechanism behind the erratic behavior. It is also possible short-circuiting would lead to such behavior; however a short circuit should lead to an unmeasurable current whereas in this case the current remains within the resolution of the potentiostat.

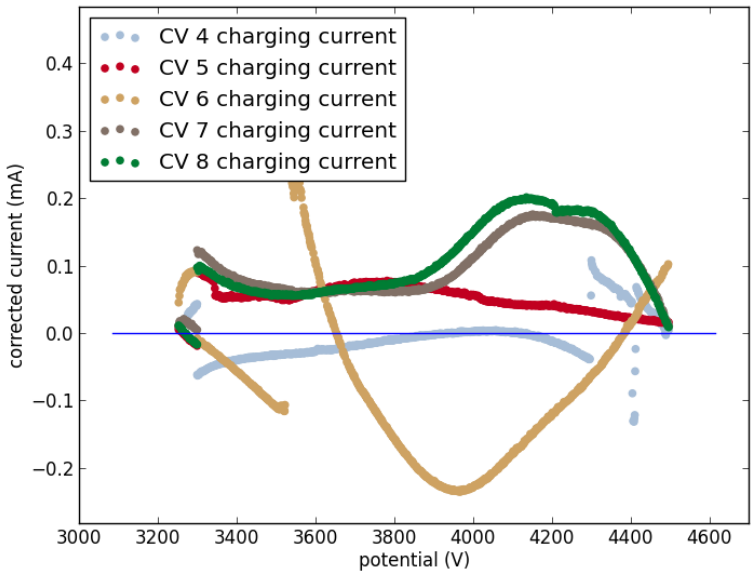

(a) Charging

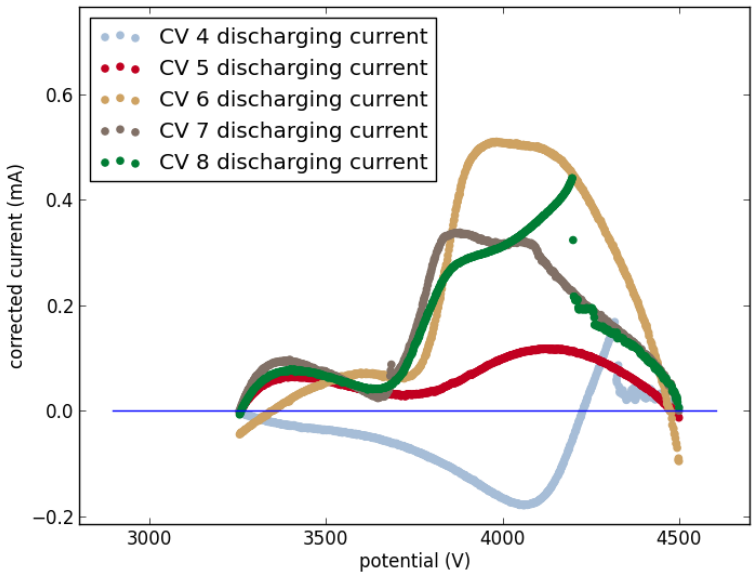

(b) Discharging

Figure 5.41: Background corrected CV data for charging and discharging current for the 4th through 8th CV cycles on the potential hold sample.

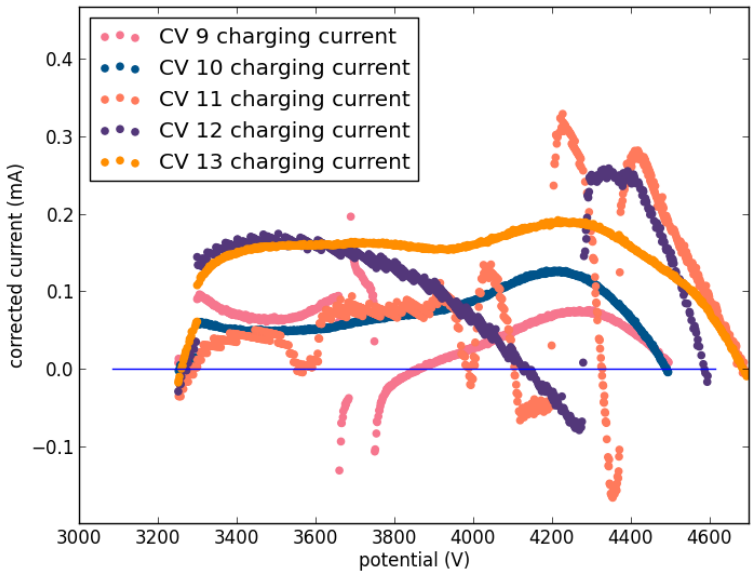

(a) Charging

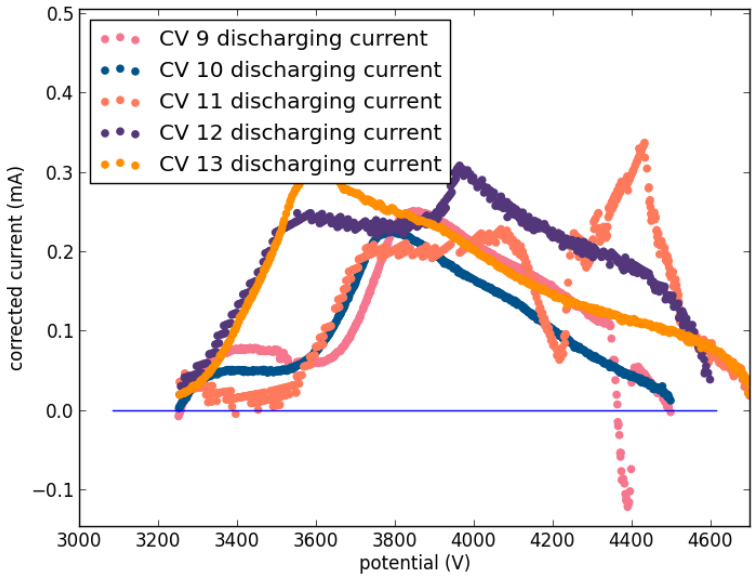

(b) Discharging

Figure 5.42: Background corrected CV data for charging and discharging current for the 9th through 13th CV cycles on the potential hold sample.

5.2.2.8 Discussion of potential hold NR results

To compare the two models applied to this sample there are a few metrics which can be used to suggest which model better represents these data. The BIC and chi-square tests comparing these models both provide insight into which model is most representative. Figure 5.43 shows the BIC and chi-square results for both models.

With both metrics the model with an SEI is better representative of these data. These results are in line with the model with SEI fitting the critical edge better as shown in figures 5.22, 5.25, 5.28, 5.31, 5.34, 5.37. Further evidence to suggest the model with an SEI is better representative is derived from observing the fitted electrolyte SLD for all electrochemical cases. Figure 5.44 shows the fitted electrolyte SLD for both models.

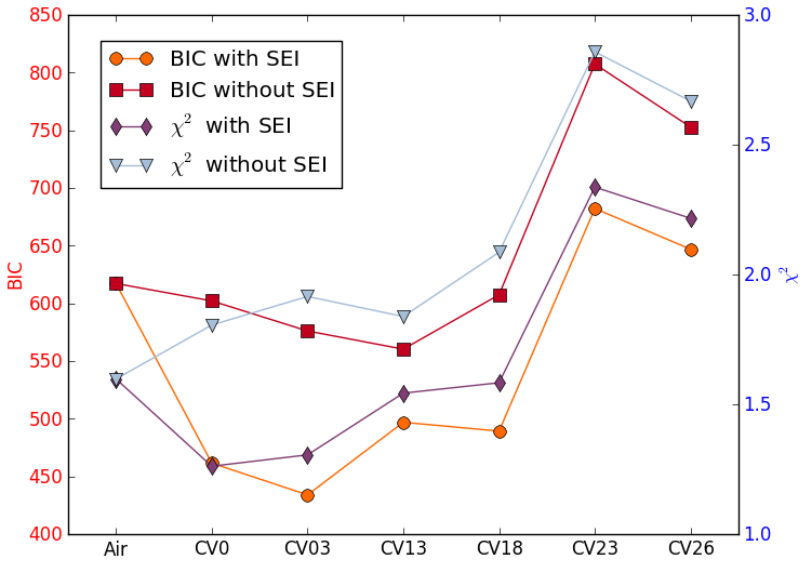

Figure 5.43: BIC and chi-square values for both models applied to the potential hold data with electrolyte and air for all electrochemical conditions. The BIC and chi-square values both indicate that the model with an SEI is more representative of these NR data. The BIC and chi-square values in air are included as a reference point.

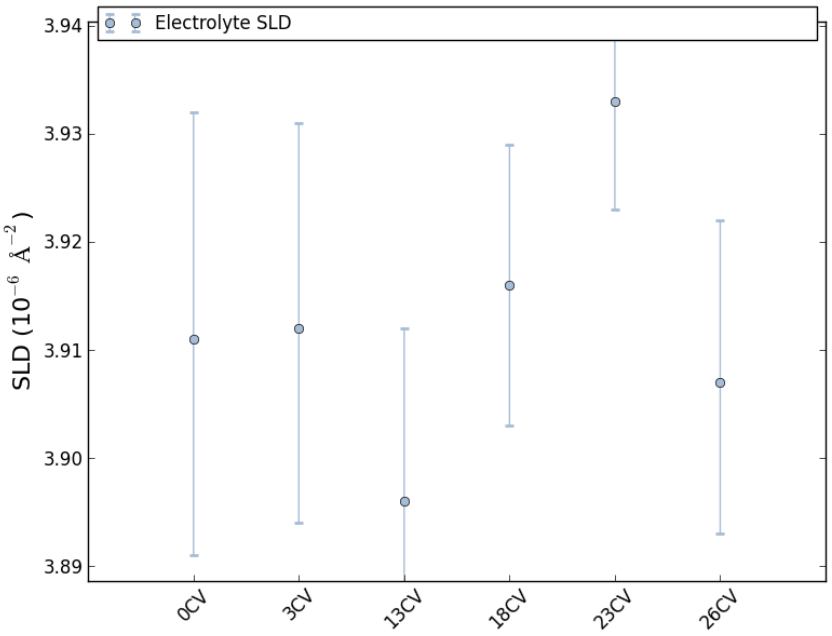

(a) With SEI

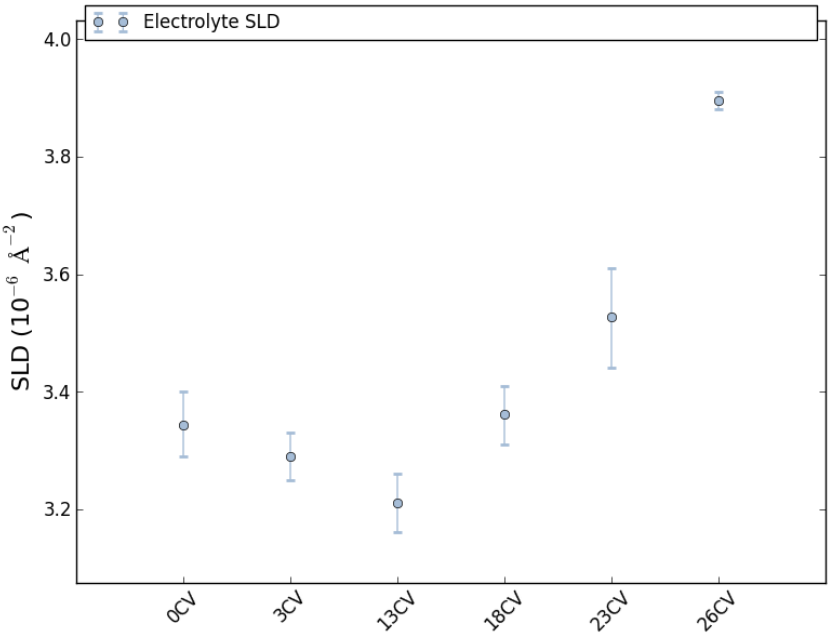

(b) Without SEI

Figure 5.44: Fitted electrolyte values for models applied to the potential hold sample at all electrochemical conditions.

The estimated SLD for the electrolyte is 3.9*10^{-6} $\mathring{A}^{-2}$, from figure 5.44 it is obvious that the model with SEI shows a consistent value for the electrolyte SLD which is very close to the estimated value. The model without an SEI shows significant

fluctuation with most values far below the estimate.

The BIC and chi-square results show better goodness-of-fit for the model with an SEI, the model with SEI better fits the critical edge, and the consistent electrolyte SLD all indicate the model with SEI is best representative of these data. This is an important result as it shows the potential for NR to study the SEI on cathode materials.

When exploring the model several interesting results become apparent. The total $LiMn_2O_4$ layer thickness increases throughout the experiment, except for the CV26 case. Figure 5.45 shows the total $LiMn_2O_4$ thickness for all NR fits on the potential hold sample including in air. Total thickness is determined by Refl1D through adding the thickness parameter Markov chains of the those two layers which describe the $LiMn_2O_4$ film where applicable.

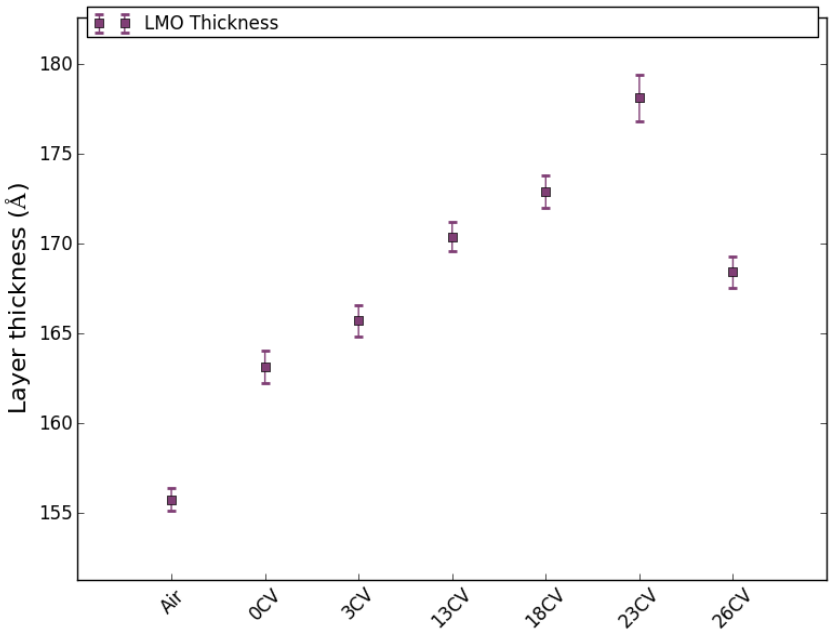

Figure 5.45: Total fitted $LiMn_2O_4$ layer thickness as a function of NR measurement with the SEI model for the potential hold sample.

The result in figure 5.45 is surprising for several reasons. $LiMn_2O_4$ exhibits contraction of the unit cell as a function of lithium loading (51). This should suggest the

two potential holds at 4000 and 4300 mV should see layer contraction. The observed total thickness changes upon addition of electrolyte. The two possibilities are a volume expansion of the cathode and an additional SEI layer is grouped with the second cathode layer. A volume expansion of the cathode could be observed, but the total observed change in thickness is on the order of 15% which makes it highly unlikely this is the case. Further a volume expansion does not agree with the observed contraction of the $LiMn_2O_4$ unit cell. The other possibility is there are two SEI layers where one is included in the modeled cathode layer(s) and the other is more diffuse which is present on the surface of the cathode.

Figure 5.46 shows the SLD profiles for all electrochemical conditions focusing on the cathode layers. The profiles are corrected such that the first cathode layer all begin at zero $\mathring{A}$ to ensure changes in fitted SiO_2 and Pt thicknesses do not affect the comparison. The in-air case shown is produced by taking the in-air fitted model and replacing the SLD of air (0 $\mathring{A}^{-2}$) with the average fitted electrolyte SLD ($3.91*10^{-6}$ $\mathring{A}^{-2}$). Additionally the cathode SLD is shifted by $1*10^{-6}$ $\mathring{A}^{-2}$ which is the change from the fitted CV0 cathode SLD and the in air SLD. The overlay highlights the significant change between the in-air case and the cases with electrolyte. The overlaid SLD profiles show a trend toward a lower SLD at the interface between the cathode layer and SEI which is supported by evidence which shows EC breakdown on the surface of $LiMn_2O_4$ (70; 71). EC in this experiment is prepared with hydrogen while the DMC is deuterated. This means that if DMC were decomposing on the sample surface there should be an increase in SLD. EC decomposing on $LiMn_2O_4$ should result in excess hydrogen at the surface which would manifest as a lower-SLD (70; 71).

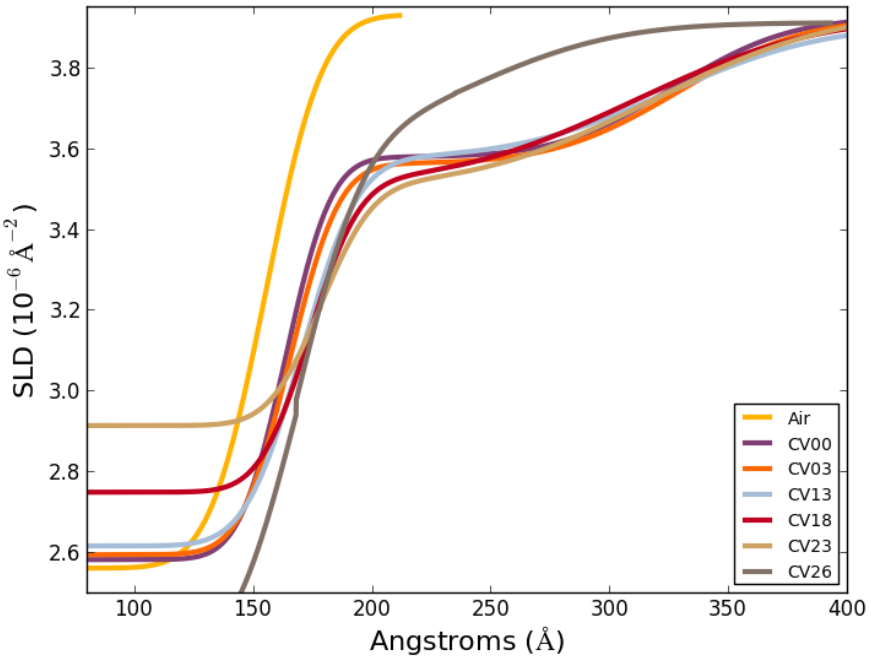

Figure 5.46: $LiMn_2O_4$ layer interfacial roughness as a function of electrochemical condition including air.

These results suggest a second SEI which should have similar composition to that of the cathode material. Attempts to fit a model with two SEI layers resulted in a fit with a similar SLD profile as the case with one SEI layer. The χ^2 of the two-SEI layer model was only slightly better than the case with one SEI layer (1.25 vs 1.26), and the BIC was found to be the same between the one-layer SEI and two-layer SEI models (461.53). These information indicate that the additional layer is not supported statistically and the two-layer SEI model is rejected. This does not mean that a second SEI layer does not exist, rather it means that within the uncertainty of the model it cannot be said that another layer exists on the surface of the cathode.

The SLD of $LiMn_2O_4$ is an important property to investigate as it highlights whether or not the cell functioned as desired. The electrochemical results highlighted in section 4.4.2 showed poor performance with a significant amount of noise in the CV curves. While some consistent features were observed, generally poor CV curves do

not necessarily indicate whether the cell was operating appropriately. The LMO layer SLD can provide insight into this problem as the SLD must change as a function of lithium loading. While holding at 3300 mV it is expected that any $LiMn_2O_4$ material will have consistent SLD. When the potential is raised to 4000 mV and 4300 mV it is expected that the LMO layer SLD will increase due to lithium being removed from the structure. Figure 5.47 shows the fitted $LiMn_2O_4$ layer SLD in air and at all electrochemical conditions. It should be noted that in figure 5.47 the SLD plotted when two layers are used to model the $LiMn_2O_4$ layer is from the thicker layer close to the electrolyte.

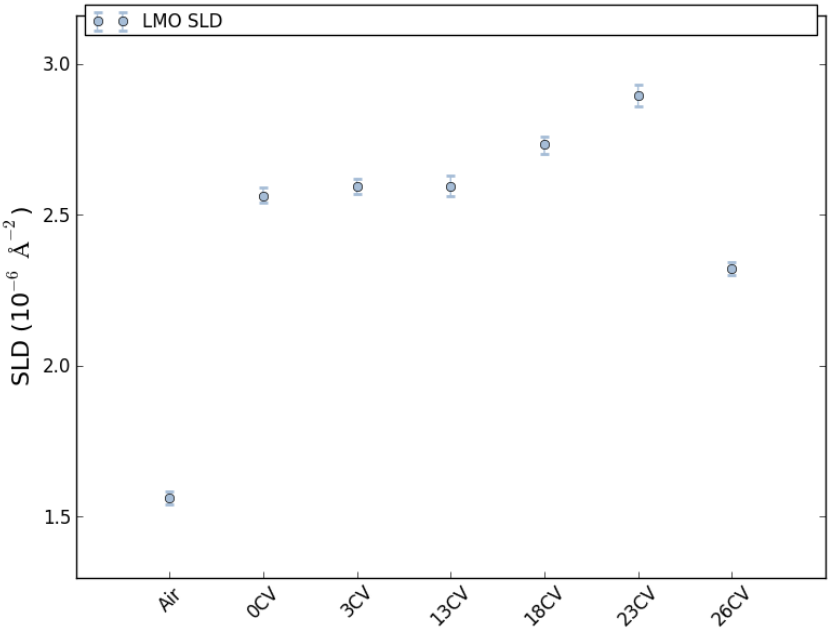

Figure 5.47: $LiMn_2O_4$ layer SLD in air and at all electrochemical conditions.

The change between the potential hold sample SLD in air and following electrolyte injection is $1.0*10^{-6}$ $\mathring{A}^{-2}$. Between the electrolyte injection and 3 CV cycles the LMO layer SLD increases by $0.031*10^{-6}$ $\mathring{A}^{-2}$. Following 13 CV cycles, the change from 3 CV cycles is $0.001*10^{-6}$ $\mathring{A}^{-2}$ which is well within the uncertainty of the fitted value. These values indicate the sample was generally the same between electrolyte injection and 13 CV cycles. The slight increase in LMO layer SLD is likely due to lithium loss

to SEI or layer dissolution which would manifest as a higher SLD. Upon holding at 4000 mV after 18 CV cycles the cathode SLD increased by $0.138*10^{-6}$ $\mathring{A}^{-2}$ from 13 CV cycles. Similarly holding at 4300 mV after 23 CV cycles the cathode SLD increased by $0.3*10^{-6}$ $\mathring{A}^{-2}$ from 13 CV cycles. These increases are expected if the cell was operating as desired. By holding at 4000 mV it is expected that about half the lithium loading in $LiMn_2O_4$ would be removed. Holding at 4300 mV is expected to remove all lithium possible by electrochemical means; this has been shown to be around 72% (50; 51). Finally the SLD change between 0 CV and 26 CV is $-0.241*10^{-6}$ $\mathring{A}^{-2}$.

The direction of change in the cathode SLD while holding at potentials higher than 3300 mV agrees with the expectation that 4000 mV should show an increase and 4300 mV show an even greater increase in SLD. The absolute magnitude of change is greater than would be expected for both cases if the cathode were composed of only $LiMn_2O_4$. Later in this analysis a volume estimate of $LiMn_2O_4$ is generated which corresponds to $\sim$72% $LiMn_2O_4$, 7% Li_2CO_3, and the balance (21 %) gas-filled pores. Given the assumption that the layer is composed of 72%$LiMn_2O_4$ the estimated SLD change in removing half the lithium at 4000 mV is $0.127*10^{-6}$ $\mathring{A}^{-2}$, close to the observed change of $0.138*10^{-6}$ $\mathring{A}^{-2}$. 72% of lithium is predicted to be removed at 4300 mV, which corresponds to an SLD change of $0.184*10^{-6}$ $\mathring{A}^{-2}$. This is much lower than the observed $0.3*10^{-6}$ $\mathring{A}^{-2}$. The SLD change from 13CV to 26 CV ($-0.241*10^{-6}$ $\mathring{A}^{-2}$) is consistent with a change from $LiMn_2O_4$ to $Li_2Mn_2O_4$ ($-0.24*10^{-6}$ $\mathring{A}^{-2}$).

The sudden change at 26 CV is difficult to explain. One possible explanation is a short-circuit where lithium in the cell comes in contact with the cathode. Short-circuiting it is expected to form $Li_2Mn_2O_4$. While holding the cell potential at 4300 mV, near the very end of the hold, a significant jitter in the measured current occurs. A short circuit may occur at this point, however there is no evidence of a short-circuit.

Determination of SEI layer properties are an important aspect of this work. Fig-

ures 5.48, 5.49, and 5.50 show, as a function of measurement the thickness, interfacial roughness, and SLD respectively. From injection of electrolyte to the end of the experiment, the SEI layer thickness decreased. In conjunction with the layer thinning the roughness at the electrolyte boundary increased throughout these measurements. When holding at potentials 4000 and 4300 mV, indicated by 18 CV and 23 CV in those figures, the SEI thickness is on the order of the SEI roughness. It is unclear if this result is due to holding at a potential far above the open circuit potential for pure $LiMn_2O_4$ ($\sim$ 3200 mV) or whether it is due to some other form of degradation. The SEI thickness and roughness for 13 CV shows thinning and roughening was occurring prior to holding the potential much above the expected open circuit value. Additionally, the 26 CV SEI layer indicates significant breakdown of the SEI where the roughness is much greater than the thickness.

In examining the SEI SLD from figure 5.50, when holding at a potential of 3300 mV, the SLD of the SEI is roughly constant. The point at 26 CV does show an increase above the first three measurements collected at 3300 mV, but the uncertainty on that point is significantly larger than the others. The SEI SLD for 18 CV and 23 CV at 4000 mV and 4300 mV show a consistently smaller SLD. It is unclear from these results what might be driving the decrease in SLD, but it is clear that changes occur when the cell is held at a charged state.

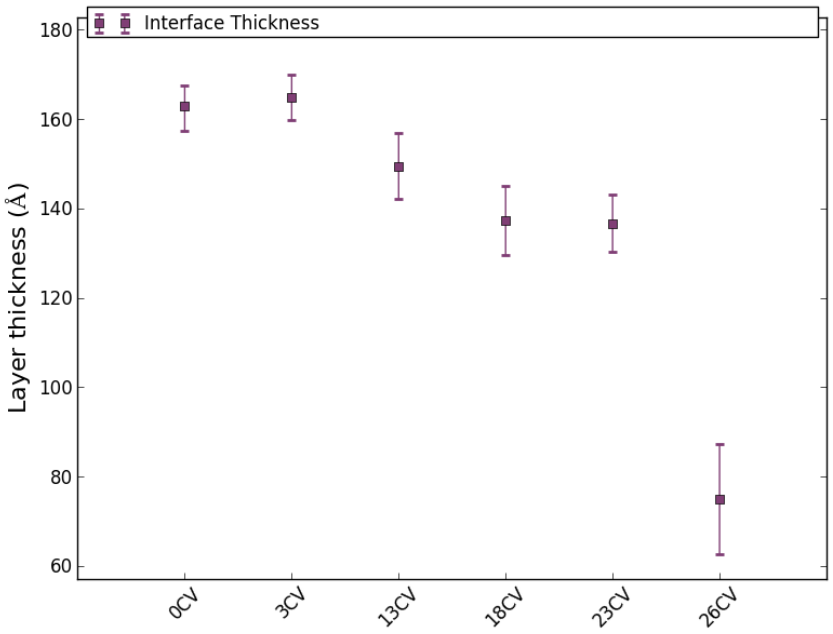

Figure 5.48: SEI layer thickness from potential-hold NR data as a function of CV cycles.

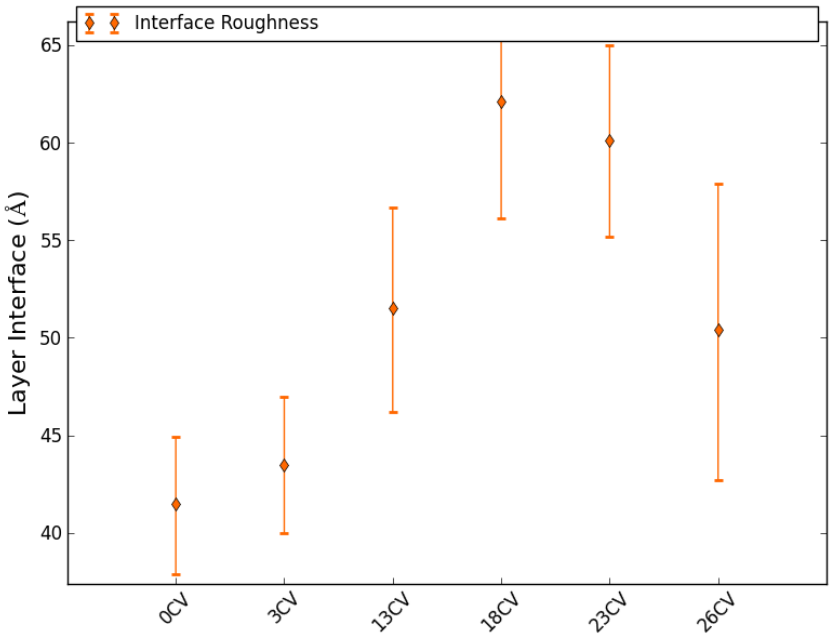

Figure 5.49: SEI layer roughness from fits to the potential hold sample NR data as a function of electrochemical measurement.

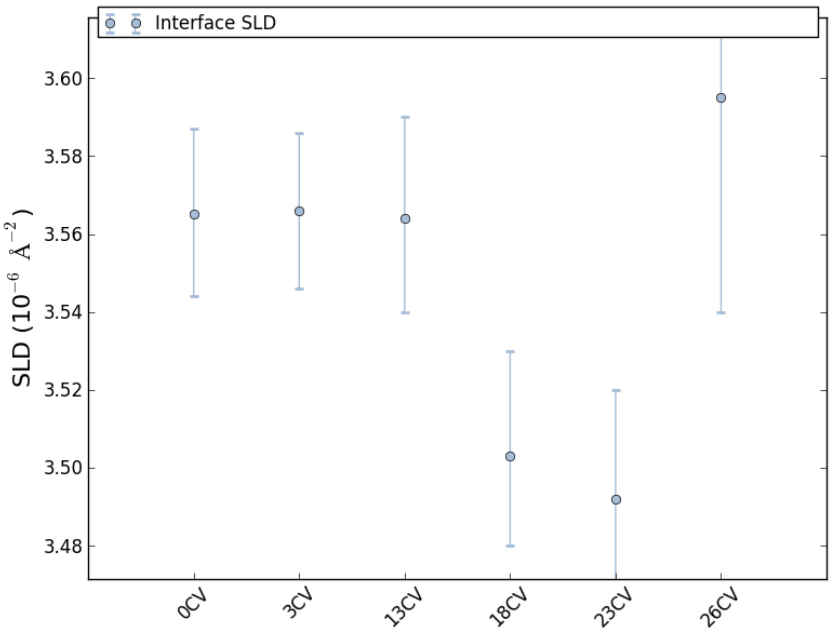

Figure 5.50: SEI layer SLD from fits to the potential hold sample NR data as a function of electrochemical measurement.

Now that the existence of an SEI layer has been established the discussion should circle back to the characterization in air which showed an apparent discrepancy between the fitted SLD for XRR and NR. Given these profiles should give very similar results the discrepancy indicates another phase is present. The problem is further expanded by an unknown layer density in addition to being multi-phase. To approach this issue we first determine the change in SLD from the sample in air to the sample with an electrolyte boundary. A first assumption is that the SLD change between the air case and electrolyte case is due to being filled with the SEI. As the SEI was shown to cover the surface of the $LiMn_2O_4$ layer this assumption is thought to be valid. If this assumption holds then the SLD change between air and electrolyte being due to the SEI means if you divide these quantities the result is the % volume which is taken up by the SEI. For this sample the change in $LiMn_2O_4$ between air ($1.562*10^{-6}$ $\mathring{A}^{-2}$) and with electrolyte ($2.562*10^{-6}$ $\mathring{A}^{-2}$) is $1*10^{-6}$ $\mathring{A}^{-2}$. The fitted SEI SLD for the sample with electrolyte prior to any electrochemical cycling is $3.562*10^{-6}$ $\mathring{A}^{-2}$.

The ratio of these two quantities is 0.2805 or the SEI composes 28.05% of the sample layer which implies 71.95% is filled by $LiMn_2O_4$

Now assume the sample in air is composed of just $LiMn_2O_4$ which as previously stated is not a very good assumption, but it provides a reasonable estimation for the sample. The SLD for the potential hold sample in air is 1.562*10^{-6} $\mathring{A}^{-2}$, where the theoretical SLD of $LiMn_2O_4$ is 1.970*10^{-6} $\mathring{A}^{-2}$. The ratio of these quantities gives an estimation for the %volume composed of $LiMn_2O_4$. This ratio is 0.7929 or 79.29% of the volume is filled with $LiMn_2O_4$. The difference between the estimation of volume in air and with electrolyte is 0.0734 or 7.34%. This difference represents the fraction of the layer which was composed of Li_2CO_3 which is known to dissolve with the introduction of electrolyte (67). With an estimate for Li_2CO_3 volume we can determine a SLD for a supposed full density $LiMn_2O_4/Li_2CO_3$ material if we also have an estimation for the density of such a layer. A first order approximation can be made by assuming the density is a fractional combination of Li_2CO_3 and $LiMn_2O_4$ by using equation 5.7,

$$\rho_{LiMn_2O_4} * (1 - x) + \rho_{Li_2CO_3} * x = \rho_{est} \tag{5.7}$$

where $\rho_{LiMn_2O_4}$ and $\rho_{Li_2CO_3}$ are the theoretical densities, x is the fraction composed of Li_2CO_3, and ρ_{est} is the estimated density. For the potential hold sample the estimated density is 4.12 g/cm^3. From the density estimation and assuming a material composed of 92.66% $LiMn_2O_4$ and 7.34% Li_2CO_3 a determination of the theoretical SLD can be made giving a neutron SLD of 2.053*10^{-6} $\mathring{A}^{-2}$ and an xray SLD of 32.629*10^{-6} $\mathring{A}^{-2}$. We can divide the SLD profile of the $LiMn_2O_4$ layers from XRR and NR measurements in air by these estimates to get a better idea if the rough determination of Li_2CO_3 is appropriate. Figure 5.51 shows the % theoretical density of the LMO layers for the potential hold sample assuming pure $LiMn_2O_4$ and with the partial $LiMn_2O_4/Li_2CO_3$. It is observed from figure 5.51 that the two curves show

very similar results. The deviation in the lower boundary is likely due to a greater lithium content. Lithium has a negative bound coherent scattering length for neutron scattering, but a positive albeit small scattering length for x-ray scattering. Neutron scattering is much more sensitive to light elements such as lithium and an increase in lithium content would make a significantly greater impact on the neutron SLD vs the x-ray SLD.

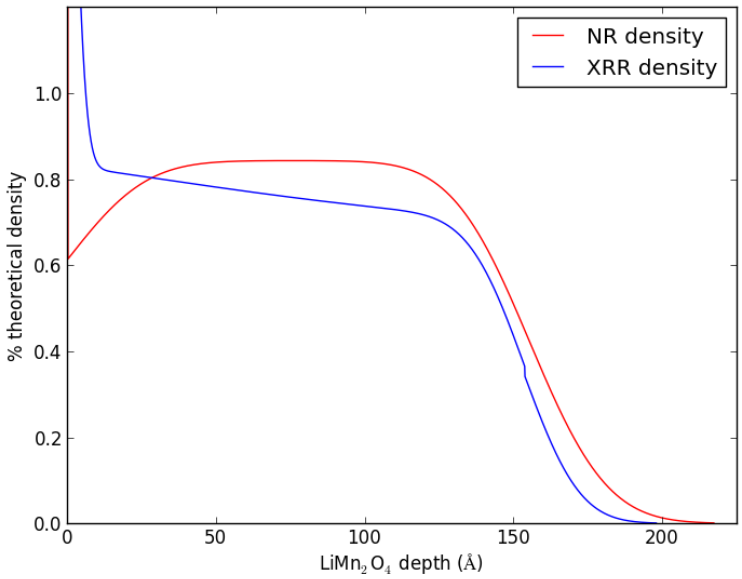

(a) $LiMn_2O_4$

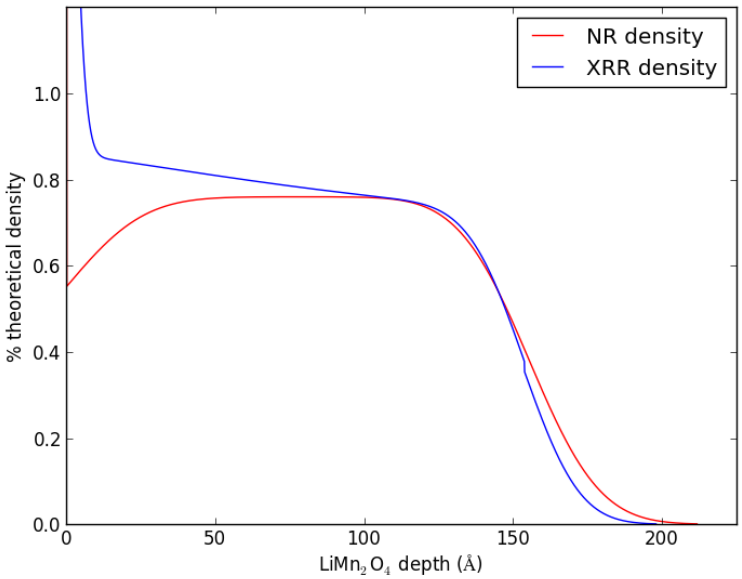

(b) 92.66% $LiMn_2O_4$/7.34% Li_2CO_3

Figure 5.51: Comparison of %theoretical density for NR and XRR results on potential hold sample in air using $LiMn_2O_4$ theoretical density of 4.281 g/cm^3 and an estimated 92.66% $LiMn_2O_4$/7.34% Li_2CO_3 theoretical density of 4.12 g/cm^3.

An aspect of these models which has not yet been discussed is the stability of the platinum charge collection layer. Initially it was assumed that the platinum

layer should remain unchanged throughout these NR measurements; however, it was quickly determined that this can not be the case. When fitting those data with the potential hold sample cell filled with electrolyte models which held the platinum layer SLD constant around the bulk value did not represent these data well. Figure 5.52 shows a fit to those data following electrolyte injection without any electrochemical cycling where the Pt SLD is held at the bulk value. These results when compared to figure 5.22 show the assumption that platinum remains unchanged does not represent these data.

Exploring the model with SEI and allowing platinum SLD to vary shows some surprising results. Figure 5.53 shows the fitted thickness and SLD for the platinum layer in this model. First the apparent thickness of the platinum layer decreases upon injection of electrolyte by a considerable $5\mathring{A}$. This difference could be due to probing different regions of the sample surface as the sample in air was probed with air as the fronting and the silicon wafer as the backing medium, whereas with electrolyte the sample is probed with the silicon wafer as the fronting medium and electrolyte as the backing medium. This argument is relatively poor as the change in mediums should not affect the thickness determination. Further surprising is the change in Pt SLD as a function of electrochemical condition also shown in figure 5.53. There is a marked decreased in Pt SLD throughout the experiment except for the final 26 CV case.

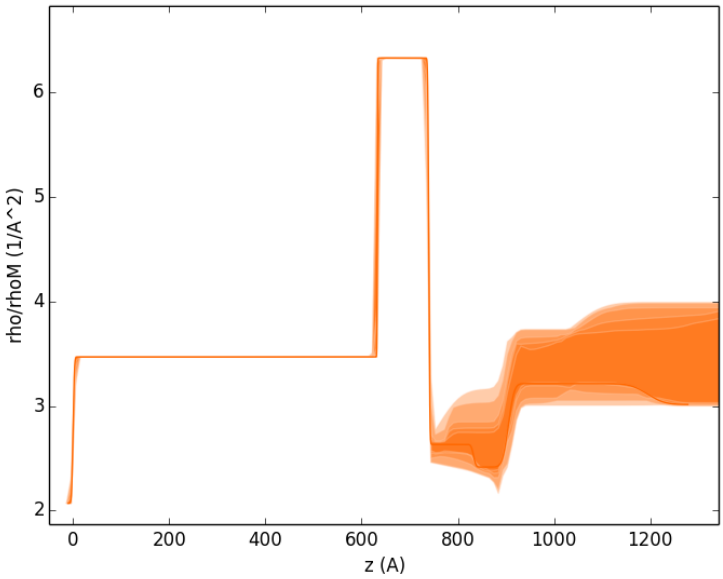

(a) CV0 SLD profile with uncertainty

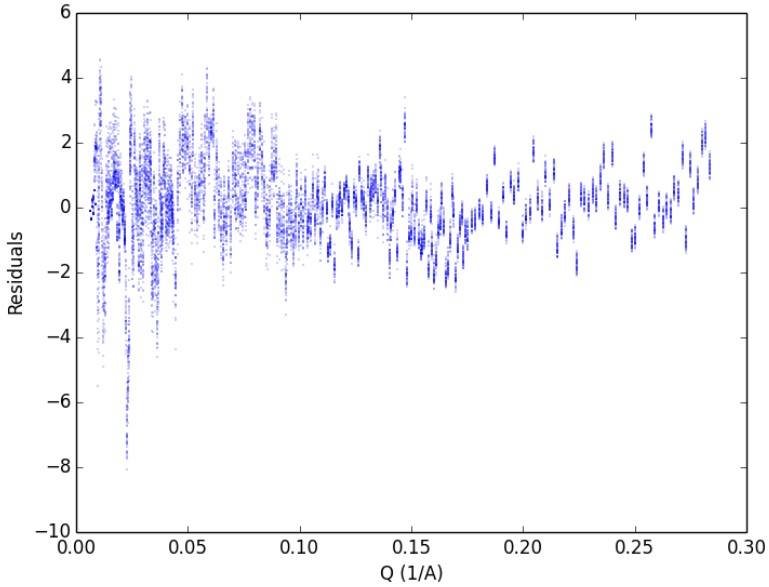

(b) Residual from fit to CV0 data

Figure 5.52: SLD profile and fit residual from potential hold sample following electrolyte injection fit to a model where the platinum layer SLD is held constant at the bulk value.

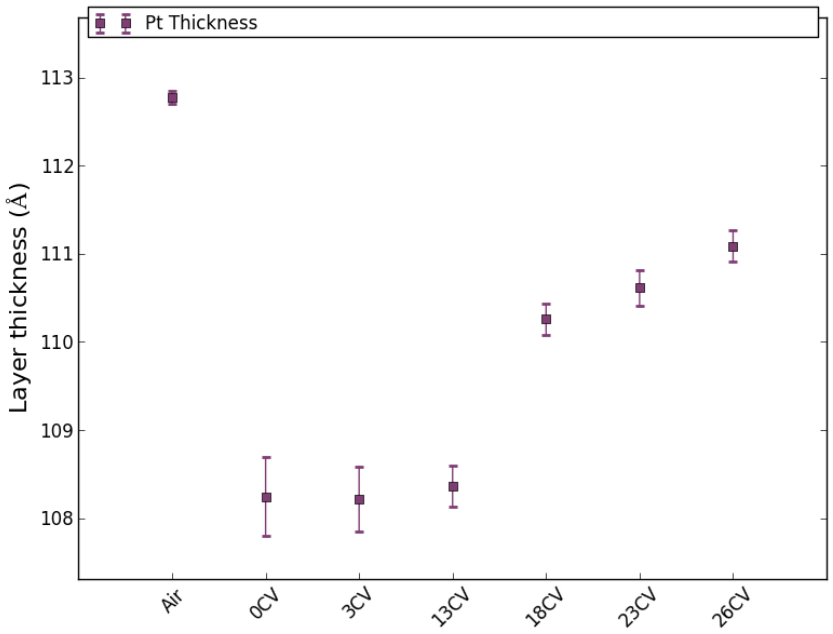

(a) Fitted platinum layer thickness

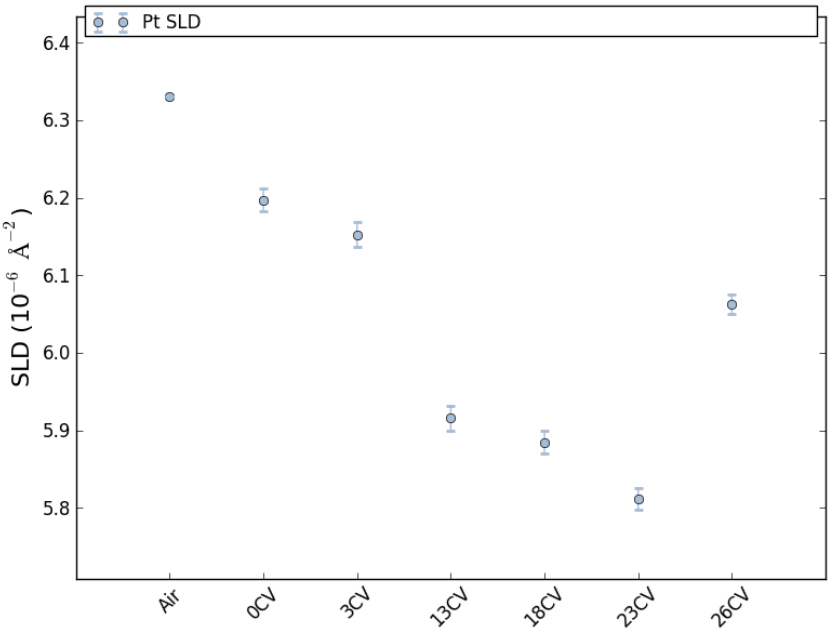

(b) Fitted platinum layer SLD

Figure 5.53: Fitted platinum layer thickness and SLD for the potential hold sample NR results from air through all electrochemical conditions.

There are three possible explanations for the change in Pt SLD throughout these experiments. Hydrogen or lithium diffusing into the Pt layer could explain the change in Pt SLD. Both are small atoms with negative bound coherent scattering lengths

which can have a significant impact on the Pt layer SLD. Of these two hydrogen is would have a greater impact as its bound coherent scattering length is more negative, requiring significantly less dissolved hydrogen than dissolved lithium. As an example, the lowest fitted Pt SLD value was $5.812*10^{-6}$ $\AA^{-2}$ at 23CV. If we assume the density of platinum remains relatively constant with dissolved hydrogen or platinum it would require $\sim$ 0.22 H for each Pt atom to arrive at the low Pt SLD. Conversely, it would require 0.38 Li for each Pt to arrive at the same low Pt SLD.

It is unlikely that hydrogen is the cause of this SLD drop due to the very low solubility of hydrogen in platinum(103) at room temperature. Lithium remains a possibility as the Li-Pt system allows for significant solubility of lithium in platinum (104). While it is possible lithium is the cause of the platinum there are a few issues related to this hypothesis. First is the very limited change in Pt layer thickness which would be expected to swell with significant lithium loading. Second is an unknown driving mechanism which would cause lithium dissolution in platinum.

The remaining potential cause of the Pt SLD change is reaction of the Pt layer with electrolyte leading to either dissolution or electrolyte breakdown on the Pt layer. As was discussed in the background chapter, Pt is not necessarily inert in these electrolyte solutions (76). If this were the case then it would be expected that the degradation should occur first on the surface of the Pt layer resulting in significant roughening which does not appear to occur.

While it is shown there are changes in the platinum layer throughout these measurements, there is not enough information to adequately point to any one of these suggested mechanisms causing a reduction in the Pt SLD. Further work is required to elucidate the cause of this phenomenon.

5.3 Post cell characterization analysis

This section provides an analysis of XPS and XRR results on both the open circuit and potential hold samples.

5.3.1 Open Circuit Sample

5.3.1.1 XRR Post-NR

Fitted XRR data on the open circuit sample following disassembly and rinsing in DMC are shown in figure 5.54. The model used to fit these data assumes the sample has a two-layer structure on top of the platinum layer. The SLD profile for this model is shown in figure 5.55 where the cathode layer is a continuously decreasing SLD profile from the the platinum/cathode interface to air. It is observed that near the platinum/cathode interface a steep drop in SLD occurs. The drop is indicative of a congregation of light elements at the platinum surface which falls in line with the fitted NR SLD for the sample in electrolyte following one CV cycle where a steep drop in SLD is observed near the platinum interface.

Fitted values for the model applied to these XRR data are found in table 5.12. The layers beyond platinum are denoted as C1 and C2 in this table as they are no longer representative of $LiMn_2O_4$. The fitted SLD at the maximum of the cathode layers is only $14.77*10^{-6}$ $\mathring{A}^{-2}$ which is much lower than the $25.5*10^{-6}$ $\mathring{A}^{-2}$ prior to placing into the electrochemical cell. This indicates loss of material which is in agreement with XPS results on this sample where delamination did not occur but significant loss of Mn was observed. Additionally, the low SLD is in agreement with significant carbon, oxygen, and lithium observed through XPS as those elements have low x-ray bound coherent scattering lengths.

The fitted SLD is also generally in agreement with the model following 1 CV cycle in the electrochemical cell. It was observed in that model that the SLD increase was

in line with significant material loss, similar to what was observed here with XRR following storage, disassembly, and rinsing in DMC.

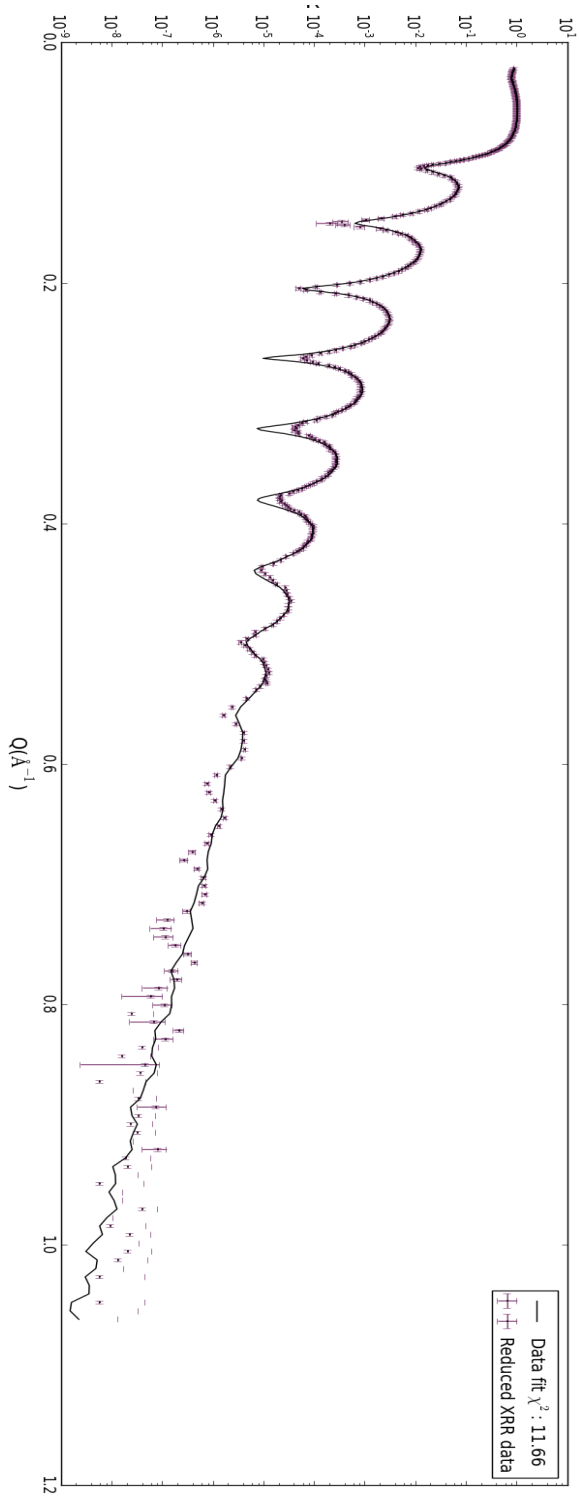

Figure 5.54: Fitted XRR from the open circuit sample following cell disassembly and rinsing in DMC.

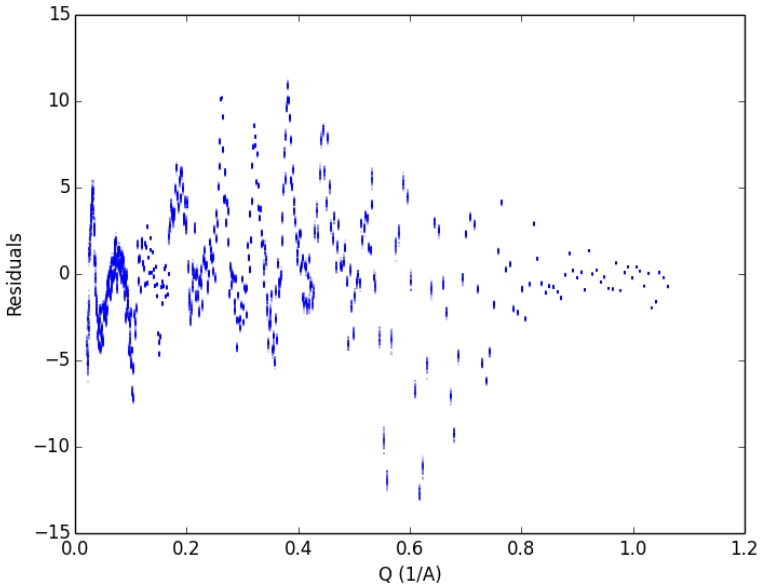

(a) Residual

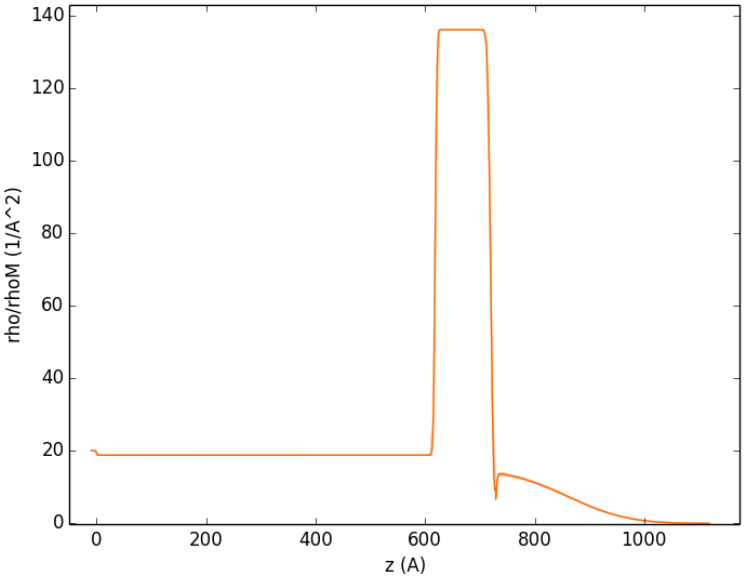

(b) SLD profile with uncertainty

Figure 5.55: Residual and SLD profile with uncertainty from XRR on the open circuit sample following cell disassembly and rinsing in DMC.

Table 5.12: Fitted NR results for the potential hold sample following cell disassembly and rinsing in DMC.

NR				
Layer	thickness ($\mathring{A}$)	SLD ($10^{-6}\mathring{A}^{-2}$)	SLDi ($10^{-6}\mathring{A}^{-2}$)	Interface ($\mathring{A}$)
Si	-	20.1	0.458	1.18 (15)
SiO_2	628.96 (20)	18.8	0.243	2.6372 (24)
Pt	112.7723 (83)	136.1	13.36	3.74 (47)
C1	149.92 (50)	2.321 (20)	2.289	26.89 (54)
C2	55.51 (45)	4.06 (39)	2.289	33.9 (16)
Air	-	0	0	-
Intensity: 1.0 Θ offset: 0.000739 (81) Background: $32*10^{-8}$(31)				

5.3.1.2 XPS

Two sample regions were chosen to investigate the bound states on a region which exhibited delamination and a region which did not. From 4.71 it was observed that no significant Mn is found in the emission spectra. Furthermore platinum is observed where for the potential hold sample no or very little platinum is observed, which indicates significant dissolution of the cathode layer. While the Mn 2p3/2 emission lines were not observed, some Mn 3p is observed where the Li 1s line appears.

From figures 5.56 and 5.57 the O 1s and C 1s fitted spectra for both regions are shown. It can be observed from figure 5.56 that there is a huge shift in the oxygen binding state. It appears that generally the same two modes are present, but the delaminated region shows a significant shift to the higher binding energy. Similarly for the C 1s spectrum from figure 5.57 the same four modes are present with very similar distributions indicating that the surface chemistry of C is unrelated to laminated/delaminated but likely more related to both being exposed to the electrolyte solution and air between the time of removal from the cell and time of XPS data collection.

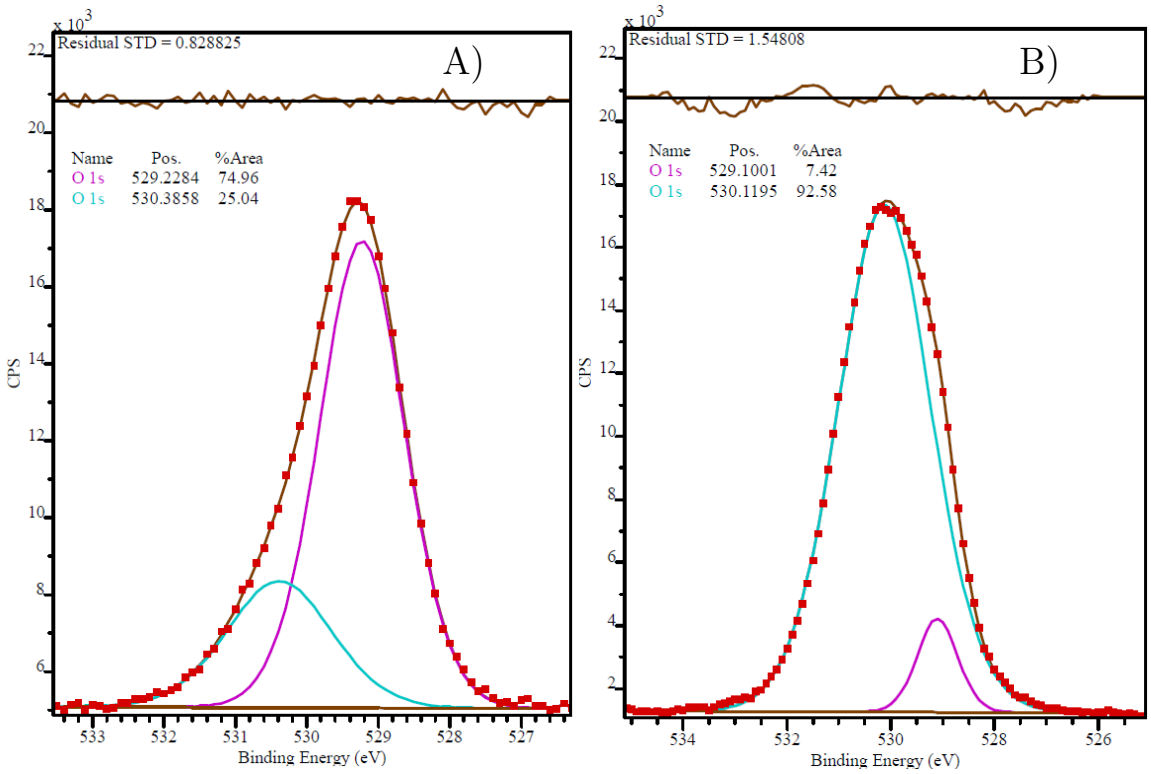

Figure 5.56: O 1s emission spectra on the open circuit sample in a region without delamination and a region with delamination with fitted Gaussian-Lorentzian peaks. A) No delamination , B) Delaminated region.

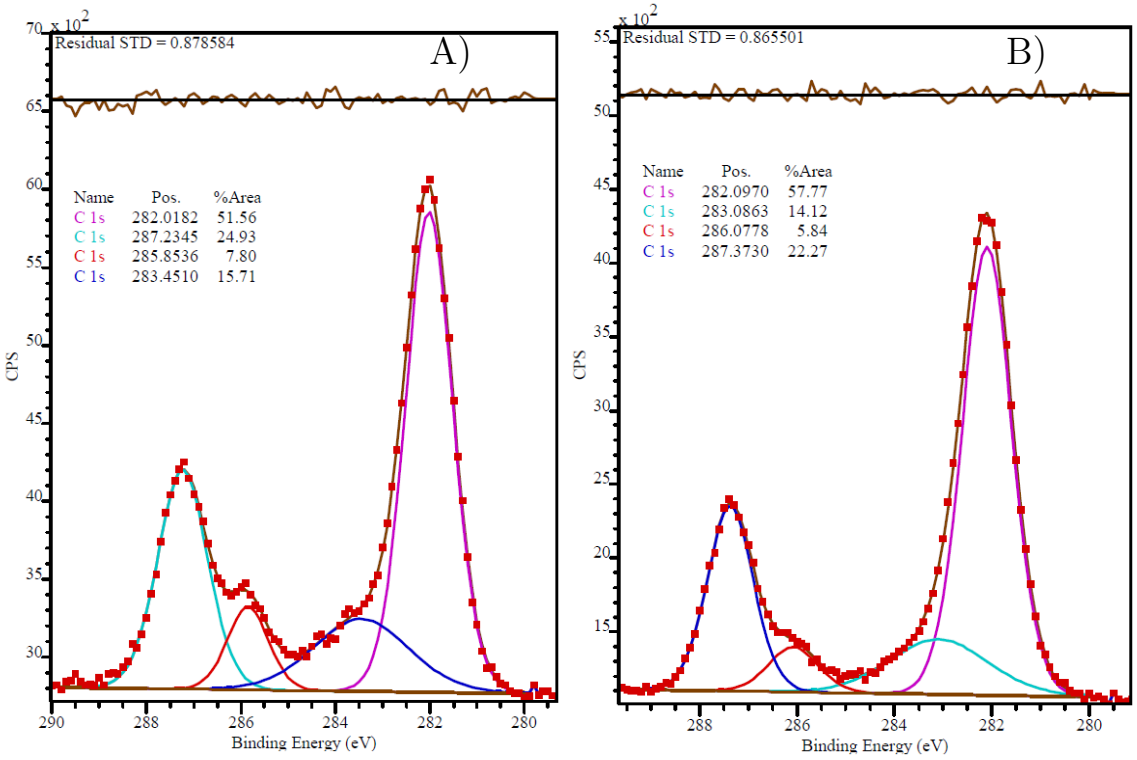

Figure 5.57: C 1s emission spectra on the open circuit sample in a region without delamination and a region with delamination with fitted Gaussian-Lorentzian peaks. A) No delamination , B) Delaminated region.

5.3.2 Potential Hold Sample

5.3.2.1 XRR Post-NR

Fitted XRR data on the potential hold sample following disassembly and rinsing in DMC are shown in figure 5.58. The model used to fit these data assumes the sample has a two-layer structure on top of the platinum layer as was observed following 26 CV cycles with NR. The fitted results indicate a single layer next to platinum with the second layer essentially adding to the roughness of the first. The second layer is

necessary to minimize the roughness inside the surface layer. An interface acts as a smoothing boundary between two layers, as the interface grows larger the smoothing curve moves into the first layer reducing the SLD near the end of the first layer. The second layer in this case limits the growth of the smoothing boundary into the first layer close to the platinum but creates the effect of a large interface. The second layer SLD is very low, and is likely due to light molecules which are known to form on the surface and the constituent atoms of Li, C, and O are observed through XPS.

Figure 5.59 shows the residual and SLD profile with uncertainty. It can be observed from the residual that the fit does not fully describe the collected XRR data. Alternative attempts at fitting a third layer resulted in a better χ^2 but a much greater uncertainty in the fitted parameters.

The fitted SLD profile is in line with what was expected following CV 26. The fitted neutron SLD at CV 26 was $2.322*10^{-6}$ $\mathring{A}^{-2}$. If it is assumed that the change in SLD from air to electrolyte injection ($1*10^{-6}$ $\mathring{A}^{-2}$) does not change then the sample without electrolyte would have a neutron SLD of $1.321*10^{-6}$ $\mathring{A}^{-2}$. If the resultant composition of the cathode layer is due to breakdown of the $LiMn_2O_4$ to Li_2MnO_3 from self-discharge, the corresponding mass density of Li_2MnO_3 to have a neutron SLD of $1.321*10^{-6}$ $\mathring{A}^{-2}$ is 2.6 g/cm^3. The X-ray SLD of Li_2MnO_3 at 2.6 g/cm^3 is $20.63 *10^{-6}$ $\mathring{A}^{-2}$, which is in fair agreement with the fitted value of $21.009*10^{-6}$ $\mathring{A}^{-2}$.

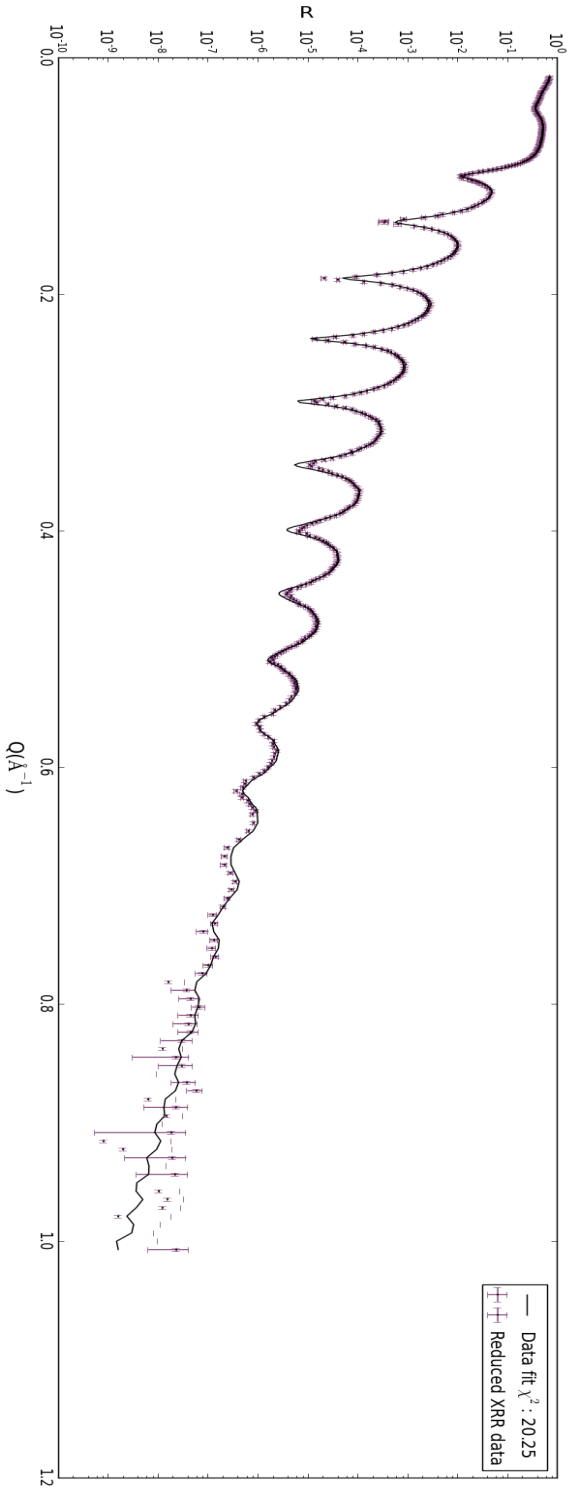

Figure 5.58: Fitted XRR from the potential hold sample following cell disassembly and rinsing in DMC.

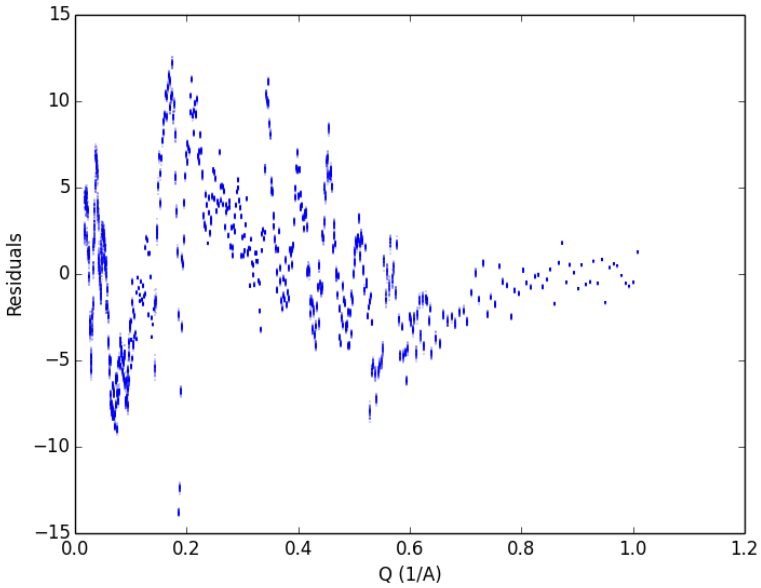

(a) Residual

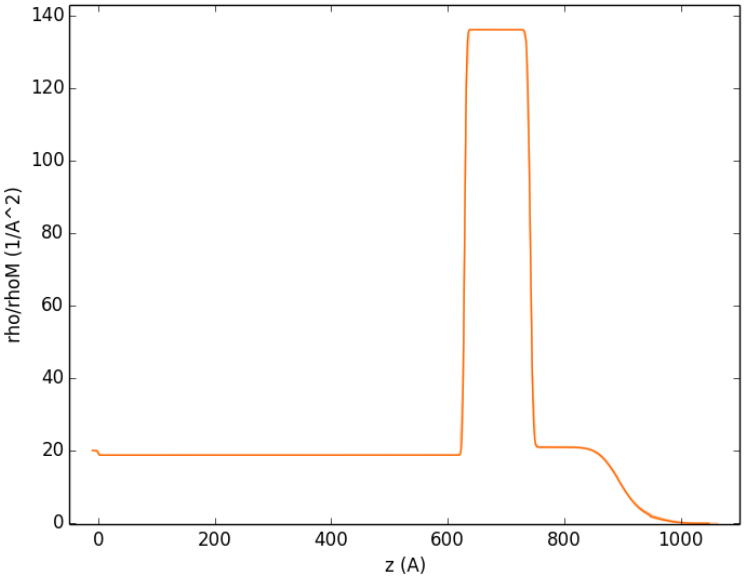

(b) SLD profile with uncertainty

Figure 5.59: Residual and SLD profile with uncertainty from XRR on the potential hold sample following cell disassembly and rinsing in DMC.

Table 5.13: Fitted NR results for the potential hold sample following cell disassembly and rinsing in DMC.

NR				
Layer	thickness ($\mathring{A}$)	SLD ($10^{-6}\mathring{A}^{-2}$)	SLDi ($10^{-6}\mathring{A}^{-2}$)	Interface ($\mathring{A}$)
Si	-	20.1	0.458	1.18 (15)
SiO_2	628.96 (20)	18.8	0.243	2.6372 (24)
Pt	112.7723 (83)	136.1	13.36	3.74 (47)
LMO	149.92 (50)	2.321 (20)	2.289	26.89 (54)
SEI	55.51 (45)	4.06 (39)	2.289	33.9 (16)
Air	-	0	0	-
Intensity: 1.0 Θ offset: 0.000739 (81) Background: 32*10^{-8}(31)				

5.3.2.2 XPS

Two regions of interest where chosen on the potential hold sample where one region showed delamination of the cathode film and the other did not. The delaminated region showed no traces of Mn, but does show considerable lithium content. The relatively low concentration of silicon indicates a surface contamination layer which covers the SiO_2 sample layer. Assuming all of the detected silicon is due to the substrate and not contamination from milling the sample to dimension approximately 43.8% of the detected oxygen content should come from SiO_2. This estimate corresponds well with the O 1s peak in the delaminated region which shows a 43%/57% split between two bound states as shown in figure 5.60. The very small platinum content coupled with the low silicon content indicates delamination occurred between the platinum and SiO_2 layers. This corresponds well with EDX information from figure 4.82.

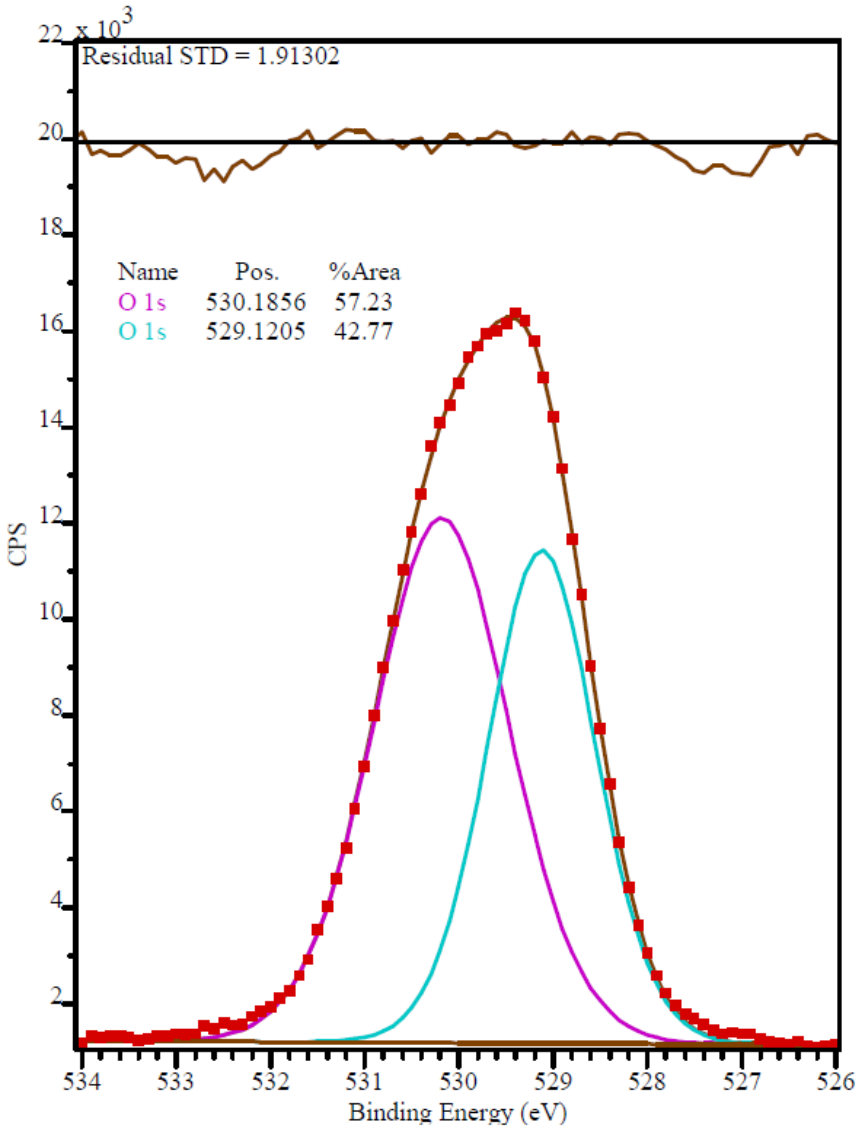

Figure 5.60: O 1s spectra for the potential hold sample following *in-situ* NR on a delaminated region.

The region which did not experience delamination shows the presence of manganese and also copper which comes from the anode. The presence of silicon in this case might be due to milling the sample to dimension or from the sample surface. The same model which was applied to XPS data on the Mn 2p3/2 peak from section 4.1.3 is applied to the region without delamination to explore the oxidation state of Mn. The fitted Mn 2p3/2 peak is found in figure 5.61. Table 5.14 shows fitted parameters

for the multiplets in the Mn 2p3/2 peak. These Mn results show generally significant decomposition of $LiMn_2O_4$ which was present at the outset of the experiment. The results indicate significant presence of Mn^{4+} and Mn^{2+} with a small amount of Mn^{3+}. The presence of significant amounts of Mn^{4+} agree with the supposition in the previous discussion of XRR results where it was suggested Li_2MnO_3 is formed from breakdown of $Li_2Mn_2O_4$ which is formed through self-discharge.

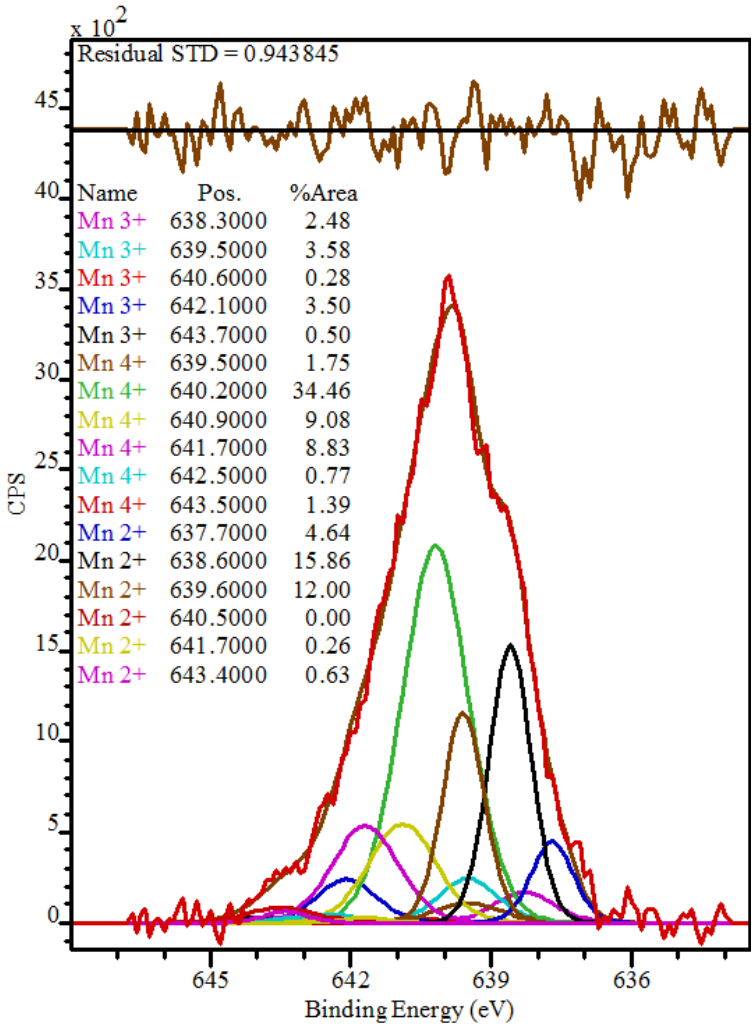

Figure 5.61: Mn 2p3/2 spectra for the potential hold sample following *in-situ* NR on a region without delamination.

Table 5.14: Table of fitted Gaussian-Lorentzian peaks to the Mn 2p3/2 peak on the potential hold sample following *in-situ* NR on a region which did not exhibit delamination.

State	BE (eV)	Area	State	BE (eV)	Area	State	BE (eV)	Area
Mn^{2+}	640.2	509.93	Mn^{3+}	640.8	272.2	Mn^{4+}	641.9	191.7
	641.1	1741.39		641.8	393.4		642.7	3787.8
	642.1	1318.3		643.1	30.3		643.4	998.3
	643.0	0		644.6	385.0		644.2	971.5
	644.2	28.1		646.2	60		645.0	85.0
	645.9	69.8					646.0	152.9
FWHM (eV)	1.05			1.68			1.65	
% Total		33.4%			10.3%			56.3%

Further exploring the Li/Mn ratio on the region without delamination the Mn 3s and Li 1s peaks are shown in figure 5.62. The composition shows 3 times as much lithium as Mn which should be expected due to formation of surface layers from breakdown of the cathode layer. The excess lithium is attributed to lithium polymer chains which have been suggested to be formed in the SEI (67), along with additional lithium to form Li_2MnO_3. These polymer chains are also observed in the C 1s peak shown in figure 5.63 where four binding energies are observed. The two modes at 286-287 eV are attributed to $ROCO_2Li$ chains (67).

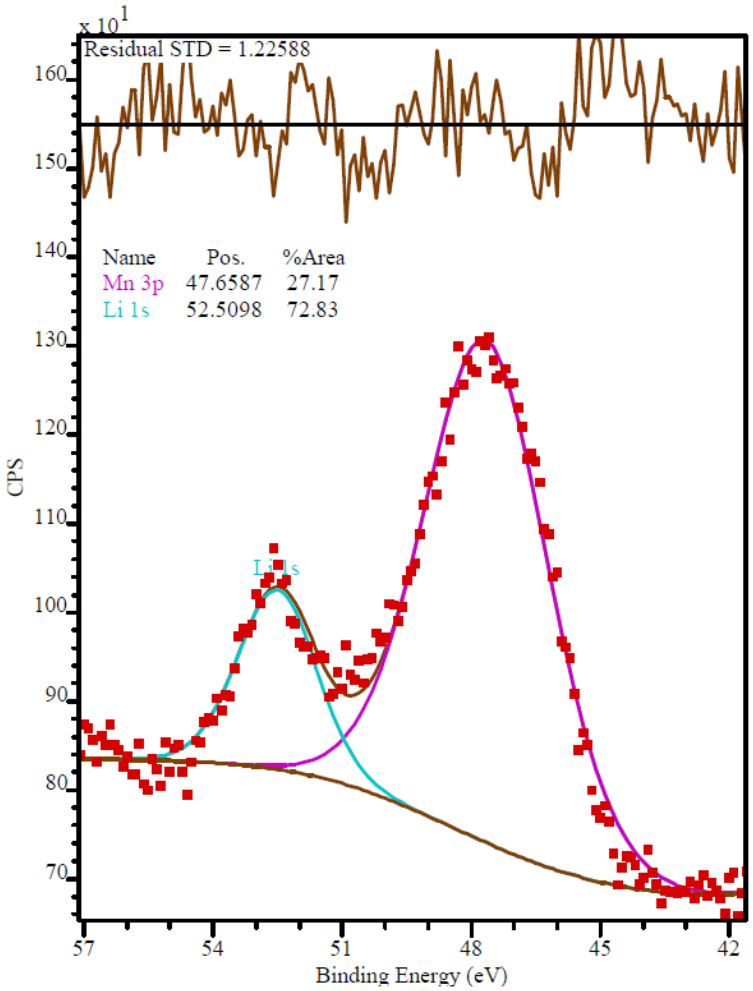

Figure 5.62: O 1s spectra for the potential hold sample following *in-situ* NR on a delaminated region.

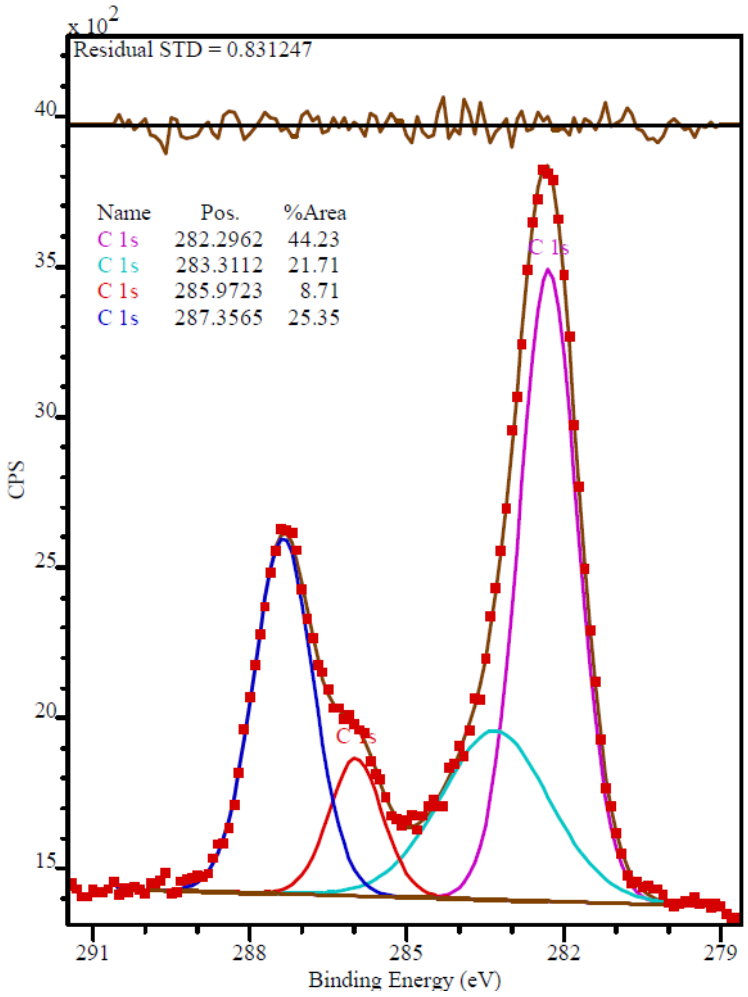

Figure 5.63: C 1s spectra for the potential hold sample following *in-situ* NR on a delaminated region.

CHAPTER VI

Conclusions

The work detailed in this thesis shows the applicability of NR to the study of interfacial phenomena in lithium-ion batteries. Significant effort was placed into preparing an experimental setup which would allow operation of a full-cell battery in the neutron beam to study the SEI layer on $LiMn_2O_4$. A method of preparing an electro-deposited anode was developed including designing and constructing an apparatus which fulfills this need. An experimental cell is designed and built which fulfills the requirements of being insulating, allowing electrical contact to the electrodes, allowing injection of electrolyte, allowing insertion of a reference electrode, and limiting background scattering in the designed cell. A method of preparing a lithium reference electrode which can be inserted into the electrochemical cell is detailed. A sample preparation procedure is developed which results in an electro-active cathode thin-film with <2 nm roughness for NR experiments. XPS is used to roughly characterize the cathode Mn oxidation state on two samples.

The cathode is tested both vs a large piece of lithium metal, and in the full-cell geometry where it is shown the sample preparation procedure produces a viable cathode for NR experiments. XRR and NR are used to characterize the cathode samples used for the full-cell experiments at open circuit and holding cell potential. Two NR experiments are performed where one sample is left at open circuit throughout

the experiment, and the other where the potential of the cell is held throughout the experiment. XPS and XRR are used to examine the cathode samples following the open circuit and potential hold experiments. SEM with EDX is used on the potential hold sample to investigate the observed delamination.

Throughout this research several significant findings were achieved:

The first significant finding in this work shows that the SEI on a cathode can be observed through NR. A distinct SEI layer was well defined in the fitted model with similar SLD for all NR measurements in electrolyte for both samples. The existence of an SEI on $LiMn_2O_4$ has been observed through other techniques namely XRR (80), TEM (81), XPS (67), and AFM (105). NR has a distinct advantage over other techniques as it is sensitive to light elements, is non-destructive, allows *in-situ* examination, and has a resolution on the order of Angstrom's in the layer profile. These advantages are highlighted in this work through an observation of the SEI and changes in the SEI through cycling.

In this work there is some evidence that two SEI layers formed on the potential hold sample. While only one obvious layer is observed, the apparent change in thickness of the cathode layer exceeds an explanation due to volume increase from a Jahn-Teller effect which is known to occur on $LiMn_2O_4$. This suggestion is also highlighted by observing the SLD profile for the cathode/SEI interface for all electrochemical conditions. The profile comparison shows a distinct change toward lower SLD indicative of protonation of the interface which has been suggested to occur through DFT calculations (70; 71). Further evidence that an SEI is hidden in the fitted cathode layer is derived from experiments which show contraction of the unit cell when charged (51). As the cathode layer SLD increases roughly in line with expectation due to deintercalation of lithium from the crystal structure, contraction of the layers should also be observed. From the fitted layer thicknesses the conditions where the potential was held at higher voltages showed expansion and layer growth

and not contraction. The layer growth is in direct conflict with the expected layer contraction indicating some other process is at work which is suggested here to be growth of a second SEI layer.

The idea of two SEI layers is suggested in literature (105) where an AFM probe is used to measure the hardness of the surface of a $LiMn_2O_4$ film. The authors discovered in many cases two forms of SEI layer, one hard and one soft. The hard layer is found close to the $LiMn_2O_4$ film, with the soft layer on top. Hwang et. al. proposed a model where the change in SEI thickness increase approximately 1.5 nm/cycle up to 20 cycles, and 0.5 nm/cycle thereafter. This model is not supported by these results presented here. In both cases where the cell potential was held constant and when the cell was left at open circuit an SEI was observed which was on the order of 10-16 nm. The attributed SEI in this work did not grow while cycling, it decreased in size. If the unusual growth in the cathode layer is attributed to an SEI on the surface then growth is observed in the SEI but at a much slower rate than is suggested by Hwang et al.

The SLD of the observed SEI layer is very consistent on the potential hold sample throughout the NR measurements. While the observed SEI layer is significantly changed by the final electrochemical condition, the fitted SLD value is in line with the previous electrochemical conditions. The cathode thickness after 26 CV cycles is lower than the 0 CV - 23 CV range. Furthermore, the observed SEI thickness decreased substantially. These three observations indicate (1) a phase change in the cathode layer, (2) once the phase change occurs, the SEI is diminshed. This suggests the SEI is partially dependent upon the potential of the cell.

The second significant finding is that the SEI formed on $LiMn_2O_4$ in the first cycles offers significant protection of the cathode layer. This point is shown by the lack of Mn observed through XPS on the open-circuit sample, but significant Mn observed on the potential hold sample. These samples were set up in similar electrochemical

cells with similar electrolyte and anodes, and were prepared through the same process using the same sol-gel. While the samples were operated differently throughout the NR measurements, they were both allowed to sit in storage for essentially the same length of time. The primary difference in their operation was preventing self-discharge throughout the NR measurements on the potential hold sample by holding the cell potential constant.

Evidence from XPS shows the presence of a Mn^{4+} and Mn^{2+} rich cathode layer on the potential hold sample which is a result of self-discharge resulting in $Li_2Mn_2O_4$ and subsequently to form Li_2MnO_3 and MnO. While it might be expected to have similar observed concentrations of Mn in those two oxidation states, MnO dissolves in acidic solutions, which should result in a portion being lost to the electrolyte (61).

The lack of a clear Mn 2p3/2 emission in XPS on the open circuit sample prevented a study of the samples Mn ratio. A rough approximation of the expected SLD on the open circuit sample in the electrolyte cell given a phase change to $Li_2Mn_2O_4$ is shown to lie close to the observed value. Furthermore the open-circuit potential for the open-circuit sample is in the same range as expected for $Li_2Mn_2O_4$.

These observations indicate that the final outcome of both sample cathode layers was to the form Li_2MnO_3 and MnO either due to self-discharge, non-equilibrium cycling, or short-circuit forming $Li_2Mn_2O_4$. Post-NR XRR results on these samples show significant loss of material from the open circuit sample, but not the potential hold sample. These show the formation of SEI upon cycling protects the cathode layers from complete breakdown even if the formation of $Li_2Mn_2O_4$ occurs.

A further significant finding in this work is the poor choice of platinum as a charge collection layer. Platinum is used as a charge collection layer in this work for several reasons. One is that it can withstand the high-temperature annealing process which the cathode layer prepared through sol-gel needs to crystallize. The second reason is it was thought to be inert and stable in the cell and should not change acting as a

stable substrate. This is certainly not the case as the platinum SLD changed with a fairly consistent trend from in-air to lower-SLD. This indicates either dissolution of the platinum layer into the cell or dissolution of lithium into the platinum layer. There is not enough evidence for either of these suggestions to point to a specific cause.

CHAPTER VII

Future Work

The work produced in pursuit of this thesis is a very small portion of work which may be done in support of SEI research. There were several flaws in this work which can be rectified in future work. The most significant of which is the method of producing the cathode layer. To have good results which are comparable to modelling techniques the cathode should be epitaxial. A type of layer-by-layer depostion such as Pulsed Laser Deposition or some other deposition method should be used to form very dense, epitaxial, smooth films. Through epitaxy experimental observation of the SEI would allow a better understaning of electrolyte breakdown effects on the crystal structure. A higher density film would remove some of the uncertainty in SLD determination of the layer, and would result in a better observation of the layer change without concerning the effects of SEI formation within the pores. A vapor deposition method would also remove the impact of warp in this work due to the annealing step used to prepare these cathode films.

The substrates should be altered to remove metals which are subject to attack by the electrolyte salt, such as the copper used as the anode charge collection layer. An understanding of the process which leads to delamination of the cathode is important. The charge collection layer should be considered a constant in this kind of work and it was shown here that the platinum metal charge collection layer is modified throughout

the experiment. This introduces unnecessary additional fitting parameters which make the process of understanding the results much more difficult.

The electro-deposition apparatus used to prepare the anode should be modified to allow two-axis rotation to prevent the rough dendritic deposition on the center of the substrate wafer. This would eliminate the need for removing the lithium which deposits on the center of the wafer.

Following the work to prepare better sample conditions there are several experimental conditions which should be investigated. The impact of salt choice on the SEI should be probed. Does each salt exhibit a different SEI or is the effect of electrolyte solvent more important? Does the electrolyte solvent mixture impact the formation of the SEI? This is known to be a factor, but direct experimental evidence on the impact of each solvent on the cathode should be explored. The impact of Vinylene Carbonate (VC) on cathode SEI should be explored as VC is regularly used as an additive in the electrolyte to form a more stable SEI.

The methods applied in this thesis can further be applied to general electrochemistry to investigate other cathode materials such as $LiFePO_4$, and $LiMn_{1.5}Ni_0.5O_4$ among others. These techniques can be applied to the study of native SEI layers as well as coatings which serve as an artificial SEI. Further these techniques can apply to samples held at elevated temperatures to promote greater SEI growth.

APPENDICES

APPENDIX A

Open Circuit NR dataset corrections

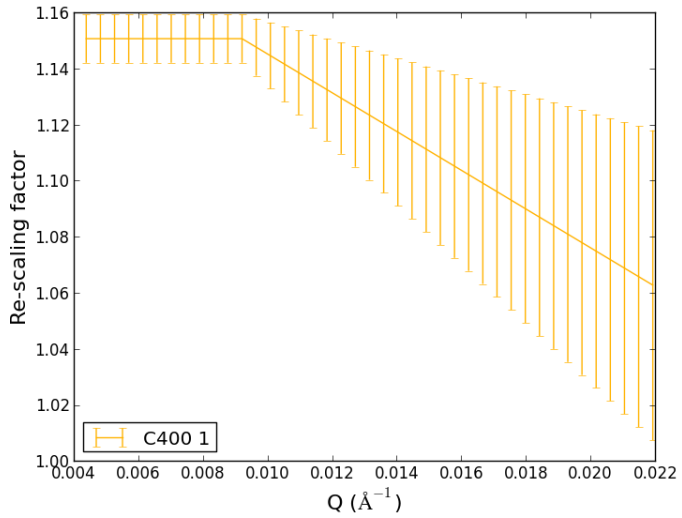

(a) Correction function applied to the first NR dataset from those data following electrolyte introduction.

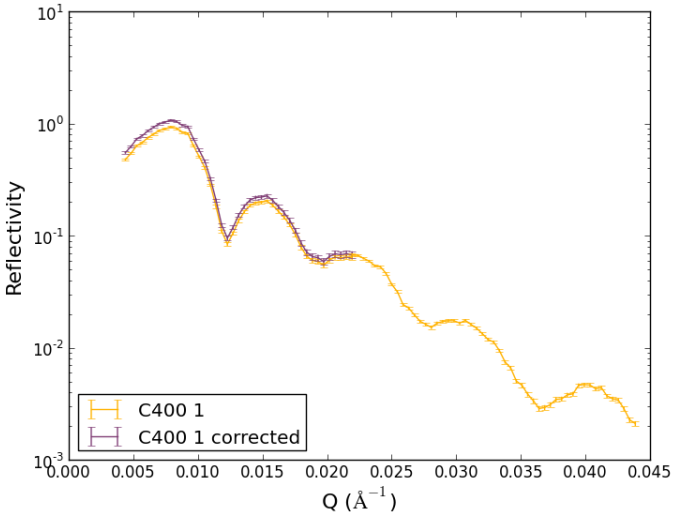

(b) First dataset collected following electrolyte introduction with correction

Figure A.1: Correction function and corrected reflectivity data for first dataset following electrolyte introduction for the open circuit sample.

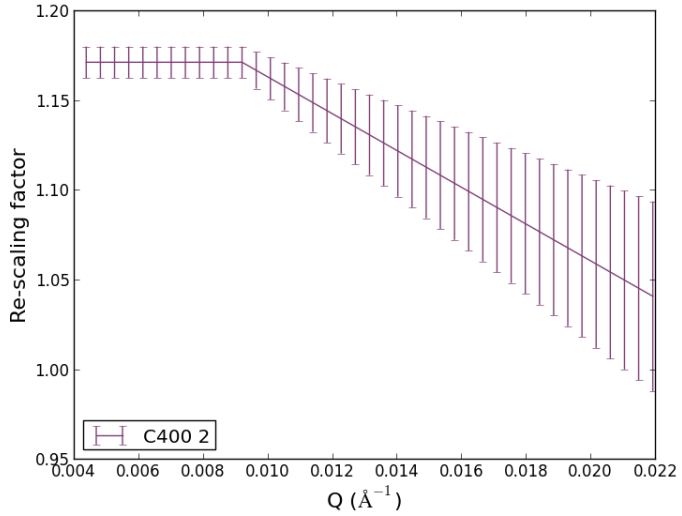

(a) Correction function applied to the second NR dataset from those data following electrolyte introduction.

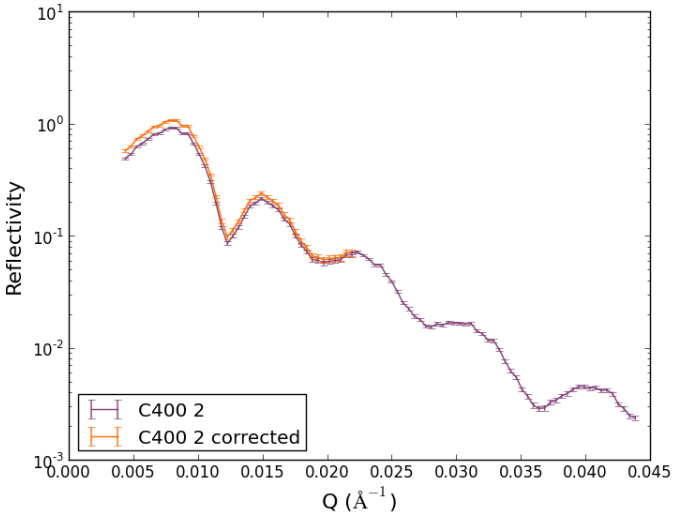

(b) Second dataset collected following electrolyte introduction with correction

Figure A.2: Correction function and corrected reflectivity data for second dataset following electrolyte introduction for the open circuit sample.

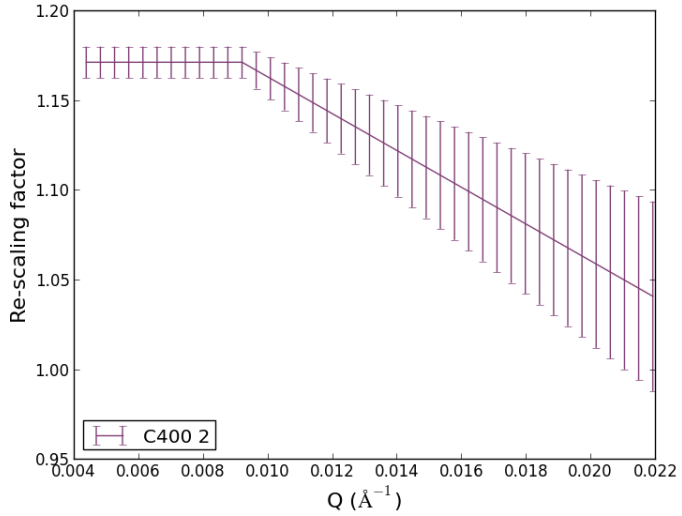

(a) Correction function applied to the third NR dataset from those data following electrolyte introduction.

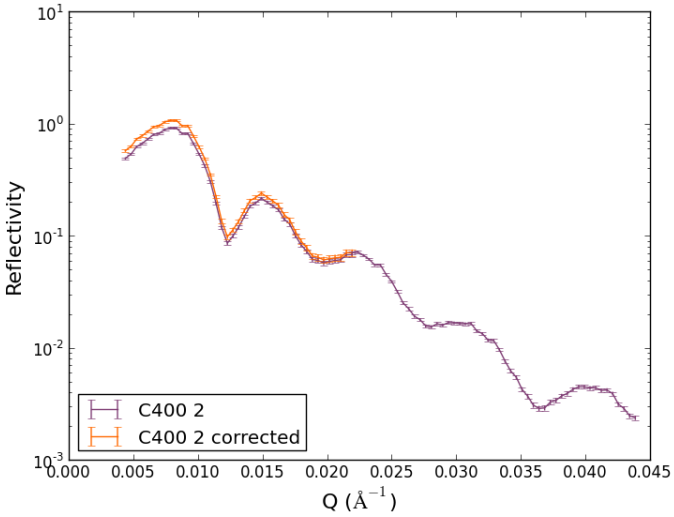

(b) Third dataset collected following electrolyte introduction with correction

Figure A.3: Correction function and corrected reflectivity data for third dataset following electrolyte introduction for the open circuit sample.

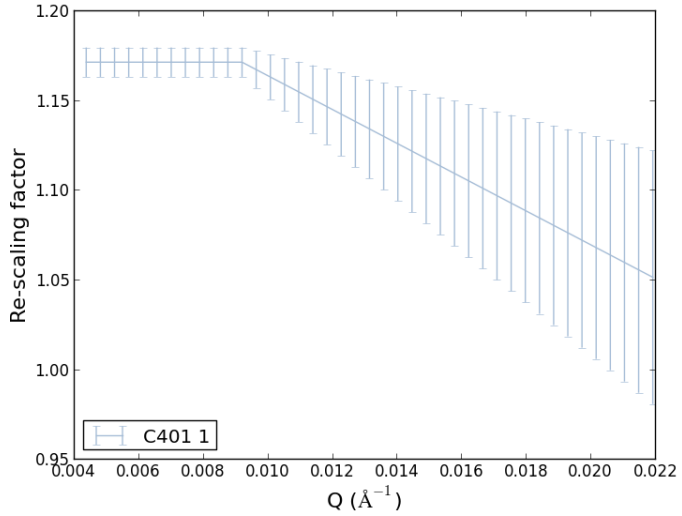

(a) Correction function applied to the first NR dataset from those data following one CV cycle.

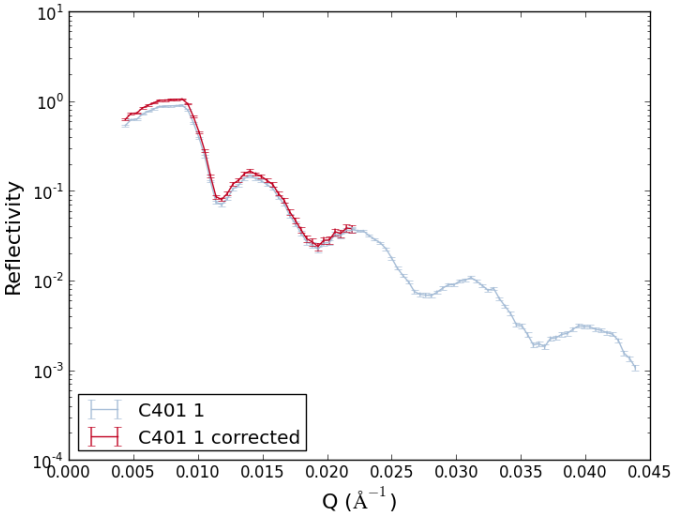

(b) First dataset collected following one CV cycle with correction

Figure A.4: Correction function and corrected reflectivity data for first dataset following one CV cycle for the open circuit sample.

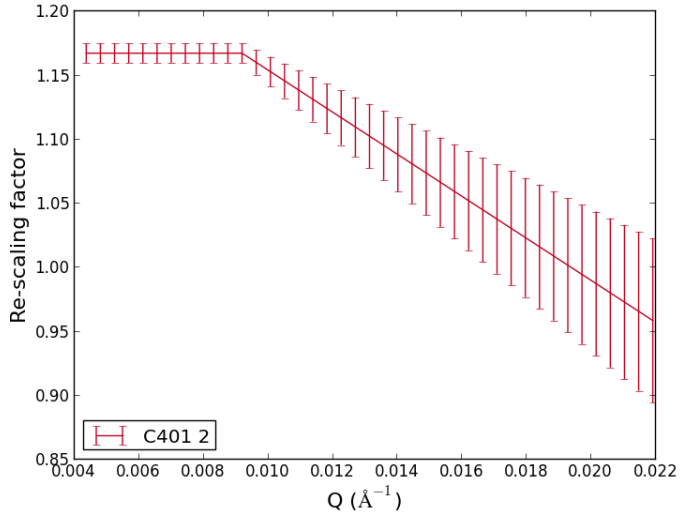

(a) Correction function applied to the second NR dataset from those data following one CV cycle.

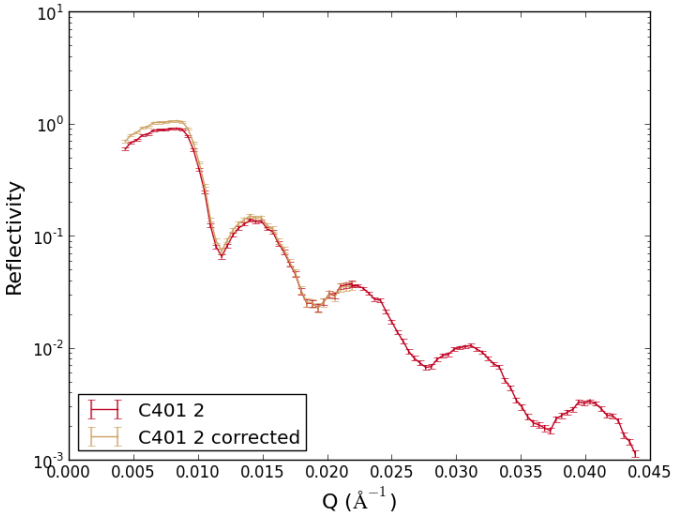

(b) Second dataset collected following one CV cycle with correction

Figure A.5: Correction function and corrected reflectivity data for second dataset following one CV cycle for the open circuit sample.

APPENDIX B

Potential Hold NR dataset corrections

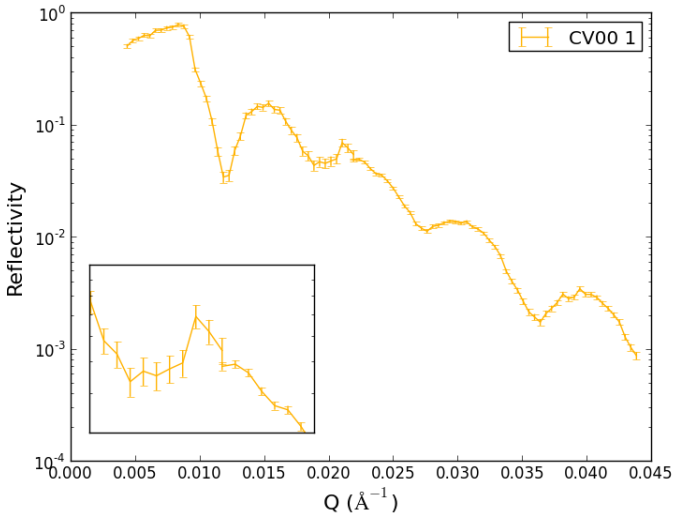

Figure B.1: Reduced NR first dataset after electrolyte injection for potential hold sample highlighting the discrepancy between the first two angular ranges.

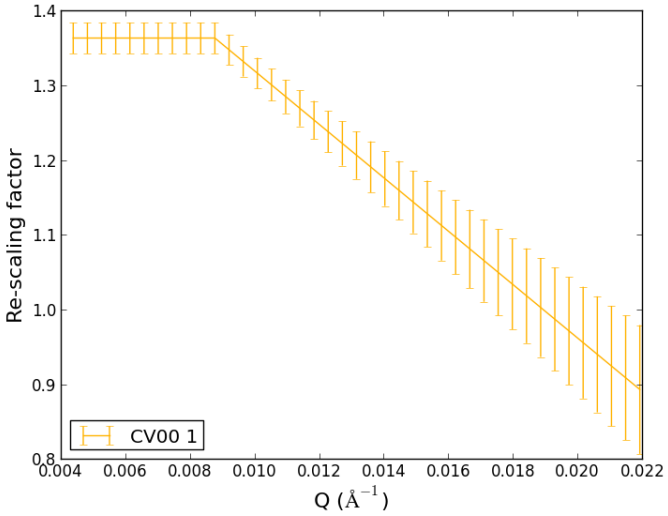

(a) Correction function applied to the first NR dataset from those data following electrolyte introduction.

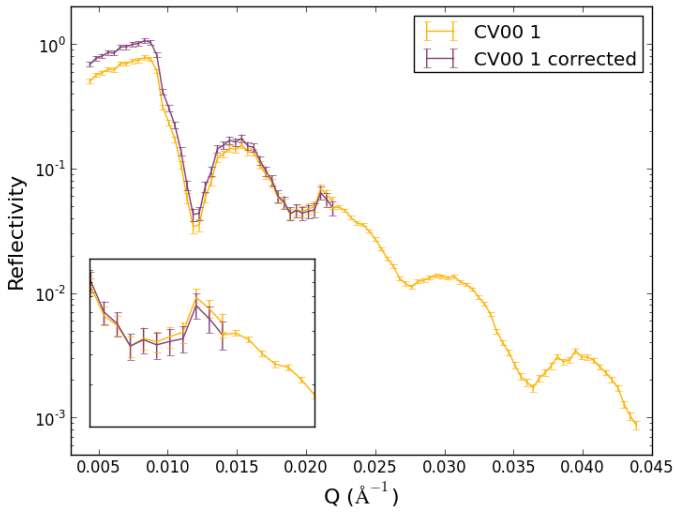

(b) First dataset collected following electrolyte introduction with correction

Figure B.2: Correction function and corrected reflectivity data for first dataset following electrolyte introduction for potential hold sample.

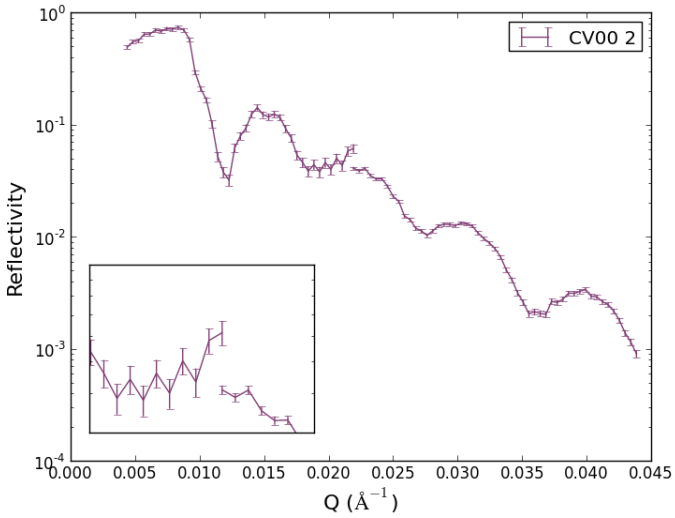

Figure B.3: Reduced NR second dataset after electrolyte injection for potential hold sample highlighting the discrepancy between the first two angular ranges.

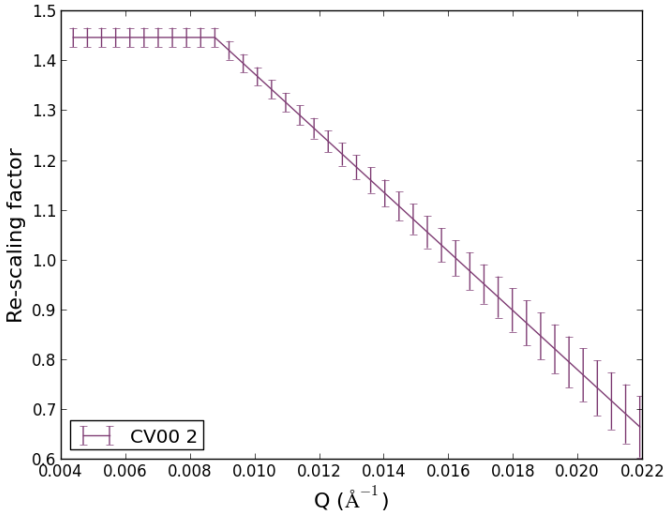

(a) Correction function applied to the second NR dataset from those data following electrolyte introduction.

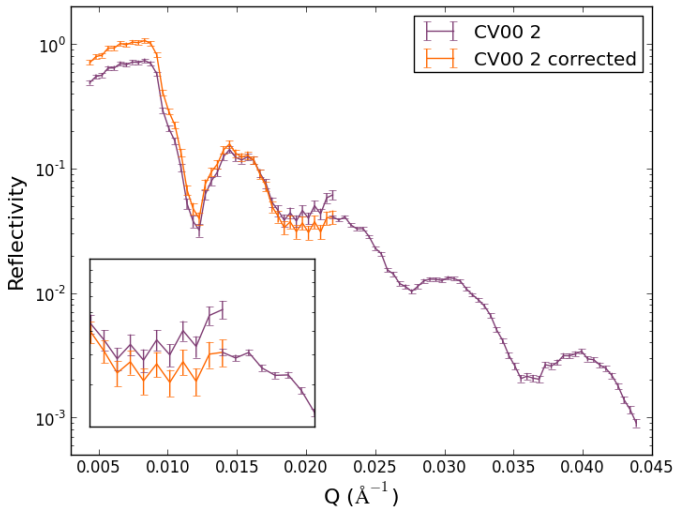

(b) Second dataset collected following electrolyte introduction with correction

Figure B.4: Correction function and corrected reflectivity data for second dataset following electrolyte introduction for potential hold sample.

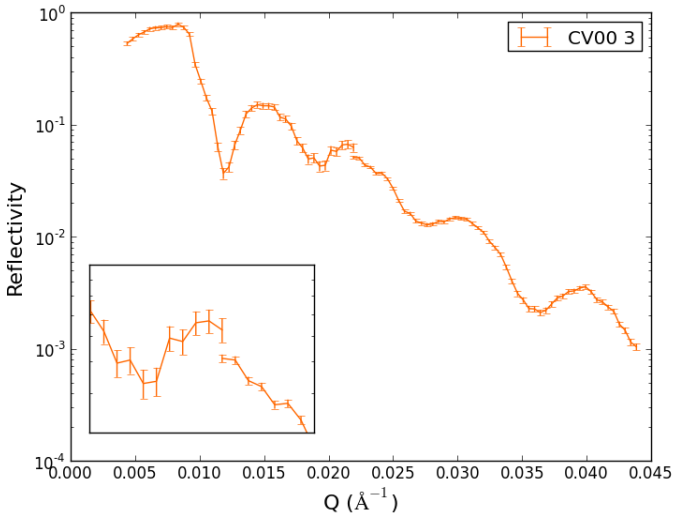

Figure B.5: Reduced NR third dataset after electrolyte injection for potential hold sample highlighting the discrepancy between the first two angular ranges.

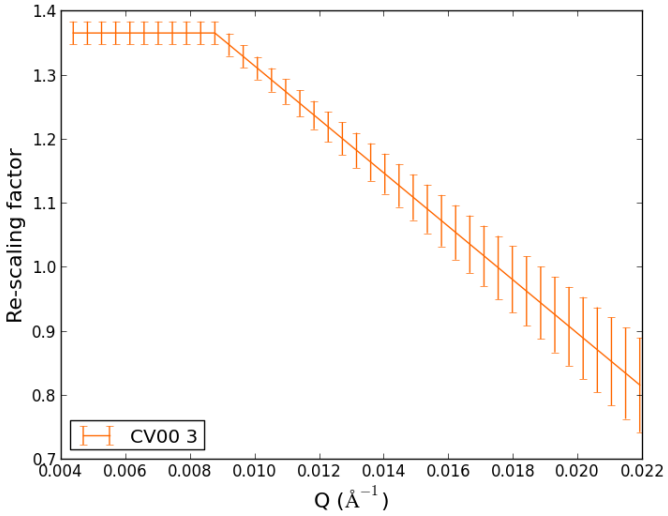

(a) Correction function applied to the third NR dataset from those data following electrolyte introduction.

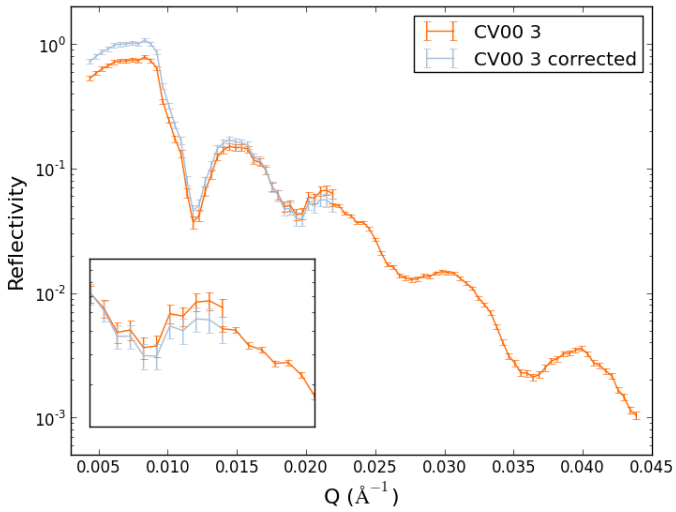

(b) Third dataset collected following electrolyte introduction with correction

Figure B.6: Correction function and corrected reflectivity data for third dataset following electrolyte introduction for potential hold sample.

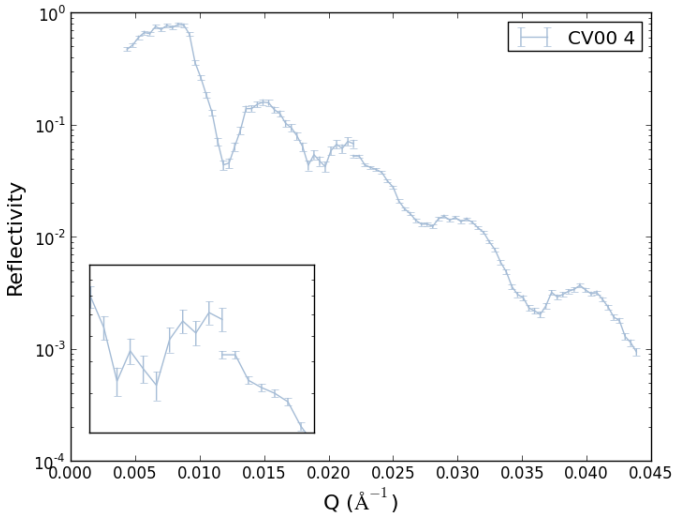

Figure B.7: Reduced NR fourth dataset after electrolyte injection for potential hold sample highlighting the discrepancy between the first two angular ranges.

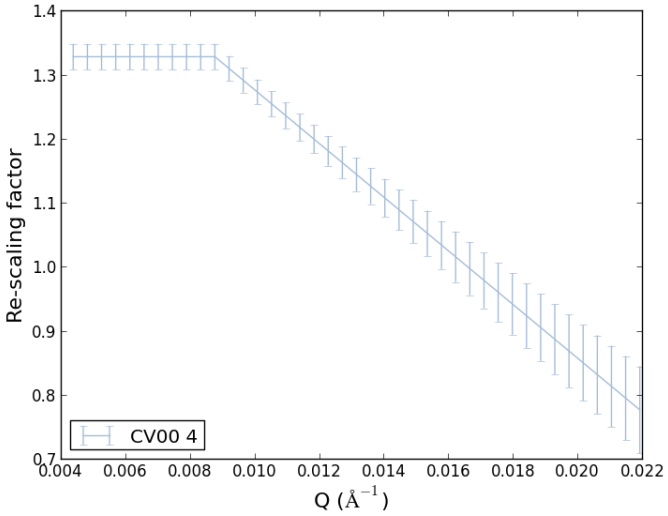

(a) Correction function applied to the fourth NR dataset from those data following electrolyte introduction.

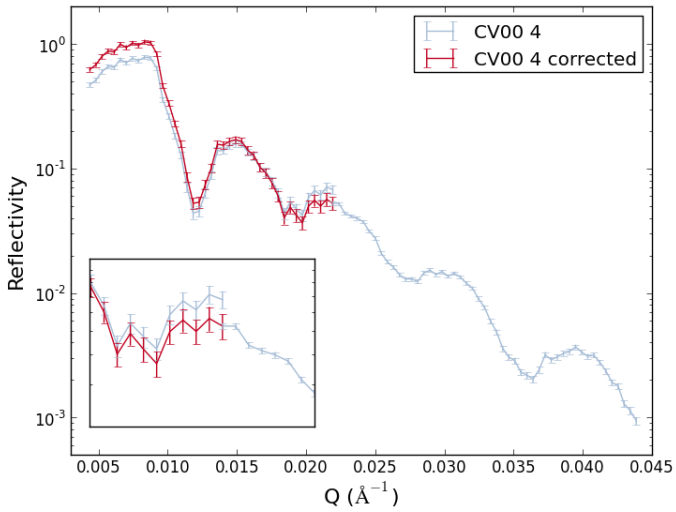

(b) Fourth dataset collected following electrolyte introduction with correction

Figure B.8: Correction function and corrected reflectivity data for third dataset following electrolyte introduction for potential hold sample.

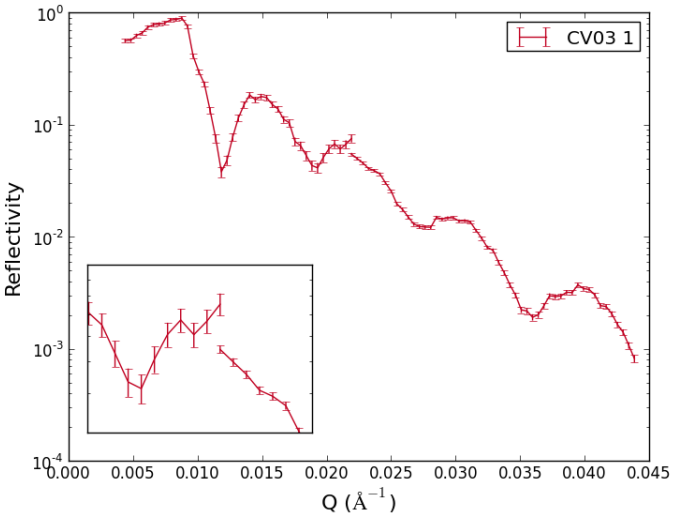

Figure B.9: Reduced NR first dataset 3 CV cycles for potential hold sample highlighting the discrepancy between the first two angular ranges.

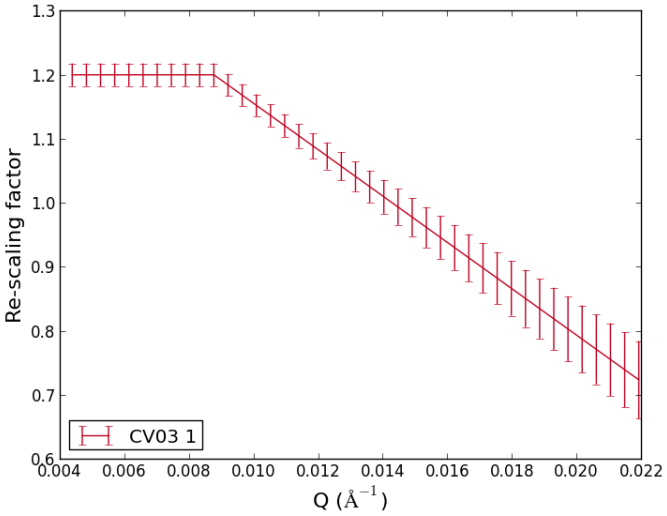

(a) Correction function applied to the first NR dataset from those data following 3 CV cycles.

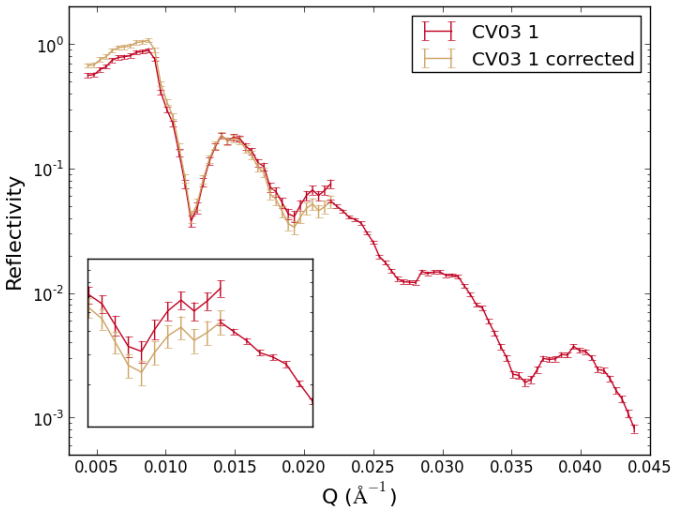

(b) First dataset collected following 3 CV cycles with correction

Figure B.10: Correction function and corrected reflectivity data for third dataset following 3 CV cycles for potential hold sample.

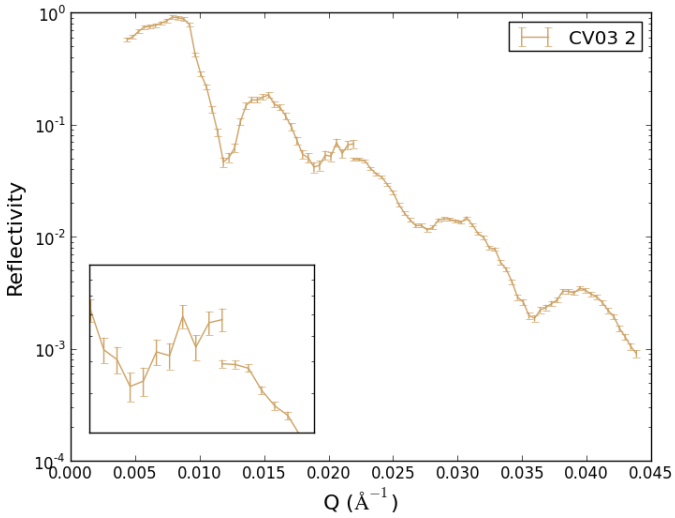

Figure B.11: Reduced NR second dataset 3 CV cycles for potential hold sample highlighting the discrepancy between the first two angular ranges.

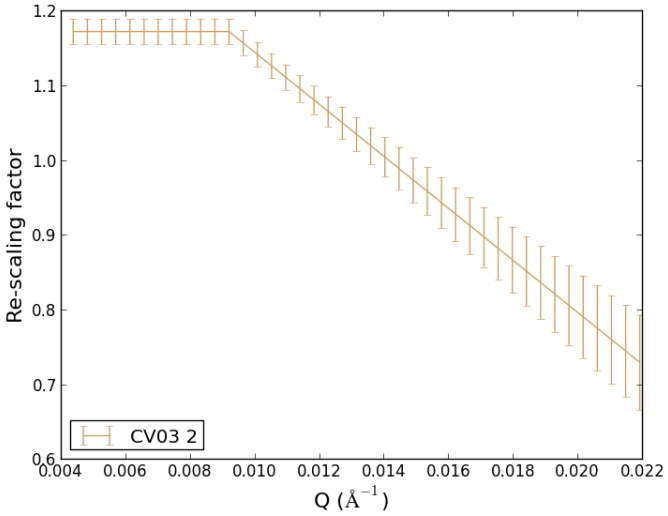

(a) Correction function applied to the second NR dataset from those data following 3 CV cycles.

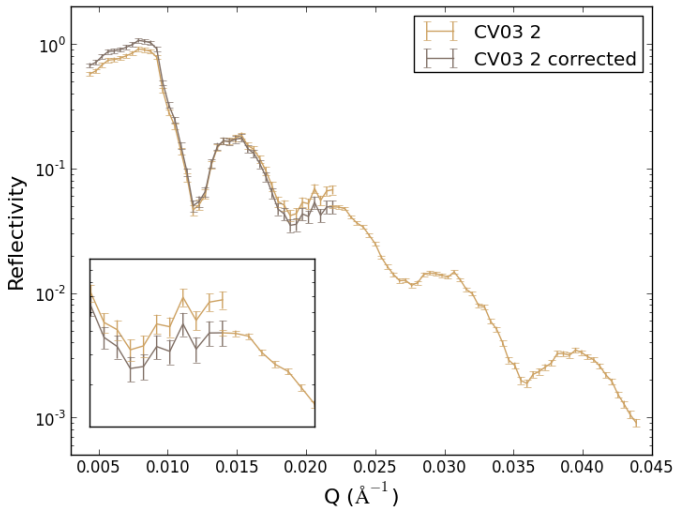

(b) Second dataset collected following 3 CV cycles with correction

Figure B.12: Correction function and corrected reflectivity data for second dataset following 3 CV cycles for potential hold sample.

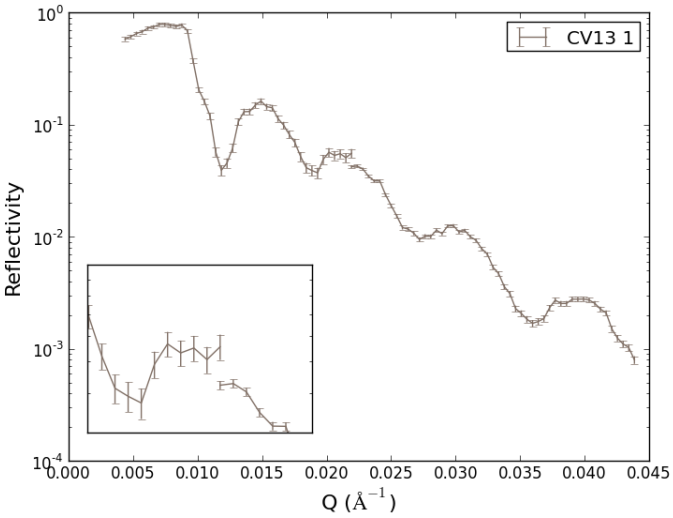

Figure B.13: Reduced NR first dataset 13 CV cycles for potential hold sample highlighting the discrepancy between the first two angular ranges.

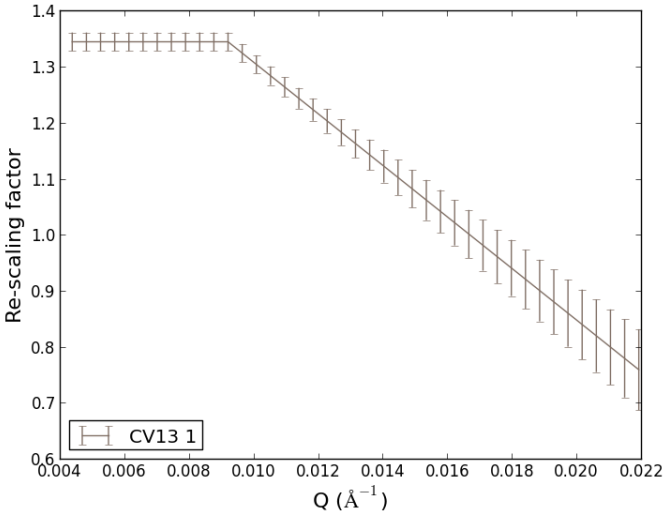

(a) Correction function applied to the first NR dataset from those data following 13 CV cycles.

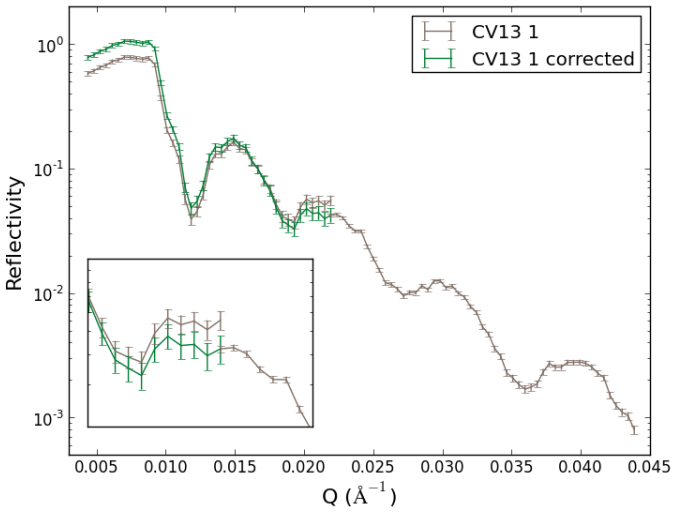

(b) First dataset collected following 13 CV cycles with correction

Figure B.14: Correction function and corrected reflectivity data for third dataset following 13 CV cycles for potential hold sample.

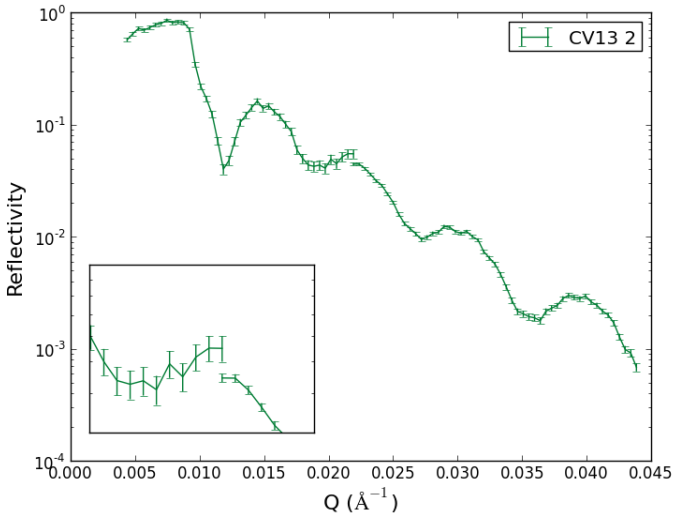

Figure B.15: Reduced NR second dataset 13 CV cycles for potential hold sample highlighting the discrepancy between the first two angular ranges.

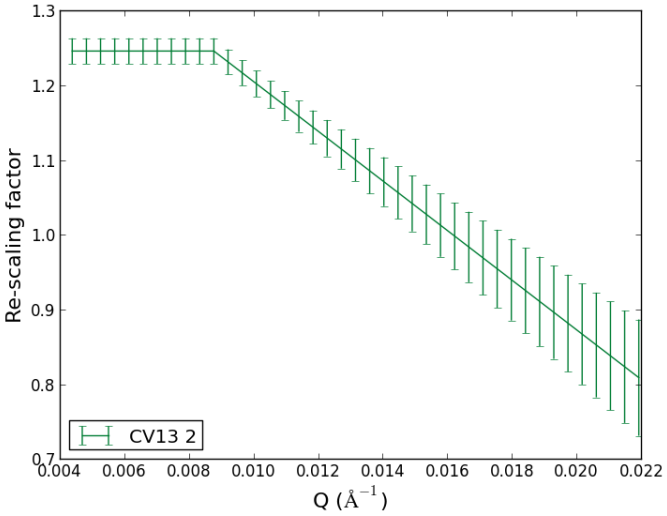

(a) Correction function applied to the second NR dataset from those data following 13 CV cycles.

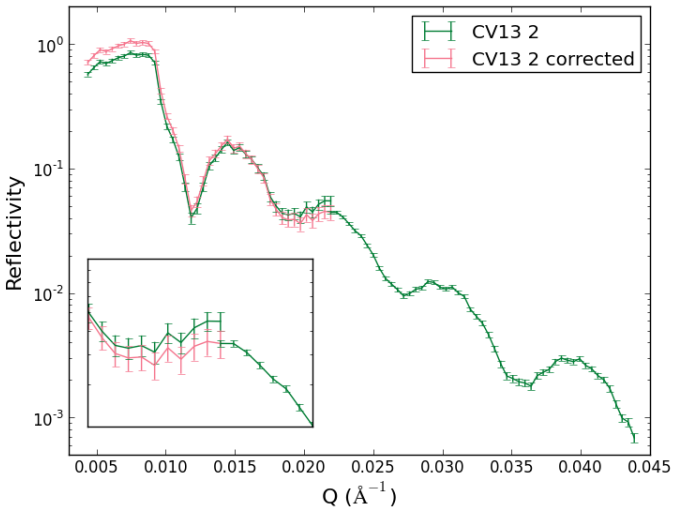

(b) Second dataset collected following 13 CV cycles with correction

Figure B.16: Correction function and corrected reflectivity data for second dataset following 3 CV cycles for potential hold sample.

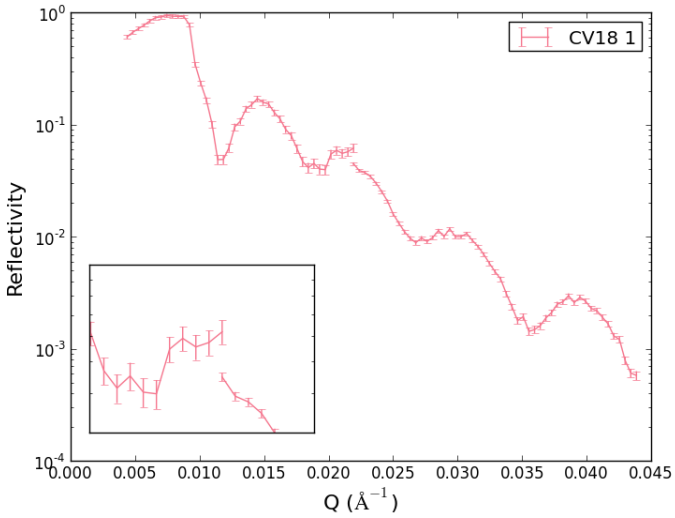

Figure B.17: Reduced NR first dataset 18 CV cycles for potential hold sample highlighting the discrepancy between the first two angular ranges.

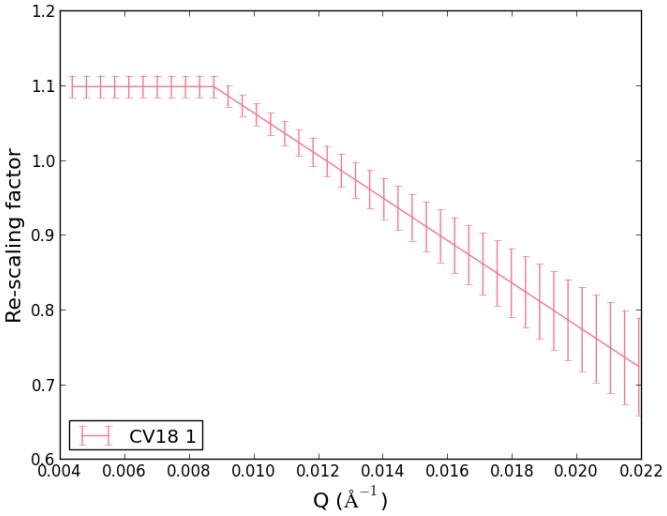

(a) Correction function applied to the first NR dataset from those data following 18 CV cycles.

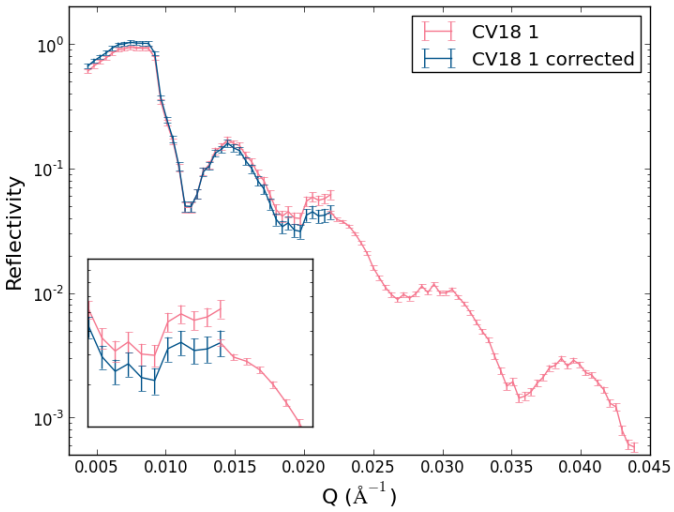

(b) First dataset collected following 18 CV cycles with correction

Figure B.18: Correction function and corrected reflectivity data for third dataset following 18 CV cycles for potential hold sample.

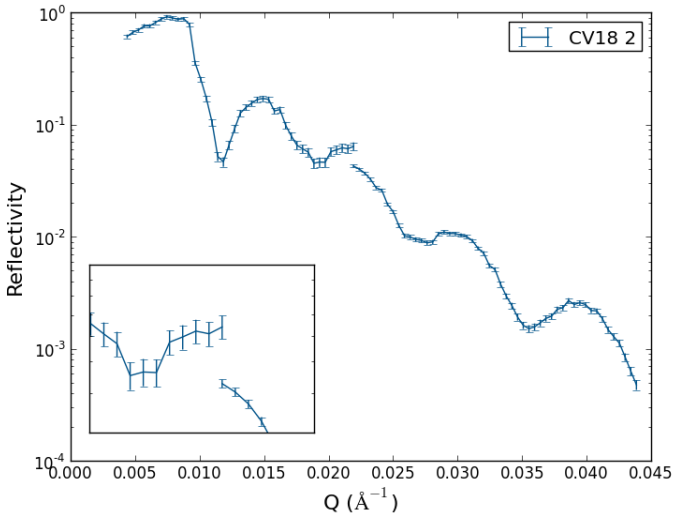

Figure B.19: Reduced NR second dataset 18 CV cycles for potential hold sample highlighting the discrepancy between the first two angular ranges.

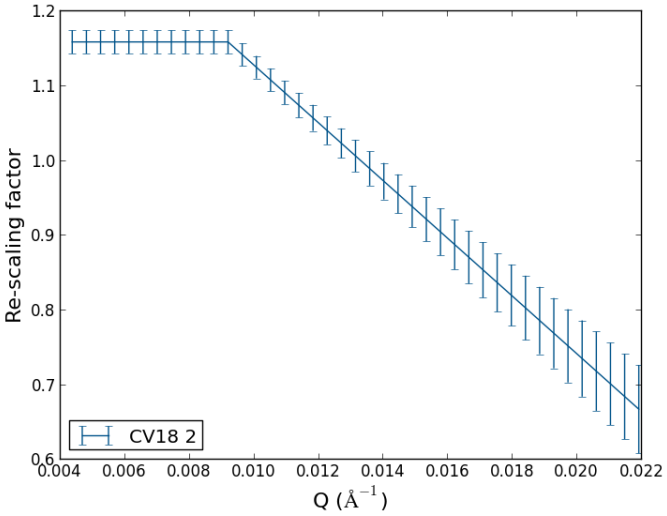

(a) Correction function applied to the second NR dataset from those data following 18 CV cycles.

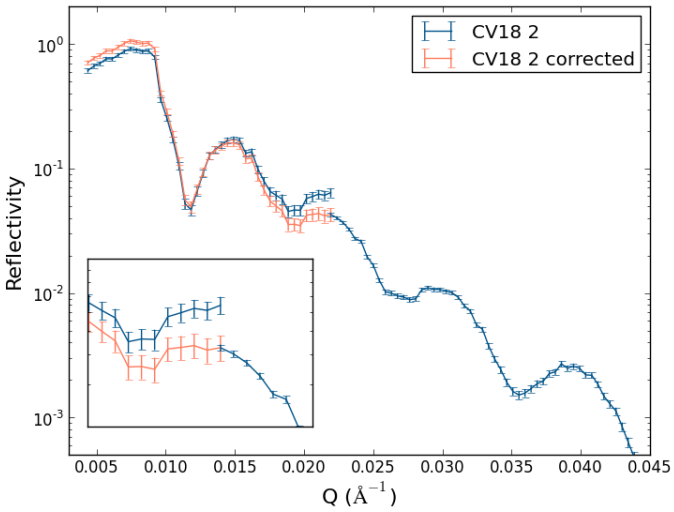

(b) Second dataset collected following 18 CV cycles with correction

Figure B.20: Correction function and corrected reflectivity data for second dataset following 18 CV cycles for potential hold sample.

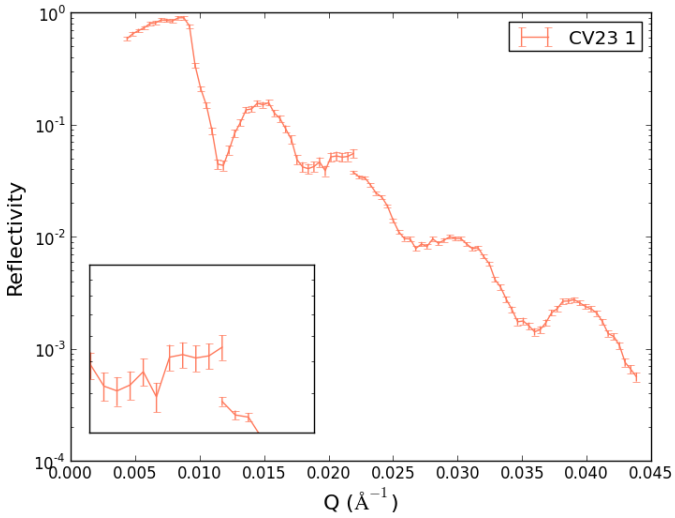

Figure B.21: Reduced NR first dataset 23 CV cycles for potential hold sample highlighting the discrepancy between the first two angular ranges.

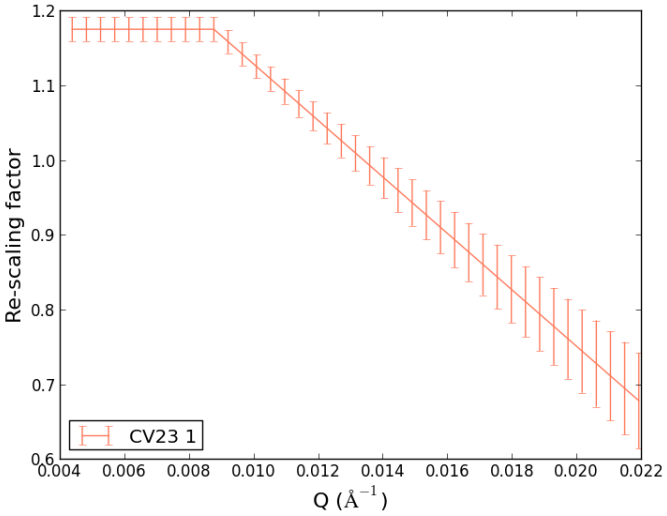

(a) Correction function applied to the first NR dataset from those data following 23 CV cycles.

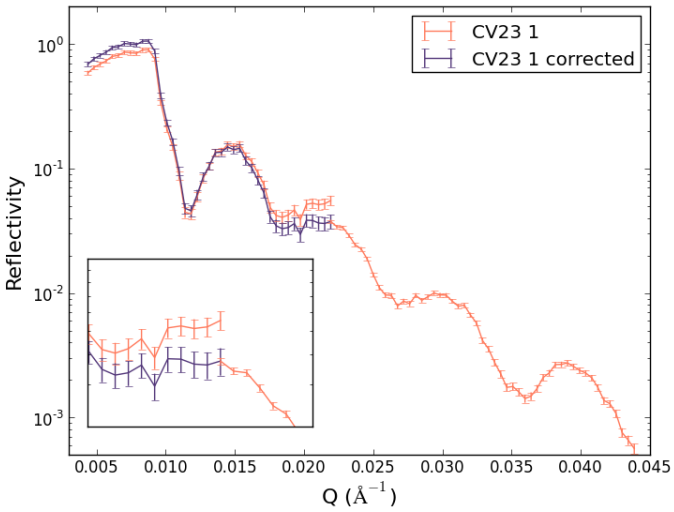

(b) First dataset collected following 23 CV cycles with correction

Figure B.22: Correction function and corrected reflectivity data for third dataset following 23 CV cycles for potential hold sample.

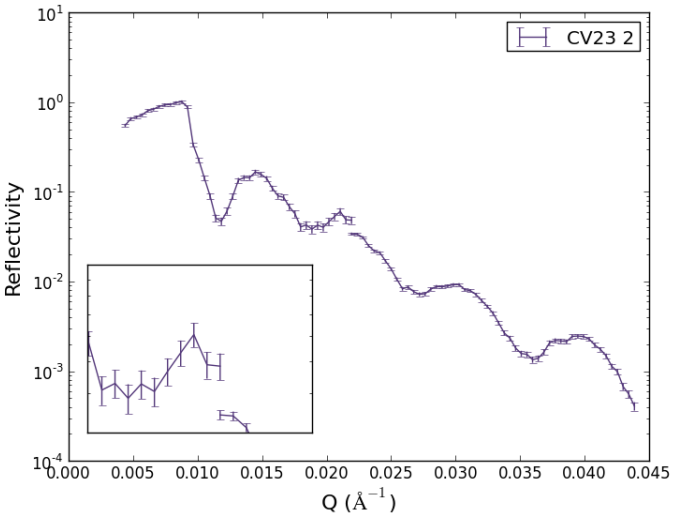

Figure B.23: Reduced NR second dataset 23 CV cycles for potential hold sample highlighting the discrepancy between the first two angular ranges.

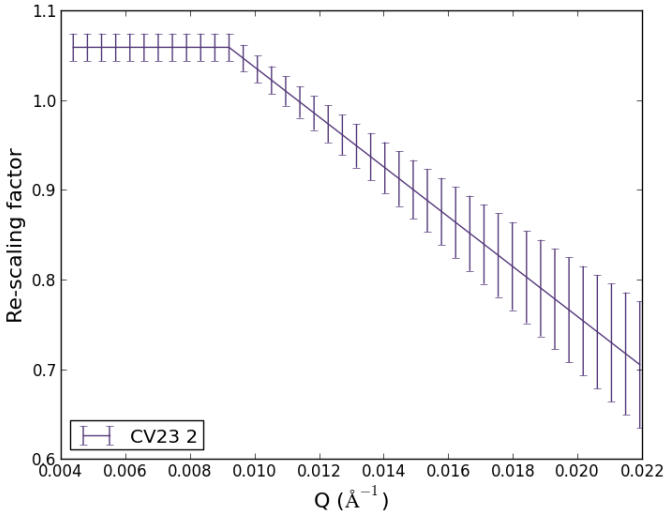

(a) Correction function applied to the second NR dataset from those data following 23 CV cycles.

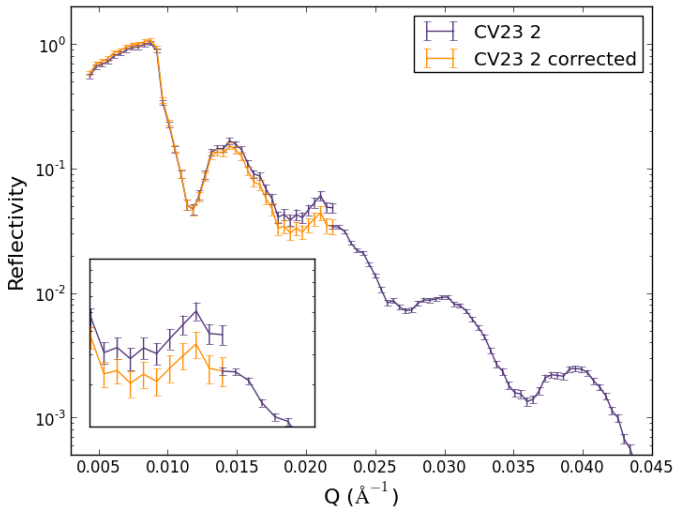

(b) Second dataset collected following 23 CV cycles with correction

Figure B.24: Correction function and corrected reflectivity data for second dataset following 23 CV cycles for potential hold sample.

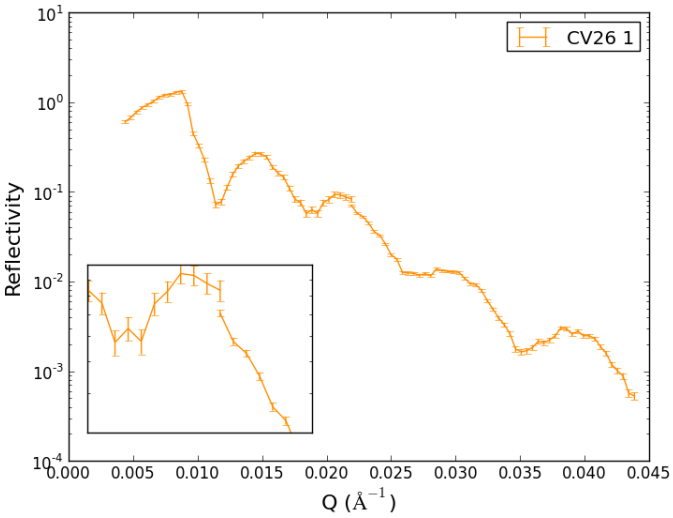

Figure B.25: Reduced NR first dataset 26 CV cycles for potential hold sample highlighting the discrepancy between the first two angular ranges.

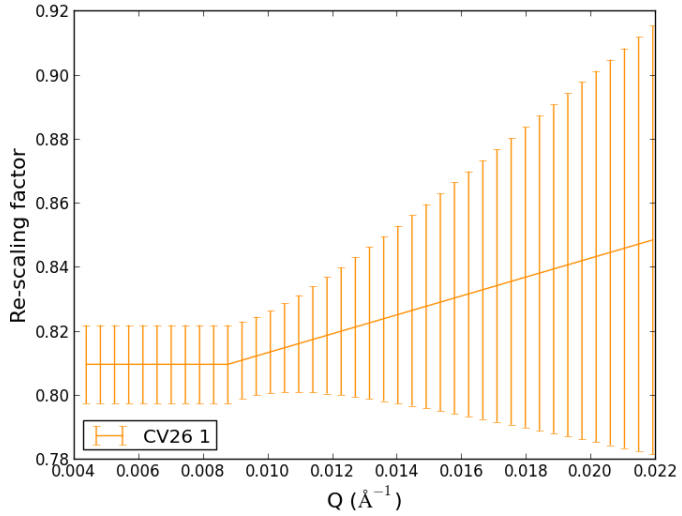

(a) Correction function applied to the first NR dataset from those data following 26 CV cycles.

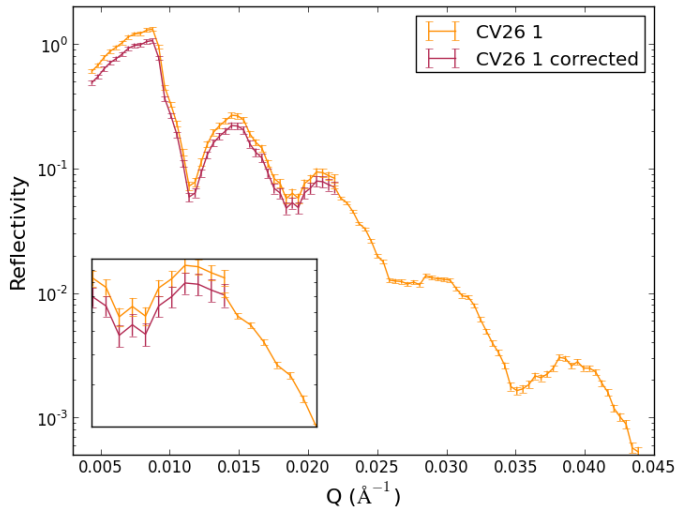

(b) First dataset collected following 26 CV cycles with correction

Figure B.26: Correction function and corrected reflectivity data for third dataset following 26 CV cycles for potential hold sample.

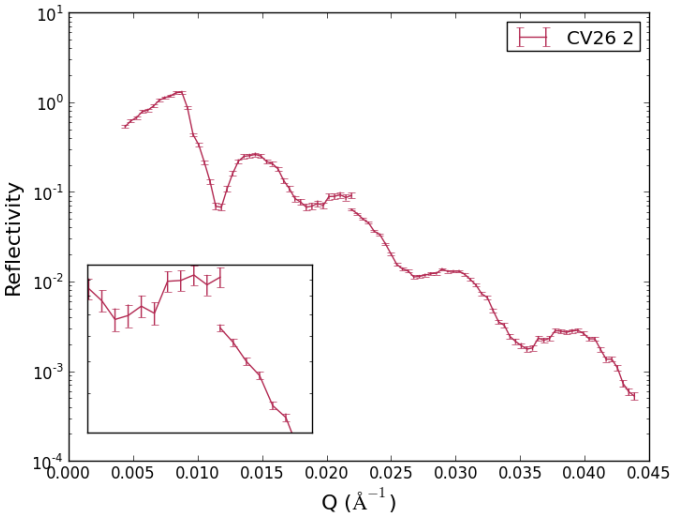

Figure B.27: Reduced NR second dataset 26 CV cycles for potential hold sample highlighting the discrepancy between the first two angular ranges.

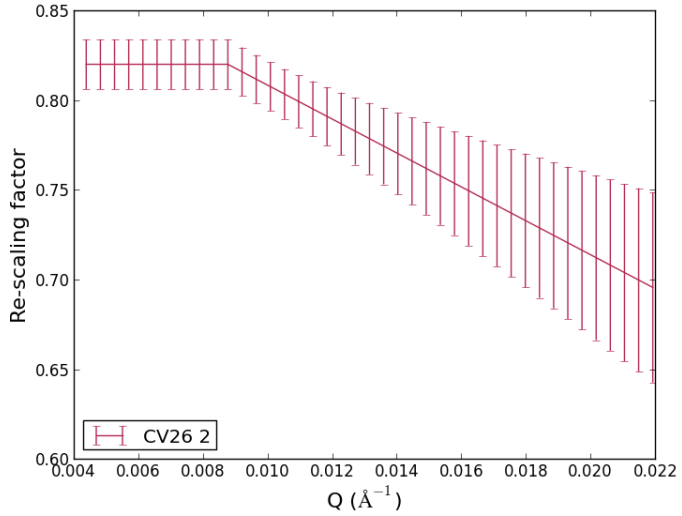

(a) Correction function applied to the second NR dataset from those data following 26 CV cycles.

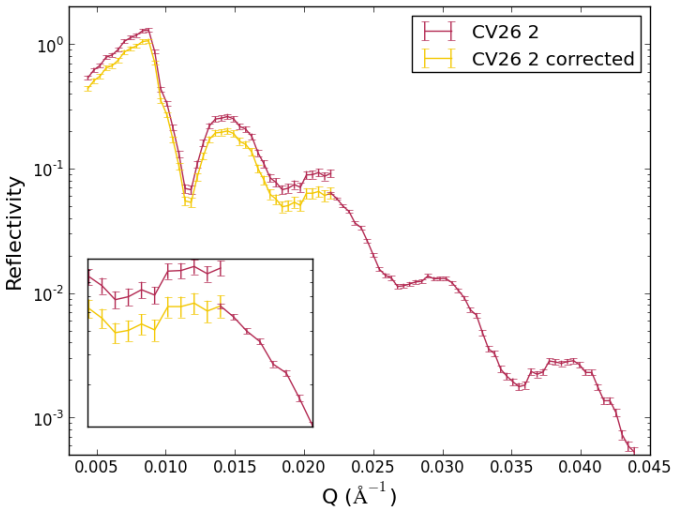

(b) Second dataset collected following 26 CV cycles with correction

Figure B.28: Correction function and corrected reflectivity data for second dataset following 26 CV cycles for potential hold sample.

BIBLIOGRAPHY

[1] J.-M. Tarascon and M. Armand, "Issues and challenges facing rechargeable lithium batteries," *Nature*, vol. 414, pp. 359–367, Nov. 2001.

[2] C. Yaws, *Yaws' Handbook of Properties of the Chemical Elements*. Knovel, 2011.

[3] J.-M. Tarascon, "Key challenges in future li-battery research," *Philosophical Transactions of the Royal Society A: Mathematical, Physical and Engineering Sciences*, vol. 368, pp. 3227–3241, July 2010.

[4] M. Winter, "The solid electrolyte interphase - the most important and least understood solid electrolyte in rechargeable li battereis," *Z. Phys. Chem*, vol. 223, no. 10-11, pp. 1395–1406, 2009.

[5] A. M. Andersson, D. P. Abraham, R. Haasch, S. MacLaren, J. Liu, and K. Amine, "Surface characterization of electrodes from high power lithium-ion batteries," *Journal of The Electrochemical Society*, vol. 149, pp. A1358–A1369, Jan. 2002.

[6] K. Amine, C. Chen, J. Liu, M. Hammond, A. Jansen, D. Dees, I. Bloom, D. Vissers, and G. Henriksen, "Factors responsible for impedance rise in high power lithium ion batteries," *Journal of Power Sources*, vol. 9798, pp. 684–687, July 2001.

[7] M. Broussely, P. Biensan, F. Bonhomme, P. Blanchard, S. Herreyre, K. Nechev, and R. Staniewicz, "Main aging mechanisms in li ion batteries," *Journal of Power Sources*, vol. 146, pp. 90–96, Aug. 2005.

[8] E. Peled, "The electrochemical behavior of alkali and alkaline earth metals in nonaqueous battery systemsthe solid electrolyte interphase model," *Journal of The Electrochemical Society*, vol. 126, pp. 2047–2051, Jan. 1979.

[9] H. H. Lee, C. C. Wan, and Y. Y. Wang, "Thermal stability of the solid electrolyte interface on carbon electrodes of lithium batteries," *Journal of The Electrochemical Society*, vol. 151, pp. A542–A547, Jan. 2004.

[10] P. Verma, P. Maire, and P. Novk, "A review of the features and analyses of the solid electrolyte interphase in li-ion batteries," *Electrochimica Acta*, vol. 55, pp. 6332–6341, Sept. 2010.

[11] J. Vetter, P. Novk, M. Wagner, C. Veit, K.-C. Mller, J. Besenhard, M. Winter, M. Wohlfahrt-Mehrens, C. Vogler, and A. Hammouche, "Ageing mechanisms in lithium-ion batteries," *Journal of Power Sources*, vol. 147, pp. 269–281, Sept. 2005.

[12] Q. Zhang and R. E. White, "Capacity fade analysis of a lithium ion cell," *Journal of Power Sources*, vol. 179, pp. 793–798, May 2008.

[13] J. Yan, B.-J. Xia, Y.-C. Su, X.-Z. Zhou, J. Zhang, and X.-G. Zhang, "Phenomenologically modeling the formation and evolution of the solid electrolyte interface on the graphite electrode for lithium-ion batteries," *Electrochimica Acta*, vol. 53, pp. 7069–7078, Oct. 2008.

[14] K. Tasaki and S. J. Harris, "Computational study on the solubility of lithium salts formed on lithium ion battery negative electrode in organic solvents," *J. Phys. Chem. C*, vol. 114, pp. 8076–8083, Apr. 2010.

[15] K. Tasaki, A. Goldberg, J.-J. Lian, M. Walker, A. Timmons, and S. J. Harris, "Solubility of lithium salts formed on the lithium-ion battery negative electrode surface in organic solvents," *Journal of The Electrochemical Society*, vol. 156, pp. A1019–A1027, Dec. 2009.

[16] K. Xu, S. Zhang, and T. R. Jow, "Formation of the graphite/electrolyte interface by lithium bis(oxalato)borate," *Electrochemical and Solid-State Letters*, vol. 6, pp. A117–A120, Jan. 2003.

[17] A. M. Andersson and K. Edstrm, "Chemical composition and morphology of the elevated temperature SEI on graphite," *Journal of The Electrochemical Society*, vol. 148, pp. A1100–A1109, Jan. 2001.

[18] N.-S. Choi, Z. Chen, S. A. Freunberger, X. Ji, Y.-K. Sun, K. Amine, G. Yushin, L. F. Nazar, J. Cho, and P. G. Bruce, "Challenges facing lithium batteries and electrical double-layer capacitors," *Angewandte Chemie International Edition*, vol. 51, no. 40, pp. 9994–10024, 2012.

[19] D. Tang, Y. Sun, Z. Yang, L. Ben, L. Gu, and X. Huang, "Surface structure evolution of LiMn2o4 cathode material upon charge/discharge," *Chem. Mater.*, vol. 26, pp. 3535–3543, May 2014.

[20] R. Vidu and P. Stroeve, "Improvement of the thermal stability of li-ion batteries by polymer coating of LiMn2o4," *Ind. Eng. Chem. Res.*, vol. 43, pp. 3314–3324, May 2004.

[21] A. Bard and L. Faulkner, *Electrochemical Methods: Fundamentals and Applications, 2nd edition*. Wiley, 2 ed., Dec. 2000.

[22] A. Fleischer, "Quarterly progress report on laboratory investigations and research toward the development of nickel cadmium alkaline storage batteries," Nov. 1947.

[23] H. Bauman, "Lithium anode limited cycle secondary battery," Dec. 1963.

[24] J. Besenhard and G. Eichinger, "High energy density lithium cells part 1. electrolytes and anodes," *Journal of The Electrochemical Society*, vol. 68, pp. 1–18, 1976.

[25] M. Hughes, N. Hampson, and S. Karunathilaka, "A review of cells based on lithium negative electrodes (anodes)," *Journal of Power Sources*, vol. 12, pp. 83–144, 1984.

[26] B. Scrosati, "Lithium rocking chair batteries: An old concept?," *Journal of The Electrochemical Society*, vol. 139, pp. 2776–2781, Oct. 1992.

[27] K. Abraham and S. Brummer, "Lithium batteries," in *Lithium Batteries* (J. Gabano, ed.), pp. 371–406, London: Academic Press, 1963.

[28] D. Aurbach, E. Zinigrad, Y. Cohen, and H. Teller, "A short review of failure mechanisms of lithium metal and lithiated graphite anodes in liquid electrolyte solutions," *Solid State Ionics*, vol. 148, pp. 405–416, June 2002.

[29] Y. S. Cohen, Y. Cohen, and D. Aurbach, "Micromorphological studies of lithium electrodes in alkyl carbonate solutions using in situ atomic force microscopy," *J. Phys. Chem. B*, vol. 104, pp. 12282–12291, Dec. 2000.

[30] D. Fauteux, "Formation of a passivating film at the lithium-PEO-LiCF3so3 interface," *Solid State Ionics*, vol. 17, pp. 133–138, Sept. 1985.

[31] K. J. Harry, D. T. Hallinan, D. Y. Parkinson, A. A. MacDowell, and N. P. Balsara, "Detection of subsurface structures underneath dendrites formed on cycled lithium metal electrodes," *Nat Mater*, vol. 13, pp. 69–73, Jan. 2014.

[32] T. Nagaura and K. Tazawa, "Unknown," *Progress of Batteries and Solar Cells*, vol. 9, p. 20, 1990.

[33] A. N. Dey, "Electrochemical alloying of lithium in organic electrolytes," *Journal of The Electrochemical Society*, vol. 118, pp. 1547–1549, Oct. 1971.

[34] D. Fauteux and R. Koksbang, "Rechargeable lithium battery anodes: alternatives to metallic lithium," *J Appl Electrochem*, vol. 23, pp. 1–10, Jan. 1993.

[35] R. Kanno, Y. Takeda, T. Ichikawa, K. Nakanishi, and O. Yamamoto, "Carbon as negative electrodes in lithium secondary cells," *Journal of Power Sources*, vol. 26, pp. 535–543, May 1989.

[36] R. Fong, U. von Sacken, and J. R. Dahn, "Studies of lithium intercalation into carbons using nonaqueous electrochemical cells," *Journal of The Electrochemical Society*, vol. 137, pp. 2009–2013, July 1990.

[37] J. Besenhard, M. Winter, J. Yang, and W. Biberacher, "Filming mechanism of lithium-carbon anodes in organic and inorganic electrolytes," *Journal of Power Sources*, vol. 54, pp. 228–231, Apr. 1995.

[38] C. Wang, H. Nakamura, H. Komatsu, M. Yoshio, and H. Yoshitake, "Electrochemical behaviour of a graphite electrode in propylene carbonate and 1,3-benzodioxol-2-one based electrolyte system," *Journal of Power Sources*, vol. 74, pp. 142–145, July 1998.

[39] D. Armand, "Materials for advanced batteries," in *Materials for Advanced Batteries* (D. Murphy, J. Broodhead, and B. Steele, eds.), p. 145, New York: Plenum Press, 1980.

[40] F. Bonino, L. Lazzari, L. Peraldo Bicelli, B. Di Pietro, and B. Scrosati, "Lithium batteries," in *Lithium Batteries* (H. Venkatasetty, ed.), Pennington, NJ: The Electrocehmical Societry Softbound Proceedings Series, 1981.

[41] B. Peng and J. Chen, "Functional materials with high-efficiency energy storage and conversion for batteries and fuel cells," *Coordination Chemistry Reviews*, vol. 253, no. 2324, pp. 2805 – 2813, 2009. Functional Hybrid Nanomaterials: Design, Synthesis, Structure, Properties and Applications.

[42] M. Lazzari and B. Scrosati, "A cyclable lithium organic electrolyte cell based on two intercalation electrodes," *Journal of The Electrochemical Society*, vol. 127, pp. 773–774, Mar. 1980.

[43] B. Di Pietro, M. Patriarca, and B. Scrosati, "On the use of rocking chair configurations for cyclable lithium organic electrolyte batteries," *Journal of Power Sources*, vol. 8, no. 2, pp. 289–299, 1982.

[44] K. Mizushima, P. Jones, P. Wiseman, and J. Goodenough, "LixCoO2 (0<x<-1): A new cathode material for batteries of high energy density," *Materials Research Bulletin*, vol. 15, pp. 783–789, June 1980.

[45] J. Desilvestro and O. Haas, "Metal oxide cathode materials for electrochemical energy storage: A review," *Journal of The Electrochemical Society*, vol. 137, pp. 5C–22C, Jan. 1990.

[46] M. M. Thackeray, "Structural considerations of layered and spinel lithiated oxides for lithium ion batteries," *Journal of The Electrochemical Society*, vol. 142, pp. 2558–2563, Aug. 1995.

[47] T. Ohzuku and A. Ueda, "Solid?state redox reactions of LiCoO2 (r3?m) for 4 volt secondary lithium cells," *Journal of The Electrochemical Society*, vol. 141, pp. 2972–2977, Nov. 1994.

[48] A. Hirano, R. Kanno, Y. Kawamoto, Y. Takeda, K. Yamaura, M. Takano, K. Ohyama, M. Ohashi, and Y. Yamaguchi, "Relationship between non-stoichiometry and physical properties in LiNiO2," *Solid State Ionics*, vol. 78, pp. 123–131, May 1995.

[49] J. B. Cook, C. Kim, L. Xu, and J. Cabana, "The effect of al substitution on the chemical and electrochemical phase stability of orthorhombic LiMnO2," *Journal of The Electrochemical Society*, vol. 160, pp. A46–A52, Jan. 2013.

[50] T. Ohzuku, M. Kitagawa, and T. Hirai, "Electrochemistry of manganese dioxide in lithium nonaqueous cell: III . x?ray diffractional study on the reduction of spinel?related manganese dioxide," *Journal of The Electrochemical Society*, vol. 137, pp. 769–775, Mar. 1990.

[51] H. Berg and J. Thomas, "Neutron diffraction study of electrochemically delithiated LiMn2o4 spinel," *Solid State Ionics*, vol. 126, pp. 227–234, Nov. 1999.

[52] T. Eriksson, A.-K. Hjelm, G. Lindbergh, and T. Gustafsson, "Kinetic study of LiMn2?o?4 cathodes by in situ XRD with constant-current cycling and potential stepping," *Journal of The Electrochemical Society*, vol. 149, pp. A1164–A1170, Sept. 2002.

[53] H. A. Jahn and E. Teller, "Stability of polyatomic molecules in degenerate electronic states. i. orbital degeneracy," *Proceedings of the Royal Society of London A: Mathematical, Physical and Engineering Sciences*, vol. 161, pp. 220–235, July 1937.

[54] R. Gummow, A. de Kock, and M. Thackeray, "Improved capacity retention in rechargeable 4 v lithium/lithium-manganese oxide (spinel) cells," *Solid State Ionics*, vol. 69, pp. 59–67, Apr. 1994.

[55] M. M. Thackeray, "Manganese oxides for lithium batteries," *Progress in Solid State Chemistry*, vol. 25, no. 12, pp. 1–71, 1997.

[56] J. M. Tarascon, E. Wang, F. K. Shokoohi, W. R. McKinnon, and S. Colson, "The spinel phase of LiMn2?o?4 as a cathode in secondary lithium cells," *Journal of The Electrochemical Society*, vol. 138, pp. 2859–2864, Oct. 1991.

[57] M. R. Palacn, Y. Chabre, L. Dupont, M. Hervieu, P. Strobel, G. Rousse, C. Masquelier, M. Anne, G. G. Amatucci, and J. M. Tarascon, "On the origin of the 3.3 and 4.5 v steps observed in LiMn2?o?4???based spinels," *Journal of The Electrochemical Society*, vol. 147, pp. 845–853, Mar. 2000.

[58] H. Xia, Z. Luo, and J. Xie, "Nanostructured LiMn2o4 and their composites as high-performance cathodes for lithium-ion batteries," *Progress in Natural Science: Materials International*, vol. 22, pp. 572–584, Dec. 2012.

[59] S. Lee, Y. Oshima, E. Hosono, H. Zhou, K. Kim, H. M. Chang, R. Kanno, and K. Takayanagi, "In situ TEM observation of local phase transformation in a rechargeable LiMn2o4 nanowire battery," *J. Phys. Chem. C*, vol. 117, pp. 24236–24241, Oct. 2013.

[60] A. Yamada, "Lattice instability in li(LixMn2?x)o4," *Journal of Solid State Chemistry*, vol. 122, pp. 160–165, Feb. 1996.

[61] J. C. Hunter, "Preparation of a new crystal form of manganese dioxide: ?-MnO2," *Journal of Solid State Chemistry*, vol. 39, pp. 142–147, Sept. 1981.

[62] R. Benedek and M. M. Thackeray, "Reaction energy for LiMn2o4 spinel dissolution in acid," *Electrochemical and Solid-State Letters*, vol. 9, pp. A265–A267, Jan. 2006.

[63] D. H. Jang and S. M. Oh, "Electrolyte effects on spinel dissolution and cathodic capacity losses in 4?v?li?/?li x mn2?o?4 rechargeable cells," *Journal of The Electrochemical Society*, vol. 144, pp. 3342–3348, Oct. 1997.

[64] D. Guyomard and J. M. Tarascon, "Rechargeable li1?+?x mn2?o?4?/?carbon cells with a new electrolyte composition: Potentiostatic studies and application to practical cells," *Journal of The Electrochemical Society*, vol. 140, pp. 3071–3081, Jan. 1993.

[65] G. Pistoia, A. Antonini, R. Rosati, and D. Zane, "Storage characteristics of cathodes for li-ion batteries," *Electrochimica Acta*, vol. 41, pp. 2683–2689, Aug. 1996.

[66] G. Pistoia, D. Zane, and Y. Zhang, "Some aspects of LiMn2?o?4 electrochemistry in the 4 volt range," *Journal of The Electrochemical Society*, vol. 142, pp. 2551–2557, Jan. 1995.

[67] T. Eriksson, A. M. Andersson, A. G. Bishop, C. Gejke, T. Gustafsson, and J. O. Thomas, "Surface analysis of LiMn2?o?4 electrodes in carbonate-based electrolytes," *Journal of The Electrochemical Society*, vol. 149, pp. A69–A78, Jan. 2002.

[68] H. Gabrisch, Y. Ozawa, and R. Yazami, "Crystal structure studies of thermally aged LiCoO2 and LiMn2o4 cathodes," *Electrochimica Acta*, vol. 52, pp. 1499–1506, Dec. 2006.

[69] D. H. Jang, Y. J. Shin, and S. M. Oh, "Dissolution of spinel oxides and capacity losses in 4?v?li?/?li x mn2?o?4 cells," *Journal of The Electrochemical Society*, vol. 143, pp. 2204–2211, Jan. 1996.

[70] K. Leung, "First-principles modeling of the initial stages of organic solvent decomposition on LixMn2o4(100) surfaces," *J. Phys. Chem. C*, vol. 116, pp. 9852–9861, Apr. 2012.

[71] N. Kumar, K. Leung, and D. J. Siegel, "Crystal surface and state of charge dependencies of electrolyte decomposition on LiMn2o4 cathode," *Journal of The Electrochemical Society*, vol. 161, pp. E3059–E3065, Jan. 2014.

[72] S. S. Zhang, K. Xu, and T. R. Jow, "Understanding formation of solid electrolyte interface film on LiMn2?o?4 electrode," *Journal of The Electrochemical Society*, vol. 149, pp. A1521–A1526, Jan. 2002.

[73] K. Edstrm, T. Gustafsson, and J. Thomas, "The cathodeelectrolyte interface in the li-ion battery," *Electrochimica Acta*, vol. 50, pp. 397–403, Nov. 2004.

[74] K. Xu, "Nonaqueous liquid electrolytes for lithium-based rechargeable batteries," *Chem. Rev.*, vol. 104, pp. 4303–4418, Sept. 2004.

[75] J. Choa and M. M. Thackeray, "Structural changes of LiMn2?o?4 spinel electrodes during electrochemical cycling," *Journal of The Electrochemical Society*, vol. 146, pp. 3577–3581, Oct. 1999.

[76] M. Moshkovich, M. Cojocaru, H. E. Gottlieb, and D. Aurbach, "The study of the anodic stability of alkyl carbonate solutions by in situ {FTIR} spectroscopy, EQCM, {NMR} and {MS}," *Journal of Electroanalytical Chemistry*, vol. 497, no. 12, pp. 84 – 96, 2001.

[77] D. Aurbach, M. D. Levi, E. Levi, H. Teller, B. Markovsky, G. Salitra, U. Heider, and L. Heider, "Common electroanalytical behavior of li intercalation processes into graphite and transition metal oxides," *Journal of The Electrochemical Society*, vol. 145, pp. 3024–3034, Sept. 1998.

[78] D. Aurbach, K. Gamolsky, B. Markovsky, G. Salitra, Y. Gofer, U. Heider, R. Oesten, and M. Schmidt, "The study of surface phenomena related to electrochemical lithium intercalation into li x MO y host materials (m = ni, mn)," *Journal of The Electrochemical Society*, vol. 147, pp. 1322–1331, Jan. 2000.

[79] D. Guyomard and J. M. Tarascon, "Li metal?free rechargeable LiMn2?o?4?/?carbon cells: Their understanding and optimization," *Journal of The Electrochemical Society*, vol. 139, pp. 937–948, Apr. 1992.

[80] M. Hirayama, N. Sonoyama, M. Ito, M. Minoura, D. Mori, A. Yamada, K. Tamura, J. Mizuki, and R. Kanno, "Characterization of electrode/electrolyte interface with x-ray reflectometry and epitaxial-film LiMn2o4 electrode," *Journal of The Electrochemical Society*, vol. 154, pp. A1065–A1072, Nov. 2007.

[81] M. Hirayama, H. Ido, K. Kim, W. Cho, K. Tamura, J. Mizuki, and R. Kanno, "Dynamic structural changes at LiMn2o4/electrolyte interface during lithium battery reaction," *Journal of the American Chemical Society*, vol. 132, no. 43, pp. 15268–15276, 2010.

[82] M. Fitzsimmons and C. Majkrzak, "Application of polarized neutron reflectometry to studies of artificially structured magnetic materials."

[83] J. Daillant and Gibaud, eds., *X-ray and Neutron Reflectivity: Principles and Application*. Springer, Berlin Heidelberg, 2009.

[84] M. Seah, "A review of the analysis of surfaces and thin films by AES and XPS," *Vacuum*, vol. 34, pp. 463–478, Mar. 1984.

[85] A.-K. Hjelm, G. Lindbergh, and A. Lundqvist, "Investigation of LiMn2o4 cathodes for use in rechargeable lithium batteries by linear sweep voltammetry: Part i. theoretical study," *Journal of Electroanalytical Chemistry*, vol. 506, pp. 82–91, June 2001.

[86] Q. Zhong, D. Inniss, K. Kjoller, and V. Elings, "Fractured polymer/silica fiber surface studied by tapping mode atomic force microscopy," *Surface Science Letters*, vol. 290, pp. L688–L692, June 1993.

[87] Y. Park, J. Kim, M. Kim, H. Chung, W. Um, M. Kim, and H. Kim, "Fabrication of LiMn2o4 thin films by solgel method for cathode materials of microbattery," *Journal of Power Sources*, vol. 76, pp. 41–47, Nov. 1998.

[88] Y. Park, J. Kim, M. Kim, H. Chung, and H. Kim, "Preparation of LiMn2o4 thin films by a solgel method," *Solid State Ionics*, vol. 130, pp. 203–214, May 2000.

[89] X. Yang, Z. Wen, X. Zhu, and S. Huang, "Electrodeposition of lithium film under dynamic conditions and its application in all-solid-state rechargeable lithium battery," *Solid State Ionics*, vol. 176, pp. 1051–1055, Mar. 2005.

[90] J. Jansta, F. P. Dousek, and J. ?iha, "Quantitative explanation of the mechanism of corrosion of poly(tetrafluoroethylene) caused by active alkali metals," *J. Appl. Polym. Sci.*, vol. 19, pp. 3201–3210, Dec. 1975.

[91] P. Kienzle, K. O'Donovan, J. Ankner, N. Berk, and C. Majkrzak, "reflpak suite," 2000.

[92] G. Knoll, *Radiation Detection and Measurement*. Wiley, 4 ed., 2010.

[93] P. Kienzle, J. Krycka, N. Patel, and I. Sahin, "Refl1d," 2011.

[94] J. A. Dura, D. J. Pierce, C. F. Majkrzak, N. C. Maliszewskyj, D. J. McGillivray, M. Lsche, K. V. ODonovan, M. Mihailescu, U. Perez-Salas, D. L. Worcester, and S. H. White, "AND/r: Advanced neutron diffractometer/reflectometer for investigation of thin films and multilayers for the life sciences," *Review of Scientific Instruments*, vol. 77, no. 7, 2006.

[95] J. Vrugt, C. ter Braak, C. Diks, B. Robinson, J. Hyman, and D. Higdon, "Accelerating markov chain monte carlo simulation by differential evolution with self-adaptive randomized subspace sampling," *International Journal of Nonlinear Sciences and Numerical Simulation*, vol. 10, pp. 273–290, Mar. 2009.

[96] S. C. DeCaluwe, P. A. Kienzle, P. Bhargava, A. M. Baker, and J. A. Dura, "Phase segregation of sulfonate groups in nafion interface lamellae, quantified via neutron reflectometry fitting techniques for multi-layered structures," *Soft Matter*, vol. 10, no. 31, pp. 5763–5776, 2014.

[97] D. W. Shin, J.-W. Choi, W.-K. Choi, Y. S. Cho, and S.-J. Yoon, "XPS/EXAFS study of cycleability improved LiMn2o4 thin film cathodes prepared by solution deposition," *Electrochemistry Communications*, vol. 11, pp. 695–698, Mar. 2009.

[98] K. Shaju, G. Subba Rao, and B. Chowdari, "Lithiated o2 phase, li(2/3)+x(co0.15mn0.85)o2 as cathode for li-ion batteries," *Solid State Ionics*, vol. 152153, pp. 69–81, Dec. 2002.

[99] H. Nesbitt and D. Banerjee, "Interpretation of XPS mn(2p) spectra of mn oxyhydroxides and constraints on the mechanism of MnO$_2$ precipitation.," *American Mineralogist*, vol. 83, pp. 305–315, 1998.

[100] M. C. Biesinger, B. P. Payne, A. P. Grosvenor, L. W. Lau, A. R. Gerson, and R. S. Smart, "Resolving surface chemical states in XPS analysis of first row transition metals, oxides and hydroxides: Cr, mn, fe, co and ni," *Applied Surface Science*, vol. 257, pp. 2717–2730, Jan. 2011.

[101] Q.-H. Wu, A. Thien, and W. Jaegermann, "Electronic structure of LiMn2o4," in *New Trends in Intercalation Compounds for Energy Storage* (C. Julien, J. Pereira-Ramos, and A. Momchilov, eds.), vol. 61 of *NATO Science Series*, pp. 585–590, Springer Netherlands, Jan. 2002.

[102] M. Thackeray, W. David, P. Bruce, and J. Goodenough, "Lithium insertion into manganese spinels," *Materials Research Bulletin*, vol. 18, pp. 461–472, Apr. 1983.

[103] Y. Ebisuzaki, W. J. Kass, and M. O'Keeffe, "Solubility and diffusion of hydrogen and deuterium in platinum," *The Journal of Chemical Physics*, vol. 49, no. 8, pp. 3329–3332, 1968.

[104] J. Sangster and A. Pelton, "The li-pt (lithium-platinum) system," *JPE*, vol. 12, pp. 678–681, Dec. 1991.

[105] J. Hwang and H. Jang, "Evolution of solid electrolyte interphase during cycling and its effect on electrochemical properties of LiMn2o4," *Journal of The Electrochemical Society*, vol. 162, pp. A103–A107, Jan. 2015.